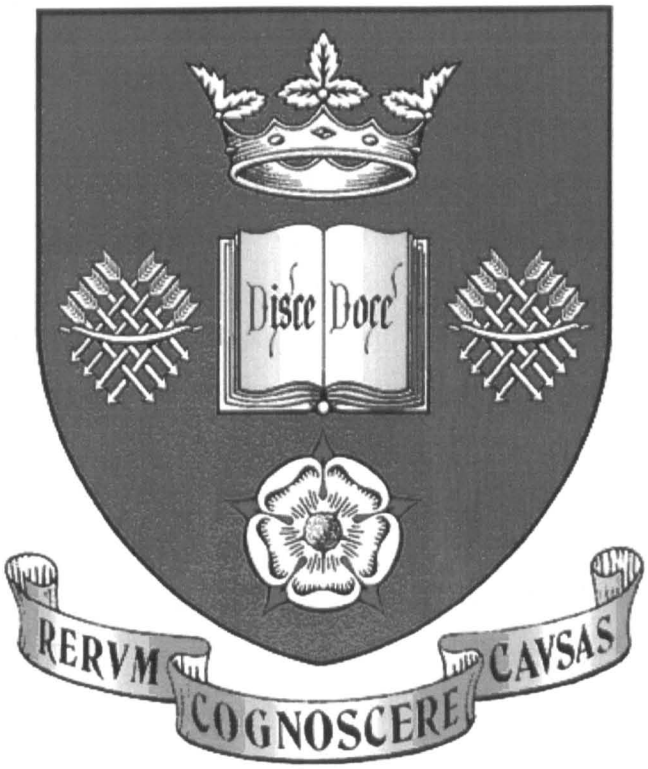

Modelling and Analysis of Radial Mode Piezoelectric Transformers and Inductor-less Resonant Power Converters

Edward Lewis Horsley

A thesis submitted for the degree of PhD in the Department of Electronic and Electrical Engineering, The University of Sheffield.

February 2011

Abstract

Within the electronics industry there is a continual demand for DC-DC power converters that achieve high power density at low cost. Since a piezoelectric transformer (PT) has an electrical equivalent circuit that is similar to several resonant converter topologies, a PT can be used to replace many of the reactive components in these topologies with a single ceramic component, thereby offering potential savings in cost, size, and mass.

The first part of this thesis presents a new equivalent circuit model for one of the most promising types of PT, the radial mode Transoner. This model relates the electrical characteristics of the PT to the physical dimensions and material properties. Considerable insight is then gained about how to design these devices to meet a particular set of converter specifications whilst simultaneously maximising PT power density.

The second part of this thesis concerns the effect of the rectifier topology on PT power density. Using concepts from material science, together with equivalent circuit models of both the PT and the rectifier topologies, it is shown that a given PT will always achieve a higher thermally limited maximum output power when used in an AC-output topology compared to a DC-output topology.

The half-bridge inductor-less PT-based converter topology is particularly attractive because it requires no additional components between the half-bridge and the rectifier. However, it is difficult to achieve zero-voltage-switching (ZVS) without significantly compromising PT power density when using this topology. The third part of this thesis details the development and experimental verification of a new model for the ZVS condition. Using a normalisation scheme and numerical optimisation techniques, the requirements for achieving inductor-less ZVS are accurately quantified for the first time. The impact of these requirements on PT power density is assessed, and design guidelines for maximising PT power density are given.

Summary

This thesis presents novel contributions in three areas of piezoelectric transformer (PT) technology:

1) A model and analysis of the radial mode Transoner PT.
2) An analysis of the effect of the rectifier topology on PT power density.
3) An analysis of the requirements for achieving zero-voltage-switching with the inductor-less half-bridge PT-based topology, and the effect of these requirements on PT power density.

The radial mode Transoner is currently the most promising PT design for many DC-DC converter applications. However, quantitative PT design and power density optimisation require equivalent circuit models that relate the device geometry and material properties to the electrical characteristics of the PT. Chapter 2 details the development of a Mason equivalent circuit for a simple radial mode Transoner design. Once simplified to a lumped equivalent circuit, this is shown to agree with one of the existing models proposed in the literature. The first part of this chapter may therefore be considered as a theoretical proof of this model. The model is verified experimentally using 15W radial mode Transoner samples.

A new model for the radial mode Transoner is then proposed in Chapter 3. Unlike previous models, this includes many of the features that are currently being employed by those at the forefront of the PT industry: electrodes that do not extend to the outer radius of the device (a manufacturing constraint), differing electrode radius in the input and output sections, and the use of additional sets of electrodes (for control or power purposes). Analysis of this model from a power converter perspective is provided, and guidelines for maximising PT power density are given.

The effect of the rectifier topology on PT power density is considered in Chapter 4. Here it is shown for the first time that, for a given PT, the use of a rectifier results in a lower thermally limited maximum PT output power than the AC-output topology. Furthermore, the DC-output capacitively smoothed topologies achieve a lower maximum output power than the DC-output inductively smoothed topologies. Hence, there is a trade-off between the increased PT power density offered by the latter, and the

additional cost and space requirements of the inductor(s). The variation in the number of layers required in the output section of a radial mode Transoner with each type of rectifier is also considered.

In many ways the inductor-less half-bridge topology is the most attractive PT-based topology because no other components are required between the half-bridge and the rectifier. However, it has been known for some time that PTs designed for inductor-less operation achieve lower power density than those designed for with-inductor operation. In Chapter 5, a new model for the zero-voltage-switching (ZVS) condition in the inductor-less topology is presented and verified experimentally. Unlike previous models, the accuracy of this model is indistinguishable from a SPICE simulation, and is therefore as accurate as the standard lumped equivalent circuit representation of a PT will allow. Through the use of a normalisation scheme, and numerical optimisation, it is shown that the ability of a PT to achieve inductor-less ZVS is dependent only on the output topology, the loading factor, the ratio of the effective capacitance at the PT input to the PT output capacitance referred across the transformer turns ratio, and the PT efficiency.

Chapter 6 considers the design requirements for achieving inductor-less ZVS with radial mode Transoner PTs. It is shown that a radial Transoner with a given sized output section, operating with a matched load, will require a larger input section if it is designed for inductor-less operation compared to with-inductor operation. The resulting decrease in PT power density is quantified. It is found that the power density of a radial mode Transoner that is capable of inductor-less ZVS is maximised by designing the PT such that the maximum required output power is to be delivered at the load condition which maximises PT output power for a given equivalent circuit tank current, even though this load condition requires the largest input section to achieve ZVS.

The decrease in PT power density that occurs when moving from a with-inductor to an inductor-less design is greatest with the AC-output topology, and smallest with the DC-output capacitively smoothed topologies. However, when combined with the results from Chapter 4, it is concluded that higher overall PT power density is still achieved with the inductor-less AC-output topology compared to the inductor-less DC-output topologies.

Finally, it is demonstrated in Chapter 7 that, if a half-bridge inductor-less PT-based DC-output capacitively smoothed converter is designed such that it just achieves ZVS at the load into which maximum power is to be delivered, then it is also capable of maintaining ZVS whilst using frequency modulation to provide output voltage regulation in response to load changes. It is also shown that the dead-time must be adjusted substantially in order to do this, and that practical implementation of this converter topology would therefore require some form of adaptive dead-time control.

The author may be contacted at: ehorsley@theiet.org

Parts of this thesis have previously been published, or submitted for publication, in the following conference proceedings and journals:

E. L. Horsley, M. P. Foster, D. A. Stone, "State-of-the-art Piezoelectric Transformer Technology", presented at European Conference on Power Electronics and Applications, 2007.

E. L. Horsley, A. V. Carazo, M. P. Foster, D. A. Stone, "A Lumped Equivalent Circuit Model for the Radial Mode Piezoelectric Transformer", presented at IEEE Applied Power Electronics Conference and Exposition (APEC), 2009.

E. L. Horsley, N. Nguyen-Quang, M. P. Foster, D. A. Stone, "Achieving ZVS in Inductor-less Half-bridge Piezoelectric Transformer based Resonant Converters", presented at International Conference on Power Electronics and Drive Systems (PEDS), 2009.

E. L. Horsley, A. V. Carazo, N. Nguyen-Quang, M. P. Foster, D. A. Stone, "Analysis of Inductor-less Zero-Voltage-Switching Piezoelectric Transformer Based Converters", submitted for publication in IEEE Transactions on Power Electronics.

Acknowledgements

I would like to express my sincere thanks to my supervisors Dr. Martin Foster and Dr. Dave Stone for their advice, support, and encouragement combined with a sense of humour. I thank the Innovative electronics Manufacturing Research Centre (IeMRC) for sponsoring this work. I also thank the Power Sources Manufacturers Association (PSMA) for the generous grant that enabled me to attend the 2009 APEC conference.

I am especially grateful to Dr. Alfredo Carazo of Micromechatronics Inc for giving up countless hours to review my work, the numerous discussions on all aspects of piezo technology, his hospitality during my visit to Micromechatronics, and for providing much valued practical insight from industry.

I would like to thank both Dr. Carazo and Professor Kenji Uchino for enabling me to present some of this work to the ICAT group at Penn State University. I learnt an enormous amount from this trip.

I also thank Dr. Nam Nguyen-Quang for taking the time to discuss my ideas and offering his considerable practical knowledge when needed. In particular, I thank him for his PIC code, which is used in Chapter 5 to generate the MOSFET switching signals.

I thank all those who took the time to answer my questions on their work, including Professor Shuyu Lin, Professor Jiashi Yang, and Professor Uchino. I thank Dr. Richard Tozer for his numerous suggestions regarding amplifier design. I also thank Professor Ray-Lee Lin for his advice, discussions, and hospitality during the 2009 PEDS conference in Taiwan.

I thank all those with whom I have shared an office during my studies. In particular I thank James Holmes for donating his photographic skills, examples of which can be found in Chapters 1 and 5.

Finally I thank all my friends and family for their encouragement, patience, and understanding.

Table of Contents

Abstract i

Summary ii

Acknowledgements v

Nomenclature ix

Chapter 1 - Introduction 1

1.1 Power supplies 1

1.2 The piezoelectric effect 2

1.3 Types of piezoelectric transformer 2

1.4 Radial mode Transoner construction 15

1.5 Equivalent circuit modelling 17

1.6 PT-based converter topologies 21

1.7 PT power density 25

1.8 Introduction to piezoelectric materials for PTs 27

1.9 Piezoelectric materials and power density considerations 28

1.10 Piezoelectric constitutive equations and device analysis 33

1.11 Identification of research goals 38

Chapter 2 - Equivalent circuit modelling of radial mode Transoner PTs (I) 50

2.1 Introduction 50

2.2 Scope, definitions, and assumptions 51

2.3 Derivation 54

2.4 Model verification 65

2.5 Investigating the effect of the constant strain approximation 70

2.6 Correcting for the difference between the model and the experimental results 74

2.7 Vibration velocity profile 78

2.8 Summary 79

2.9 References 80

Chapter 3 - Equivalent circuit modelling of radial mode Transoner PTs (II) 82

3.1 Introduction 82

3.2 Mason equivalent circuit for the radial motion of a composite piezoelectric thin disc with three sets of electrodes 86

3.3 Mason equivalent circuit for the radial motion of a composite piezoelectric thin ring with two sets of electrodes 89

3.4 Mason equivalent circuit for the radial motion of a non-piezoelectric composite thin ring 97
3.5 The complete equivalent circuit model for the radial mode Transoner PT 99
3.6 Comparison between the full and simplified equivalent circuits 111
3.7 Analysis of the equivalent circuit model in a power converter context 119
3.8 Practical design considerations that affect power density 127
3.9 The centre-tapped rectifier problem 130
3.10 Comparison between radial and longitudinal Transoner PTs 131
3.11 Summary 132
3.12 References 133
Chapter 4 - Effect of the output topology on PT power density 135
4.1 Introduction 135
4.2 Output topology analysis 137
4.3 Experimental verification 145
4.4 Implications for PT design 155
4.5 Thermal behaviour of a PT at high power levels 158
4.6 Effect of the rectifier topology on output section layer number 159
4.7 Summary 161
4.8 References 162
Chapter 5 - Analysis of inductor-less zero-voltage-switching piezoelectric transformer based converters 164
5.1 Introduction 164
5.2 Inductor-less PT-based converter operation 165
5.3 Analysis 167
5.4 Model verification 177
5.5 The ZVS profile of a PT 178
5.6 Design criteria for inductor-less ZVS with the AC-output topology 183
5.7 Consideration of mechanical losses 186
5.8 Design chart for the AC-output topology 188
5.9 Design criteria for inductor-less ZVS with DC-output topologies 188
5.10 Design criteria for inductor-less ZVS with the DC-output full-bridge capacitively smoothed topology 190
5.11 Design criteria for inductor-less ZVS with the DC-output full-bridge inductively smoothed topology 193

5.12 Design criteria for inductor-less ZVS with the half-wave capacitively smoothed and current doubler topologies 196
5.13 Design charts for the DC-output topologies 196
5.14 Summary 197
5.15 References 199
Chapter 6 - Analysis of inductor-less ZVS with radial mode Transoner PTs 200
6.1 Introduction 200
6.2 Analysis of radial mode Transoner PTs with input and output section electrode radius equal to the outer radius 200
6.3 Impact of unequal electrode radii on the ZVS condition and power density 207
6.4 Guidelines for maximising the power density of PTs capable of inductor-less ZVS 212
6.5 Relative overall PT power density comparisons 216
6.6 Summary 218
6.7 References 218
Chapter 7 - Inductor-less PT-based DC-output capacitively smoothed converters with output voltage regulation 219
7.1 Introduction 219
7.2 PT design method 220
7.3 Theoretically optimum design example 224
7.4 Practical design considerations 226
7.5 Effect of output voltage regulation on ZVS 227
7.6 Summary 233
7.7 References 234
Chapter 8 - Conclusions and further work 235
8.1 Conclusions 235
8.2 Further work 237
Appendix A - Longitudinal mode Transoner equivalent circuit 239
Appendix B - Rectifier models 246
Appendix C - Amplifier schematic 251

Nomenclature

Symbol	Description	Units
A	"Force factor"	newton per volt
A_1, A_2, A_3, B_1, B_2, B_3	Constants in the equations of motion (Chapters 2 and 3 only)	
B_1, B_2, B_3, B_4	Constants in the solutions to the differential equations which describe the behaviour of modes 1 and 3 (Chapter 5 only)	
a, b, c	Radii of the various regions within a radial mode Transoner PT	meter
C	Capacitance	farad
d	Piezoelectric constant	meter per volt, or coulomb per newton
D	Electric displacement	coulomb per square meter
D (superscript)	At constant electric displacement	
E	Electric field	volt per meter
E (superscript)	At constant electric field	
f	thickness fraction	
F	Force	newton
i, I	Current	ampere
j	$\sqrt{(-1)}$	
$J_0(\,)$	Bessel function of the first kind and zero order	
$J_1(\,)$	Bessel function of the first kind and first order	
k_p	Planar coupling factor	
k_{31}	Transverse coupling factor	
k_{33}	Longitudinal coupling factor	
k_t	Thickness coupling factor	
l	Length	meter
L	Inductance	henry
M	Loading factor. Defined as the ratio of the actual load resistance to the load resistance which maximises total PT output power for a given tank current.	
n	Number of layers	
N	Equivalent number of turns on an ideal transformer	
P	Power	watt
$P_{density}$	Power density	watt per cubic meter
$\overline{P}$	An effective radial Young's modulus	newton per square meter
Q	Charge	coulomb
Q_m	Mechanical quality factor (of a single material)	

$\overline{Q}_m$	Effective mechanical quality factor of the complete device	
r	Radial coordinate	meter
R	1) Resistance (always appears with a subscript) 2) The first positive value that satisfies the equation governing the location of the radial resonances.	1) ohm 2)
s	Elastic compliance	square meter per newton
S	Strain	
S (superscript)	At constant strain	
t	1) Time 2) Thickness	1) second 2) meter
t_d	Dead-time. The length of time between one MOSFET turning off and the other MOSFET turning on	second
t_{df}	Dead-time fraction, $t_{df} = t_d / T$	
t_{in}	The thickness of the piezoelectric ceramic in a single input section layer	meter
t_{out}	The thickness of the piezoelectric ceramic in a single output section layer	meter
t_{ter}	The thickness of the piezoelectric ceramic in a single tertiary section layer	meter
t_{in}^{total}	The total thickness of piezoelectric ceramic in the input section. $t_{in}^{total} = n_{in} t_{in}$	meter
t_{out}^{total}	The total thickness of piezoelectric ceramic in the output section. $t_{out}^{total} = n_{out} t_{out}$	meter
t_{ter}^{total}	The total thickness of piezoelectric ceramic in the tertiary section. $t_{ter}^{total} = n_{ter} t_{ter}$	meter
t_{total}	The total thickness of the PT	meter
T	1) Stress 2) Switching period (i.e. the inverse of the switching frequency)	1) newton per square meter 2) second
T (superscript)	At constant stress	
v	1) Voltage 2) Vibration velocity	1) volt 2) meter per second
V	Voltage	volt
V_d	The on-state voltage drop of a single rectifier diode	volt
V_{df}	The ratio of the on-state voltage drop across a single rectifier diode to the voltage across the load resistance	
W	Width	meter
x_1, x_2, x_3	Cartesian coordinates	meter
X	A normalisation factor defined as $\frac{C_1}{N^2 C_{out}}$	
Y	A normalisation factor defined as $\frac{C_{eff}}{N^2 C_{out}}$	

Y_{max}	The largest value of Y at which inductor-less ZVS can be achieved.	
Y_E	Young's modulus of the electrode material	newton per square meter
Y_I	Young's modulus of the isolation material	newton per square meter
Y_N	Young's modulus of the non-piezoelectrically active (i.e. unpoled) ceramic material	newton per square meter
$\overline{Y}_r$	An effective radial Young's modulus	newton per square meter
$\overline{Y}_l$	Effective longitudinal Young's modulus	newton per square meter
$Y_0(\,)$	Bessel function of the second kind and zero order	
$Y_1(\,)$	Bessel function of the second kind and first order	
z	Axial coordinate	meter
Z	Electrical impedance	ohm
α	An angle in the models for the inductively smoothed rectifier topologies (Chapters 4, 5, and Appendix B only).	radians
α_1, α_2	Constants in the solutions to the differential equations which describe the behaviour of modes 1 and 3 (Chapters 5 and 7 only)	
β	1) Impermittivity (Chapter 1 only) 2) Equivalent wave number (Chapters 2, 3, and Appendix A only) 3) An angle in the models for the inductively smoothed rectifier topologies (Chapters 4, 5, and Appendix B only).	1) meter per farad 2) radians per meter 3) radians
β_1, β_2, β_3	Equivalent wave number in regions 1, 2, and 3 respectively (Chapter 3 only)	radians per meter
β_1, β_2	Constants in the solutions to the differential equations which describe the behaviour of modes 1 and 3 (Chapters 5 and 7 only)	
ε	Permittivity	farad per meter
ϕ	Phase angle of the tank impedance	degrees or radians
θ	Azimuthal coordinate	degrees or radians
ρ	Mass density	kilogram per cubic meter
σ	Poisson's ratio	
$\overline{\upsilon}$	Effective speed of sound in a composite device	meter per second
ω	Angular frequency (2π .frequency)	radians per second
ξ	Displacement	meter
ψ	Loss factor (the inverse of the electrical efficiency of the PT)	

Chapter 1 - Introduction

1.1 Power supplies

Within the electronics industry there is a continual drive to make products that are smaller, cheaper, and lighter, with ever increasing functionality. A power supply of some form is present in the vast majority of end-user products, and is subject to similar demands; greater power density (power per unit volume), lower mass density (mass per unit volume), and lower cost. More recently, concern about the unsustainable manner in which energy is currently being "used" has led to high efficiency becoming increasingly important, and the introduction of various standards. However, high efficiency and high power density are usually intrinsically linked.

Switch mode power supplies (SMPS) have become the power supply of choice in both AC-DC and DC-DC applications. Since they operate at much higher frequencies than the mains supply, the reactive components can generally be made much smaller and lighter than the traditional combination of line-frequency transformer, rectifier, and linear regulator that was used in AC-DC applications. Many SMPS topologies have been commercialised, and new variations are continually being proposed. In general SMPS can be grouped into those which are hard-switched, and those which are soft-switched. Examples of hard-switched converters include the Buck, Boost, Buck-boost, Cúk, and Flyback converter.

As the switching frequency of a hard-switched converter is increased, the power dissipation due to switching losses in the semiconductor power switches also increases, and begins to limit the switching frequency that can be used efficiently. In general, one aims to keep the semiconductor switches in a SMPS either fully-on, or fully-off. Power dissipation is low in each of these states due to the voltage across the device being very small, and the current through the device being very small, respectively. However, whilst switching between the two states in a hard-switched converter, there is simultaneously a substantial voltage across and current through the device, resulting in power loss in the form of heat. Soft-switching was introduced to circumvent this, and involves the use of topologies and switching strategies that result in either the voltage across the switches or the current through the switches being zero at the point of turn-on

and turn-off. The topologies that are discussed in this thesis are all of the soft-switched load-resonant type.

1.2 The piezoelectric effect

Piezoelectric materials develop a charge when mechanically stressed (the direct piezoelectric effect) and develop a strain when an electric field is applied (the converse piezoelectric effect) [1]. A piezoelectric transformer (PT) uses both of these effects to couple energy electromechanically from one set of terminals to another, in an analogous way to a conventional transformer using electromagnetic coupling. PTs are usually made from piezoelectric ceramics, and the first PT was demonstrated by C. A. Rosen in the 1950s [2-5].

PTs can achieve very high power densities [6, 7] and high efficiencies, allow a high level of converter integration to be achieved, create little electromagnetic interference (EMI), and can be made cost effective when manufactured in large quantities. However, because they behave like a resonant band-pass filter with a high Q factor, high power throughput can only be achieved when operating close to the resonant frequency. The frequencies of mechanical (and therefore electrical) resonance are determined by the size and shape of the PT, the nature of the materials employed, and by the load(s) connected to the PT output(s).

1.3 Types of piezoelectric transformer

Many different PT designs have been proposed. They are classified here according to the type of vibration mode they are designed to utilise: longitudinal, radial, thickness, or thickness-shear. The modes of an object are basically the natural frequencies, which are the frequencies at which the object will resonate. Each mode has a natural frequency and a characteristic displacement profile, called the mode shape (see page 2 of [8]). The displacement and stress profile of a long thin bar operating at the first and second longitudinal modes is shown in Figure 5.46 of [9].

A. Longitudinal

Longitudinal mode PTs are usually rectangular cuboids, with a length dimension considerably larger than the width and thickness dimensions, which are operated at a frequency close to one of the longitudinal resonances. Devices operating at the first resonance are often referred to as $\lambda/2$ mode devices, whilst those operating at the second are referred to as λ mode devices. The best known longitudinal mode PT is the Rosen, shown in Figure 1.1.

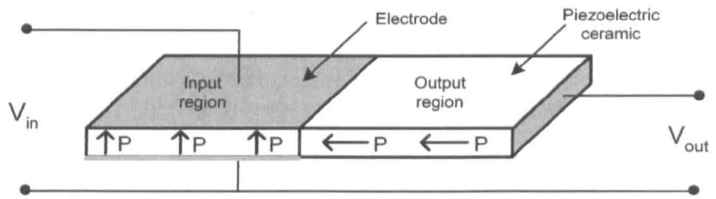

Figure 1.1: Single-layer Rosen PT. The arrows marked "P" indicate the direction of poling.

Rosen PTs have an input section that is poled in the thickness direction, and an output section poled in the longitudinal direction. Key publications on the Rosen transformer include [2-4, 9-13]. When an AC voltage is applied to the thickness poled half of the ceramic, a continual longitudinal vibration occurs throughout the entire device at the frequency of the applied voltage (the converse piezoelectric effect). The vibrations then induce a potential difference in the output section (the direct piezoelectric effect). Thus, the input region behaves like a piezoelectric actuator, and the output region behaves like a piezoelectric transducer. When driven at resonance, the amplitude of the vibrations and the associated strains are maximal for a given input voltage. Although the device shown in Figure 1.1 has a single-layer input section, designs with multilayer input sections are common because they yield higher transformation ratios. For the single layer design shown in Figure 1.1, the transformation ratio (N in the equivalent circuit, see Section 1.5) will be approximately proportional to the ratio of the length of the output section to the thickness of the PT [9]. A commercial multilayer Rosen PT is shown in Figure 1.2. This is a completely co-fired device (see Section 1.4) and has a rated output power and power density of 5W and 9.26W/cm^3 [14].

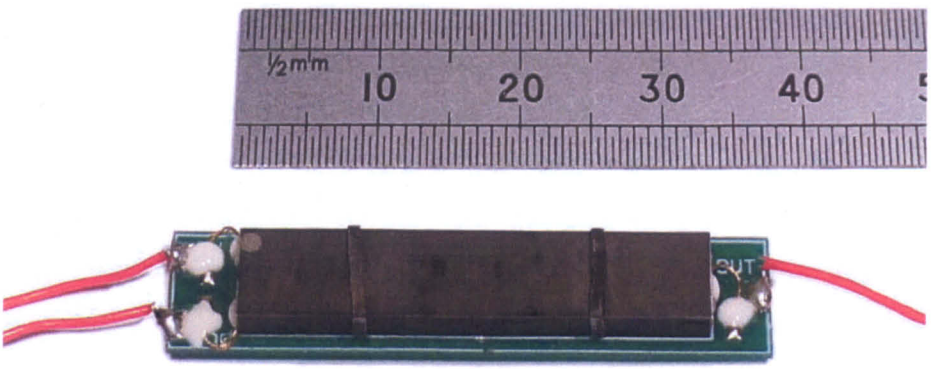

Figure 1.2: Commercial 5W Rosen PT.

Rosen PTs find commercial use where very high voltages and low currents are required. Such applications include cold cathode fluorescent lamp (CCFL) backlighting for LCDs, negative ion generators, photomultipliers, and field emission displays (FEDs). Although Rosen PTs are still the most popular choice in step-up applications, they are generally less suitable for use in step-down applications requiring high power density.

The electromechanical coupling factors of a piezoelectric material describe how well the material can convert electrical energy to mechanical energy, or vice versa [1]. The coupling factors that correspond to the transformations that occur in the input and output sections of a Rosen PT are the transverse coupling factor k_{31} and longitudinal coupling factor k_{33} respectively. k_{31} is the lowest of the main coupling factors in most piezoelectric materials, and this is probably one reason why Rosen PTs tend to have modest power densities compared to other designs. Analytical expressions for the power density of a PT design usually involve the coupling factors, and hence a high coupling factor is essential for achieving high power density. However, because there are other geometrical factors involved, it is not sufficient to compare the power density of one type of PT against another based solely on the coupling factors that apply to each. Furthermore, since the coupling factors do not reflect the losses or the proportion of unconverted energy that is recovered, they do not define the overall electrical efficiency of a PT.

Several other types of longitudinal mode PT have been proposed [15-23], including that shown in Figure 1.3 [24]. Conceptually, the design shown in Figure 1.3 is attractive because it uses k_{33} coupling in both input and output sections, and k_{33} is often the largest coupling factor of a piezoelectric material. However, this design is likely to

require a large number of layers to deliver considerable power at low output voltages because the area of an individual electrode is constrained by the overall geometry (since the length must be considerably larger than the width and thickness) to be relatively small. The designs proposed in [15-23] are all similar to a Rosen in that the input and output sections are situated one-after-the-other along the direction of wave propagation. A fundamentally different arrangement is that of the longitudinal Transoner®, also referred to as a T3 design, shown in Figure 1.4 and Figure 1.5. Here, the input and output sections are positioned side-by-side and run concurrently along the direction of motion. Note that whilst the input and output sections are shown as being poled in the thickness direction in Figure 1.4, the input and/or output may instead be poled longitudinally (and have electrodes positioned accordingly). If a considerable voltage step-up is required, the input will be poled in thickness and the output poled longitudinally. The longitudinal mode Transoner shown in Figure 1.5 has two input sections, with the output section sandwiched in between. This arrangement helps to ensure a more uniform longitudinal strain profile in the thickness direction.

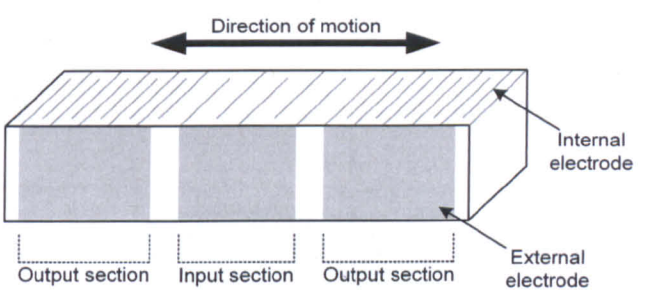

Figure 1.3: Longitudinal mode transformer using k_{33} coupling [24].

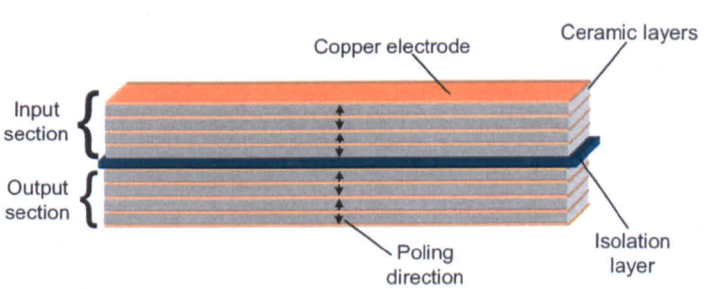

Figure 1.4: Diagram showing the construction of a longitudinal mode Transoner. The device shown here is purely bonded (see Section 1.4), with all layers poled in the thickness direction.

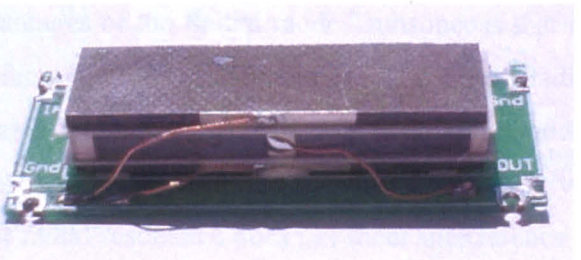

Figure 1.5: Longitudinal mode Transoner, 10W design. Construction is co-fired and bonded (see Section 1.4) with a split input section. Photo courtesy of Micromechantronics Inc.

b) Radial mode

Radial mode devices are disc or ring-shaped and operated at a frequency close to a radial resonance. Several arrangements of radial mode device have been proposed, of which the radial mode Transoner is probably the best known. Key publications on the radial mode Transoner include [25-27]. Although primarily concerned with contour mode devices (see below), [28] should also be regarded as a key work on the radial mode Transoner. The construction of a very simple, single layer input, single layer output, radial mode Transoner is shown in Figure 1.6. Note that the input and output sections run concurrently along the direction of motion; this is the defining feature of a Transoner [25, 29]. Radial mode Transoners are also referred to as T1 devices.

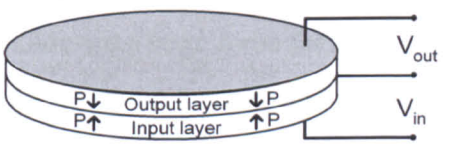

Figure 1.6: Single layer input, single layer output, radial mode Transoner PT.

Radial mode Transoners are suitable for use in step-up and step-down converters, and have been demonstrated in a wide range of applications from inductor-less fluorescent lamp ballasts [27, 30-32] to laptop power supplies [33, 34]. The coupling factor that most closely corresponds to radial mode vibration is k_p. For most piezoelectric materials k_p is one of the largest coupling factors, and this helps radial mode PTs achieve high power densities. Radial mode Transoner PTs have been demonstrated at power levels exceeding 100W and through further development are expected to exceed 200W [5].

One of the main advantages of the Radial mode Transoner is that it is relatively simple to design and manufacture. Unlike thickness mode devices, radial mode Transoners have a geometry which naturally results in the first radial mode having the lowest resonant frequency of the major vibration modes. As such, it is very easy to design a device where the first radial resonance does not incur interference from other vibration modes. In general, it is extremely important that a resonant piezoelectric device has only one resonance occurring in the frequency range in which it is designed to be used, otherwise the resonances will interfere with one another and tend to cancel each other or result in a highly disturbed gain-frequency response and poor efficiency. Like radial mode devices, longitudinal mode PTs also have a geometry that naturally results in the low order longitudinal modes being undisturbed.

Since a PT transfers energy electromechanically, it is important that the method by which the device is mounted to the PCB does not damp its motion. Disc shaped PTs in radial motion have a nodal point (a point where the amplitude of the displacement is zero) at the centre of the disc. Thus, a simple adhesive pad can be placed in the centre of one of the PTs major surfaces to securely mount the device without noticeably affecting its electromechanical behaviour.

The geometry and layout of a radial mode Transoner allows for the electrodes to have a large radius, which in turn allows for large force factors to be achieved (see Chapters 2 and 3). One of the problems with trying to make a longitudinal mode device which uses k_{33}, such as that shown in Figure 1.3, is that a very large number of layers are required to achieve reasonable sized force factors because the overall geometry of such a device dictates that the area of a single electrode will be relatively small.

Because radial mode Transoners have: 1) a geometry that naturally results in a clean frequency response around the first radial resonance, 2) a relatively large coupling factor, 3) a layout that allows for large electrode radii and force factors, 4) an overall shape and electrode profile that is simple to manufacture, and 5) a conveniently located nodal point, they are currently one of the most promising designs for use in resonant power converters, and hence the subject of a large part of this thesis. Much of the early research work on radial mode Transoners was conducted at Virginia Tech [27, 31, 35], where the main focus was to create inexpensive lamp ballasts that required no magnetic components. Two key themes of the Virginia Tech work were equivalent circuit

modelling of the devices [27], and the modelling of a converter topology that required no magnetic components [27, 32]. A considerable part of this thesis is devoted to building on these two themes (see Chapters 2, 3, 5, and 6).

Another type of radial mode device, often referred to as a "ring-dot" arrangement, is shown in Figure 1.7 [36-46]. This layout is similar to a Rosen in that the input and output sections are situated, one-after-the-other, along the direction of motion. Although there have been several recent works proposing equivalent circuit models of this PT, the model of E. C. Munk [47] for a single layer disc with two concentric electrodes was probably the first.

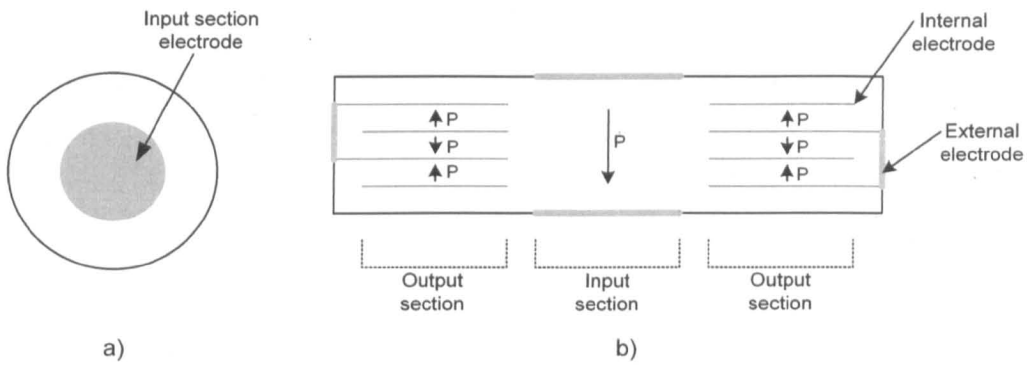

Figure 1.7: Ring-dot PT. a) Aerial view. b) Cross-section.

Ring-shaped radial mode PTs with concentric electrode patterns, such as that shown in Figure 1.8, have also been proposed [48-52]. These often use relatively high order radial modes, such as the third or fourth, and consequently operate at relatively high frequencies for their size. The author is not aware of multilayer versions of these devices having been tested. Whilst multilayer constructions are certainly possible for devices with only two concentric regions, there are obvious problems with regard to making connections to the middle section of a fourth radial mode device (such as that shown in Figure 1.8) if that section has multiple layers in the thickness direction. It is the author's opinion that it is essential to be able to vary the number of electrode layers within the input and output section of a PT if a wide range of relatively high power converter designs are to be achievable; whilst there may be some specifications of converter that can be achieved with single layer input and output sections, step-down converters for delivering significant power into low resistance loads will almost certainly require many layers to be used in the output section, regardless of the specific type of PT that is used. Therefore designs with only two concentric rings of electrodes

are likely to be more flexible in terms of the converter specifications that can be achieved than high order mode devices with many concentric sets of electrodes.

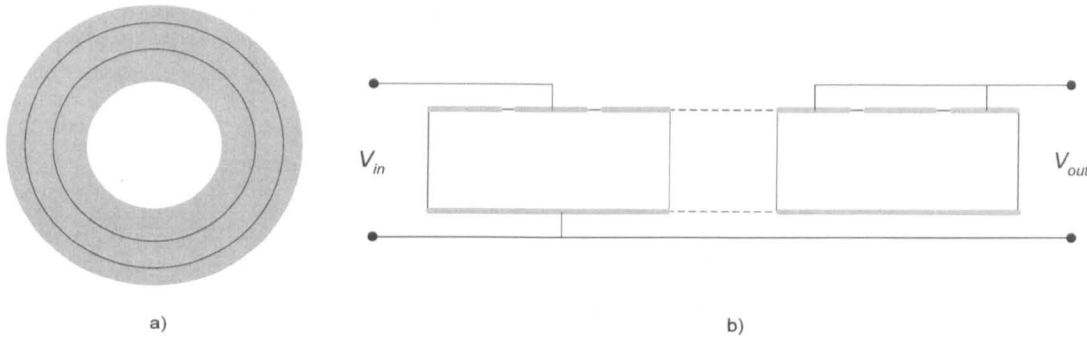

Figure 1.8: Fourth radial extensional mode ring-shaped transformer [48]. a) Aerial view, b) Cross-sectional view.

With any type of PT (or indeed any type of piezoelectric resonator), it is important to ensure that the electrode configuration is such that the polarity of the electric field profile is in agreement with the polarity of the stress profile that is associated with the desired vibration mode. Otherwise, the mode will only be weakly excited, or in some cases (where complete cancellation occurs) not at all. This is why the electrode pattern shown in Figure 1.8 is required to excite the fourth radial mode of a ring in an effective manner [48], and why a fully electroded longitudinal mode resonator bar (such as that shown later in Figure 1.25) cannot be excited at the second longitudinal mode (i.e. the λ mode). Further information can be found in [48] and pages 226 to 228 of [9]. Generally, the higher the mode number, the more complex the electrode layout will need to be along the direction of wave propagation in order to effectively excite it. The first radial resonance of a thin disc has a radial stress profile as shown in Figure 1.9; since the stress has the same polarity at all points along the radial direction, this mode can be effectively excited in a piezoelectric ceramic disc poled in the thickness direction by fully electroding the major surfaces, and this is the approach used in the radial mode Transoner. Note that the stress at the outer radius is zero because the disc is assumed to be unconstrained in the radial direction (this constitutes one of the boundary conditions used in the analysis of the free radial vibration of a disc – see Chapter 2).

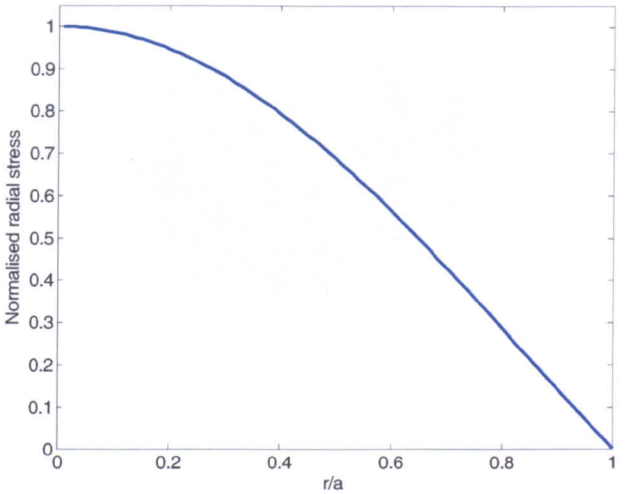

Figure 1.9: Radial stress profile for the first radial mode of a disc. Stress is shown normalised to the peak stress, which is the stress at the centre of the disc (i.e. the nodal point). r is the radial coordinate, a is the radius of the disc.

The modelling work of Holland [53-56] is of particular note for PTs with concentric electrode patterns, and other types of PT, because the approach he developed can be used for devices with an arbitrarily complex electrode pattern along the direction of motion. However, it is not clear whether such an approach could be immediately applied to a radial mode Transoner design because a piecewise description of electric field would be required as a function of both thickness and radial directions, rather than just the radial direction.

Finally, during the 1990s, NEC developed the so-called contour vibration mode PT [28, 57, 58], shown in Figure 1.10. This device consists of a square piece of ceramic with circular electrodes stacked in the thickness direction, and is therefore a Transoner-type layout. This device was modelled by NEC as a radial mode device [28, 58]. NEC conducted research into many different types of PT throughout the 1990's, and their publications (most of which are to be found in the Japanese Journal of Applied Physics) cover all facets of piezoelectric transformer technology. Although an analytical model has yet to be developed for the contour vibration, it is likely that the corners of the device (which are not covered by the circular electrodes) contribute only to the mechanical losses of the device, without aiding power handling. Thus, for a given electrical specification, a radial mode Transoner is likely to result in a higher power density than a contour vibration mode device. This prediction is based solely on the author's experience with modelling radial mode Transoners where the electrodes do not extend to the outer radius of the device (see Chapter 3).

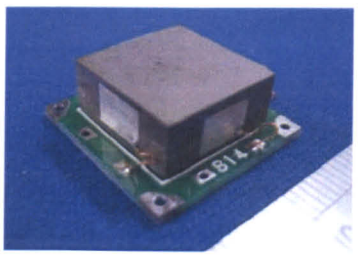

Figure 1.10: Contour vibration mode PT. Photo courtesy of Micromechantronics Inc.

c) Thickness mode

Thickness mode devices have a thickness dimension that is much less than the other dimensions (i.e. radius in the case of a disc shape, or width and length in the case of a cuboid), and are operated at a frequency that corresponds to a thickness extension vibration mode [5, 59-81]. The input section and output section are situated in the conventional manner, one-after-the-other, along the direction of motion. The input and output section layers are poled in the thickness direction. The coupling factor that applies to this geometry and vibration mode (i.e. thickness much less than other dimensions and motion in the thickness direction) is k_t, which is distinct from k_{33}. Note that if the thickness dimension was made much larger than the other dimensions, then the device would effectively become the longitudinal mode design shown in Figure 1.3, and the applicable coupling factor would become k_{33}.

A thickness mode design similar to that proposed in [59, 63, 78] is shown in Figure 1.11. The diagram in Figure 1.11b has been expanded in the thickness direction in order to show the electrode layout and is therefore not to scale. The overall device proportions are as shown in Figure 1.11a. This type of PT behaves like a thin plate in a thickness vibration mode, and therefore requires that the lateral dimensions be much larger than the dimension associated with the elastic wave propagation (i.e. the thickness direction) (see page 299 of [82]). The transformation ratio (N in the equivalent circuit, see Section 1.5) of a thickness mode device is approximately proportional to the ratio of the thickness of a single output layer to the thickness of a single input layer [59].

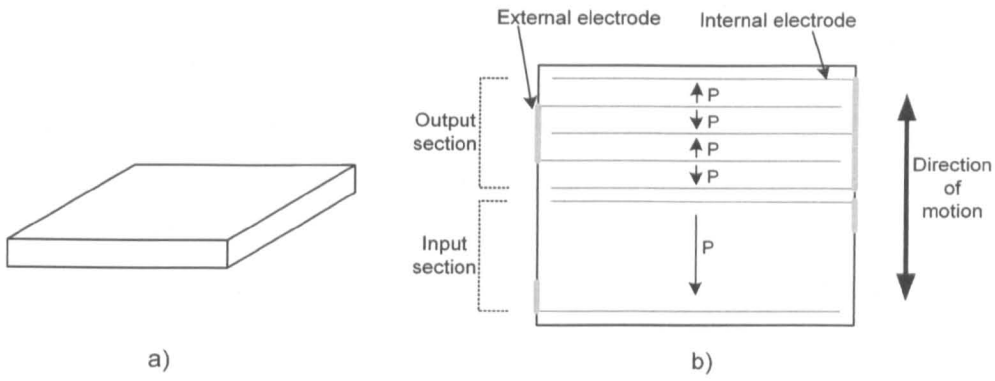

Figure 1.11: Thickness mode device similar to that in [63]. a) Outer dimensions shown approximately to scale (note that the thickness dimension is considerably smaller than length and width). b) Cross sectional diagram expanded in the thickness direction in order to show electrode configuration (and therefore not to scale).

A fundamental problem with thickness mode devices is that, because the direction of wave propagation is not the largest dimension (as it is with longitudinal and radial mode devices), high order length extensional and width extensional resonances occur in the vicinity of the thickness resonances [6, 83]. In other words, because the length and width are much larger than the thickness, the frequency of the first length mode and width mode is much lower than the first thickness mode, which means that high order length and width modes tend to occur in the same frequency region as the first thickness mode. High order spurious modes that occur in the vicinity of the desired vibration mode result in a jagged, non-smooth frequency response, as shown in Figure 4a of [63]. Apart from the obvious converter control issues, spurious vibration modes increase the PT losses and attenuate the main vibration mode, result in poor efficiency, and compromise power density. It is therefore desirable for the frequency response of a PT to have minimal disturbance from spurious modes in the vicinity of the resonance at which the PT is designed to operate.

Since the largest dimension of a PT will define the lowest resonant frequency, one way of avoiding spurious vibration modes would be to alter the device geometry such that the thickness dimension became larger than the length and width dimensions. However, doing so would effectively create a longitudinal mode device, with geometry such that the area of a single electrode would be relatively small (see Section 1.3a). Therefore previous research has concentrated on suppressing the high order modes. The approach in [59, 63, 78] was to use a barium titanate ceramic with a high level of piezoelectric anisotropy, such that the coupling factor of the other modes was relatively small. A

comparison of devices with and without suppression of the high order modes is shown in Fig. 4. of [63].

In 2000, a ring-shaped thickness mode design was patented by Noliac [76]. An example of this design is shown in Figure 1.12. The location of the high order radial modes in a ring can be adjusted by altering the ratio of the inner radius to outer radius [84]. Furthermore, as this ratio tends to unity (i.e. very small wall thickness), the frequency of the second radial mode tends to infinity [84] (see also [76, 85]). Thus, by adjusting this ratio, the designer can ensure that high order radial modes do not occur in the frequency range of the first thickness mode, and a relatively clean frequency response can be obtained. The advantage of the ring shaped design can be seen by comparing the frequency response of the thickness mode PT designs in [78] and [76]; i.e. less disturbance from other modes. However, the need to suppress the radial modes in this manner introduces additional constraints on the design (i.e. there are more requirements that must be simultaneously met), and probably has a negative impact on the designer's ability to maximise power density. The relatively complex shape (including the profile at the inner and outer radius) may also increase production costs.

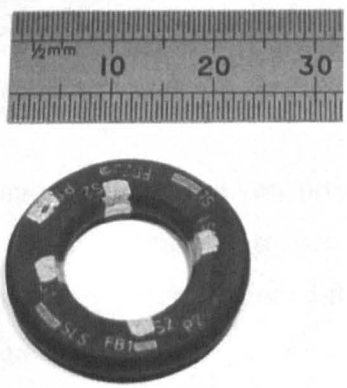

Figure 1.12: Noliac ring-type thickness mode PT.

A substantial amount of research was conducted on the Noliac device, and other aspects of PT technology, by a team at Universidad Politécnica de Madrid (UPM), Spain [64-73]. Much of the work published by a team at Universidad de Oviedo [86-95], also made use of Noliac devices. At the time of writing, this device is being developed further by Noliac and a team at the Technical University of Denmark [96].

D. Thickness-shear vibration mode

The thickness-shear vibration mode PT differs from the designs previously described, in that the electric fields are applied and generated orthogonally to, rather than parallel to, the direction of poling in the input and output sections of the PT. Key publications on thickness-shear mode PTs include [97-103]. Excitation of the input section causes a shear strain to develop throughout the PT body, which in turn generates a voltage in the output section. Most PZT materials suitable for use in PTs have a large shear mode electromechanical coupling factor k_{15}, allowing high power densities to be achieved with this type of PT. Like the thickness and radial mode designs, a thickness-shear mode PT has unidirectional poling. However, the production process is complicated by the need to apply one set of electrodes to pole the material, and another set to actually operate the device. A diagram of a device demonstrated by Du et al. in [101] is shown in Figure 1.13.

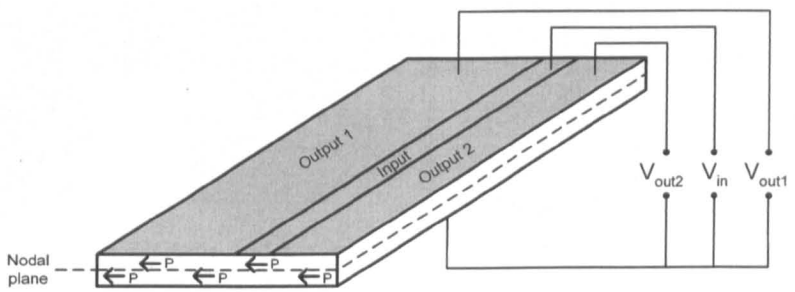

Figure 1.13: Thickness-shear vibration mode PT [101].

Although several research publications have shown very promising performance figures with this design (7.9W output at 20°C temperature rise with a power density of 52.7W/cm^3 in [99]), it remains somewhat less developed than the other three. To the author's knowledge, multilayer devices have not yet been demonstrated, and lumped equivalent circuit models which include multilayer input and output sections and which relate the electrical currents and voltages to the vibration velocity within the device have yet to be developed, making quantitative design somewhat difficult (see Section 1.5). Like thickness mode devices, it can be difficult to obtain a clean frequency response from a thickness-shear mode device due to interference from high order length and width modes (see Fig. 7 in [101]).

1.4 Radial mode Transoner construction

There are three types of Transoner PT construction: purely bonded, co-fired and bonded, and purely co-fired. Examples of each are shown in Figures 1.14, 1.15, and 1.16. The purely bonded radial mode Transoner consists of two or more individual piezoelectric discs. Each disc has a very thin silver electrode on the major surfaces, as shown in Figure 1.14c and d. Copper electrodes with a small tab that extends past the radius of the ceramic discs are placed between the discs and on the top of the top disc and on the bottom of the bottom disc. The layers of copper and ceramic are bonded to each other using a suitable adhesive; a comparison of three different types was published in [104]. If an isolation layer is required between the input and output sections, a thin layer of alumina is often used, as shown in Figure 1.14a. In contrast to the other two types of construction, the individual discs that make up a purely bonded device are usually poled before they are bonded together.

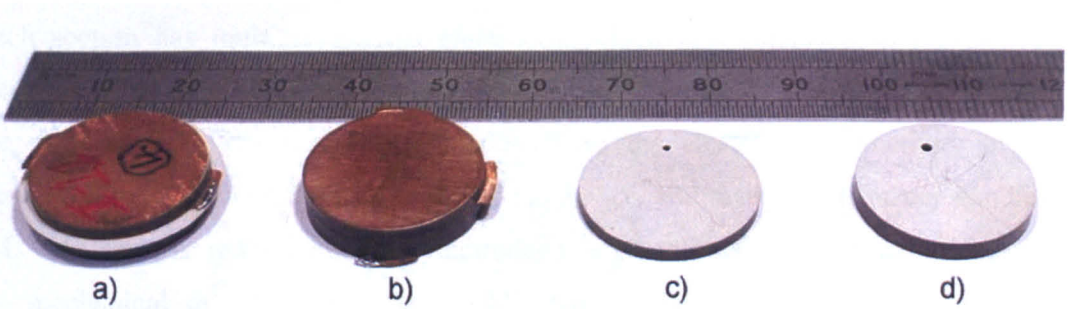

Figure 1.14: Purely bonded radial mode Transoner PTs and piezoelectric discs. a) Isolated 15W T1-15W radial mode Transoner PT, b) non-isolated 15W T1-15W radial mode Transoner PT, c) input section disc used in T1-15W devices (material is American Piezo Ceramics Inc. APC841), d) output section disc used in T1-15W devices.

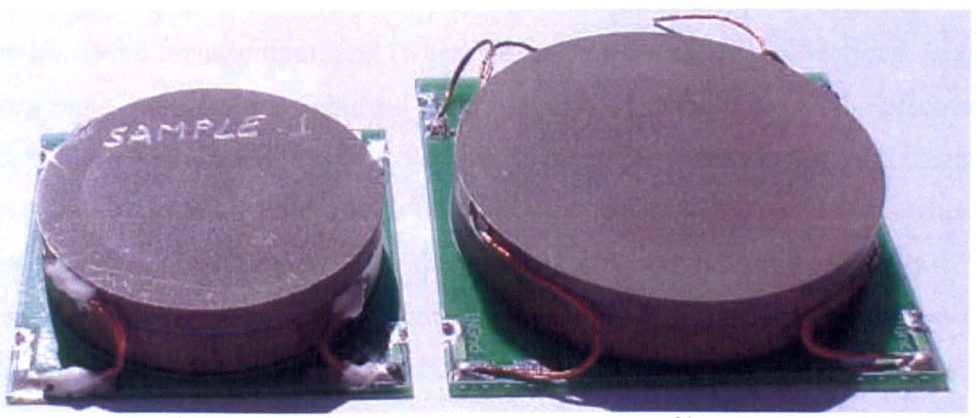

a) b)

Figure 1.15: Co-fired and bonded radial mode Transoner PTs. Note that the input and output sections each consist of a single piece of ceramic (with internal electrodes), and that the two sections are bonded together with an isolation layer between them. a) 35W design, b) 50W design. Photos courtesy of Micromechatronics Inc.

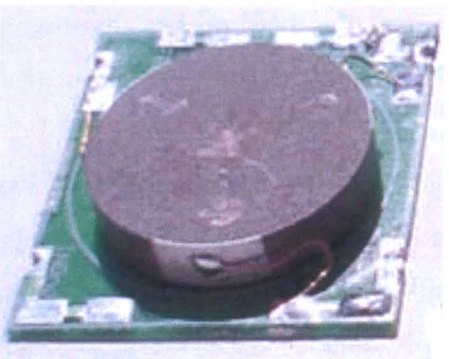

Figure 1.16: Purely co-fired radial mode Transoner PT, 15W design. Note that the complete device is made from a single piece of ceramic. Photo courtesy of Micromechatronics Inc.

Devices that are co-fired and bonded, such as those shown in Figure 1.15 have an input and output section that each consist of a single piece of multilayer ceramic. The two sections are then bonded together, with or without an isolation layer between them. Each section has multiple internal electrodes, which are connected to the external electrodes visible in Figures 1.15 and 1.16. The thickness of the internal electrodes and the material from which they are made affects the electrical conductivity of the electrodes and the thermal conductivity of the device, and therefore its power handling [24, 105]. Increasing the number of electrodes in a given sized device tends to decrease the mechanical quality factor [106, 107], but increase thermal conductivity (see discussion on page 3210 of [24]). The thermal conductivity of the electrode material is usually superior to that of the ceramic.

Purely co-fired devices consist of a single piece of ceramic containing the internal electrodes of the input, output, and (when present) feedback/tertiary sections. Isolation between input and output is achieved with a layer of ceramic between the electrode at the edge of one section and the electrode at the edge of the other. The internal electrodes do not extend right to the outer radius of the device, except in the small areas where the internal electrodes are connected to the external electrodes. Commercially available PTs, such as the Rosen shown in Figure 1.2, are usually always completely co-fired. However, when prototyping a new radial mode Transoner design, it is often faster to make the input and output sections separately and bond them together, because optimising the manufacturing process of a completely co-fired device with significantly different input and output section electrode configurations requires more time, due to the differing thermal expansion coefficients of the two sections. Furthermore, manufacturing each section separately allows each part to be tested on its own (as a

simple piezoelectric resonator), which helps the designer to optimise the performance of the overall device. Purely co-fired, and co-fired and bonded devices are poled after manufacture (see Section 1.8).

In general, piezoelectric devices are usually classified as being either bulk or multilayer. A bulk device has a single set of electrodes on the top and bottom of a piece of piezoelectric ceramic, whereas a multilayer device is co-fired with multiple internal electrodes within a single piece of piezoelectric ceramic. A purely bonded Transoner is therefore sometimes referred to as a bulk device, even though it has multiple layers. Purely co-fired and co-fired and bonded Transoners are true multilayer devices.

1.5 Equivalent circuit modelling

Equivalent circuits are often used to provide an electrical description of the behaviour of a conventional magnetic transformer. These can vary in detail, from a simple transformation ratio and magnetising inductance, to those including leakage inductance, copper and iron losses, inter-winding capacitances, etc [108]. These equivalent circuits are very useful when designing resonant converters because the parasitics can be used as part of the resonant tank design, thereby reducing size, cost, and component count.

Equivalent circuits are also used extensively for modelling the electrical behaviour of a piezoelectric transformer. The lumped equivalent circuit that is most often seen in the literature, and which is commonly used for experimentally characterizing a PT, is shown in Figure 1.17. It must be emphasised that this circuit is only applicable to the frequency range of a single resonance. C_{in} and C_{out} represent either the clamped input and output capacitance of the PT, or the damped input and output capacitance of the PT, depending on how the behaviour of the additional resonances that are not modelled by the RLC branch (often called the motional branch) are considered; further discussion of this point is made in Chapter 2, and a discussion in the context of simple resonators may be found on page 139 of [109]. The mechanical losses are modelled by R_1 and the (short circuit) resonant characteristics by L_1 and C_1. The turns ratio $1:N$ represents the electrical-to-mechanical-to-electrical transformation ratio of the PT, and is usually given by the ratio of two force factors (see Chapters 2 and 3). The transformer symbol that appears in Figure 1.17 is used here, and throughout the rest of this thesis, as a

completely ideal element. Dielectric loss resistances are also sometimes included in the equivalent circuit, either in series or parallel with C_{in} and C_{out}.

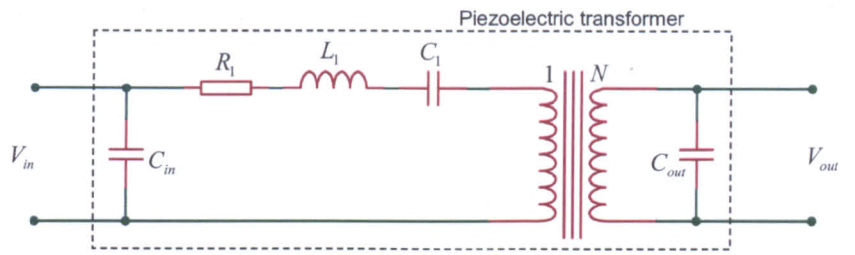

Figure 1.17: Lumped equivalent circuit for a PT.

The equivalent circuit component values of a PT are usually measured with an impedance analyser, such as the Agilent 4294A. The impedance-frequency characteristics are measured over the range of the chosen resonance, from the input terminals with the output shorted, and from the output terminals with the input shorted. Each response is then fitted to a typical resonator equivalent circuit (i.e. a capacitance in parallel with a series RLC branch), and from these the components of Figure 1.17 are found. Further information may be found in [27]. Most impedance analysers apply only a very small voltage when measuring the impedance-frequency response from which the equivalent circuit component values are subsequently calculated. However, PTs exhibit non-linear behaviour, particularly when driven up to their maximum power handling, and their characteristics are also temperature dependent. Hence, the value of the mechanical loss resistance R_1 will depend on the power level at which it is measured.

Piezoelectric transformers tend to have equivalent circuit component values such that the resonant tank has a relatively high Q factor (i.e. >2.5), even when a matched load is used such that the damping is maximised (see below). This means fundamental mode approximation (FMA) may be used, where it is assumed that only the fundamental component (the frequency of which will be close to the resonance described by the PT equivalent circuit) of the voltage waveform across the PT input results in power transfer through the resonant tank. Thus, the tank current is assumed to be sinusoidal [110], and this greatly simplifies the analysis of converter topologies in which PTs are used. However, it is important to remember that a piezoelectric device will generally have many resonances, that these may be excited by harmonics in the input voltage waveform, and that their effects are not included in the standard lumped equivalent circuit. Multi-branch equivalent circuits attempt to take these other resonances into

account [27]. In general however, a piezoelectric device that is designed to operate at a low order mode (e.g. the first radial mode) will have a weak response to high order modes because the electrode layout is not suitable for effectively exciting those modes (see Section 1.3b) and interference tends to occur between the various high order modes.

The load resistance which maximises the efficiency of a PT in a simple AC-output topology (i.e. where the output of the PT is directly connected to a purely resistive load) is the matched load. Since the loaded Q factor of a PT is large enough to ensure the tank current in Figure 1.17 is sinusoidal, the circuit of Figure 1.17 can be represented with that shown in Figure 1.18, where

$$R_s = \frac{R_L}{\left(R_L{}^2\omega^2 C_{out}{}^2 + 1\right)} \tag{1.1}$$

$$C_s = \frac{\left(R_L{}^2\omega^2 C_{out}{}^2 + 1\right)}{R_L{}^2\omega^2 C_{out}} \tag{1.2}$$

where R_L is the resistive load connected in parallel with the PT output in Figure 1.17. Ignoring dielectric losses, and with reference to Figure 1.18, PT efficiency can be written as

$$\eta = \frac{I_1\left(\frac{R_s}{N^2}\right)}{I_1\left(\frac{R_s}{N^2}\right) + I_1 R_1} = \frac{R_s}{R_s + R_1 N^2} = \frac{R_L}{R_L + R_1 N^2\left(1 + R_L{}^2\omega^2 C_{out}{}^2\right)} \tag{1.3}$$

where I_1 is the RMS of the (sinusoidal) current through L_1. Differentiating the right hand side of (1.3) with respect to R_L, equating to zero, and solving for R_L, the load that maximises PT efficiency is

$$R_L = \frac{1}{\omega C_{out}}. \tag{1.4}$$

Note that (1.4) involves the load resistance matching the magnitude of the impedance of C_{out}. Of course, the same result can also be obtained by simply considering the load that maximises R_s in Figure 1.18. Since the maximum output power of a given PT is usually governed by thermal considerations, maximum PT output power is usually obtained when using the matched load (see Chapter 4).

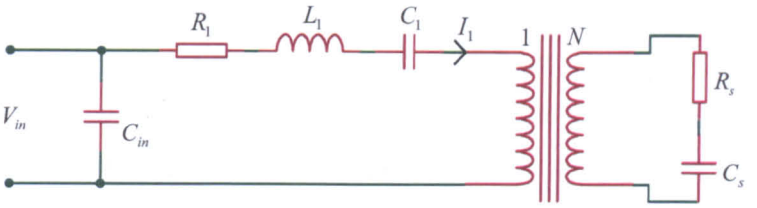

Figure 1.18: Simplified equivalent circuit for a PT connected to a purely resistive load.

When designing a PT for a particular application, it is extremely useful to know how the material properties and device dimensions relate to the equivalent circuit component values. Therefore much research effort has focused on deriving equivalent circuit models for the various types of PT (for example, [3, 4, 12, 27, 28, 40, 45, 51, 59, 61, 102, 111]). It is also helpful to know how the maximum vibration velocity within the PT relates to the various voltages and currents in the equivalent circuit, because PT output power is strongly dependent on vibration velocity (see Chapter 3), and the onset of severe non-linearity is also strongly related to the vibration velocity (see Section 1.9). Therefore it is advantageous to solve the constants in the equation of motion in terms of vibration velocities (as is the common practice when deriving a Mason equivalent circuit (see [9, 82] and Chapters 2 and 3) because a direct relationship between the currents in the equivalent circuit and vibration velocity within the device is obtained, rather than to solve them in terms of the electric fields (as done in [47]). Since the quantitative design of PTs that achieve high-power density whilst simultaneously meeting a set of converter specifications is virtually impossible without such models, the development of new, more detailed models for the radial mode Transoner is a key priority for this research work (see Chapters 2 and 3).

Whilst equivalent circuit modelling is very useful for the electrical part of the PT design, finite element analysis (FEA) also plays an important role in ensuring that the particular resonance which the device is designed to operate at is free from interference from other resonances. This is particularly important with devices like the Noliac ring-type because the characteristic thickness mode geometry has an inherent tendency for interference from high order modes. Equivalent circuit models are usually based on an analysis that assumes only one vibration mode is excited. Therefore FEA, which calculates the frequency and nature of all the modes, is a useful tool for testing whether this assumption is valid for a particular design.

1.6 PT-based converter topologies

The magnetic components in a power electronic circuit are usually the largest and most expensive [83, 112]. Comparing the PT equivalent circuit of Figure 1.17 to the transformer and resonant tank arrangement found in several resonant converter topologies, it can be seen that a PT can be used to replace many of the reactive components in these topologies, thereby offering potential savings in cost, size, and mass. PTs are usually used in a push-pull, class-E, or half-bridge arrangement, and the merits of each are now briefly discussed.

A. Push-pull

The PT-based push-pull topology is shown in Figure 1.19 with a simple resistive load [5, 20, 113-116]. This topology is predominantly used for step-up converters due to the high step-up ratios and simple control requirements it offers [5]. Although this topology does not require an isolated gate-drive for either of the MOSFET switches, it does require two additional inductors.

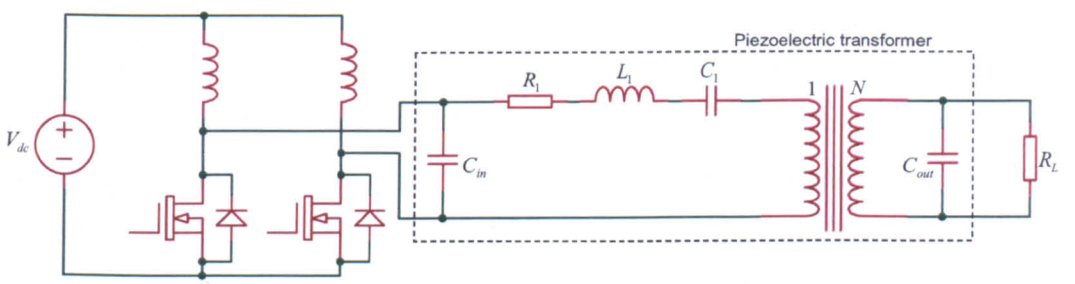

Figure 1.19: Push-pull PT-based converter topology.

B. Class-E

The PT-based class-E topology is shown in Figure 1.20 [59, 63, 78, 86, 117-125]. The main advantage of this topology is that only a single power switch is required. However, the switch will usually have to withstand comparatively large voltages, and the overall efficiency of this topology is usually not as high as that of the half-bridge configurations. In [117] it was concluded that for step-down applications, Class-E and half-bridge are best suited for low and high power levels respectively. Furthermore, it is usually more difficult to meet a particular converter specification with a PT-based class-E design compared to a PT-based half-bridge with-inductor design.

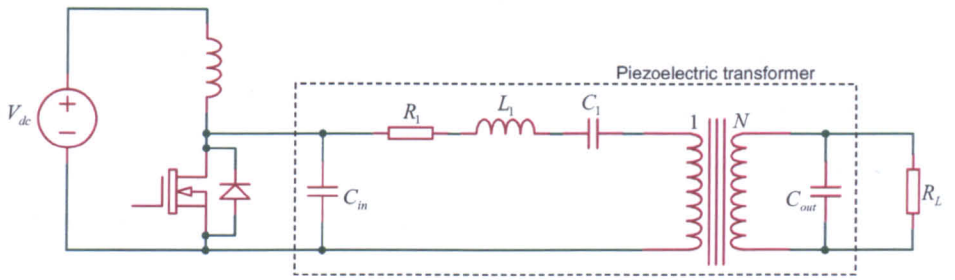

Figure 1.20: Class-E PT-based converter topology.

A considerable amount of work on the PT-based Class-E topology has been published by the Fraunhofer Institute [117-125], and considers applications such as fluorescent lamp ballasts and LED lighting supplies. Various control strategies were evaluated, and the use of a feedback section (like a third winding on a conventional transformer) to provide information on the tank current in the PT equivalent circuit was demonstrated [120, 124, 125].

C. Half-bridge with-inductor

The half-bridge with-inductor topology shown in Figure 1.21 uses an inductor in series with the PT input. This allows zero-voltage-switching (ZVS) to be achieved relatively easily, and forms an LC filter with the PT input capacitance which attenuates much of the harmonic content present in the square (though actually slightly trapezoidal) wave across the half-bridge MOSFET switches, leaving a quasi-sinusoid across the PT input. The draw-back to using a half-bridge is that an isolated gate drive is required for the high-side MOSFET, increasing cost. This topology has been used in many research works, and some guidelines for its use with radial mode Transoner PTs are given in [26].

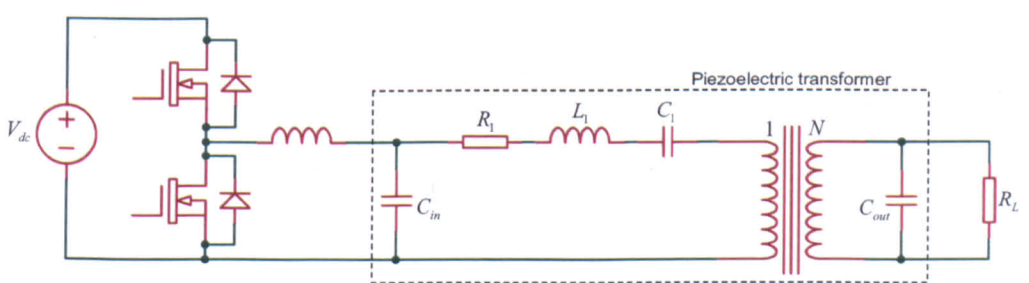

Figure 1.21: Half-bridge with-inductor PT-based converter topology.

Several other half-bridge PT-based topologies with an inductor at the input have been proposed. The topology shown in Figure 1.22a uses an inductor in parallel with the PT input, and a capacitor in series with the half-bridge output to prevent the DC component being short circuited through the inductor. This topology was used quite widely [21, 40, 126-129], but has largely been replaced by that shown in Figure 1.21. A discussion of the advantages of Figure 1.21 over Figure 1.22a can be found in [126]. The arrangement shown in [130] is also quite similar to Figure 1.22a.

The arrangement in Figure 1.22b requires yet more additional components [61, 77, 131]. In the present author's opinion, the use of so many additional reactive components at the PT input would not be a problem if the converter were also to provide power factor correction, such as the topologies shown in [27, 132-137]. However, the use of three additional components in the power stage of a simple DC-DC topology makes it somewhat unattractive from both size and cost perspectives. Furthermore, it seems unlikely that a converter manufacturer would entertain the idea of using a PT-based converter in an ordinary application if two additional magnetic components were required at the input, given that an inductor is essentially half a transformer anyway.

Some discussion and comparison between the topologies shown in Figure 1.21, Figure 1.22a, and Figure 1.23 is given in [128]. At present, the arrangement shown in Figure 1.21 is the most popular half-bridge PT-based topology, and will simply be referred to as the "half-bridge with-inductor" topology throughout the rest of this thesis.

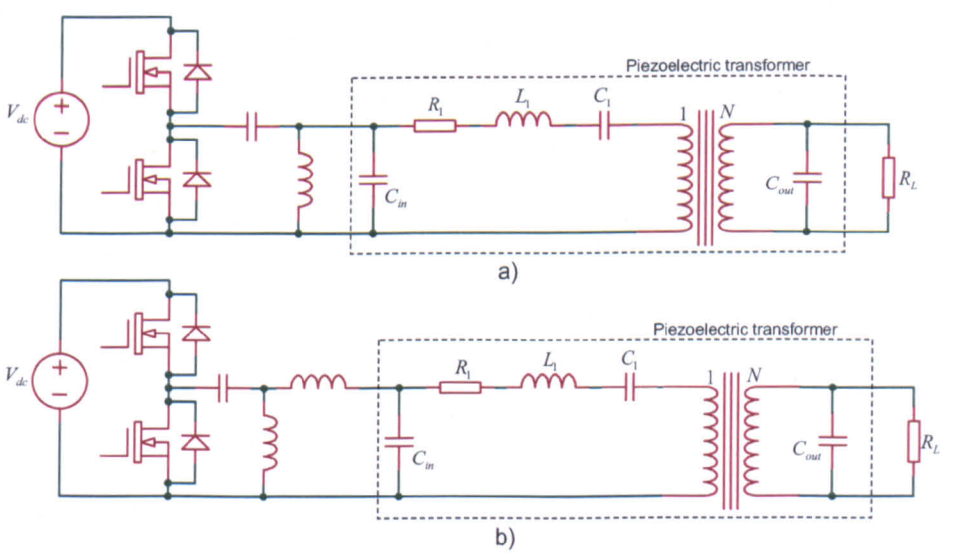

Figure 1.22: Other half-bridge PT-based topologies.

D. Half-bridge inductor-less

A major advantage of the inductor-less topology is that it requires no additional components to be used between the half-bridge and the resistive load or rectifier, as shown in Figure 1.23. Like the with-inductor topology, an isolated gate drive is required for the high-side MOSFET. However, achieving ZVS is considerably more difficult with this topology because the (relatively large) input capacitance of the PT must be charged to the DC link voltage, and discharged to 0V, prior to the high and low side MOSFETs turning on respectively. To the author's knowledge, the feasibility of this topology was first established by R.-L. Lin [27, 30]. Other publications that consider this topology include [32, 96, 128, 138].

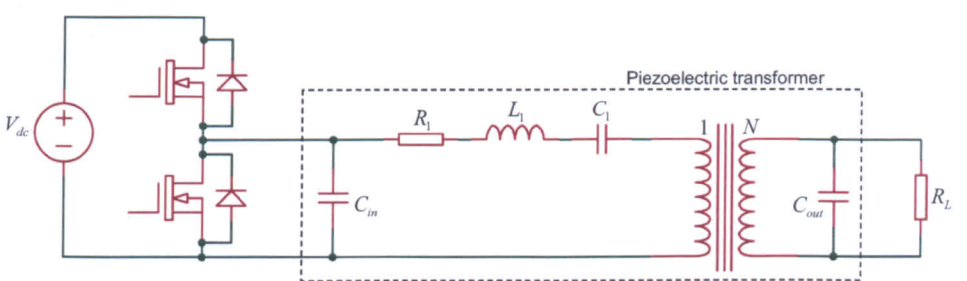

Figure 1.23: Half-bridge inductor-less PT-based converter topology.

It has been known within the PT industry for some time that, for a given converter specification (input voltage, output voltage, load, etc), a PT designed for the inductor-less topology has to be made larger than a PT designed for the with-inductor topology. In other words, inductor-less converters achieve lower PT power density than with-inductor converters. However, this must be viewed in the context of the with-inductor requiring more external components. The underlying reasons behind the decrease in PT power density that occurs when moving from a with-inductor to an inductor-less topology are the subject of a substantial part of this thesis (see Chapters 5 and 6).

Table 1.1 summarises the attributes of the various PT-based converter topologies.

	Push-pull	Class-E	Half-bridge with-inductor	Half-bridge inductor-less
Number of switches required	2	1	2	2
Number of inductors required at PT input	2	1	1	0
Isolated gate drive required for high-side switch	No	No	Yes	Yes

Table 1.1: Comparison of converter topologies.

1.7 PT power density

The maximum power density that can be achieved is a key performance measure for both magnetic and piezoelectric transformers. There are several factors that could potentially limit the power density of a PT:

1) Dielectric breakdown or depoling due to large electric fields.

2) Mechanical failure due to excessive stress or strain.

3) Temperature rise due to losses.

In most practical PTs, excessive temperature rise is nearly always the limiting factor. The ultimate thermal limit for a piezoelectric ceramic is the Curie temperature (320°C in the case of APC841 [139]), because this is the temperature at which the ceramic will become depoled and lose all its macroscopic piezoelectric properties. However, since the properties of the ceramic begin to degrade before the Curie temperature is reached, the manufacturer will usually state the maximum operating temperature to be some way below this [139, 140]; American Piezo Ceramics state the maximum operating temperature to be half the Curie temperature (in degrees Celsius) [139]. It should also be noted that in the case of a bonded PT (see Section 1.4), the bonding agent is likely to fail before the Curie temperature is reached.

In practice however, PT losses increase rapidly with temperature (see Section 1.9), making operation at high temperatures very unpredictable and susceptible to thermal runaway (see Chapter 4). Thus, the maximum output power of a PT is usually stated as the maximum output power that can be obtained for a given rise in temperature above the ambient, and the allowed temperature rise is usually very modest, e.g. between 10 and 30°C above ambient [7, 18, 24, 28, 33, 59, 99, 101, 104].

Conceptually, the maximum output power of a PT is really the maximum output power that can be delivered whilst operating in a thermally stable manner, rather than a fixed rise in temperature above ambient. In general, however, the piezoelectric ceramics that are currently used in PTs do not remain stable (that is their losses begin to increase substantially) even at relatively modest temperature increases, which is probably why maximum output power for a 20°C rise in temperature has become a popular measure. Further discussion can be found in Chapter 4.

Whilst it is tempting to quote power density figures for the various types of PT, they are very difficult to compare without considerable qualification. Theoretically, it is expected that the power density of a radial mode Transoner will increase as radius is decreased (see [28, 58] and Chapter 3). Since the ratio between radius and thickness must be kept large enough to prevent interference from thickness modes, it is expected that PT power density will decrease as PT volume is increased. Considering the force factor and clamped capacitance relationships for various piezoelectric elements (see pages 233-239 in [82]), similar behaviour is likely to occur with other types of PT. In general, the maximum output power of a PT will increase with size. Therefore it could be argued that any PT power density figure should also be accompanied with a maximum output power figure, because it is likely to be much easier to obtain a high power density with a physically small design that has a low maximum power handling. Whilst the author is not aware of any study that experimentally demonstrates that power density increases as size is decreased, there are several forms of anecdotal evidence: 1) PTs with high power handling have not yet been demonstrated. 100W has been achieved, but there is no evidence of a PT achieving say 1kW, a power level that can comfortably be achieved with a planar magnetic transformer [141]. 2) There are examples of very small PTs achieving very high power densities, such as the device shown in [6] with a volume of less than $1mm^3$ and a claimed power density of $250W/cm^3$.

The maximum output power of a PT is heavily dependent on the piezoelectric material that is used. Therefore comparisons between PT designs can only be made if they use exactly the same material. Finally, the composition of a PT can affect its power handling. A PT with many internal layers may not achieve the same power density as another PT of the same size but with fewer layers because losses tend to increase as the

number of layers increases. On the other hand, however, increasing the number of internal electrodes tends to increase the thermal conductivity of the PT, resulting in a more uniform temperature profile. Thus, it can be very difficult to compare the power density of one type of PT to that of another, particularly if they have been designed to meet a particular set of specifications.

1.8 Introduction to piezoelectric materials for PTs

Although single crystal materials such as those demonstrated in [7] are attractive for use in PTs because of their very large electromechanical coupling factors [142], most PTs are currently made from polycrystalline ceramics.

Lead zirconate titanate (PZT) based ceramics are particularly popular due to their high coupling coefficients, high Curie temperature, and ease of poling [1]. Furthermore, the high solid solubility of PZT allows the material properties to be controlled and tailored towards a specific application through incorporation of dopants and modifiers [1]. A PZT ceramic consists of many individual piezoelectric crystals, referred to as crystallites or grains. When the ceramic is first formed, the domains (i.e. the regions of uniform poling) within the crystallites are arranged so as to minimise the electrostatic forces within the material, resulting in no macroscopic piezoelectric behaviour. During the process of poling, the majority of the domains are aligned in the same direction under the action of a high electric field at raised temperature. Once poled, the ceramic will demonstrate a macroscopic piezoelectric effect and from an electromechanical perspective behave substantially like a single-crystal piezoelectric material [1]. The density of PZT is usually around $7.7 g/cm^3$.

PZT exists in a number of structural forms, or polymorphs. To maximise the desired piezoelectric and coupling coefficients (see Section 1.10), a PZT composition which lies on the morphotropic phase boundary (MPB) is usually sought. At the MPB there is a coexistence of the tetragonal and rhombohedral polymorphs, resulting in a material with 14 possible poling directions (6 from the tetragonal and 8 from the rhombohedral). The large piezoelectric coefficients and coupling factors that occur in MPB compositions are believed to result from the increased ease of reorientation during poling [1, 142].

The characteristics of a piezoelectric ceramic are often described as being "hard" or "soft". A hard ceramic is defined in [142] as having a coercive field (the electric field at which the polarization of a material returns to zero, see polarisation versus electric field hysteresis loop in [1]) greater than 1kV/mm. A soft ceramic is defined as having a coercive field less than 100V/mm, and materials with a coercive field between these figures are described as being "semihard" [142]. The higher coercive field in a hard composition is due to greater domain wall stability. Soft ceramics characteristically have large piezoelectric charge coefficients (d, see Section 1.10), large coupling factors, high dielectric losses, low mechanical quality factor Q_m (i.e. high mechanical losses), high dielectric constants, and relatively low Curie temperature. Hard ceramics characteristically have the opposite; in particular they have low losses (i.e. high Q_m). In general, soft ceramics are used in sensing applications whilst hard ceramics are used in "high power" applications where low losses are essential. However, some materials display varying degrees of both hard and soft characteristics, and of particular note are those described in [105, 143-145].

Since PT power density is usually limited by thermal considerations, it is essential that the piezoelectric material has low losses (see Section 1.9).

1.9 Piezoelectric materials and power density considerations

Since the power handling of a PT is almost always thermally limited, it is essential that PT losses are kept to a minimum. There are 3 types of loss that occur in piezoelectric materials [146]:

1) dielectric
2) mechanical
3) piezoelectric

In addition to these, a PT will also incur ohmic losses from the electrode materials. Hence, there are 4 loss mechanisms associated with PTs. The overall mechanical loss of a PT will have contributions not just from the piezoelectric material itself, but from all the materials present in the PT, including bonding agents and isolation materials where present. Indeed, the effect of the bonding agents and/or isolation material are shown to have a substantial effect on PT losses in Chapter 2 (compare the experimentally measured R_1 for the isolated T1-15W to the non-isolated T1-15W, remembering that

the contribution of the extra bonding layers and isolation layer to the overall PT volume is very small).

The maximum output power of a radial mode Transoner PT is approximately proportional to the square of the maximum vibration velocity [28, 105] (see also Chapter 3). Therefore materials that can operate at high vibration velocity allow for high power density PTs to be realised.

However, when a piezoelectric resonator is operated near resonance, the temperature rise that occurs is closely related to the maximum vibration velocity that occurs within the device [105, 147-153]. The spatial variation in vibration velocity amplitude within a piezoelectric device depends on the vibration mode (longitudinal, radial, etc). However, the quantity of interest is usually the maximum vibration velocity that occurs anywhere within the device. For a long thin bar (such as a longitudinal mode Transoner) operating near the first longitudinal resonance, longitudinal vibration velocity is maximum at either end of the bar [147]. For a thin disc in radial motion (such as a radial mode Transoner), radial vibration velocity is approximately maximum at the outer radius of the disc (see Chapter 2). Since the maximum occurs at the extremities of these shapes, it can be determined experimentally with a laser Doppler vibrometer [154, 155].

Although it is seldom mentioned on a material manufacturer's datasheet, an absolutely crucial property of any piezoelectric material that is to be used in the construction of a PT is therefore the ability to operate in a thermally stable manner at high vibration velocities. Materials that are capable of doing so are often referred to as "high power" piezoelectric materials [105, 145, 156]. High power piezoelectric materials are often characterised by the vibration velocity that corresponds to a 20°C or 30°C rise in resonator temperature above the ambient temperature [105, 143-145, 154, 156]. Most of the existing commercially available ceramics that are suitable for use in PTs (such as American Piezo Ceramics' APC841) have an RMS maximum vibration velocity of about 0.2m/s or 0.3m/s [105]. However, a substantial amount of research has focused on the development of high power piezoelectric materials, and the figure of merit usually quoted is the vibration velocity that corresponds to a 20°C temperature rise. By doping PZT based ceramics with various rare earth materials, materials that can achieve 1m/s have been demonstrated [105, 143-145]. However, in order for a PT to achieve high power density, a combination of both high electromechanical coupling factor *and* high

vibration velocity stability is required (see Chapter 3). Materials with both of these properties, such as those reported in [143] ($k_p = 0.61$ in combination with 1.1m/s vibration velocity at 20°C temperature rise), have the potential to greatly increase the power density of PTs.

The mechanical quality factor Q_m of a piezoelectric material is another important parameter to consider, and is closely related to vibration velocity. Whilst the value that is quoted in a manufacturer's datasheet (which is measured at low excitation level) is useful, the way in which Q_m changes with vibration velocity and temperature is very important. Under normal circumstances, as the vibration velocity of a piezoelectric resonator is increased, the temperature rises [105, 147-153]. But there are at least two effects at play here. Umeda et al. devised a method for measuring the quality factor of a material without increasing its temperature using the electrical transient response [147, 157]. This allowed the effects of temperature and vibration velocity on Q_m to be separated. Using this method it has been shown in many papers that increasing temperature alone decreases Q_m, and that increasing vibration velocity alone decreases Q_m [106, 147, 158, 159]. Therefore in normal circumstances, when a piezoelectric material is driven up to a particular vibration velocity, the vibration velocity causes Q_m to decrease (i.e. the losses increase), which generates more heat, and this increased heat causes the Q_m to decrease still further, generating yet more heat. If this heat generation can be balanced by thermal conduction and convection, then a steady-state temperature is reached. However, sometimes a thermal runaway condition can occur (see Chapter 4).

In summary, as vibration velocity is increased during normal operation (i.e. where temperature is allowed to rise), temperature increases and Q_m decreases [147, 149]. Furthermore, temperature increase and Q_m decrease tend to reinforce one another, and provide a mechanism by which thermal runaway can occur.

For a simple transducer resonator, Q_m is related to the loss resistance shown in the resonator equivalent circuit of Figure 1.24 by [153, 160]

$$Q_m = \frac{\omega_r L_1}{R_1} \tag{1.5}$$

where ω_r is the angular resonant frequency of the mode in question. It should be noted, however, that several other equivalent circuits have been proposed to try and more accurately model the nature of the losses [105-107, 146, 156, 157].

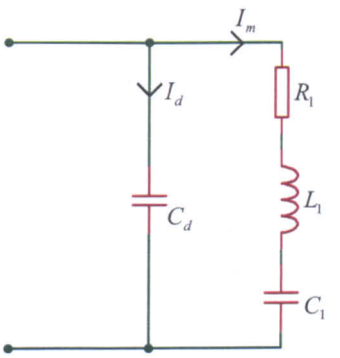

Figure 1.24: The equivalent circuit of a piezoelectric resonator near resonance [160, 161].

In many ways, a PT can be thought of as a highly damped resonator. For a normal transducer resonator, such as those used in the high power studies [106, 147-149, 151-153, 157-159, 162, 163], the only damping that occurs at resonance is due to Q_m (note that R_1 in Figure 1.24 can be written in terms of Q_m using (1.5)), whereas a piezoelectric transformer that is operating with a matched load has an equivalent R_1 in Figure 1.24 that is (hopefully – otherwise efficiency will be poor!) primarily composed of the load, as it is seen through the piezoelectric coupling of the output terminals to the mechanical system, and the piezoelectric coupling of the mechanical system to the input terminals. Again, it must be emphasised that Figure 1.24 is a very simple representation as far as losses at high power are concerned; the important point is that as vibration velocity increases, the losses (however they are modelled in an equivalent circuit) increase, and temperature increases. A piezoelectric material that can operate at high vibration velocities in a thermally stable manner therefore has a Q_m against vibration velocity profile (measured under normal conditions where temperature is allowed to rise) where Q_m does not start to rapidly decrease until a high vibration velocity is reached.

The reason that maximum vibration velocity is used as a figure of merit, rather than displacement, is that "displacement is a function of size, while velocity is not" [105] (see also [142]). In other words, the vibration velocity at which temperature begins to rapidly increase and Q_m rapidly decrease is approximately dependent only on the

piezoelectric material itself, and not on the size and shape of the resonator. Maximum vibration velocity is therefore somewhat analogous to maximum flux density in magnetics.

Apart from temperature and vibration velocity and their effect on the Q_m of the piezoelectric material, there are a number of other factors that can affect the overall Q_m of a PT. As the number of layers within a given sized piezoelectric device is increased, the Q_m at a particular vibration velocity decreases [106]. It is therefore desirable to avoid using a large number of layers in a PT design when possible, and in the case of DC-output applications the rectifier topology should be chosen accordingly (see Chapter 4). The adhesive used in bonded PTs, although very thin, also decreases Q_m, as does the incorporation of isolation layers (see R_i values for the T1-15W isolated and non-isolated in Chapter 2). For a given size, a PT with many layers is therefore likely to generate more heat for a given vibration velocity, and may therefore not be able to operate at the same vibration velocity as a single layer device. However, increasing the number of layers tends to increase the thermal conductivity of the device, resulting in a more uniform temperature profile [24].

The Q_m of a PT (at a low excitation level) is usually much lower than the Q_m of the piezoelectric material used within it (at low excitation level). For example, the manufacturer quotes a figure of 1400 for APC841 material, whereas the Q_m of a PT can be in the region of a couple of hundred, depending on its composition. It is therefore essential to use materials (particularly bonding agents) and manufacturing processes that result in a PT having an overall Q_m that is as high as possible in relation to the Q_m of the piezoelectric material, as well as using a piezoelectric material which maintains a high Q_m at high vibration velocities.

In summary, high power density PTs require piezoelectric materials which:

1) Have a large electromechanical coupling factor associated with the type of coupling used by the PT.
2) Are able to operate at high vibration velocity in a thermally stable manner.

1.10 Piezoelectric constitutive equations and device analysis

Of the 32 crystal classes, 21 lack a centre of symmetry (they are said to be non-centrosymmetric). Of these 21, there are 20 that show piezoelectric behaviour [1, 56, 82, 164, 165]. The constitutive piezoelectric equations are derived from thermodynamic considerations [56, 82, 109], and quantify the behaviour of a piezoelectric material. There are 4 sets of constitutive equations, with each set having a different combination of dependent and independent variables (i.e. the quantities that appear on the left and right hand sides of the equations respectively). The constitutive equations are most readily expressed in matrix form. When electric field and stress are taken as the independent variables [9, 56, 82]

$$\begin{aligned}[S] &= [s^E][T] + [d_t][E] \\ [D] &= [d][T] + [\varepsilon^T][E]\end{aligned} \tag{1.6}$$

where S is strain, T is stress, E is electric field, D is electric displacement (i.e. the electric flux density, or stored electric charge per unit area [142]), s is compliance, d is the piezoelectric constant, and ε is permittivity. The subscript t in (1.6a) indicates the transpose of the matrix; thus, d_t is obtained by interchanging the rows and columns of the d matrix. The superscript E simply indicates that the quantity should be measured at constant electric field; the superscript T that the quantity should be measured at constant stress.

If stress and electric displacement are taken as the independent variables [9, 56, 82]

$$\begin{aligned}[S] &= [s^D][T] + [g_t][D] \\ [E] &= -[g][T] + [\beta^T][D].\end{aligned} \tag{1.7}$$

If strain and electric field are taken as the independent variables [9, 56, 82]

$$\begin{aligned}[T] &= [c^E][S] - [e_t][E] \\ [D] &= [e][S] + [\varepsilon^S][E].\end{aligned} \tag{1.8}$$

If strain and electric displacement are taken as the independent variables [9, 56, 82]

$$\begin{aligned}[T] &= [c^D][S] - [h_t][D] \\ [E] &= -[h][S] + [\beta^S][D].\end{aligned} \tag{1.9}$$

The quantities in (1.6) to (1.9) are related to one another as follows [9, 56]

$$[\beta^T] = [\varepsilon^T]^{-1} \tag{1.10}$$

$$[g] = [\beta^T][d] \tag{1.11}$$

$$[s^D] = [s^E] - [d_t][\beta^T][d] \tag{1.12}$$

$$[c^E] = [s^E]^{-1} \tag{1.13}$$

$$[e] = [d][c^E] \tag{1.14}$$

$$[\varepsilon^S] = [\varepsilon^T] - [d][c^E][d_t] \tag{1.15}$$

$$[c^D] = [s^D]^{-1} = [c^E] + [e_t][\beta^S][e] = [c^E] + [h_t][\varepsilon^S][h] \tag{1.16}$$

$$[h] = [\beta^S][e] = [g][c^D] \tag{1.17}$$

$$[\beta^S] = [\varepsilon^S]^{-1} = [\beta^T] + [h][s^D][h_t] = [\beta^T] + [g][c^D][g_t]. \tag{1.18}$$

Note that the rules of matrix algebra must be followed when using (1.6) to (1.18), i.e. $c_{11}^E \neq 1/s_{11}^E$.

The electric field, electric displacement, stress, and strain matrices are as follows [9]

$$[E] = \begin{bmatrix} E_1 \\ E_2 \\ E_3 \end{bmatrix}, \qquad [D] = \begin{bmatrix} D_1 \\ D_2 \\ D_3 \end{bmatrix}, \qquad [T] = \begin{bmatrix} T_1 \\ T_2 \\ T_3 \\ T_4 \\ T_5 \\ T_6 \end{bmatrix}, \qquad [S] = \begin{bmatrix} S_1 \\ S_2 \\ S_3 \\ S_4 \\ S_5 \\ S_6 \end{bmatrix}, \tag{1.19}$$

where the subscripts indicate the direction of the quantity. Subscripts 1, 2, and 3 refer to the three normal directions in the Cartesian coordinate system, as shown later in Figure 1.25. Note that the "right hand rule" is observed when depicting the directions of the Cartesian coordinate axes. Subscripts 4, 5, and 6 are used to define shear stresses or strains about the 1, 2, and 3 axes respectively (see page 221 of [1] and page 347 of [165]).

The elastic coefficients, $[s^E]$, $[s^D]$, $[c^E]$, and $[c^D]$, are therefore 6 by 6 matrices. The dielectric coefficients, $[\varepsilon^T]$, $[\varepsilon^S]$, $[\beta^T]$, and $[\beta^S]$, are 3 by 3 matrices, and the piezoelectric coefficients, $[d]$, $[e]$, $[g]$, and $[h]$, are 3 by 6 matrices [9, 56, 109]. Methods for determining these material coefficients are set out in the various IRE/IEEE standards on piezoelectricity [160, 161, 164, 166, 167]. For a particular material, the nature of these matrices depends on the crystal class. Elasto-piezo-dielectric matrix diagrams describe which elements of the various matrices are zero and which are the same as another element. Diagrams for all 32 crystal classes can be found in [56, 166]. Poled polycrystalline ceramics, such as PZT and barium titanate, have an elasto-piezo-dielectric matrix of the same form as the crystal class C_{6v} [166].

By convention, unless otherwise stated, the direction of poling in a piezoelectric ceramic is taken as the x_3 direction [1, 165]. Using the elasto-piezo-dielectric matrix diagram for C_{6v}, the constitutive equations where stress and electric field are the independent variables can be written out in full for a piezoelectric ceramic poled in the x_3 direction as follows [10]

$$\begin{bmatrix} S_1 \\ S_2 \\ S_3 \\ S_4 \\ S_5 \\ S_6 \end{bmatrix} = \begin{bmatrix} s_{11}^E & s_{12}^E & s_{13}^E & 0 & 0 & 0 \\ s_{12}^E & s_{11}^E & s_{13}^E & 0 & 0 & 0 \\ s_{13}^E & s_{13}^E & s_{33}^E & 0 & 0 & 0 \\ 0 & 0 & 0 & s_{44}^E & 0 & 0 \\ 0 & 0 & 0 & 0 & s_{44}^E & 0 \\ 0 & 0 & 0 & 0 & 0 & s_{66}^E \end{bmatrix} \begin{bmatrix} T_1 \\ T_2 \\ T_3 \\ T_4 \\ T_5 \\ T_6 \end{bmatrix} + \begin{bmatrix} 0 & 0 & d_{31} \\ 0 & 0 & d_{31} \\ 0 & 0 & d_{33} \\ 0 & d_{15} & 0 \\ d_{15} & 0 & 0 \\ 0 & 0 & 0 \end{bmatrix} \begin{bmatrix} E_1 \\ E_2 \\ E_3 \end{bmatrix}$$

$$\begin{bmatrix} D_1 \\ D_2 \\ D_3 \end{bmatrix} = \begin{bmatrix} 0 & 0 & 0 & 0 & d_{15} & 0 \\ 0 & 0 & 0 & d_{15} & 0 & 0 \\ d_{31} & d_{31} & d_{33} & 0 & 0 & 0 \end{bmatrix} \begin{bmatrix} T_1 \\ T_2 \\ T_3 \\ T_4 \\ T_5 \\ T_6 \end{bmatrix} + \begin{bmatrix} \varepsilon_{11}^T & 0 & 0 \\ 0 & \varepsilon_{11}^T & 0 \\ 0 & 0 & \varepsilon_{33}^T \end{bmatrix} \begin{bmatrix} E_1 \\ E_2 \\ E_3 \end{bmatrix}. \tag{1.20}$$

Using the same matrix diagram, the other sets of constitutive equations could also be written out in full for a poled piezoelectric ceramic.

Conceptually, the analysis of a piezoelectric problem can be undertaken using any of the 4 sets of constitutive equations. However, the assumptions that can be made with certain types of problem often mean that a particular set is more convenient than the others.

For example, consider a long thin bar with electrodes on two opposing major surfaces, as shown in Figure 1.25. The bar is made from piezoelectric ceramic, poled in the x_3 direction, and is free to vibrate. Let the bar be driven at the frequency of the first longitudinal resonance. Such a bar will have negligible stress in all directions except the longitudinal direction, therefore [10, 82, 161]

$$T_2 = T_3 = T_4 = T_5 = T_6 = 0. \tag{1.21}$$

The electrodes are equipotential surfaces. Thus, at these surfaces [82],

$$E_1 = E_2 = 0. \tag{1.22}$$

Because the cross section of the bar is negligible, (1.22) also applies throughout the bar [82]. Furthermore, for this electrode configuration [10]

$$\frac{\partial E_3}{\partial x_3} = 0. \tag{1.23}$$

Because the geometry, vibration mode, and electrode layout allow most of the electric field and stress components to be assumed negligible, it is most convenient to choose the constitutive equations where electric field and stress are the independent variables. Substituting (1.21) and (1.22) into (1.20) results in

$$S_1 = s_{11}^E T_1 + d_{31} E_3 \tag{1.24}$$

$$S_2 = s_{12}^E T_1 + d_{31} E_3 \tag{1.25}$$

$$S_3 = s_{13}^E T_1 + d_{33} E_3 \tag{1.26}$$

$$S_4 = S_5 = S_6 = 0 \tag{1.27}$$

$$D_1 = D_2 = 0 \tag{1.28}$$

$$D_3 = d_{31} T_1 + \varepsilon_{33}^T E_3 \tag{1.29}$$

The equations required for the subsequent analysis are (1.24) and (1.29), (see page 235 of [82], or page 106 of [9]). Although one of the other sets of constitutive equations *could* have been used, a very considerable amount of mathematical rearrangement would have been necessary to arrive at the simple relationships in (1.24) to (1.29).

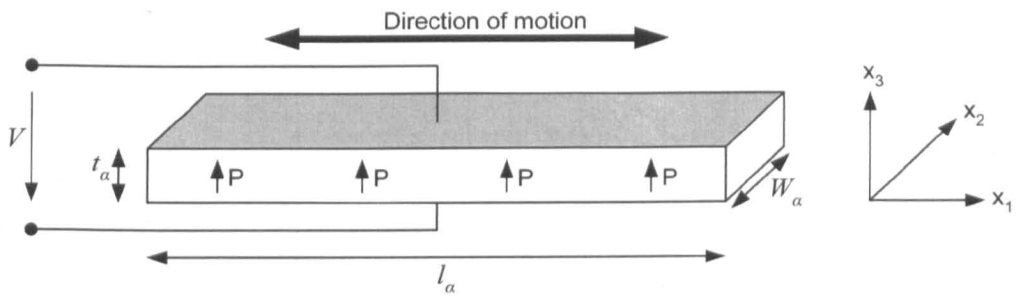

Figure 1.25: Longitudinal mode resonator with electric field perpendicular to the direction of wave propagation.

As a contrasting example, consider a thin piezoelectric ceramic plate operating at a thickness mode. The plate is electroded on the major surfaces, and poled in the thickness direction (which is taken as the x_3 direction), as shown in Figure 1.26. Because "the lateral dimensions are much larger than in the direction of elastic wave propagation" [82], the plate is assumed to be laterally clamped (i.e. all motion is negligible except for in the thickness direction), giving [82]

$$S_1 = S_2 = S_4 = S_5 = S_6 = 0\,. \tag{1.30}$$

If the permittivity of the bar is large compared to its surroundings, then fringing electric fields will not occur, and the electric flux lines will be parallel to the direction of wave propagation [9, 82]. Thus [9, 82]

$$D_1 = D_2 = 0 \tag{1.31}$$

$$\frac{\partial D_3}{\partial x_3} = 0\,. \tag{1.32}$$

Because the geometry, vibration mode, and electrode layout allow most of the electric displacement and strain components to be assumed negligible, it is more convenient to use the constitutive equations where electric displacement and strain are the independent variables. Substituting (1.30) to (1.32) into (1.9) results (for a piezoelectric ceramic), in

$$T_1 = c_{13}^D S_3 - h_{31} D_3 \tag{1.33}$$

$$T_2 = c_{13}^D S_3 - h_{31} D_3 \tag{1.34}$$

$$T_3 = c_{33}^D S_3 - h_{33} D_3 \tag{1.35}$$

$$T_4 = T_5 = T_6 \tag{1.36}$$

$$E_1 = E_2 = 0 \tag{1.37}$$

$$E_3 = -h_{33} S_3 + \beta_{33}^S D_3 \tag{1.38}$$

The equations required for the subsequent analysis are (1.35) and (1.38), (see page 238 of [82], or page 106 of [9]).

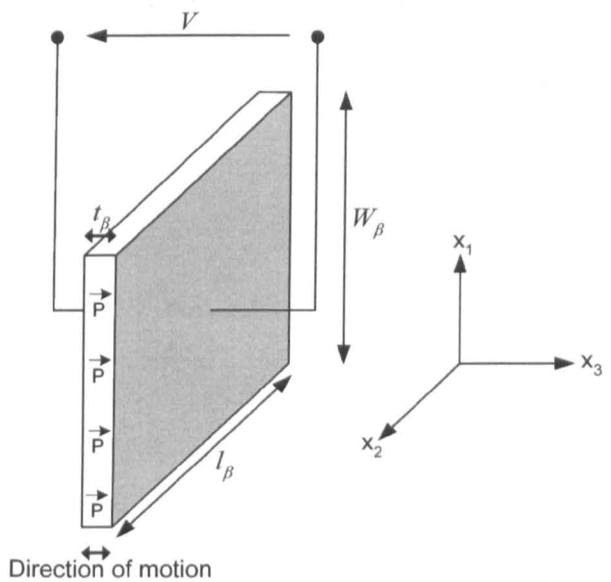

Figure 1.26: Thickness mode resonator with electric field parallel to the direction of wave propagation.

The process of obtaining the correct, simplified, constitutive equations for a particular problem may be summarised as follows:

1) Identify the crystal class of the material and the form of the dielectric, piezoelectric, and elastic matrices.
2) Consider the geometry, vibration mode, and electrode layout of the device, and identify which electric field, electric displacement, stress, and strain components may be regarded as negligible.
3) Choose the set of constitutive equations that most readily allow the approximations from 2) to be applied. Apply the approximations, and obtain the simplified constitutive equations for the problem in question.

The simplified constitutive equations from one problem cannot be applied to another unless exactly the same set of approximations are valid (see discussion in [13]). The constitutive piezoelectric equations will be used extensively throughout Chapters 2 and 3 of this thesis.

1.11 Identification of research goals

The radial mode Transoner is currently the most promising design for many DC-DC converter specifications. Since equivalent circuit modelling is essential for quantitatively designing PTs, and for ensuring that a particular converter specification is met in a manner that also maximises power density, the development of equivalent circuit models for the radial mode Transoner is a key focus for this work. These models may be found in Chapters 2 and 3.

To date, the application in which PTs have seen the greatest success is CCFL backlight inverters, which is a DC-AC type application rather than DC-DC. An important question is therefore: what effect does the use of a rectifier have on the power density of a PT? This question is answered, through the use of PT modelling and rectifier modelling, in Chapter 4.

In many ways, the half-bridge inductor-less topology is the most attractive PT-based topology because it requires no other components to be used between the half-bridge and the rectifier. It has been known for some time that PTs designed for inductor-less

operation achieve lower PT power density than those designed for with-inductor operation. However, because accurate models for the inductor-less topology have not yet been developed, the reasons behind this decreased power density have not been fully understood. The development of such models, and their translation into a set of design criteria for maximising PT power density, is another key focus for this work and may be found in Chapters 5 and 6.

Finally, if inductor-less radial mode Transoner based converters are to be successful in DC-DC applications, regulation of the output voltage in response to load changes will be required. Given the way in which the inductor-less topology works, a key question is whether a more conservative PT design (i.e. a larger design) is required in order for ZVS to be maintained whilst providing output voltage regulation through frequency modulation, compared to obtaining ZVS at the load into which maximum output power is to be delivered. This question is answered, from a theoretical perspective, in Chapter 7.

References

[1] R. W. Schwartz, J. Ballato, and G. H. Haertling, "Piezoelectric and Electro-optic Ceramics (Chapter 4)," in *Ceramic Materials for Electronics*, R. C. Buchanan, Ed., 3rd ed: Marcel Dekker Inc., 2004.

[2] C. A. Rosen, K. A. Fish, and H. C. Rothenberg, "Electromechanical Transducer," in *U.S. Patent 2,830,274*, 1958.

[3] C. A. Rosen, "Ceramic Transformers and Filters," *Proceedings of the Electronic Components Symposium (1956)*, pp. 205-211, 1956.

[4] C. A. Rosen, "Analysis and design of ceramic transformers and filter elements," PhD thesis, Syracuse University, USA, 1956.

[5] A. V. Carazo, "50 Years of piezoelectric transformers. Trends in the technology," presented at Materials Research Society Symposium, Boston, MA, United States, 2003.

[6] I. Kartashev, T. Vontz, and H. Florian, "Regimes of piezoelectric transformer operation," *Measurement Science and Technology*, vol. 17, pp. 2150-2158, 2006.

[7] Y. Zhuang, S. Ural, R. Gosain, S. Tuncdemir, A. Amin, and K. Uchino, "High Power Piezoelectric Transformers with Pb(Mg1/3Nb2/3)O3-PbTiO3 Single Crystals," *Applied Physics Express*, vol. 2, pp. 121402-1 to 121402-2, 2009.

[8] J. He and Z.-F. Fu, *Modal Analysis*: Butterworth-Heinemann, 2001.

[9] H. W. Katz, *Solid State Magnetic and Dielectric Devices*: John Wiley & Sons, Inc. New York, 1959.

[10] J. S. Yang and X. Zhang, "Extensional vibration of a nonuniform piezoceramic rod and high voltage generation," *International Journal of Applied Electromagnetics and Mechanics*, vol. 16, pp. 29-42, 2002.

[11] J. Yang, *Analysis of Piezoelectric Devices*: World Scientific Publishing, 2006.

[12] C. Nadal and F. Pigache, "Multimodal electromechanical model of piezoelectric transformers by Hamilton's principle," *IEEE Transactions on Ultrasonics, Ferroelectrics, and Frequency Control*, vol. 56, pp. 2530-2543, 2009.

[13] J. Yang, "Comment on Y.-H. Hsu et al., "Electrical and mechanical fully coupled theory and experimental verification of rosen-type piezoelectric transformers"," *IEEE Transactions on Ultrasonics, Ferroelectrics, and Frequency Control*, vol. 54, pp. 699-700, 2007.

[14] "LNA3207A High Voltage 5W Rosen Piezoelectric Transformer," *Micromechatronics datasheet*, 2009.

[15] Y. Fuda, K. Kumasaka, M. Katsuno, H. Sato, and Y. Ino, "Piezoelectric Transformer for Cold Cathode Fluorescent Lamp Inverter," *Japanese Journal of Applied Physics, Part 1*, vol. 36, pp. 3050-3052, 1997.

[16] K. Kanayama and N. Maruko, "Properties of Alternately Poled Piezoelectric Transformers," *Japanese Journal of Applied Physics, Part 1*, vol. 36, pp. 3048-3049, 1997.

[17] K. Sakurai, K. Ohnishi, and Y. Tomikawa, "Presentation of a New Equivalent Circuit of a Piezoelectric Transformer under High-Power Operation," *Japanese Journal of Applied Physics, Part 1*, vol. 38, pp. 5592-5597, 1999.

[18] Y. Sasaki, M. Yamamoto, A. Ochi, T. Inoue, and S. Takahashi, "Small Multilayer Piezoelectric Transformers with High Power Density -Characteristics of Second and Third-Mode Rosen-Type Transformers-," *Japanese Journal of Applied Physics, Part 1*, vol. 38, pp. 5598-5602, 1999.

[19] H. Kawai, Y. Sasaki, T. Inoue, T. Inoi, and S. Takahashi, "High Power Transformer Employing Piezoelectric Ceramics," *Japanese Journal of Applied Physics, Part 1*, vol. 35, pp. 5015-5017, 1996.

[20] M. Shoyama, K. Horikoshi, T. Ninomiya, T. Zaitsu, and Y. Sasaki, "Steady-state characteristics of the push-pull piezoelectric inverter," presented at Power Electronics Specialists Conference (PESC), 1997.

[21] T. Zaitsu, Y. Fuda, Y. Okabe, T. Ninomiya, S. Hamamura, and M. Katsuno, "New piezoelectric transformer converter for AC-adapter," presented at Applied Power Electronics Conference and Exposition (APEC), 1997.

[22] L. Li, N. Zhang, C. Bai, X. Chu, and Z. Gui, "Multilayer piezoelectric ceramic transformer with low temperature sintering," *Journal of Materials Science*, vol. 41, pp. 155-161, 2006.

[23] S.-T. Ho, "Design of the Longitudinal Mode Piezoelectric Transformer," presented at International Conference on Power Electronics and Drive Systems (PEDS), 2007.

[24] J. Hu, Y. Fuda, M. Katsuno, and T. Yoshida, "A Study on the Rectangular-Bar-Shaped Multilayer Piezoelectric Transformer Using Length Extensional Vibration Mode," *Japanese Journal of Applied Physics, Part 1*, vol. 38, pp. 3208-3212, 1999.

[25] R. P. Bishop, "Multi-layer piezoelectric transformer," in *U.S. Patent 5,834,882*, 1998.

[26] A. V. Carazo, "Piezoelectric Converters for DC/DC and AC/DC applications," presented at Portable Power Developer's Conference, 2005.

[27] R.-L. Lin, "Piezoelectric Transformer Characterization and Application of Electronic Ballast," PhD thesis, Virginia Polytechnic Institute and State University, USA, 2001.

[28] M. Yamamoto, Y. Sasaki, A. Ochi, T. Inoue, and S. Hamamura, "Step-Down Piezoelectric Transformer for AC-DC Converters," *Japanese Journal of Applied Physics, Part 1*, vol. 40, pp. 3637-3642, 2001.

[29] A. V. Carazo, "Multilayer piezoelectric transformer," in *U.S. Patent 6,614,144*, 2003.

[30] R.-L. Lin, F. C. Lee, E. M. Baker, and D. Y. Chen, "Inductor-less piezoelectric transformer electronic ballast for linear fluorescent lamp," presented at IEEE Applied Power Electronics Conference and Exposition, 2001.

[31] E. M. Baker, "Design of Radial Mode Piezoelectric Transformers for Lamp Ballast Applications," MSc thesis, Virginia Polytechnic Institute and State University, USA, 2002.

[32] E. M. Baker, W. Huang, D. Y. Chen, and F. C. Lee, "Radial mode piezoelectric transformer design for fluorescent lamp ballast applications," *IEEE Transactions on Power Electronics*, vol. 20, pp. 1213-1220, 2005.

[33] T. Ezaki, S. Manuspiya, P. Moses, K. Uchino, and A. V. Carazo, "Piezoelectric Transformers For A High Power Module," *Materials Technology*, vol. 19, pp. 79-83, 2004.

[34] K. Uchino, "Piezoelectric Actuators 2006 Expansion from IT/Robotics to Ecological/Energy Applications," *Journal of Electroceramics*, vol. 20, 2008.

[35] W. Huang, "Design of a Radial Mode Piezoelectric Transformer for a Charge Pump Electronic Ballast with High Power Factor and Zero Voltage Switching," MSc thesis, Virginia Polytechnic Institute and State University, USA, 2003.

[36] K. Uchino, S. Priya, S. Ural, and T. Ezaki, "High power piezoelectric transformers - Their applications to smart actuator systems," *Ceramic Transactions*, vol. 167, pp. 383-395, 2005.

[37] P. Půlpán and J. Erhart, "Transformation ratio of "ring-dot" planar piezoelectric transformer," *Sensors and Actuators A: Physical*, vol. 140, pp. 215-224 2007.

[38] S. Priya, S. Ural, H. W. Kim, K. Uchino, and T. Ezaki, "Multilayered unipoled piezoelectric transformers," *Japanese Journal of Applied Physics, Part 1: Regular Papers and Short Notes and Review Papers*, vol. 43, pp. 3503-3510, 2004.

[39] S. Priya, H. Kim, S. Ural, and K. Uchino, "Erratum: High power universal piezoelectric transformer (IEEE Transactions on Ultrasonics, Ferroelectrics and Frequency Control (Jan. 2006) 53:1 (23-29))," *IEEE Transactions on Ultrasonics, Ferroelectrics, and Frequency Control*, vol. 53, pp. 810-816, 2006.

[40] S. Choi, T. Kim, S. Lee, and B. H. Cho, "Modeling and characterization of radial-mode disk-type piezoelectric transformer for AC/DC adapter," presented at PESC Record - IEEE Annual Power Electronics Specialists Conference, 2005.

[41] T. Hemsel and S. Priya, "Model based analysis of piezoelectric transformers," *Ultrasonics*, vol. 44, supplement 1, pp. e741-e745 2006.

[42] P. Laoratanakul, A. V. Carazo, P. Bouchilloux, and K. Uchino, "Unipoled Disk-type Piezoelectric Transformers," *Japanese Journal of Applied Physics, Part 1*, vol. 41, pp. 1446-1450, 2002.

[43] M. Guo, D. M. Lin, K. H. Lam, S. Wang, H. L. W. Chan, and X. Z. Zhao, "A lead-free piezoelectric transformer in radial vibration modes," *Review of Scientific Instruments*, vol. 78, 2007.

[44] D. A. Berlincourt, "Piezoelectric starter and ballast for gaseous discharge lamps," in *U.S. Patent 3,764,848*, 1973.

[45] S.-T. Ho, "Modeling of a Disk-Type Piezoelectric Transformer," *IEEE Transactions on Ultrasonics, Ferroelectrics, and Frequency Control*, vol. 54, pp. 2110-2119, 2007.

[46] I. Kim, H. Joo, J. Song, S. Jeong, and M. Kim, "Ring-dot-shaped Multilayer Piezoelectric Step-down Transformers Using PZT-based Ceramics," *Journal of the Korean Physical Society*, vol. 57, pp. 963-966, 2010.

[47] E. C. Munk, "The Equivalent Electrical Circuit For Radial Modes Of A Piezoelectric Ceramic Disc With Concentric Electrodes," *Philips Research Reports*, vol. 20, pp. 170-189, 1965.

[48] H. L. Li, J. H. Hu, and H. L. W. Chan, "Finite Element Analysis on Piezoelectric Ring Transformer," *IEEE Transactions on Ultrasonics, Ferroelectrics, and Frequency Control*, vol. 51, pp. 1247-1254, 2004.

[49] J. H. Hu, H. L. Li, H. L. W. Chan, and C. L. Choy, "A Ring-shaped piezoelectric transformer operating in the third symmetric extensional vibration mode," *Sensors and Actuators, A: Physical*, vol. 88, pp. 79-86, 2001.

[50] K.-T. Chang, H.-C. Chiang, and K.-S. Lyu, "Effects of electrode layouts on voltage gain characteristics for ring-shaped piezoelectric transformers," *Sensors and Actuators, A: Physical*, vol. 141, pp. 166-172, 2007.

[51] S.-T. Ho, "Modeling and Analysis on Ring-Type Piezoelectric Transformers," *IEEE Transactions on Ultrasonics, Ferroelectrics, and Frequency Control*, vol. 54, pp. 2376-2384, 2007.

[52] M. Guo, K. H. Lam, S. Wang, K. W. Kwok, H. L. W. Chan, and X. Z. Zhao, "A study on the disk-shaped piezoelectric transformer with multiple outputs," *Review of Scientific Instruments*, vol. 78, 2007.

[53] R. Holland, "The Equivalent Circuit of a Symmetric N-Electrode Piezoelectric Disk," *IEEE Transactions on Sonics and Ultrasonics*, vol. 14, pp. 21-32, 1967.

[54] R. Holland, "The Equivalent Circuit of an N-Electrode Piezoelectric Bar," *Proceedings of the IEEE*, vol. 54, pp. 968-975, 1966.

[55] R. Holland, "Analysis of Multiterminal Piezoelectric Plates," *Journal of the Acoustical Society of America*, vol. 41, pp. 940-952, 1966.

[56] R. Holland and E. P. EerNisse, *Design of Resonant Piezoelectric Devices*: M.I.T. Press, Cambridge, Massachusetts, 1969.

[57] S. Hamamura, T. Ninomiya, M. Yamamoto, and M. Katsuno, "Combined PWM and PFM control for universal line voltage of a piezoelectric transformer off-line converter," *IEEE Transactions on Power Electronics*, vol. 18, pp. 270-277, 2003.

[58] M. Yamamoto, Y. Sasaki, T. Inoue, A. Ochi, and S. Hamamura, "Piezoelectric transformer for 30W output AC-DC converters," presented at IEEE International Symposium on Applications of Ferroelectrics, 2002.

[59] T. Zaitsu, "Power Conversion Using Piezoelectric Transformer," PhD thesis, Kyushu University, Fukuoka, Japan, 1997.

[60] O. M. Stuetzer, "Linear theory of piezoelectric power transformers," Sandia Laboratory Report No. SC-RR-66-414, 1966.

[61] C.-y. Lin, "Design and Analysis of Piezoelectric Transformer Converters," PhD thesis, Virginia Polytechnic Institute and State University, USA, 1997.

[62] M. Guo, X. P. Jiang, K. H. Lam, S. Wang, C. L. Sun, H. L. W. Chan, and X. Z. Zhao, "Lead-free multilayer piezoelectric transformer," *Review of Scientific Instruments*, vol. 78, 2007.

[63] O. Ohnishi, H. Kishie, A. Iwamoto, Y. Sasaki, T. Zaitsu, and T. Inoue, "Piezoelectric ceramic transformer operating in thickness extensional vibration mode for power supply," presented at IEEE Ultrasonics Symposium, 1992.

[64] A. M. Sánchez, M. Sanz, R. Prieto, J. A. Oliver, P. Alou, and J. A. Cobos, "Design of piezoelectric transformers for power converters by means of analytical and numerical methods," *IEEE transactions on Industrial Electronics*, vol. 55, pp. 79-88, 2008.

[65] J. A. Oliver, R. Prieto, M. Sanz, J. A. Cobos, and J. Uceda, "1D modeling of multi-layer piezoelectric transformers," presented at IEEE Power Electronics Specialists Conference (PESC), 2001.

[66] M. Sanz, A. M. Sánchez, J. A. Oliver, J. A. Cobos, and J. Uceda, "FEA based model of multi-layer Piezoelectric Transformer working in thickness mode," presented at IEEE Power Electronics Specialists Conference (PESC), 2004.

[67] A. M. Sánchez, R. Prieto, M. Sanz, J. A. Oliver, and J. A. Cobos, "Modeling and design of piezoelectric transformers for low power applications," presented at International Power Electronics Congress, 2004.

[68] R. Prieto, M. Sanz, J. A. Cobos, P. Alou, O. García, and J. Uceda, "Design considerations of multi-layer piezoelectric transformers," presented at Applied Power Electronics Conference and Exposition (APEC), 2001.

[69] M. Sanz, P. Alou, J. A. Oliver, R. Prieto, J. A. Cobos, and J. Uceda, "Interleaving of electrodes in piezoelectric transformers," presented at IEEE Power Electronics Specialists Conference (PESC), 2002.

[70] A. M. Sánchez, M. Sanz, P. Alou, R. Prieto, and J. A. Cobos, "Experimental validation of an optimized Piezoelectric Transformer design with interleaving of electrodes," presented at IEEE Power Electronics Specialists Conference (PESC), 2004.

[71] M. Sanz, P. Alou, R. Prieto, J. A. Cobos, and J. Uceda, "Magnetic-less converter based on Piezoelectric Transformers for step-down DC/DC and low power application," presented at Applied Power Electronics Conference and Exposition (APEC), 2003.

[72] M. Sanz, A. M. Sánchez, P. Alou, R. Prieto, J. A. Cobos, and J. Uceda, "Step by step multi-layer piezoelectric transformer design procedure," presented at Power Electronics Specialists Conference (PESC), 2004.

[73] A. M. Sánchez, M. Sanz, R. Prieto, J. A. Oliver, and J. A. Cobos, "Mixed analytical and numerical design method for piezoelectric transformers," presented at Power Electronics Specialists Conference (PESC), 2003.

[74] J. Navas, T. Bove, J. A. Cobos, F. Nunño, and K. Brebol, "Miniaturised battery charger using piezoelectric transformers," presented at IEEE Applied Power Electronics Conference and Exposition (APEC), 2001.

[75] T. Bove, W. Wolny, E. Ringgaard, and K. Breboel, "New type of piezoelectric transformer with very high power density," presented at IEEE International Symposium on Applications of Ferroelectrics, 2000.

[76] K. Brebøl, "Piezoelectric Transformer," in *U.S. Patent 6,707,235*, 2004.

[77] T. Zaitsu, K. Ohnishi, T. Inoue, M. Shoyama, T. Ninomiya, F. C. Lee, and G. C. Hua, "Piezoelectric transformer operating in thickness extensional vibration and its application to switching converter," presented at Power Electronics Specialists Conference (PESC), 1994.

[78] T. Zaitsu, T. Inoue, O. Ohnishi, and Y. Sasaki, "2 MHz power converter with piezoelectric ceramic transformer," *IEICE Transactions on Electronics*, vol. E77-C, pp. 280-286, 1994.

[79] T. Inoue, O. Ohnishi, and N. Ohde, "Thickness Mode Vibration Piezoelectric Transformer," in *U.S. Patent 5,118,982*, 1992.

[80] Y. Sasaki, K. Uehara, and T. Inoue, "Piezoelectric ceramic transformer being driven with thickness extensional vibration," in *U.S. Patent 5,241,236*, 1993.

[81] J.-H. Kim, D.-Y. Han, M.-H. Nam, and S.-M. Kang, "Analysis of a three-layered piezoelectric ceramic transformer filter," *IEEE Transactions on Circuits and Systems I: Fundamental Theory and Applications*, vol. 42, pp. 307-313, 1995.

[82] D. A. Berlincourt, D. R. Curran, and H. Jaffe, "Piezoelectric and Piezomagnetic Materials and Their Function in Transducers," in *Physical Acoustics: Principles and Methods*, vol. I part A, W. P. Mason, Ed.: Academic Press, New York, 1964.

[83] D. Guyomar, C. Magnet, E. Lefeuvre, and C. Richard, "Power capability enhancement of a piezoelectric transformer," *Smart Materials and Structures*, vol. 15, pp. 571-580, 2006.

[84] S. Lin, "Electro-mechanical equivalent circuit of a piezoelectric ceramic thin circular ring in radial vibration," *Sensors and Actuators A: Physical*, vol. 134, pp. 505-512, 2007.

[85] A. Lula, N. Lamberti, R. Carotenuto, and M. Pappalardo, "Analysis of the radial symmetrical modes of thin piezoceramic rings," *IEEE Transactions on Ultrasonics, Ferroelectrics, and Frequency Control*, vol. 46, pp. 1047-1049, 1999.

[86] J. Ribas, J. A. Martín, J. García, J. Cardesin, A. J. Calleja, and M. Rico-Secades, "Fluorescent lamp ballast based on a class-E resonant inverter using a piezoelectric transformer," presented at IAS Annual Meeting (IEEE Industry Applications Society) 2006.

[87] F. Nuno, J. A. Martin, J. Diaz, M. J. Prieto, and F. M. Fernandez-Linera, "Quantum mode control for piezoelectric transformers in AC/DC applications," presented at IEEE International Power Electronics Congress, 2002.

[88] J. Diaz, F. Nuno, J. M. Lopera, and J. A. Martin-Ramos, "A new control strategy for an AC/DC converter based on a piezoelectric transformer," *IEEE Transactions on Industrial Electronics*, vol. 51, pp. 850-856, 2004.

[89] M. J. Prieto, J. Diaz, J. A. Martin, and F. Nuno, "A very simple DC/DC converter using piezoelectric transformer," presented at Power Electronics Specialists Conference (PESC), 2001.

[90] M. J. Prieto, J. Diaz, J. A. Martin, F. F. Linera, and F. Nuno, "Design guidelines for DC/DC converter using piezoelectric transformer," presented at IEEE IECON, 2002.

[91] J. Diaz, F. Nuno, M. J. Prieto, J. A. Martin-Ramos, and P. J. Villegas Saiz, "Closing a Second Feedback Loop in a DC–DC Converter Based on a Piezoelectric Transformer," *IEEE Transactions on Power Electronics*, vol. 22, pp. 2195-2201, 2007.

[92] J. Diaz, F. Nuno, D. Gacio, J. Villegas Saiz, and M. J. Prieto, "Paralleling DC/DC Switched Converters Based on Piezoelectric Transformers," presented at IEEE Industry Applications Society Annual Meeting, 2009.

[93] J. A. Martin-Ramos, M. A. J. Prieto, F. N. Garcia, J. D. Gonzalez, and F. M. F. Linera, "A new full-protected control mode to drive piezoelectric transformers in DC-DC converters," *IEEE Transactions on Power Electronics*, vol. 17, pp. 1096-1103, 2002.

[94] J. M. Alonso, C. Ordiz, M. A. Dalla Costa, J. Ribas, and J. Cardesin, "High-Voltage Power Supply for Ozone Generation Based on Piezoelectric Transformer," *IEEE Transactions on Industry Applications*, vol. 45, pp. 1513-1523 2009.

[95] J. M. Alonso, C. Ordiz, and M. A. Dalla Costa, "A Novel Control Method for Piezoelectric-Transformer Based Power Supplies Assuring Zero-Voltage-Switching Operation," *IEEE Transactions on Industrial Electronics*, vol. 55, pp. 1085-1089 2008.

[96] K. S. Meyer, M. A. E. Andersen, and F. Jensen, "Parameterized analysis of Zero Voltage Switching in resonant converters for optimal electrode layout of Piezoelectric Transformers," presented at IEEE Power Electronics Specialists Conference, 2008.

[97] J. S. Yang and W. Zhang, "A thickness-shear high voltage piezoelectric transformer," *International Journal of Applied Electromagnetics and Mechanics*, vol. 10, pp. 105-121, 1999.

[98] J. S. Yang and X. Zhang, "Analysis of a thickness-shear piezoelectric transformer," *International Journal of Applied Electromagnetics and Mechanics*, vol. 21, pp. 131-141, 2005.
[99] K. J. Tseng, J. Du, and J. Hu, "Piezoelectric transformer with high power density and multiple outputs," *Electronics Letters*, vol. 40, pp. 786-788, 2004.
[100] J. Du, J. Hu, and K. J. Tseng, "Modeling of the Dual-Output Piezoelectric Transformer Operating at Thickness Shear Vibration Mode," presented at IEEE International Symposium on Applications of Ferroelectrics, 2004.
[101] J. Du, J. Hu, and K. J. Tseng, "High-power, multioutput piezoelectric transformers operating at the thickness-shear vibration mode," *IEEE Transactions on Ultrasonics, Ferroelectrics, and Frequency Control*, vol. 51, pp. 502-509, 2004.
[102] J. Du, J. Hu, K. J. Tseng, C. S. Kai, and C. S. Goh, "Modeling and Analysis of Dual-Output Piezoelectric Transformer Operating at the Thickness-Shear Vibration Mode," *IEEE Transactions on Ultrasonics, Ferroelectrics, and Frequency Control*, vol. 53, pp. 579-585, 2006.
[103] J. Hu, K. H. Chan, and B. S. Ng, "Output voltage regulation of a k15 mode piezoelectric transformer by an external L/C component," *Ultrasonics*, vol. 49, pp. 532-527, 2009.
[104] P. Laoratanakul and K. Uchino, "Designing a radial mode laminated piezoelectric transformer for high power applications," presented at IEEE International Symposium on Applications of Ferroelectrics, 2005.
[105] K. Uchino, "High Power Piezoelectrics," in *Advanced Piezoelectric Materials: Science and Technology*, K. Uchino, Ed.: Woodhead Publishing Ltd, 2010.
[106] Y. Sasaki, M. Umeda, S. Takahashi, M. Yamamoto, A. Ochi, and T. Inoue, "High-power Characteristics of Multilayer Piezoelectric Ceramic Transducers," *Japanese Journal of Applied Physics, Part 1*, vol. 40, 2001.
[107] Y. Sasaki, S. Takahashi, and M. Yamamoto, "Mechancial Quality Factor of Multilayer Piezoelectric Ceramic Transducers," *Japanese Journal of Applied Physics, Part 1*, vol. 40, pp. 3549-3551, 2001.
[108] R. W. Erickson and D. Maksimovic, *Fundamentals of Power Electronics (Second Edition)*: Springer, 2001.
[109] T. Ikeda, *Fundamentals of Piezoelectricity*: Oxford University Press, 1990.
[110] M. K. Kazimierczuk and D. Czarkowski, *Resonant Power Converters*: John Wiley & Sons Inc, 1995.
[111] E. M. Syed, "Analysis and modeling of piezoelectric transformers," Masters thesis, University of Toronto, Canada, 2001.
[112] A. M. Flynn and S. R. Sanders, "Fundamental limits on energy transfer and circuit considerations for piezoelectric transformers," *IEEE Transactions on Power Electronics*, vol. 17, pp. 8-14, 2002.
[113] M. Shoyama, K. Horikoshi, T. Ninomiya, T. Zaitsu, and Y. Sasaki, "Operation analysis of the push-pull piezoelectric inverter," presented at Applied Power Electronics Conference and Exposition (APEC), 1997.
[114] M. Day and B. S. Lee, "Understanding piezoelectric transformers in CCFL backlight applications," in *Texas Instruments Application Note SLYT107*, 2005.
[115] E. Wells, "Comparing magnetic and piezoelectric transformer approaches in CCFL applications," in *Texas Instruments Application Note SLYT125*, 2005.
[116] "Multi-topology piezoelectric transformer controller (UCC2975, UCC2976, UCC2977, UCC3975, UCC3975, UCC3976, UCC3977)," *Texas Instruments Datasheet*, 2002.
[117] F. E. Bisogno, M. Radecker, A. Knoll, A. V. Carazo, A. Riedlhammer, G. Deboy, N. Norvez, and J. M. Pacas, "Comparison of resonant topologies for

step-down applications using piezoelectric transformers," presented at IEEE Annual Power Electronics Specialists Conference, 2004.

[118] Y. Yang, F. E. Bisogno, A. Schittler, S. Nittayarumphong, M. Radecker, W. J. Fischer, and M. Fahlenkamp, "Comparison of Inductor-Half-Bridge and Class-E resonant topologies for piezoelectric transformer applications," presented at IEEE Energy Conversion Congress and Exposition, 2009.

[119] Y. Yang, F. Bisogno, S. Nittayarumphong, M. Radecker, M. Fahlenkamp, and W. J. Fischer, "Smart universal control IC for high loaded factor resonant converters," presented at Custom Integrated Circuits Conference, 2010.

[120] S. Nittayarumphong, F. E. Bisogno, M. Radecker, and A. V. Carazo, "Comparison of Control Concepts for Off-Line Power Supplies using Piezoelectric Transformers in Class-E Topology," presented at Power Electronics Specialists Conference (PESC), 2006.

[121] M. Radecker, F. Bisogno, A. Knoll, G. Lohmann, A. V. Carazo, and G. Deboy, "A low-size multi-power-level single-transistor ballast for low pressure fluorescent lamps, using a piezoelectric transformer," presented at IEEE Industry Applications Society Annual Meeting, 2004.

[122] S. Nittayarumphong, F. Bisogno, M. Radecker, A. Knoll, A. V. Carazo, and A. Riedlhammer, "Dynamic behaviour of PI controlled class-E resonant converter for step-down applications using piezoelectric transformers," presented at European Conference on Power Electronics and Applications, 2005.

[123] F. Bisogno, S. Nittayarumphong, M. Radecker, A. V. Carazo, M. Kronberg, A. Riedlhammer, and M. Herfurth, "Dynamical modeling of class-E resonant converter for step-down applications using piezoelectric transformers," presented at Power Electronics Specialists Conference (PESC), 2005.

[124] F. E. Bisogno, S. Nittayarumphong, M. Radecker, A. V. Carazo, and R. N. do Prado, "A Line Power-Supply for LED Lighting using Piezoelectric Transformers in Class-E Topology," presented at Power Electronics and Motion Control Conference, 2006.

[125] S. Nittayarumphong, F. Bisogno, M. Radecker, A. V. Carazo, A. Riedlhammer, and H. Guldner, "High efficiency control methods for class-E resonant converter for step-down applications using Piezoelectric Transformers (PT)," presented at European Conference on Power Electronics and Applications, 2007.

[126] T. Yamane, S. Hamamura, T. Zaitsu, T. Ninomiya, M. Shoyama, and Y. Fuda, "Efficiency Improvement of Piezoelectric-Transformer DC-DC Converter," presented at IEEE Power Electronics Specialists Conference (PESC), 1998.

[127] S. Hamamura, T. Zaitsu, T. Ninomiya, and M. Shoyama, "Noise Characteristics of Piezoelectric-Transformer DC-DC Converter," presented at Power Electronics Specialists Conference (PESC), 1998.

[128] M. Sanz, P. Alou, R. Prieto, J. A. Cobos, and J. Uceda, "Comparison of different alternatives to drive piezoelectric transformers," presented at IEEE Applied Power Electronics Conference and Exposition, 2002.

[129] S. Choi, T. Kim, and B. H. Cho, "Design of half-bridge piezo-transformer converters in the AC adapter applications," presented at Conference Proceedings - IEEE Applied Power Electronics Conference and Exposition - APEC, 2005.

[130] T. Ninomiya, M. Shoyama, T. Zaitsu, and T. Inoue, "Zero-voltage-switching techniques and their application to high-frequency converter with piezoelectric transformer," presented at IECON Proceedings (Industrial Electronics Conference), 1994.

[131] T. Zaitsu, T. Shigehisa, T. Inoue, M. Shoyama, and T. Ninomiya, "Piezoelectric Transformer Converter with Frequency Control," presented at International Telecommunications Energy Conference (INTELEC), 1995.

[132] W. Huang, D. Chen, E. M. Baker, J. Zhou, H.-I. Hsieh, and F. C. Lee, "Design of a Power Piezoelectric Transformer for a PFC Electronic Ballast," *IEEE Transactions on Industrial Electronics*, vol. 54, pp. 3197-3204, 2007.
[133] J. Zhou, F. Tao, and F. C. Lee, "Inductor-less charge pump PFC electronic ballast," presented at IEEE Industry Applications Conference (IAS), 2001.
[134] S. Choi, K. Lee, and B. H. Cho, "Design of fluorescent lamp ballast with PFC using a power piezoelectric transformer," *IEEE Transactions on Industrial Electronics*, vol. 52, pp. 1573-1581, 2005.
[135] R.-L. Lin and H.-M. Shih, "Piezoelectric Transformer Based Current-Source Charge-Pump Power-Factor-Correction Electronic Ballast," *IEEE Transactions on Power Electronics*, vol. 23, 2008.
[136] R.-L. Lin and H.-M. Shih, "A Family of Piezoelectric Transformer Based Bridgeless Continuous-Conduction-Mode Charge-Pump Power-Factor-Correction Electronic Ballasts," presented at IEEE Industry Applications Conference (IAS), 2007.
[137] R.-L. Lin, H.-M. Shih, C.-Y. Liu, and J.-B. Liu, "Piezoelectric Transformer Based Continuous-conduction-mode Voltage Source Charge-pump Power Factor Correction Electronic Ballast," presented at European Particle Accelerator Conference (EPAC), Edinburgh, Scotland, 2006.
[138] S. Bronstein and S. Ben-Yaakov, "Design considerations for achieving ZVS in a half bridge inverter that drives a piezoelectric transformer with no series inductor," presented at IEEE Applied Power Electronics Conference and Exposition, 2002.
[139] APC International website: http://www.americanpiezo.com, 2010.
[140] Ferroperm Piezoceramics website: http://www.ferroperm-piezo.com, 2010.
[141] "Planar Transformer catalogue," *Payton Planar Magnetics Ltd*, 2009.
[142] K. Uchino, *Ferroelectric Devices (Second Edition)*: CRC Press, 2009.
[143] Z. Zhu, G. Li, B. Li, Q. Yin, and K. Jiang, "The influence of Yb and Nd substituents on high-power piezoelectric properties of PMS-PZT ceramics," *Ceramics International*, vol. 34, pp. 2067-2072, 2008.
[144] J. Ryu, H. W. Kim, K. Uchino, and J. Lee, "Effect of Yb Addition on the Sintering Behavior and High Power Piezoelectric Properties of Pb(Zr,Ti)O3–Pb(Mn,Nb)O3," *Japanese Journal of Applied Physics*, vol. 42, pp. 1307-1310, 2003.
[145] Y. K. Gao, Y. H. Chen, J. G. Ryu, K. Uchino, and D. Viehland, "Eu and Yb Substituent Effects on the Properties of Pb(Zr0.52Ti0.48)O3–Pb(Mn1/3Sb2/3)O3 Ceramics: Development of a New High-Power Piezoelectric with Enhanced Vibrational Velocity," *Japanese Journal of Applied Physics*, vol. 40, pp. 687-693 2001.
[146] K. Uchino and S. Hirose, "Loss Mechanisms in Piezoelectrics: How to Measure Different Losses Seperately," *IEEE Transactions on Ultrasonics, Ferroelectrics, and Frequency Control*, vol. 48, pp. 307-321, 2001.
[147] M. Umeda, S. Takahashi, Y. Sasaki, K. Nakamura, and S. Ueha, "Vibration stress and temperature dependence of piezoelectric resonators with lead-zirconate-titanate ceramics," *Electronics and Communications in Japan, Part II: Electronics*, vol. 83, pp. 1-7, 2000.
[148] S. Takahashi, M. Yamamoto, and Y. Sasaki, "Nonlinear Piezoelectric Effect in Ferroelectric Ceramics," *Japanese Journal of Applied Physics, Part 1*, vol. 37, pp. 5292-5296, 1998.
[149] K. Uchino, A. Joshi, Y.-H. Chen, and Yoshikawa, "High Power Characterization of Piezoelectric Materials," *Journal of Electroceramics*, vol. 2, pp. 33-40, 1998.

[150] M. Katsuno, Y. Fuda, and M. Tamura, "High-Power Ceramic Materials for Piezoelectric Transformers," *Electronics and Communications in Japan, Part 3*, vol. 82, pp. 86-92, 1999.

[151] S. Hirose, S. Takahashi, M. Aoyagi, and Y. Tomikawa, "High-Power Characteristics of Piezoelectric Materials," presented at Ninth IEEE International Symposium on Applications of Ferroelectrics, 1995.

[152] S. Takahashi and S. Hirose, "Vibration-Level Characteristics for Iron-Doped Lead-Zirconate-Titanate Ceramic," *Japanese Journal of Applied Physics, Part 1*, vol. 32, pp. 2422-2425, 1993.

[153] S. Takahashi and S. Hirose, "Vibration-Level Characteristics of Lead-Zirconate-Titanate Ceramics," *Japanese Journal of Applied Physics, Part 1*, vol. 31, pp. 3055-3057, 1992.

[154] S. Ural, S. Tuncdemir, Y. Zhuang, and K. Uchino, "Development of a High Power Piezoelectric Characterization System and Its Application for Resonance/Antiresonance Mode Characterization," *Japanese Journal of Applied Physics*, vol. 48, 2009.

[155] S. Ural, Y. Zhuang, S. Tuncdemir, and K. Uchino, "Comparison of Power Density Characteristics among Disk and Plate Shaped Piezoelectric Devices," *Japanese Journal of Applied Physics*, vol. 49, 2010.

[156] K. Uchino, J. H. Zheng, Y. H. Chen, X. H. Du, J. Ryu, Y. Gao, S. Ural, S. Priya, and S. Hirose, "Loss mechanisms and high power piezoelectrics," *Journal of Materials Science*, vol. 41, pp. 217-228, 2006.

[157] M. Umeda, K. Nakamura, and S. Ueha, "The Measurement of High-Power Characteristics for a Piezoelectric Transducer Based on the Electrical Transient Response," *Japanese Journal of Applied Physics, Part 1*, vol. 37, pp. 5322-5325, 1998.

[158] M. Umeda, K. Nakamura, and S. Ueha, "Effects of Vibration Stress and Temperature on the Characteristics of Piezoelectric Ceramics under High Vibration Amplitude Levels Measured by Electrical Transient Responses," *Japanese Journal of Applied Physics, Part 1*, vol. 38, pp. 5581-5585, 1999.

[159] S. Takahashi, Y. Sasaki, M. Umeda, K. Nakamura, and S. Ueha, "Nonlinear behavior in piezoelectric ceramic transducers," presented at International Symposium on Applications of Ferroelectrics (ISAF), 2000.

[160] "IRE Standards on Piezoelectric Crystals-The Piezoelectric Vibrator: Definitions and Methods of Measurement, 1957," *Proceedings of the IRE*, vol. 45, pp. 353-358, 1957.

[161] "IEEE standard on piezoelectricity," *ANSI/IEEE Std 176-1987*, 1988.

[162] S. Takahashi, Y. Sasaki, S. Hirose, and K. Uchino, "Stability of PbZrO 3-PbTiO 3-Pb(Mn 1/3Sb 2/3)O 3 Piezoelectric Ceramics under Vibration-Level Change," *Japanese Journal of Applied Physics*, vol. 34, pp. 5328-5331, 1995.

[163] S. Takahashi, S. Hirose, K. Uchino, and O. Ki-Young, "Electro-mechanical characteristics of lead-zirconate-titanate ceramics under vibration-level change," presented at International Symposium on Applications of Ferroelectrics (ISAF), 1994.

[164] "Standards on Piezoelectric Crystals, 1949," *Proceedings of the IRE*, vol. 37, pp. 1378-1395, 1949.

[165] A. J. Moulson and J. M. Herbert, "Piezoelectric ceramics (Chapter 6)," in *Electroceramics*, 2 ed: John Wiley & Sons Ltd, 2003, pp. 339-410.

[166] "IRE Standards on Piezoelectric Crystals: Determination of the Elastic, Piezoelectric, and Dielectric Constants - The Electromechanical Coupling Factor, 1958," *Proceedings of the IRE*, vol. 46, pp. 764-778, 1958.

[167] "IRE Standards on Piezoelectric Crystals: Measurements of Piezoelectric Ceramics, 1961," *Proceedings of the IRE*, vol. 49, pp. 1161-1169, 1961.

Chapter 2 - Equivalent circuit modelling of radial mode Transoner PTs (I)

2.1 Introduction

Like a conventional resonant converter, a PT based converter must be specifically designed for its target application if high efficiency and high power density are to be achieved. To facilitate this, it is essential to have a model that relates the electrical characteristics of a PT to the physical parameters of the device; that is, an equivalent circuit model where each of the electrical components is fully specified in terms of the physical dimensions and material parameters of the device.

Three lumped equivalent circuit models have been published for the radial mode Transoner PT [1-3], and all three mathematically differ from one another. Comparing [1] to many other works involving the radial motion of a thin disc, it can be seen that the equation of motion on which [1] is based is not correct. The radial motion of a thin disc has a Bessel function description [4, 5]. Therefore the use of a sinusoidal function on page 158 of [1] for the radial strain (which is the derivative of the equation of motion with respect to the radial coordinate) is not correct. A second problem with [1] was highlighted by Dr. Carazo of Micromechatronics Inc. Neglecting air resistance, the radial force at the outer radius of the PT is zero. Therefore the approach of splitting the PT into an input section and an output section and coupling the radial force at the outer radius of the input section to that at the outer radius of the output section is incorrect because the boundary condition (i.e. the force being zero) is not implemented. The model presented in [2] uses the correct equation of motion, but like [1], does not appear to implement the boundary conditions correctly. Whilst [3] primarily deals with contour vibration mode devices, the lumped equivalent circuit model it contains is stated to be for a radial mode device. However, no derivation, list of assumptions, or experimental verification was provided.

This chapter presents the derivation of a Mason type equivalent circuit for a simple radial mode PT. A lumped equivalent circuit representation is then obtained, and comparisons are made between the simulated and experimental component values of

isolated and non-isolated Transoner T1 radial mode PTs. Reasons for the discrepancies between simulation and experiment are discussed, and methods for improving the accuracy of the model are suggested. The Mason equivalent circuit then forms a key part of the more complete model that is developed in Chapter 3.

2.2 Scope, definitions, and assumptions

Figure 2.1 shows the construction of a typical, purely bonded, radial mode Transoner PT. The ceramic and the copper electrodes in the input and output section have the same radius. Whilst the radius of the isolation layer is usually made slightly larger than that of the electrodes and ceramic in order to improve the breakdown voltage, the amount of material that extends past the radius of the electrode and ceramic layers is very small, and will therefore be neglected. Thus, for modelling purposes, all layers of the PT are assumed to be the same radius. The PT is assumed to have an input section consisting of n_{in} identical layers connected electrically in parallel, and a secondary section consisting of n_{out} identical layers connected in parallel. The thickness of a single input section layer and a single output section layer are referred to as t_{in} and t_{out} respectively. In practice, the device may be manufactured such that the input (or output) section is split into two sections, with $n_{in}/2$ layers above the output section and $n_{in}/2$ layers below the output section, because this helps to reduce the effect of bending modes and ensures a more uniform radial strain profile in the thickness direction. However, arranging the layers in such a manner does not change the analysis that follows because strain is assumed constant in the thickness direction (see later).

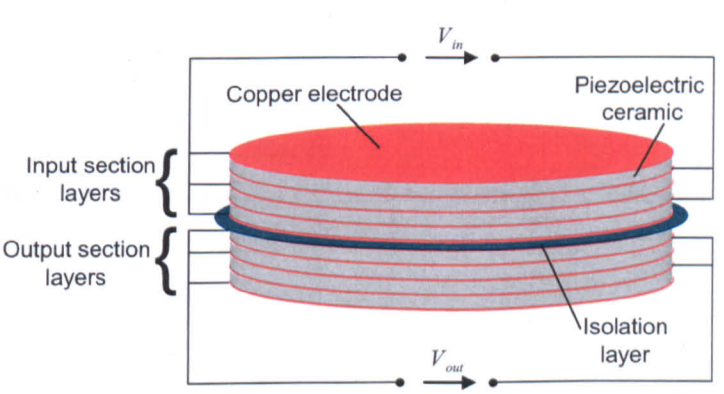

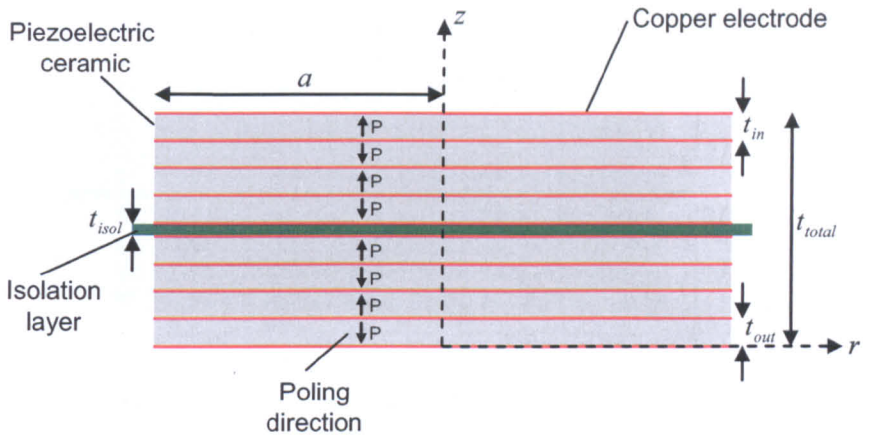

Figure 2.1: Diagrams showing the construction and electrical connections of a simple radial mode Transoner PT. Note that all ceramic and electrode layers have the same radius.

The PT is shown positioned in the Cartesian and cylindrical coordinate systems in Figure 2.2. The radial force at the outer radius of the PT is labelled F_a, whilst the radial vibration velocity of a particle at the outer radius is labelled v_a. Note that throughout this thesis, the direction of an arrow will always correspond to the direction in which the associated quantity is defined as being positive. Thus, both F_a and v_a are defined as being positive in the opposite direction to the r axis. The voltages and currents in the input and output section are defined in relation to the coordinate systems and poling directions as shown in Figure 2.3. A Mason equivalent circuit is now developed to relate the voltages and currents in the input and output section to the radial force and radial vibration velocity at the outer radius of the PT. A 3-port network representation of the Mason equivalent circuit is shown in Figure 2.4.

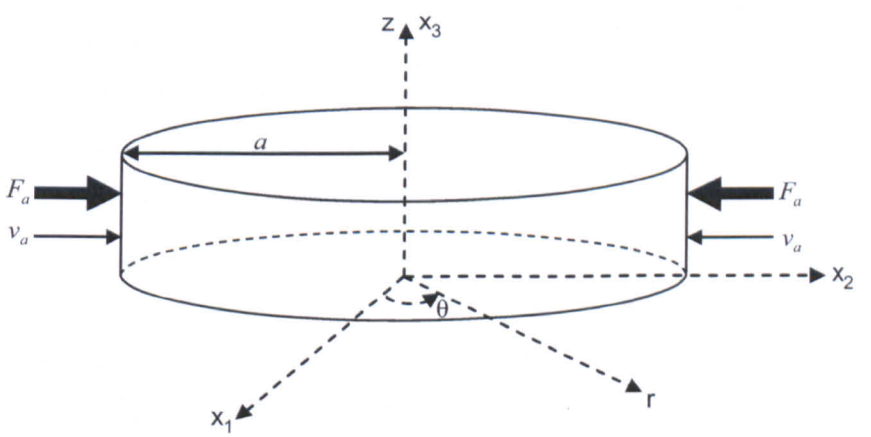

Figure 2.2: PT positioned in the Cartesian and cylindrical coordinate systems.

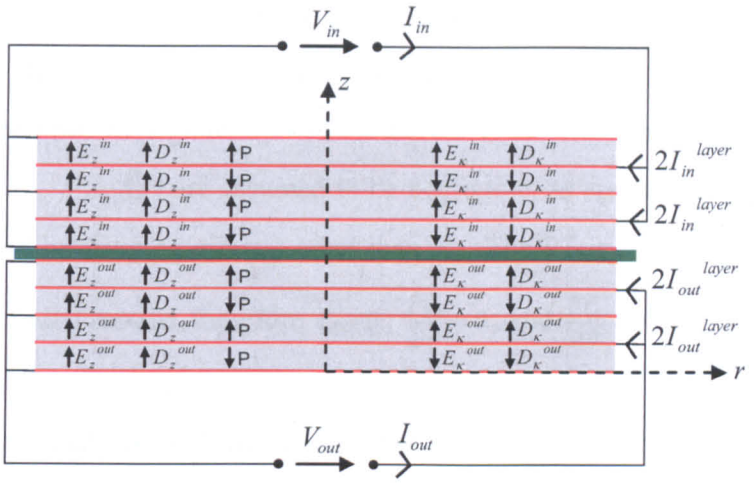

Figure 2.3: Voltage and current definitions in relation to the cylindrical coordinate system. Note that I_{in} and I_{out} are shown here as being equal to $4I_{in}^{layer}$ and $4I_{out}^{layer}$, respectively, to reflect the fact that the device is shown here with 4 input section layers and 4 output section layers.

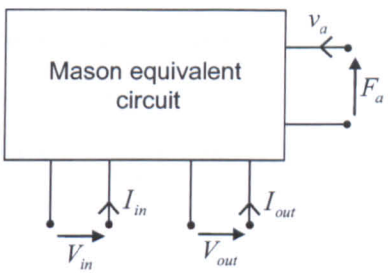

Figure 2.4: A 3-port network representation of the Mason equivalent circuit of the radial mode Transoner PT. The force and vibration velocity at the outer radius of the PT are represented as a voltage and current respectively.

Two key assumptions will be used throughout the following analysis:

- The PT is considered to be a thin composite disc in radial motion. Thus, stress in the thickness direction is assumed to be negligibly small compared to the radial and azimuthal stresses. In practice, this means that the ratio of the PT radius to total thickness must be sufficiently large, thereby ensuring that the first thickness vibration mode is not too close to the first radial vibration mode.
- Radial displacement, radial strain, and azimuthal strain are assumed to be constant with thickness. Whilst all layers are assumed to experience the same radial and azimuthal strains, the stresses developed within a particular layer will depend upon the compliance of that layer, and in the case of piezoelectric layers, the electric flux density and electric field.

The variables ξ, T, S, E, D, and ε are used for displacement, stress, strain, electric field, electric flux density, and permittivity, respectively. Since stress in the thickness direction is assumed negligible, $T_z \approx 0$. Furthermore, all shear stresses and strains (T_{rz}, $T_{r\theta}$, $T_{\theta z}$, and S_{rz}, $S_{r\theta}$, $S_{\theta z}$) are assumed to be negligible, as are any electric fields (such as those caused by fringing effects) other than E_z. The PT is assumed to be in perfect axisymmetric radial motion, therefore $\xi_\theta = 0$, $\frac{\partial \xi_\theta}{\partial \theta} = 0$, and $\frac{\partial T_\theta}{\partial \theta} = 0$.

Throughout the analysis, a distinction is kept between the material properties of the ceramic in the input section and those of the ceramic in the output section, as these are known to vary with geometry and the extent to which the material is poled. Quantities that pertain to the input or output sections are designated as such by the use of the superscripts "in" and "out". The derivation proceeds under a lossless assumption (all dielectric, mechanical, and piezoelectric constants are taken to be pure real). However, mechanical losses will be considered once the Mason equivalent circuit is simplified to a lumped equivalent circuit representation. Finally, the analysis is conducted for sinusoidal steady state conditions; therefore appropriate variables have a suppressed $e^{j\omega t}$ dependence.

2.3 Derivation

A. Identifying the constitutive piezoelectric equations

Consider a single piezoelectric disc, poled in the thickness direction, and positioned in Cartesian and cylindrical coordinate systems such that the direction of poling corresponds to the z and x_3 coordinate axes. Let the disc be thin, electroded on the major surfaces, and driven into radial vibration. Since $T_z \approx 0$, the appropriate constitutive equations for such a disc are [6]

$$S_r = s_{11}^E T_r + s_{12}^E T_\theta + d_{31} E_z \tag{2.1}$$

$$S_\theta = s_{12}^E T_r + s_{11}^E T_\theta + d_{31} E_z \tag{2.2}$$

$$D_z = d_{31} T_r + d_{31} T_\theta + \varepsilon_{33}^T E_z . \tag{2.3}$$

Since the PT is regarded as thin, the constitutive equations for the thin disc scenario are applicable. Thus, for the input section layers that are poled in the same direction as the z (and x_3) axes,

$$S_{rC}^{in} = s_{11}^{E\,in} T_{rC}^{in} + s_{12}^{E\,in} T_{\theta C}^{in} + d_{31}^{in} E_z^{in} \tag{2.4}$$

$$S_{\theta C}^{in} = s_{12}^{E\,in} T_{rC}^{in} + s_{11}^{E\,in} T_{\theta C}^{in} + d_{31}^{in} E_z^{in} \tag{2.5}$$

$$D_z^{in} = d_{31}^{in} T_{rC}^{in} + d_{31}^{in} T_{\theta C}^{in} + \varepsilon_{33}^{T\,in} E_z^{in}. \tag{2.6}$$

The subscript "C" on the stress and strain variables is simply to indicate that the quantities apply to ceramic. For the input section discs where the direction of poling opposes the z coordinate axis (see Figure 2.1 and Figure 2.3), the piezoelectric constants change sign [7] and the appropriate equations become

$$S_{rC}^{in} = s_{11}^{E\,in} T_{rC}^{in} + s_{12}^{E\,in} T_{\theta C}^{in} - d_{31}^{in} E_z^{in} \tag{2.7}$$

$$S_{\theta C}^{in} = s_{12}^{E\,in} T_{rC}^{in} + s_{11}^{E\,in} T_{\theta C}^{in} - d_{31}^{in} E_z^{in} \tag{2.8}$$

$$D_z^{in} = -d_{31}^{in} T_{rC}^{in} - d_{31}^{in} T_{\theta C}^{in} + \varepsilon_{33}^{T\,in} E_z^{in}. \tag{2.9}$$

An electric field, E_κ^{in}, is now defined such that in the discs poled $\uparrow$P, $E_\kappa^{in} = E_z^{in}$, whereas in the discs poled $\downarrow$P, $E_\kappa^{in} = -E_z^{in}$. Likewise, an electric flux density D_κ^{in} is defined such that in the layers poled $\uparrow$P, $D_\kappa^{in} = D_z^{in}$, whereas in the layers poled $\downarrow$P, $D_\kappa^{in} = -D_z^{in}$. Thus, E_κ^{in} and D_κ^{in} are defined as shown in Figure 2.3. A single set of equations can then be used for all input section discs, regardless of poling direction

$$S_{rC}^{in} = s_{11}^{E\,in} T_{rC}^{in} + s_{12}^{E\,in} T_{\theta C}^{in} + d_{31}^{in} E_\kappa^{in} \tag{2.10}$$

$$S_{\theta C}^{in} = s_{12}^{E\,in} T_{rC}^{in} + s_{11}^{E\,in} T_{\theta C}^{in} + d_{31}^{in} E_\kappa^{in} \tag{2.11}$$

$$D_\kappa^{in} = d_{31}^{in} T_{rC}^{in} + d_{31}^{in} T_{\theta C}^{in} + \varepsilon_{33}^{T\,in} E_\kappa^{in}. \tag{2.12}$$

Equations (2.10) and (2.11) can be rewritten in terms of the Poisson's ratio of the ceramic σ_C^E as

$$S_{rC}^{in} = s_{11}^{E\,in} T_{rC}^{in} - s_{11}^{E\,in} \sigma_C^{E\,in} T_{\theta C}^{in} + d_{31}^{in} E_\kappa^{in} \tag{2.13}$$

$$S_{\theta C}^{in} = -\sigma_C^{E\,in} s_{11}^{E\,in} T_{rC}^{in} + s_{11}^{E\,in} T_{\theta C}^{in} + d_{31}^{in} E_\kappa^{in} \tag{2.14}$$

where

$$\sigma_C^{E\,in} = \frac{-s_{12}^{E\,in}}{s_{11}^{E\,in}}. \tag{2.15}$$

Finally, it is more convenient to have (2.13) and (2.14) solved for T_{rC}^{in} and $T_{\theta C}^{in}$. Thus, the final set of equations for the input section discs is

$$T_{rC}^{\ in} = \frac{1}{s_{11}^{E\,in}\left(1-\sigma_C^{E\,in^2}\right)}\left(S_{rC}^{\ in} + \sigma_C^{E\,in} S_{\theta C}^{\ in} - d_{31}^{\ in} E_\kappa^{\ in}\left(1+\sigma_C^{E\,in}\right)\right) \tag{2.16}$$

$$T_{\theta C}^{\ in} = \frac{1}{s_{11}^{E\,in}\left(1-\sigma_C^{E\,in^2}\right)}\left(S_{\theta C}^{\ in} + \sigma_C^{E\,in} S_{rC}^{\ in} - d_{31}^{\ in} E_\kappa^{\ in}\left(1+\sigma_C^{E\,in}\right)\right) \tag{2.17}$$

$$D_\kappa^{\ in} = d_{31}^{\ in} T_{rC}^{\ in} + d_{31}^{\ in} T_{\theta C}^{\ in} + \varepsilon_{33}^{T\,in} E_\kappa^{\ in}. \tag{2.18}$$

Likewise, for the output section discs,

$$T_{rC}^{\ out} = \frac{1}{s_{11}^{E\,out}\left(1-\sigma_C^{E\,out^2}\right)}\left(S_{rC}^{\ out} + \sigma_C^{E\,out} S_{\theta C}^{\ out} - d_{31}^{\ out} E_\kappa^{\ out}\left(1+\sigma_C^{E\,out}\right)\right) \tag{2.19}$$

$$T_{\theta C}^{\ out} = \frac{1}{s_{11}^{E\,out}\left(1-\sigma_C^{E\,out^2}\right)}\left(S_{\theta C}^{\ out} + \sigma_C^{E\,out} S_{rC}^{\ out} - d_{31}^{\ out} E_\kappa^{\ out}\left(1+\sigma_C^{E\,out}\right)\right) \tag{2.20}$$

$$D_\kappa^{\ out} = d_{31}^{\ out} T_{rC}^{\ out} + d_{31}^{\ out} T_{\theta C}^{\ out} + \varepsilon_{33}^{T\,out} E_\kappa^{\ out} \tag{2.21}$$

where $E_\kappa^{\ out}$ and $D_\kappa^{\ out}$ are defined as shown in Figure 2.3.

B. Equation of motion

Neglecting shear stresses, the equation of equilibrium for the radial motion of a thin disc is [6]

$$\frac{\partial T_r}{\partial r} + \frac{T_r - T_\theta}{r} = \rho \frac{\partial^2 \xi_r}{\partial t^2} \tag{2.22}$$

where ξ_r is radial displacement, t is time, and ρ is density. If the disc is assumed to be in perfect axisymmetric radial motion, the radial and azimuthal strains are related to radial displacement by [6]

$$S_r = \frac{\partial \xi_r}{\partial r} \tag{2.23}$$

$$S_\theta = \frac{\xi_r}{r}. \tag{2.24}$$

In order to apply (2.22) to the composite shown in Figure 2.1, average T_r, T_θ, and ρ are then found. Average or effective quantities are denoted by a horizontal bar above the relevant symbol. The average density of the PT is given by

$$\bar{\rho} = f_C^{\ in} \rho_C^{\ in} + f_C^{\ out} \rho_C^{\ out} + f_I \rho_I + f_E \rho_E \tag{2.25}$$

where f is the thickness fraction of a particular material, i.e. (number of layers × layer thickness) / total thickness (see Figure 2.1). For the input and output sections, these are

$$f_C^{\ in} = \frac{n_{in} t_{in}}{t_{total}} \tag{2.26}$$

$$f_C{}^{out} = \frac{n_{out} t_{out}}{t_{total}}. \tag{2.27}$$

The subscripts C, I, and E are used to refer to the piezoelectric ceramic, isolation, and electrode material respectively. Since stress is force per unit area, and the composition of the device remains constant in the r and θ directions, the overall average radial and azimuthal stresses in the composite can be expressed in terms of the stresses within each material as (see, for example, page 61 of [8])

$$\overline{T}_r = f_C{}^{in} T_{rC}{}^{in} + f_C{}^{out} T_{rC}{}^{out} + f_I T_{rI} + f_E T_{rE} \tag{2.28}$$

$$\overline{T}_\theta = f_C{}^{in} T_{\theta C}{}^{in} + f_C{}^{out} T_{\theta C}{}^{out} + f_I T_{\theta I} + f_E T_{\theta E}. \tag{2.29}$$

The stresses within the piezoelectric discs are related to the strains (and therefore to radial displacement) using the constitutive equations in Section 2.3A. For the isotropic non-piezoelectric isolation and electrode layers, Hooke's law in cylindrical coordinates is applied. Since $T_z = 0$ is assumed in all layers, this gives

$$T_{rI} = \frac{Y_I}{1-\sigma_I{}^2}\left(S_{rI} + \sigma_I S_{\theta I}\right) \tag{2.30}$$

$$T_{\theta I} = \frac{Y_I}{1-\sigma_I{}^2}\left(S_{\theta I} + \sigma_I S_{rI}\right) \tag{2.31}$$

$$T_{rE} = \frac{Y_E}{1-\sigma_E{}^2}\left(S_{rE} + \sigma_E S_{\theta E}\right) \tag{2.32}$$

$$T_{\theta E} = \frac{Y_E}{1-\sigma_E{}^2}\left(S_{\theta E} + \sigma_E S_{rE}\right) \tag{2.33}$$

where Y_I and Y_E are the Young's modulus of the isolation and electrode material respectively. Since radial and azimuthal strain is assumed to be constant in the thickness direction,

$$S_{rE} = S_{rI} = S_{rC}{}^{out} = S_{rC}{}^{in} = \frac{\partial \xi_r}{\partial r} \tag{2.34}$$

$$S_{\theta E} = S_{\theta I} = S_{\theta C}{}^{out} = S_{\theta C}{}^{in} = \frac{\xi_r}{r}. \tag{2.35}$$

Using (2.28), (2.29), (2.16), (2.17), (2.19), (2.20), and (2.30) to (2.33), the overall radial and azimuthal stress in the composite is

$$\begin{aligned}\overline{T}_r = {} & f_C{}^{in} \frac{1}{s_{11}^{E\,in}\left(1-\sigma_C^{E\,in\,2}\right)}\left(\frac{\partial \xi_r}{\partial r} + \sigma_C^{E\,in}\frac{\xi_r}{r} - d_{31}{}^{in} E_\kappa{}^{in}\left(1+\sigma_C^{E\,in}\right)\right) \\ & + f_C{}^{out} \frac{1}{s_{11}^{E\,out}\left(1-\sigma_C^{E\,out\,2}\right)}\left(\frac{\partial \xi_r}{\partial r} + \sigma_C^{E\,out}\frac{\xi_r}{r} - d_{31}{}^{out} E_\kappa{}^{out}\left(1+\sigma_C^{E\,out}\right)\right) \\ & + f_I \frac{Y_I}{\left(1-\sigma_I{}^2\right)}\left(\frac{\partial \xi_r}{\partial r} + \sigma_I \frac{\xi_r}{r}\right) + f_E \frac{Y_E}{\left(1-\sigma_E{}^2\right)}\left(\frac{\partial \xi_r}{\partial r} + \sigma_E \frac{\xi_r}{r}\right)\end{aligned} \tag{2.36}$$

$$\bar{T}_\theta = f_C{}^{in}\frac{1}{s_{11}^{E\,in}\left(1-\sigma_C^{E\,in\,2}\right)}\left(\frac{\xi_r}{r}+\sigma_C^{E\,in}\frac{\partial\xi_r}{\partial r}-d_{31}{}^{in}E_\kappa{}^{in}\left(1+\sigma_C^{E\,in}\right)\right)$$

$$+f_C{}^{out}\frac{1}{s_{11}^{E\,out}\left(1-\sigma_C^{E\,out\,2}\right)}\left(\frac{\xi_r}{r}+\sigma_C^{E\,out}\frac{\partial\xi_r}{\partial r}-d_{31}{}^{out}E_\kappa{}^{out}\left(1+\sigma_C^{E\,out}\right)\right) \tag{2.37}$$

$$+f_I\frac{Y_I}{\left(1-\sigma_I{}^2\right)}\left(\frac{\xi_r}{r}+\sigma_I\frac{\partial\xi_r}{\partial r}\right)+f_E\frac{Y_E}{\left(1-\sigma_E{}^2\right)}\left(\frac{\xi_r}{r}+\sigma_E\frac{\partial\xi_r}{\partial r}\right)$$

which can be rewritten as

$$\bar{T}_r = \frac{\partial\xi_r}{\partial r}\bar{Y}_r+\frac{\xi_r}{r}\bar{P}-f_C{}^{in}\frac{d_{31}{}^{in}E_\kappa{}^{in}}{s_{11}^{E\,in}\left(1-\sigma_C^{E\,in}\right)}-f_C{}^{out}\frac{d_{31}{}^{out}E_\kappa{}^{out}}{s_{11}^{E\,out}\left(1-\sigma_C^{E\,out}\right)} \tag{2.38}$$

$$\bar{T}_\theta = \frac{\xi_r}{r}\bar{Y}_r+\frac{\partial\xi_r}{\partial r}\bar{P}-f_C{}^{in}\frac{d_{31}{}^{in}E_\kappa{}^{in}}{s_{11}^{E\,in}\left(1-\sigma_C^{E\,in}\right)}-f_C{}^{out}\frac{d_{31}{}^{out}E_\kappa{}^{out}}{s_{11}^{E\,out}\left(1-\sigma_C^{E\,out}\right)} \tag{2.39}$$

where

$$\bar{Y}_r = f_C{}^{in}\frac{1}{s_{11}^{E\,in}\left(1-\sigma_C^{E\,in\,2}\right)}+f_C{}^{out}\frac{1}{s_{11}^{E\,out}\left(1-\sigma_C^{E\,out\,2}\right)}+f_I\frac{Y_I}{\left(1-\sigma_I{}^2\right)}+f_E\frac{Y_E}{\left(1-\sigma_E{}^2\right)} \tag{2.40}$$

$$\bar{P} = f_C{}^{in}\frac{\sigma_C^{E\,in}}{s_{11}^{E\,in}\left(1-\sigma_C^{E\,in\,2}\right)}+f_C{}^{out}\frac{\sigma_C^{E\,out}}{s_{11}^{E\,out}\left(1-\sigma_C^{E\,out\,2}\right)}+f_I\frac{\sigma_I Y_I}{\left(1-\sigma_I{}^2\right)}+f_E\frac{\sigma_E Y_E}{\left(1-\sigma_E{}^2\right)}. \tag{2.41}$$

The quantities $\bar{Y}_r$ and $\bar{P}$ are analogous to the c_{11}^P and c_{12}^P quantities that were introduced in the most recent IEEE standard on piezoelectricity [9]. In this work they are simply referred to as effective Young's moduli, with units of newton per square meter. Reviewing (2.22) to (2.41), it can be seen that devices with different compositions (e.g. with inactive ceramic layers, etc) simply require $\bar{Y}_r$, $\bar{P}$, and $\bar{\rho}$ to be suitably modified.

Since $E_\kappa{}^{in}$ and $E_\kappa{}^{out}$ are independent of r, substituting (2.38) and (2.39) into (2.22) yields the following wave equation for the radial motion of the composite

$$\frac{\bar{Y}_r}{\bar{\rho}}\left(\frac{\partial^2\xi_r}{\partial r^2}+\frac{1}{r}\frac{\partial\xi_r}{\partial r}-\frac{\xi_r}{r^2}\right)=\frac{\partial^2\xi_r}{\partial t^2}. \tag{2.42}$$

Assuming harmonic excitation, the radial motion of the PT can be written as,

$$\xi_r = \xi_{ra}e^{j\omega t} \tag{2.43}$$

which allows (2.42) to be rewritten as

$$\frac{\partial^2\xi_{ra}}{\partial r^2}+\frac{1}{r}\frac{\partial\xi_{ra}}{\partial r}-\frac{\xi_{ra}}{r^2}+\beta^2\xi_{ra}=0 \tag{2.44}$$

where the average radial speed of sound $\bar{v}_r$ and radial wave number β are given by

$$\overline{v_r} = \sqrt{\frac{\overline{Y_r}}{\overline{\rho}}} \tag{2.45}$$

$$\beta = \frac{\omega}{\overline{v_r}}. \tag{2.46}$$

The solution to the differential equation (2.44) is of the form

$$\xi_{ra} = A_1 J_1(\beta r) + B_1 Y_1(\beta r) \tag{2.47}$$

where A_1 and B_1 are constants. J_1 and Y_1 are Bessel functions of the first kind and first order, and second kind and first order respectively. Substituting (2.47) into (2.43) gives a general solution for the equation of radial motion,

$$\xi_r = (A_1 J_1(\beta r) + B_1 Y_1(\beta r)) e^{j\omega t}. \tag{2.48}$$

When deriving the Mason equivalent circuit of a piezoelectric transducer element, the constants in the equation of motion are solved in terms of the vibration velocity at either end of the element [5, 10]. Thus, the constants of (2.48) are found in terms of the radial velocity of a particle at the centre of the PT and at the outer radius of the PT. The radial velocity of a particle is given by

$$v = \frac{\partial \xi_r}{\partial t} = j\omega (A_1 J_1(\beta r) + B_1 Y_1(\beta r)) e^{j\omega t}. \tag{2.49}$$

Since there is a nodal point at the centre of the PT $(r = 0)$, the velocity there is zero. Hence

$$B_1 = 0. \tag{2.50}$$

At the outer radius $(r = a)$ of the device

$$-v_a = j\omega A_1 J_1(\beta a) e^{j\omega t} \tag{2.51}$$

where v_a is the radial velocity of a particle at the outer radius. The negative sign in (2.51) is due to v_a being defined as positive in the opposite direction to the r coordinate (see Figure 2.3). From (2.51),

$$A_1 = -\frac{v_a}{j\omega J_1(\beta a) e^{j\omega t}}. \tag{2.52}$$

Since the velocity v_a varies sinusoidally with time (i.e. $v_a = v_{a0} e^{j\omega t}$), A_1 is constant. Substituting (2.50) and (2.52) into (2.48) provides the equation of radial motion in terms of the velocity at the outer radius of the device,

$$\xi_r = \frac{j v_a J_1(\beta r)}{\omega J_1(\beta a)}. \tag{2.53}$$

Since v_a will vary sinusoidally with time, so does the radial motion described by (2.53), as expected.

C. Electrical equations

Initially, a single layer in the input section is considered. The current through the layer is found using

$$I_{in}^{layer} = \frac{dQ}{dt} = j\omega Q = j\omega \int_0^a D_\kappa^{in} 2\pi r\, dr \tag{2.54}$$

where Q is charge, and harmonic excitation is assumed, i.e.

$$Q = Q_0 e^{j\omega t}. \tag{2.55}$$

Note that I_{in}^{layer} and D_κ^{in} are both defined as positive in the same direction, regardless of poling direction (see Figure 2.3). Substituting (2.18) into (2.54),

$$I_{in}^{layer} = j\omega 2\pi \int_0^a \left(d_{31}^{in} T_{rC}^{in} + d_{31}^{in} T_{\theta C}^{in} + \varepsilon_{33}^{T\,in} E_\kappa^{in}\right) r\, dr. \tag{2.56}$$

Substituting (2.16) and (2.17), followed by (2.34) and (2.35), into (2.56)

$$I_{in}^{layer} = j\omega 2\pi \int_0^a \left(\frac{d_{31}^{in}\left(1+\sigma_C^{E\,in}\right)}{s_{11}^{E\,in}\left(1-\sigma_C^{E\,in\,2}\right)} \left(\frac{\partial \xi_r}{\partial r} + \frac{\xi_r}{r} - 2d_{31}^{in} E_\kappa^{in} \right) + \varepsilon_{33}^{T\,in} E_\kappa^{in} \right) r\, dr. \tag{2.57}$$

From Figure 2.3 it can be seen that V_{in} is defined as positive in the opposite direction to E_κ^{in}, regardless of poling direction. Hence,

$$E_\kappa^{in} = \frac{V_{in}}{t_{in}}. \tag{2.58}$$

Substituting (2.53) and (2.58) into (2.57) and evaluating

$$I_{in}^{layer} = V_{in}\left(\frac{j\omega\pi a^2 \varepsilon_{33}^{T\,in}}{t_{in}} + \frac{j\omega 2\pi a^2 d_{31}^{in\,2}}{t_{in} s_{11}^{E\,in}\left(\sigma_C^{E\,in}-1\right)} \right) + \frac{2\pi d_{31}^{in} a}{s_{11}^{E\,in}\left(\sigma_C^{E\,in}-1\right)} v_a. \tag{2.59}$$

Since there are n_{in} identical layers connected in parallel in the input section, the total input section current is given by $I_{in} = n_{in} I_{in}^{layer}$. Hence,

$$I_{in} = V_{in}\left(\frac{j\omega\pi a^2 \varepsilon_{33}^{T\,in} n_{in}}{t_{in}} - \frac{j\omega 2\pi a^2 d_{31}^{in\,2} n_{in}}{t_{in} s_{11}^{E\,in}\left(1-\sigma_C^{E\,in}\right)} \right) - \frac{2\pi d_{31}^{in} a n_{in}}{s_{11}^{E\,in}\left(1-\sigma_C^{E\,in}\right)} v_a. \tag{2.60}$$

Repeating the process outlined in this section for the output section,

$$I_{out} = V_{out}\left(\frac{j\omega\pi a^2 \varepsilon_{33}^{T\,out} n_{out}}{t_{out}} - \frac{j\omega 2\pi a^2 d_{31}^{out\,2} n_{out}}{t_{out} s_{11}^{E\,out}\left(1-\sigma_C^{E\,out}\right)} \right) - \frac{2\pi d_{31}^{out} a n_{out}}{s_{11}^{E\,out}\left(1-\sigma_C^{E\,out}\right)} v_a \tag{2.61}$$

D. Mechanical equations

In this section, a relationship between the radial force acting on the outer circumference of the main body of the PT and the voltages across the input and output section layers is developed. The force acting (inward) on the outer circumference of the PT is given by

$$F_a = -\overline{T}_r\Big|_{r=a} S_a \tag{2.62}$$

where the surface area on which the force acts is

$$S_a = 2\pi a t_{total}\,. \tag{2.63}$$

Substituting (2.63), (2.53), (2.38), (2.26), (2.27), (2.58), and $E_\kappa^{\ out} = V_{out}/t_{out}$ into (2.62) and evaluating,

$$F_a = v_a\left(\frac{2\pi t_{total}\overline{Y}_r}{j\omega}\left(\frac{J_0(\beta a)\beta a}{J_1(\beta a)} - 1 + \frac{\overline{P}}{\overline{Y}_r}\right)\right) + V_{in}\left(\frac{2\pi a {d_{31}}^{in} n_{in}}{s_{11}^{E\,in}\left(1-\sigma_C^{E\,in}\right)}\right) + V_{out}\left(\frac{2\pi a {d_{31}}^{out} n_{out}}{s_{11}^{E\,out}\left(1-\sigma_C^{E\,out}\right)}\right) \tag{2.64}$$

where J_0 is a Bessel function of the first kind and zero order.

E. Equivalent circuit representation

Equations (2.60), (2.61), and (2.64) can be rewritten as:

$$I_{in} = V_{in} j\omega C_{in} - A_{in} v_a \tag{2.65}$$

$$I_{out} = V_{out} j\omega C_{out} - A_{out} v_a \tag{2.66}$$

$$F_a = v_a Z_{m1} + V_{in} A_{in} + V_{out} A_{out} \tag{2.67}$$

where

$$C_{in} = \frac{\pi a^2 n_{in} \varepsilon_{33}^{T\,in}}{t_{in}}\left(1-{k_p}^{in\,2}\right) = \frac{\pi a^2 {n_{in}}^2 \varepsilon_{33}^{T\,in}}{t_{in}^{total}}\left(1-{k_p}^{in\,2}\right) \tag{2.68}$$

$$C_{out} = \frac{\pi a^2 n_{out} \varepsilon_{33}^{T\,out}}{t_{out}}\left(1-{k_p}^{out\,2}\right) = \frac{\pi a^2 {n_{out}}^2 \varepsilon_{33}^{T\,out}}{t_{out}^{total}}\left(1-{k_p}^{out\,2}\right) \tag{2.69}$$

$$A_{in} = \frac{2\pi a {d_{31}}^{in} n_{in}}{s_{11}^{E\,in}\left(1-\sigma_C^{E\,in}\right)} \tag{2.70}$$

$$A_{out} = \frac{2\pi a {d_{31}}^{out} n_{out}}{s_{11}^{E\,out}\left(1-\sigma_C^{E\,out}\right)} \tag{2.71}$$

$$Z_{m1} = \frac{2\pi t_{total}\overline{Y}_r}{j\omega}\left(\frac{J_0(\beta a)\beta a}{J_1(\beta a)} - 1 + \frac{\overline{P}}{\overline{Y}_r}\right) \tag{2.72}$$

where the planar coupling factors of the input and output section layers are [11]

$${k_p}^{in} = \sqrt{\frac{2{d_{31}}^{in\,2}}{\varepsilon_{33}^{T\,in} s_{11}^{E\,in}\left(1-\sigma_C^{E\,in}\right)}} \tag{2.73}$$

$$k_p^{out} = \sqrt{\frac{2{d_{31}}^{out^2}}{\varepsilon_{33}^{T\,out} s_{11}^{E\,out}\left(1-\sigma_C^{E\,out}\right)}} \tag{2.74}$$

and t_{in}^{total} and t_{out}^{total} are the total thicknesses of piezoelectrically active ceramic in the input and output sections. Hence, $t_{in}^{total} = n_{in} t_{in}$ and $t_{out}^{total} = n_{out} t_{out}$.

By treating force in an analogous way to voltage, and velocity in an analogous way to current, (2.65) to (2.67) can be represented with the Mason equivalent circuit shown in Figure 2.5. A_{in} and A_{out} are known as the force-factors. The turns ratios $1 : A_{in}$ and $1 : A_{out}$ represent the electrical-to-mechanical transformation ratios of the input and output sections respectively. C_{in} and C_{out} are the clamped capacitances of the input and output sections, and represent the capacitances that would be seen if the device was clamped such that no motion could occur (i.e. $v_a = 0$). Z_{m1} represents the mechanical impedance of the device.

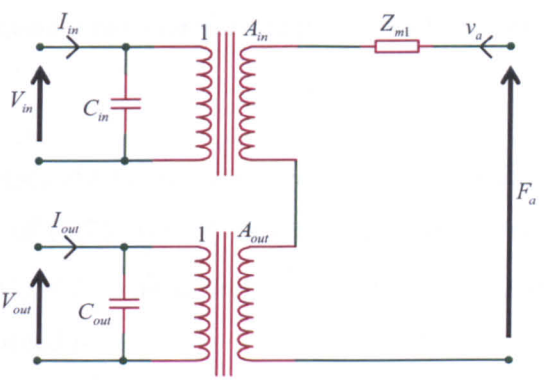

Figure 2.5: Mason equivalent circuit for the radial mode Transoner PT.

Neglecting air resistance, the radial force on the outer radius of the PT is zero. Hence $F_a = 0$. Applying this boundary condition, the circuit of Figure 2.5 simplifies to that shown in Figure 2.6.

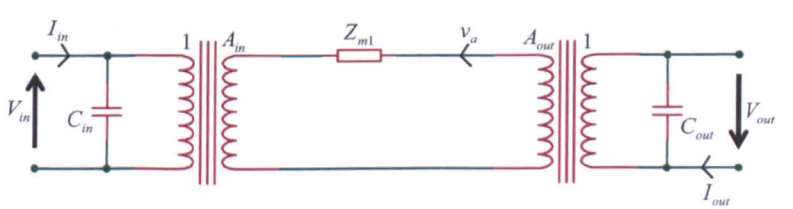

Figure 2.6: Equivalent circuit after application of the boundary condition $F_a = 0$.

The circuit of Figure 2.6 is suitable for modelling the electrical behaviour of a radial mode Transoner PT when operating in the vicinity of any radial resonance (providing it is undisturbed by other vibration modes). However, since only a specific resonance is usually of interest, the mechanical impedance in Figure 2.6 can be linearised about the resonant frequency of interest, allowing the impedance to be represented by an inductance and capacitance connected in series. Not only does this make simulation of the PT in SPICE packages very straightforward, it also allows a mechanical loss resistance to be introduced through knowledge of the inductance and the mechanical Q factor. In this work, the linearization is made at the first radial resonance. When the output of the PT is short circuited, the resonant frequencies of the radial vibration modes are given by the points at which the mechanical impedance reaches zero. From (2.72) this occurs at the solutions to

$$\frac{J_0(\beta a)\beta a}{J_1(\beta a)} - 1 + \bar{\sigma} = 0 \tag{2.75}$$

where an effective Poisson's ratio for the composite has been defined as

$$\bar{\sigma} = \frac{\bar{P}}{\bar{Y}_r}. \tag{2.76}$$

Equation (2.75) is transcendental and must be solved numerically. If R is taken to be the first positive root of (2.75) (i.e. R is the first positive value of βa that satisfies (2.75)), then from (2.46), the resonant frequency of the first radial vibration mode when the output is short circuited is

$$\omega_{rsc} = \frac{R\bar{v}_r}{a}. \tag{2.77}$$

Note that R is dependent only on the effective Poisson's ratio of the PT. Approximating (2.72) with the first two terms of its Taylor series taken about the short circuit resonant frequency,

$$Z_{m1} \approx 0 + \Delta\omega \frac{2j\pi t_{total}\bar{Y}_r a^2}{\bar{v}_r^2}\frac{\left(R^2 + \bar{\sigma}^2 - 1\right)}{R^2} \tag{2.78}$$

where $\Delta\omega = \omega - \omega_{rsc}$. Representing the impedance of a series LC circuit, $L_m C_m$, by the first two terms of its Taylor series, taken about its resonant frequency $\omega_{rsc} = \sqrt{1/(L_m C_m)}$

$$Z_{L_m C_m} \approx 0 + \Delta\omega 2jL_m. \tag{2.79}$$

Equating (2.78) and (2.79), and making use of (2.45)

$$L_m = \pi a^2 t_{total}\bar{\rho}\left(\frac{R^2 + \bar{\sigma}^2 - 1}{R^2}\right) = Mass\left(\frac{R^2 + \bar{\sigma}^2 - 1}{R^2}\right). \tag{2.80}$$

where $Mass$ is the total mass of the PT. Then, since $\omega_{rsc} = \sqrt{1/(L_m C_m)} = \frac{R\bar{v}_r}{a}$,

$$C_m = \frac{1}{L_m \omega_{rsc}^{\ 2}} = \frac{1}{L_m \left(\frac{R\overline{v}_r}{a}\right)^2} = \frac{1}{t_{total}\pi\overline{Y}_r\left(R^2 + \overline{\sigma}^2 - 1\right)}. \tag{2.81}$$

A loss resistance R_m can then be introduced as

$$R_m = \frac{\omega_{rsc} L_m}{\overline{Q}_m} = \frac{R\overline{v}_r L_m}{a\overline{Q}_m} = \frac{t_{total} a\pi\overline{Y}_r}{R\overline{v}_r \overline{Q}_m}\left(R^2 + \overline{\sigma}^2 - 1\right) \tag{2.82}$$

where $\overline{Q}_m$ is the mechanical quality factor of the overall composite. Hence, the lumped equivalent circuit for the radial mode PT can be expressed as shown in Figure 2.7.

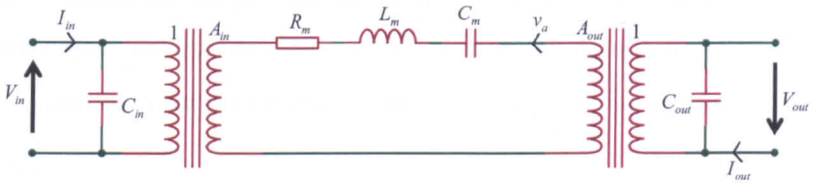

Figure 2.7: The lumped equivalent circuit for the radial mode Transoner PT.

Finally, by referring the mechanical branch across the first force factor, the simplified lumped equivalent circuit shown in Figure 2.8 is obtained, where

$$N = \frac{A_{in}}{A_{out}} = \frac{d_{31}^{\ in} s_{11}^{E\,out}\left(1 - \sigma_C^{\ out}\right)n_{in}}{d_{31}^{\ out} s_{11}^{E\,in}\left(1 - \sigma_C^{\ in}\right)n_{out}} \tag{2.83}$$

$$R_1 = \frac{R_m}{A_{in}^{\ 2}} \qquad L_1 = \frac{L_m}{A_{in}^{\ 2}} \qquad C_1 = C_m A_{in}^{\ 2} \qquad v_a = \frac{v_a'}{A_{in}}. \tag{2.84}$$

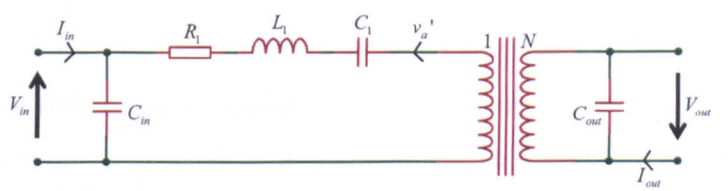

Figure 2.8: The simplified lumped equivalent circuit for the Transoner mode PT.

Comparing Figure 2.7 and (2.68) to (2.71), and (2.80) to (2.82), with those reported in [3], the two models are found to be in agreement. Whilst the circuit of Figure 2.8 corresponds to the general description of a PT most often used in the literature, the circuit of Figure 2.7 is more useful from a design perspective because the tank current is simply the vibration velocity at the outer radius of the device.

2.4 Model verification

To verify the model, the equivalent circuit component values of an isolated and non-isolated Transoner T1-15W radial mode PT were calculated and compared to those experimentally measured using an Agilent 4294A impedance analyser. The dimensions of the devices are detailed in Table 2.1 and photos may be found in Chapter 1. The electrical, mechanical, and electromechanical material constants that apply to bulk sections of the materials used in the PTs are shown in Table 2.2, and the simulated and experimental component values are given in Table 2.3 and Table 2.4. A full set of material properties for the APC841 ceramic may be found in [12]. Note that the calculated R_m and R_1 values in these tables use the Q_m of the piezoelectric ceramic for the overall $\overline{Q}_m$.

Although A_{in}, A_{out}, L_m, C_m, and R_m cannot be measured directly with an impedance analyser, knowledge of any one allows all the others to be calculated. If a PT design is found to be overheating in its intended application, two possible causes are the mechanical loss resistance being unexpectedly large, or the vibration velocity becoming too great. Assuming the output capacitance has been suitably sized, the latter would require the force factors to be adjusted. Therefore it is useful to be able to experimentally determine the force factors of an existing design. From Figure 2.7 and Figure 2.8, A_{in} is the ratio of $I_{in} - j\omega V_{in} C_{in}$ to v_a, and the ratio of the square root of L_m to the square root of L_1. Thus, the following methods are suggested for measuring A_{in}:

1) A sinusoidal voltage is applied to the input terminals of the PT, and the output terminals are connected to a purely resistive load. The radial velocity of a particle at the outer radius of the PT is measured with a laser vibrometer. The frequency is adjusted to find the resonant frequency (by looking for the frequency at which the vibration velocity becomes maximum), and the input current to the PT is then measured. Since the tank is at resonance, the real part of the PT input current will be the current entering the input section force factor. A_{in} is then calculated from the ratio of the amplitude of the real part of the PT input current to the amplitude of the vibration velocity. The output section force factor could be determined using the same method, but with the PT reversed.
2) Since the $\left(R^2 + \overline{\sigma}^2 - 1\right)/R^2$ term in (2.80) changes very slowly over the range of $\overline{\sigma}$ values that are of interest, the error caused by assuming $\left(R^2 + \overline{\sigma}^2 - 1\right)/R^2 = 0.794$, regardless of $\overline{\sigma}$, will be less than 3%. Hence, L_m can be

assumed to be 0.794 times the mass of the PT, and A_{in} can be calculated from $A_{in} = \sqrt{L_m / L_1}$ once the mass of the PT has been measured. A_{out} can be determined using $A_{out} = A_{in} / N$. Since L_m will be accurate to within 3%, the force factors will be accurate to within 1.49%

Since a laser vibrometer with sufficient resolution was not available, the second method was used to calculate the experimental values of A_{in} and A_{out} in Table 2.3 and Table 2.4. The mass of each PT was measured with a top pan balance with the PT wires removed.

	Ceramic input layers	Ceramic output layers	Alumina isolation layers	Copper electrode layers
Radius (mm)	9.525	9.525	10.795	9.525
Thickness (mm)	1.52	2.29	0.25	0.0762
Quantity (T1-15W non-isolated)	1	1	1	4
Quantity (T1-15W isolated)	1	1	0	4

Table 2.1: Dimensions of Transoner T1-15W samples.

APC 841 Ceramic layers					
Q_m	d_{31} (C.N^{-1})	$\varepsilon_{33}^T / \varepsilon_0$	s_{11}^E (m^2.N^{-1})	σ_C^E	ρ_C (kg.m^{-3})
1400	-109×10^{-12}	1400	12×10^{-12}	0.38	7600
Alumina isolation layers and copper electrode layers					
Y_I (N.m^{-2})	σ_I	ρ_I (kg.m^{-3})	Y_E (N.m^{-2})	σ_E	ρ_E (kg.m^{-3})
303×10^9	0.21	3720	130×10^9	0.34	8960

Table 2.2: Electrical, mechanical, and piezoelectric constants for bulk sections of material.

	Mass (g)	$\lvert A_{in}\rvert$	$\lvert A_{out}\rvert$	L_m (mH)	C_m (pF)	R_m (Ω)	C_{in} (nF)	C_{out} (nF)	L_1 (mH)	C_1 (pF)	R_1 (Ω)	N
Simulation	9.03	0.873	0.873	7.26	218	4.12	1.73	1.15	9.53	166	5.42	1.00
Experimental, device 1	9.09[#2]	0.821[#4]	0.879[#5]	7.22[#3]	246[#6]	5.75[#7]	1.89[#1]	1.28[#1]	10.7[#1]	166[#1]	8.54[#1]	0.934[#1]
Experimental, device 5	9.10[#2]	0.826[#4]	0.922[#5]	7.22[#3]	246[#6]	6.88[#7]	1.90[#1]	1.30[#1]	10.6[#1]	168[#1]	10.1[#1]	0.895[#1]

Table 2.3: Simulated and experimental equivalent circuit component values for non-isolated Transoner T1-15W.

	Mass (g)	$\lvert A_{in}\rvert$	$\lvert A_{out}\rvert$	L_m (mH)	C_m (pF)	R_m (Ω)	C_{in} (nF)	C_{out} (nF)	L_1 (mH)	C_1 (pF)	R_1 (Ω)	N
Simulation	9.30	0.873	0.873	7.40	187	4.49	1.73	1.15	9.72	143	5.90	1.00
Experimental, device 3	9.64[#2]	0.898[#4]	0.868[#5]	7.65[#3]	197[#6]	11.0[#7]	2.10[#1]	1.26[#1]	9.48[#1]	159[#1]	13.7[#1]	1.04[#1]
Experimental, device 4	9.63[#2]	0.880[#4]	0.958[#5]	7.65[#3]	198[#6]	9.91[#7]	2.00[#1]	1.34[#1]	9.88[#1]	153[#1]	12.8[#1]	0.918[#1]
Experimental, device 6	9.70[#2]	0.912[#4]	0.912[#5]	7.70[#3]	197[#6]	10.6[#7]	2.09[#1]	1.29[#1]	9.26[#1]	164[#1]	12.7[#1]	1.00[#1]

Table 2.4: Simulated and experimental equivalent circuit component values for isolated Transoner T1-15W.

[#1] measured directly using an impedance analyser

[#2] measured directly using a top pan balance

[#3] determined directly from mass measurement

[#4] determined from L_m and L_1

[#5] determined from A_{in} and N

[#6] determined from C_1 and A_{in}

[#7] determined from R_1 and A_{in}

With the exception of the loss resistances, the model and the bulk section material parameters provide a good first-estimate of the equivalent circuit component values of the T1-15W devices. The differences between the simulated and experimental results are thought to be caused by

- The assumption that displacement and strain are constant with thickness.
- The assumption that the material properties that apply to bulk sections of material will also apply to the materials in the PT.
- The assumption that the PT behaves like a thin disc (i.e. that $T_z = 0$).
- The effects of high order radial modes, and other vibration modes such as thickness and bending.
- The effect of the bonding material.

The physical properties of polarised ceramic are known to vary with geometry. To quote from the IRE standard [11]:

"The properties of ceramics are functions of the preparation process, and are subject to systematic and statistical fluctuations within a given batch. These fluctuations may be caused by the inhomogeneous chemical composition, mechanical differences in the

forming process, varying shrinkage and chemical modification during firing, and by varying response to the poling treatment."
In other words, the material properties supplied by the manufacturer should not be expected to correspond exactly to the ceramic discs that appear in the transformer. Like a commercial capacitor, the properties of the discs have tolerances, and the tolerance figures quoted for standard compositions are usually between 5 and 20%.

The estimate of the mechanical loss resistance, R_l or R_m, is strongly dependent on the mechanical quality factor $\overline{Q}_m$. However, the $\overline{Q}_m$ of the overall device is always much lower than that of an individual disc, and is difficult to calculate analytically. Factors that affect $\overline{Q}_m$ include the choice of isolation material, the number of layers within the PT, the choice of piezoelectric material, the manufacturing process (bonded, co-fired, or co-fired and bonded), and the adhesive used in the bonding process [13]. Therefore in practice, the best way to estimate the expected $\overline{Q}_m$ of a PT is probably through knowledge of other devices of similar composition made with a similar manufacturing process.

A value of $\overline{Q}_m$ could be determined in a similar way to a simple resonator using the impedance analyser. However, the apparent mechanical quality factor of a piezoelectric material is dependent upon many factors, including electric field strength, ambient temperature, and vibration velocity [14-17]. Therefore the value found by the impedance analyser would only apply at low power levels anyway. Even if a value $\overline{Q}_m$ could be measured under conditions similar to those in which the PT would actually operate in a converter, the value would still be a very simplistic indicator of the expected losses. It will be shown in Chapter 4 that the efficiency of a PT changes considerably with frequency, and this behaviour cannot be explained by any single value of $\overline{Q}_m$. Therefore whilst the R_l, R_m, or $\overline{Q}_m$ of a PT does give a first indication of the expected efficiency, and is probably of some use in determining how well the manufacturing process is working, it is no substitute for a full characterisation of the PT at high power levels. The behaviour of a PT at high power levels is shown in Chapter 4.

In Section 2.3E, the mechanical impedance Z_{ml} was expanded only about the first radial resonance. However, a more accurate representation of Z_{ml} is obtained by expanding about additional resonances. Figure 2.9 shows a plot of Z_{ml} for $t_{total} = 4 \times 10^{-3}$,

$\overline{Y}_r = 1.1\times10^{11}$, $\overline{\sigma} = 0.35$, $\overline{\rho} = 7700$, $a = 9.5\times10^{-3}$. The impedance of a single LC branch, the combined impedance of two LC branches in parallel, and the combined impedance of three LC branches in parallel is also shown. The first LC branch is from a Taylor expansion of Z_{m1} about the first resonance, the second LC branch is from an expansion about the second radial resonance, etc. When only one LC branch is considered, only the behaviour of the mechanical impedance in the vicinity of the first resonance is modelled. When two are considered, the first two are modelled. But, not only do the additional branches allow the behaviour of the higher resonances to be modelled, they also improve the accuracy of the impedance plot in the vicinity of the lower resonances. Therefore the LC branches that model the behaviour of the higher resonances have a small effect on the impedance that is seen over the frequency range of the first resonance.

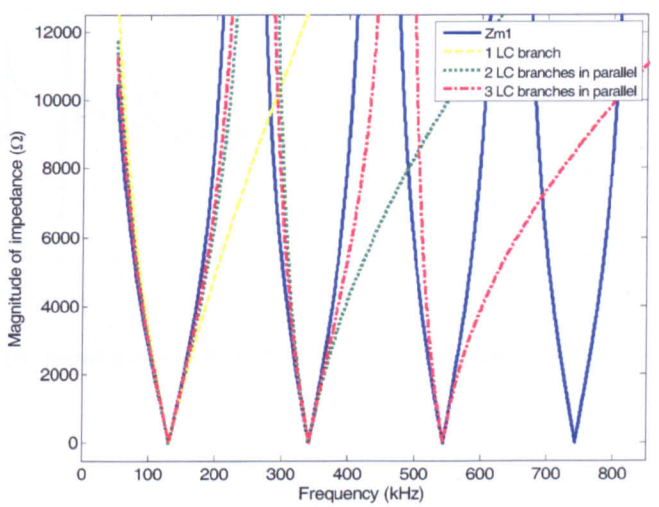

Figure 2.9: Comparison of the impedance of Z_{m1} to multiple LC branches in parallel.

The case described above is for an ideal scenario where no other types of vibration mode (such as thickness modes and bending modes) occur. In practice, this rarely occurs. Indeed, looking at the impedance plot of Figure 2.10, there is a resonance at around 60kHz which is probably due to a bending mode. Another spurious resonance can be seen at 149kHz, and is in quite close proximity to the first radial mode at 130kHz. Other resonances continue to occur as the frequency is increased. In [1], Lin modelled a more complete frequency response of a PT by including extra branches for the other vibration modes, not just the radial modes. Therefore the equivalent circuit of a practical PT can be thought of as having multiple LC branches, some of which model radial modes, whilst others correspond to thickness and bending modes. Although the

effect of these branches will be very small over the frequency range of the resonance of interest, they are likely to affect the equivalent circuit component values that are measured with the impedance analyser. In particular, the branches representing the higher resonances will appear increasingly capacitive when viewed from the first resonance of the mode of interest [6]. In [6], Ikeda discusses the fact that the branches representing the higher resonances of a piezoelectric resonator are therefore likely to increase the measured value of the clamped capacitance, and hence refers to the measured value as a "damped" capacitance. A similar effect will occur with a PT because when one set of terminals is short circuited and the impedance analyser is used to measure the equivalent circuit component values from the other set of terminals, the PT is simply a resonator, and the additional LC branches appear in parallel with the clamped capacitance.

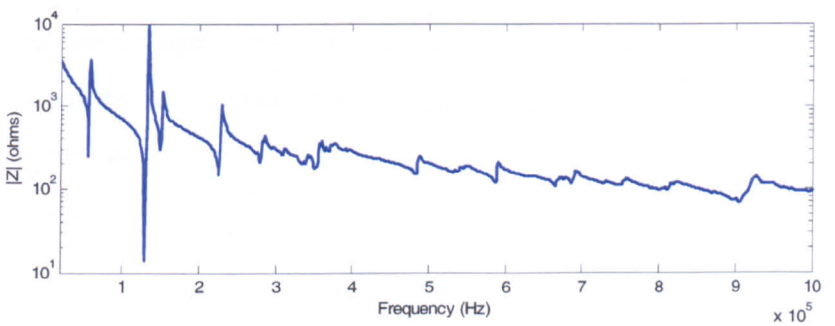

Figure 2.10: Input impedance of T1-15W device 3 with output short-circuited.

2.5 Investigating the effect of the constant strain approximation

A key assumption when deriving the equivalent circuit model in Section 2.3 was that radial displacement, radial strain, and azimuthal strain do not vary with thickness. In other words, it was assumed that $\frac{\partial \xi_r}{\partial z} = 0$. In reality this is not strictly true, particularly if the input section is relatively small compared to the rest of the device.

In this section the possible effect of $\frac{\partial \xi_r}{\partial z} \neq 0$ is investigated by considering the case where the input and output section of a Transoner PT are connected electrically in parallel. By connecting the input and output sections in parallel, such that the poling directions of the layers in the input and output sections are in agreement, it is expected that radial displacement will be considerably more uniform in the thickness direction.

Hence, we now look to see whether the accuracy of the model derived in Section 2.3 is improved when the PT is connected in this manner.

Note that the input and output sections must be connected together such that the poling directions all have the same orientation with respect to the applied voltage. Otherwise the input section will try to expand when the output section is trying to contract, thereby preventing the device from being driven into radial resonance.

Consider (2.65), (2.66), and (2.67). Let

$$I_T = I_{in} + I_{out} \tag{2.85}$$

and

$$V_T = V_{in} = V_{out}\,. \tag{2.86}$$

I_T is the total current entering the Transoner when the two sections are connected in parallel. V_T is the voltage across each layer in the input and output sections of the Transoner. When the two sections are connected in parallel, (2.65), (2.66), and (2.67) can then be written as

$$I_T = V_T j\omega C_T - v_a A_T \tag{2.87}$$

$$F_a = v_a Z_{m1} + V_T A_T \tag{2.88}$$

where

$$C_T = C_{in} + C_{out} \tag{2.89}$$

$$A_T = A_{in} + A_{out}\,. \tag{2.90}$$

(2.87) and (2.88) are then represented with an equivalent circuit. The boundary condition $F_a = 0$ is applied, Z_{m1} is linearised about the first radial resonance and approximated by a series LC circuit as described in Section 2.3, and a mechanical loss resistance is introduced as previously described. The resulting lumped equivalent circuit is shown Figure 2.11, where L_m, C_m, and R_m are given by (2.80), (2.81), and (2.82), respectively.

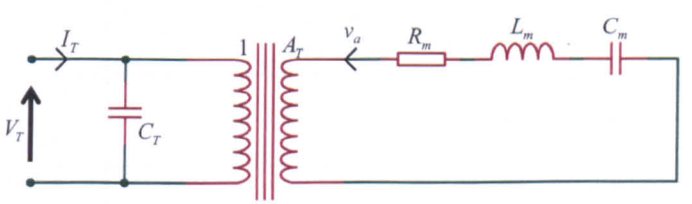

Figure 2.11: Lumped equivalent circuit for a Transoner PT where the input and output sections are connected electrically in parallel.

Referring the elements in the mechanical branch across the force factor A_T results in the circuit of Figure 2.12, where

$$R_{1T} = \frac{R_m}{A_T^{\,2}} \qquad L_{1T} = \frac{L_m}{A_T^{\,2}} \qquad C_{1T} = C_m A_T^{\,2}. \tag{2.91}$$

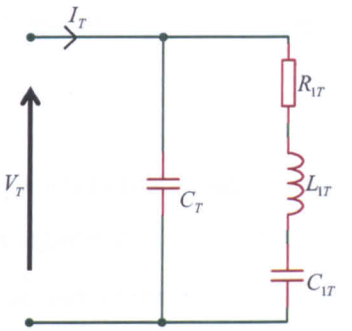

Figure 2.12: Simplified lumped equivalent circuit for a Transoner PT where the input and output sections are connected electrically in parallel.

The wires from the T1-15W PTs had been removed prior to measuring the mass of each device for the results in Table 2.3 and Table 2.4. After the wires had been re-soldered to device 6, the equivalent circuit component values were re-measured with the impedance analyser, and the results are shown in Table 2.5. The input and output sections of device 6 were then connected in parallel, and the values of the components in the equivalent circuit of Figure 2.12 were determined. The values were measured 3 times, and the results are shown in columns 2, 3, and 4 of Table 2.6.

	C_{in} (nF)	C_{out} (nF)	L_1 (mH)	C_1 (pF)	R_1 (Ω)	N
Experimental, device 6	2.06	1.26	9.46	161	12.5	1.00

Table 2.5: Equivalent circuit component values for isolated T1-15W radial mode Transoner PT device 6.

	Experimentally measured results, set 1	Experimentally measured results, set 2	Experimentally measured results, set 3	Simulated values
L_{1T} (mH)	2.371	2.370	2.370	2.431
C_{1T} (pF)	641.3	641.5	641.6	570.6
R_{1T} (Ω)	3.137	3.154	3.148	1.474
C_T (nF)	2.992	2.993	2.994	2.876
$\lvert A_T \rvert$				1.746

Table 2.6: Comparison between the simulated and experimentally measured equivalent circuit component values for T1-15W isolated radial mode Transoner PT, device 6, with the input and output sections connected in parallel.

The model derived in Section 2.3 can then be used in conjunction with (2.89), (2.90), and (2.91) to calculate the expected equivalent circuit component values of device 6 when the input and output sections are connected in parallel. This is equivalent to taking the simulated values shown in Table 2.4 for R_m, L_m, C_m, A_{in}, A_{out}, C_{in}, and C_{out}, and applying them to (2.89), (2.90), and (2.91). The resulting values are shown in column 5 of Table 2.6.

Comparing the simulated and experimental values in Table 2.6, it can be seen that the clamped capacitance of this arrangement, C_T, is substantially more accurately predicted compared to the clamped input and output capacitances in Table 2.4; the simulated value for C_{in} was 17% smaller than that experimentally recorded, the simulated value for C_{out} was 11% smaller, but the simulated value for C_T is only 3.9% smaller than that experimentally recorded. This suggests that the $\frac{\partial \xi_r}{\partial z} = 0$ approximation may be significantly contributing to the error in the calculated values for C_{in} and C_{out}.

Further support for this theory comes from considering just the experimentally measured equivalent circuit component values (which eliminates the effect of any uncertainties in the accuracy of the material parameters used in the model). Given the form of the standard lumped equivalent circuit of a PT, it would be expected that the clamped (or rather 'damped', see discussion in Section 2.4) capacitance measured when the input and output are connected in parallel and the resulting resonator is characterised against the standard resonator equivalent circuit (see Chapter 1) would be equal to the sum of the C_{in} and C_{out} capacitances that are measured from the input with the output short circuited and from the output with the input short circuited. However, from Table 2.6, the experimentally measured C_T was 2.99nF, whereas from Table 2.4, the sum of the experimentally measured C_{in} and C_{out} for device 6 is 3.38nF. We believe this discrepancy is due to the effect of having a more uniform radial displacement profile in the thickness direction when the device is connected with both sections in parallel.

It is important to note that $\frac{\partial \xi_r}{\partial z} = 0$ is not completely achieved when the input and output sections of the T1-15W PT are connected together because the input section and output section layers do not the same thickness, but are subjected to the same voltage during

the measurements. Furthermore, connecting the two sections together is also likely to reduce the effect of bending modes. Therefore the behaviour shown in this section cannot (at present) be said to be solely due to $\frac{\partial \xi_r}{\partial z} \neq 0$.

Nevertheless, we predict that as the physical size of a particular section of the PT (i.e. the input section or the output section) is decreased relative to the size of the rest of the PT, the model's prediction for the clamped capacitance of that section is likely to become more and more of an underestimate, because the $\frac{\partial \xi_r}{\partial z} = 0$ assumption will become increasing inaccurate for the conditions under which the capacitance is measured, and (possibly) because the influence of bending modes will increase.

2.6 Correcting for the difference between the model and the experimental results

The design of a PT is usually an iterative process to some extent. Initially, prototypes of several different physical designs are often produced for a single converter specification. The performance of each is then evaluated in the context of the required electrical specifications. Changes to the design(s) are then made, and prototypes of the refined design(s) produced and evaluated. The changes between the first and second prototypes can be made in a more precise manner if the 'correct' values of the material properties in the model are known. Two approaches for determining these are proposed.

A. Approach 1

The first approach is to experimentally determine the value of each and every material property on which the model depends. $s_{11}^{E\,in}$, $s_{11}^{E\,out}$, $\sigma_C^{E\,in}$, $\sigma_C^{E\,out}$, $s_{11}^{E\,in}$, $k_p{}^{in}$, $k_p{}^{out}$, $\varepsilon_{33}^{T\,in}$, $\varepsilon_{33}^{T\,out}$ can all be determined from individual discs of the same geometry as those used in the PT using the methods detailed in [11, 18]. Since it is known that the coupling factor, compliance, and Poisson's ratio of a piezoelectric disc can vary depending upon the geometry, it is important to use discs of the same geometry as those used in the PT itself.

The average density of the PT can be found by measuring the mass and the volume. When the output (or input) of a PT is short circuited, the resonant frequencies of the radial vibration modes are given by (2.77). Comparing this to the expression for the resonant frequencies of a simple piezoelectric disc, it is apparent that the methods in [11, 18] can be used to determine $\bar{Y}_r$ and $\bar{\sigma}$ for a radial mode Transoner PT. Therefore $\bar{\sigma}$ is determined from the ratio of resonant frequencies of the first two radial modes with the output (or input) shorted. Once $\bar{\sigma}$ (and $\bar{\rho}$) are known, $\bar{Y}_r$ can be found from (2.77) and (2.45). Since the method for determining $\bar{\sigma}$ relies on the first two radial resonances being observable on an impedance-frequency response plot, the dimensions of the PT must be such that no interference occurs in the vicinity of these resonances. Unfortunately this method could not be demonstrated with the T1 devices because the second radial resonance (which would be expected around 338kHz) suffers interference from another vibration mode, as shown in Figure 2.10. For devices that are co-fired and bonded, this interference will be less of a problem; since the co-fired input and output sections will be designed such that their radius to combined total thickness ratio is such that the first radial resonance remains undisturbed, it is highly likely that each section on its own will have a radius to thickness ratio that results in the second radial resonance also being undisturbed. Hence, Poisson's ratio and effective Young's modulus for each section could be determined, and overall values for the complete device then estimated with a high degree of accuracy.

${k_p}^{in}$, ${k_p}^{out}$, $\varepsilon_{33}^{T\,in}$, and $\varepsilon_{33}^{T\,out}$ can also be determined directly from the PT itself. Whilst $\varepsilon_{33}^{T\,in}$ and $\varepsilon_{33}^{T\,out}$ can be measured in much the same way as for a standalone disc, the formula in the standards on piezoelectricity cannot be used to determine ${k_p}^{in}$ and ${k_p}^{out}$ directly from the PT. Therefore appropriate replacements are now derived. The method described below follows Mason's [4], but uses the model derived in Section 2.3, rather than that of a single disc.

From Figure 2.6, (2.68), and (2.72), when the output is short-circuited, the admittance measured from the input terminals is

$$\frac{1}{Z_{in}} = j\omega C_{in} + \frac{{A_{in}}^2}{Z_{m1}} = \frac{j\omega\pi a^2 n_{in}\varepsilon_{33}^{T\,in}\left(1-{k_p}^{in\,2}\right)}{t_{in}} + \frac{j\omega 2\pi a^2 {n_{in}}^2 {d_{31}}^{in\,2}}{s_{11}^{E\,in\,2}\left(1-\sigma_C^{E\,in}\right)^2 t_{total}\bar{Y}_r\left(\dfrac{J_0(\beta a)\beta a}{J_1(\beta a)}-1+\bar{\sigma}\right)} \qquad (2.92)$$

which can be written as

$$\frac{1}{Z_{in}} = \frac{j\omega\pi a^2 n_{in} \varepsilon_{33}^{T\,in} \Gamma}{s_{11}^{E\,in}\left(1-\sigma_C^{E\,in}\right) t_{total} \bar{Y}_r \left(\frac{J_0(\beta a)\beta a}{J_1(\beta a)} - 1 + \bar{\sigma} \right) t_{in}} \tag{2.93}$$

where

$$\Gamma = n_{in} {k_p}^{in^2} t_{in} + \left(1 - {k_p}^{in^2}\right) s_{11}^{E\,in}\left(1-\sigma_C^{E\,in}\right) t_{total} \bar{Y}_r \left(\frac{J_0(\beta a)\beta a}{J_1(\beta a)} - 1 + \bar{\sigma} \right). \tag{2.94}$$

The frequency of the first radial resonance is $\omega_{rsc} = \frac{R\bar{v}_r}{a}$ when the output is short circuited, where R is the first positive value of βa that satisfies (2.75). When Γ is then approximated by the first two terms of the Taylor series of (2.94) taken about the first radial resonance

$$\Gamma \approx n_{in} {k_p}^{in^2} t_{in} - (\omega - \omega_{rsc}) \frac{\left(1 - {k_p}^{in^2}\right) s_{11}^{E\,in}\left(1-{\sigma_C}^{in}\right) t_{total} \bar{Y}_r \left(R^2 + \bar{\sigma}^2 - 1\right)}{\omega_{rsc}}. \tag{2.95}$$

When the output is short circuited, the antiresonant frequency associated with the first radial resonance, ω_{asc}, occurs when the right hand side of (2.93) reaches zero, which occurs when $\Gamma = 0$. Hence, from (2.95)

$$n_{in} {k_p}^{in^2} t_{in} - (\omega_{asc} - \omega_{rsc}) \frac{\left(1 - {k_p}^{in^2}\right) s_{11}^{E\,in}\left(1-{\sigma_C}^{in}\right) t_{total} \bar{Y}_r \left(R^2 + \bar{\sigma}^2 - 1\right)}{\omega_{rsc}} = 0 \tag{2.96}$$

which after re-arrangement gives

$$\frac{(\omega_{asc} - \omega_{rsc})}{\omega_{rsc}} = \frac{n_{in} {k_p}^{in^2} t_{in}}{\left(1 - {k_p}^{in^2}\right) s_{11}^{E\,in}\left(1-{\sigma_C}^{in}\right) t_{total} \bar{Y}_r \left(R^2 + \bar{\sigma}^2 - 1\right)}. \tag{2.97}$$

The resonant and antiresonant frequencies can be measured from the device using an impedance analyser. If $\bar{Y}_r$ and $\bar{\sigma}$ have previously been determined, then all the terms in (2.97) are known except ${k_p}^{in}$, and hence ${k_p}^{in}$ can be solved numerically. As $n_{in} t_{in} / t_{total}$ is increased, it can be seen the separation between the resonant and antiresonant frequencies increases. The corresponding expression for finding ${k_p}^{out}$ by measuring from the output terminals with the input short circuited is simply

$$\frac{(\omega_{asc} - \omega_{rsc})}{\omega_{rsc}} = \frac{n_{out} {k_p}^{out^2} t_{out}}{\left(1 - {k_p}^{out^2}\right) s_{11}^{E\,out}\left(1-{\sigma_C}^{out}\right) t_{total} \bar{Y}_r \left(R^2 + \bar{\sigma}^2 - 1\right)}. \tag{2.98}$$

B. Approach 2

The overall aim is to adjust the model such that it fits the behaviour of an existing device, and therefore allows more accurate prediction of the equivalent circuit when

changes to the design are made. In itself, this does not require all the true material properties to be known. In approach 1, where the majority of the material parameters are determined from individual discs, there is no guarantee that the model will then fit because other important factors, such as strain not being constant with thickness, and $T_z \neq 0$, are not being accounted for. In the second part of approach 1, where the coupling factors and dielectric constants are determined from PT itself, these other factors are being accounted for. However, what is then being measured is not the true k_p, but rather k_p as seen through a system that does not wholly fulfil the criteria under which such a factor should be measured. Given that what is measured is only an effective factor at best, it would seem logical to take this a step further and completely break the connection with the true material properties in order to obtain better agreement between the model and the device.

Approach 2 is therefore to lump together all the material properties in each of the elements in the equivalent circuit into effective factors. Since the connection between the equivalent circuit components and the true material parameters is then disregarded, it is not required that the effective factors are self-consistent in terms of the material parameters that they have replaced. The equivalent circuit formulas become

$$C_{in} = \frac{\pi a^2 n_{in}}{t_{in}} \Phi_1 \tag{2.99}$$

$$C_{out} = \frac{\pi a^2 n_{out}}{t_{out}} \Phi_2 \tag{2.100}$$

$$A_{in} = 2\pi a n_{in} \Phi_3 \tag{2.101}$$

$$A_{out} = 2\pi a n_{out} \Phi_4 \tag{2.102}$$

$$L_m = \pi a^2 t_{total} \Phi_5 \tag{2.103}$$

$$C_m = \frac{1}{t_{total} \pi} \Phi_6 \tag{2.104}$$

$$R_m = t_{total} a \pi \Phi_7 \tag{2.105}$$

where Φ are the factors that have replaced the material parameters. The Φ factors can be determined using the experimentally measured equivalent circuit component values. Table 2.7 shows the mean average of the experimentally determined equivalent circuit component values for the isolated T1-15W devices and the Φ factors they result in.

Mean average experimental equivalent circuit component values for isolated T1-15W	Φ factor
$C_{in} = 2.06\text{nF}$	$\Phi_1 = 1.100\times10^{-8}$
$C_{out} = 1.29\text{nF}$	$\Phi_2 = 1.040\times10^{-8}$
$A_{in} = 0.897$	$\Phi_3 = 14.98$
$A_{out} = 0.913$	$\Phi_4 = 15.25$
$L_m = 7.67\text{mH}$	$\Phi_5 = 6.163\times10^{3}$
$C_m = 197\text{pF}$	$\Phi_6 = 2.706\times10^{-12}$
$R_m = 10.5\Omega$	$\Phi_7 = 8.560\times10^{4}$

Table 2.7: Experimental equivalent circuit component values and the Φ factors they result in.

2.7 Vibration velocity profile

When designing a resonant piezoelectric device, it is extremely important to be able to predict what the maximum vibration velocity within the device will be for a particular set of operating conditions. By substituting (2.50) and (2.52) into (2.49), the magnitude of the radial vibration velocity can be expressed in terms of the velocity at the outer radius as

$$|v| = \frac{|v_a| J_1(\beta r)}{J_1(\beta a)}. \tag{2.106}$$

Using (2.46) and (2.77), (2.106) becomes

$$\frac{|v|}{|v_a|} = \frac{J_1\left(\frac{\omega}{\omega_{rsc}}\frac{r}{a}R\right)}{J_1\left(\frac{\omega}{\omega_{rsc}}R\right)} \tag{2.107}$$

where ω_{rsc} is the short circuit resonant frequency of the PT. This function is plotted in Figure 2.13 for $\bar{\sigma} = 0.35$. Usually the operating frequency of the PT will be between 1 and 1.1 times the short circuit resonant frequency when delivering maximum power. From Figure 2.13 it can therefore be seen that the peak vibration velocity will be somewhere between 1.05 and 1.1 times the vibration velocity at the outer radius, and occurs at a radius of between 0.8a and 0.9a, depending on the operating frequency. Since the vibration velocity at the outer radius is simply the current through the motional branch in Figure 2.7, a major advantage of the equivalent circuit is the ability to directly relate the operating conditions (i.e. input voltage, load resistance, and frequency) to the maximum vibration velocity within the device.

Instead of solving the constants in the equation of motion in terms of vibration velocities, A could have been solved directly in terms of E_K^{in} and E_K^{out} using $T_r|_{r=a} = 0$, (2.38), and (2.48), in a similar way to that shown in [19]. Whilst this may appear quicker, it would result in an equivalent circuit without a direct relationship between the motional branch current and the maximum vibration velocity within the device, and would therefore be less useful from a design perspective.

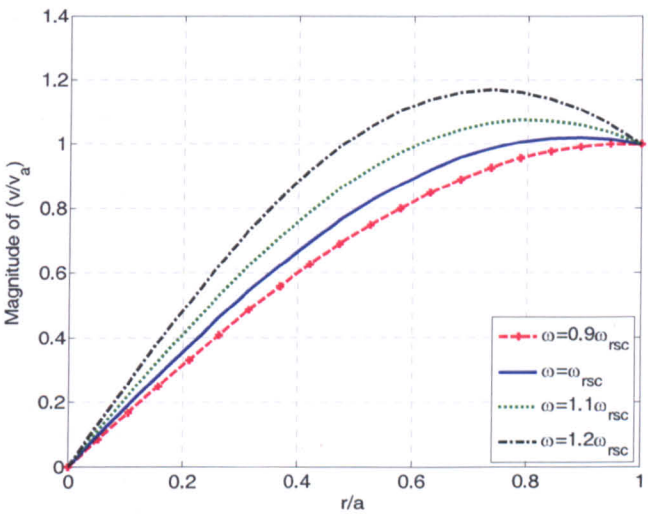

Figure 2.13: Radial velocity profile for a simple radial mode Transoner PT.

2.8 Summary

A Mason equivalent circuit for the radial vibration of a composite disc with two sets of electrodes has been derived using the assumptions that the disc is thin ($T_z = 0$), and that radial displacement, radial strain, and azimuthal strain are constant with thickness. Once appropriate boundary conditions were applied, a lumped element representation was found to agree with that published in [3], and differ from those published in [1, 2]. The equivalent circuit component values of isolated and non-isolated T1-15W radial mode PTs were calculated using standard material data, and good agreement was found, particularly in the non-isolated case. Reasons for the discrepancies have been suggested, and two strategies described for adjusting the model to more accurately predict the effects of any changes that are made between design iterations. It was shown that the difference between the vibration velocity at the outer radius of the device and the maximum vibration velocity occurring within the device is small under normal operating conditions, thereby simplifying the PT design process. The Mason equivalent

circuit is now taken forward into the next chapter, where a more complete model for the radial mode Transoner PT is proposed.

2.9 References

[1] R.-L. Lin, "Piezoelectric Transformer Characterization and Application of Electronic Ballast," PhD thesis, Virginia Polytechnic Institute and State University, USA, 2001.

[2] Y. H. Huang, K. Y. Zhou, J. Shi, and Y. Gu, "Equivalent circuit model and characteristic of radial vibration mode piezoelectric transformer," *Tien Tzu Hsueh Pao/Acta Electronica Sinica*, vol. 30, pp. 1585-1588, 2002.

[3] M. Yamamoto, Y. Sasaki, A. Ochi, T. Inoue, and S. Hamamura, "Step-Down Piezoelectric Transformer for AC-DC Converters," *Japanese Journal of Applied Physics, Part 1*, vol. 40, pp. 3637-3642, 2001.

[4] W. P. Mason, "Electrostrictive Effect in Barium Titanate Ceramics," *Physical Review*, vol. 74, pp. 1134-1147, 1948.

[5] S. Lin, "Electro-mechanical equivalent circuit of a piezoelectric ceramic thin circular ring in radial vibration," *Sensors and Actuators A: Physical*, vol. 134, pp. 505-512, 2007.

[6] T. Ikeda, *Fundamentals of Piezoelectricity*: Oxford University Press, 1990.

[7] J. Yang, *Analysis of Piezoelectric Devices*: World Scientific Publishing, 2006.

[8] D. Hull and T. W. Clyne, "An Introduction to Composite Materials (Second Edition)," 1996, pp. 61.

[9] "IEEE standard on piezoelectricity," *ANSI/IEEE Std 176-1987*, 1988.

[10] D. A. Berlincourt, D. R. Curran, and H. Jaffe, "Piezoelectric and Piezomagnetic Materials and Their Function in Transducers," in *Physical Acoustics: Principles and Methods*, vol. I part A, W. P. Mason, Ed.: Academic Press, New York, 1964.

[11] "IRE Standards on Piezoelectric Crystals: Measurements of Piezoelectric Ceramics, 1961," *Proceedings of the IRE*, vol. 49, pp. 1161-1169, 1961.

[12] L. Burianova, M. Prokopova, M. Pustka, and J. Nosek, "Characterization of the hard APC841 ceramics, report no. 2," Technical University of Liberec, supplied by American Piezo Ceramics, 2005.

[13] P. Laoratanakul and K. Uchino, "Designing a radial mode laminated piezoelectric transformer for high power applications," presented at IEEE International Symposium on Applications of Ferroelectrics, 2005.

[14] Y. Sasaki, M. Umeda, S. Takahashi, M. Yamamoto, A. Ochi, and T. Inoue, "High-power Characteristics of Multilayer Piezoelectric Ceramic Transducers," *Japanese Journal of Applied Physics, Part 1*, vol. 40, 2001.

[15] M. Umeda, K. Nakamura, and S. Ueha, "Effects of Vibration Stress and Temperature on the Characteristics of Piezoelectric Ceramics under High Vibration Amplitude Levels Measured by Electrical Transient Responses," *Japanese Journal of Applied Physics, Part 1*, vol. 38, pp. 5581-5585, 1999.

[16] S. Takahashi, M. Yamamoto, and Y. Sasaki, "Nonlinear Piezoelectric Effect in Ferroelectric Ceramics," *Japanese Journal of Applied Physics, Part 1*, vol. 37, pp. 5292-5296, 1998.

[17] M. Umeda, S. Takahashi, Y. Sasaki, K. Nakamura, and S. Ueha, "Vibration stress and temperature dependence of piezoelectric resonators with lead-

zirconate-titanate ceramics," *Electronics and Communications in Japan, Part II: Electronics*, vol. 83, pp. 1-7, 2000.

[18] D. S. Campbell and A. M. MacSwan, "The coupling factor of piezoelectric ceramic disks," *British Journal of Applied Physics*, vol. 12, pp. 188-192, 1961.

[19] E. C. Munk, "The Equivalent Electrical Circuit For Radial Modes Of A Piezoelectric Ceramic Disc With Concentric Electrodes," *Philips Research Reports*, vol. 20, pp. 170-189, 1965.

Chapter 3 - Equivalent circuit modelling of radial mode Transoner PTs (II)

3.1 Introduction

Commercially produced PTs are usually completely co-fired, or co-fired and bonded, rather than completely bonded. The structure of a co-fired device differs from that of a completely bonded device in that the internal electrodes do not extend right up to the outer radius of the device, and the isolation between the input and output sections can often be achieved with a ceramic layer, rather than a layer of alumina. Furthermore, the radius of the electrodes in the input and output section do not have to be the same. Indeed, devices have been produced in industry with significantly different electrode radius in the input and output sections. This chapter develops an equivalent circuit model that incorporates the effect these differences have on the electrical behaviour of the devices.

The structure of a co-fired device is shown in Figures 3.1, 3.2, and 3.3. This device is shown with 3 sets of electrodes: input, output, and tertiary. The tertiary set can be used as an extra output, in much the same way as a conventional magnetic transformer having multiple windings. Alternatively, it can be used to provide feedback for control purposes [1], in which case it would probably consist of a single very thin layer. Initially the tertiary electrodes are assumed to be the same radius as the output section electrodes. Consideration of the case where the tertiary electrodes are the same radius as the input section is given later. For the purposes of the derivation, it is assumed that the radius of the input section electrodes is less than or equal to that of the output section electrodes. The choice of which region to call 'input' and 'output' is of course arbitrary, and the end result is simply swapped around for devices where the output section electrode radius is smaller than the input section electrode radius.

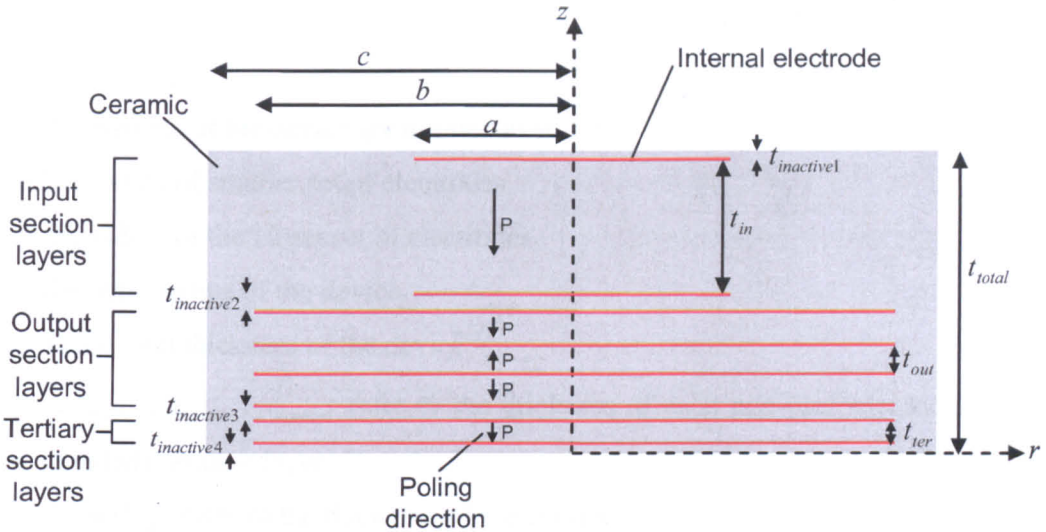

Figure 3.1: Construction and electrode layout of the radial mode Transoner PT.

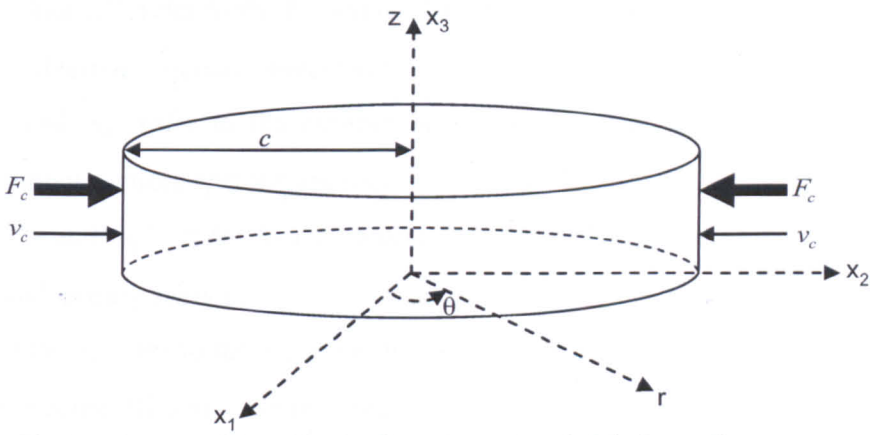

Figure 3.2: PT positioned in the Cartesian and cylindrical coordinate systems.

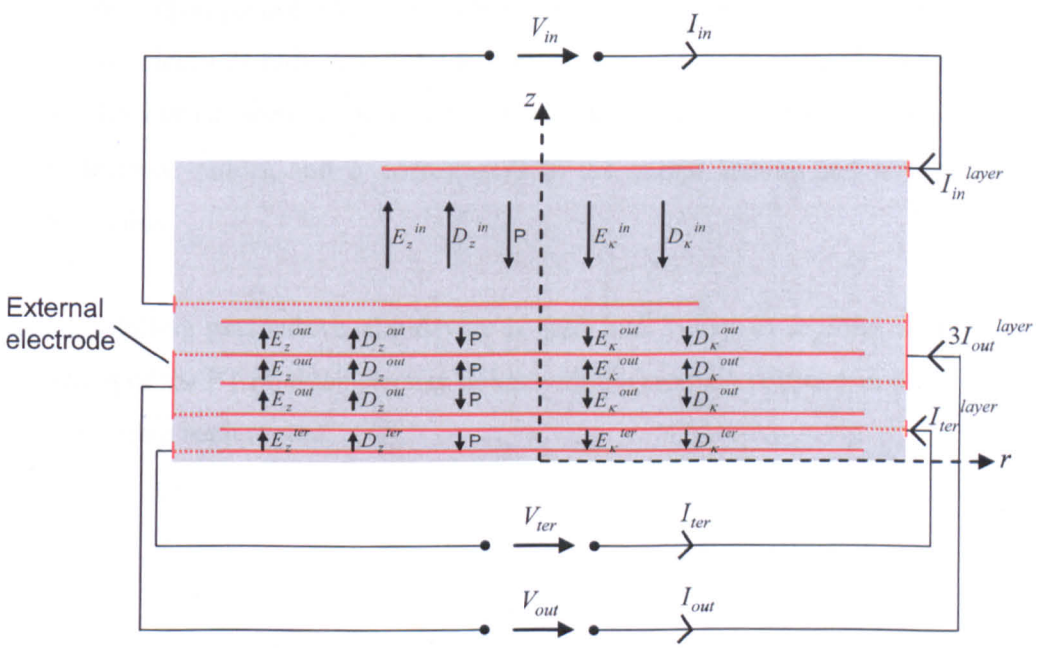

Figure 3.3: Voltage and current definitions in relation to the coordinate systems. Note that I_{out} is shown as being equal to $3I_{out}^{layer}$ to reflect the fact that the device is shown with three output layers.

The dimensions of the device are defined as follows:

a is the radius of smaller set of electrodes

b is the radius of the larger set of electrodes

c is the outer radius of the device.

t_{total} is the total thickness of the device

$t_{inactive1}$, $t_{inactive2}$, $t_{inactive3}$, $t_{inactive4}$ refer to the thickness of each non-piezoelectrically active (i.e. unpoled) ceramic layer.

t_{in}, t_{out}, and t_{ter} refer to the thickness of the ceramic in a single input layer, single output layer, and single tertiary layer, respectively.

t_E^{in}, t_E^{out}, and t_E^{ter} refer to the thickness of a single electrode in the input section, output section, and tertiary section, respectively.

n_{in}, n_{out}, and n_{ter} refer to the number of piezoelectrically active layers in the input section, output section, and tertiary section respectively.

n_E^{in}, n_E^{out}, and n_E^{ter} refer to the number of electrodes in the input section, output section, and tertiary section.

Y_N, σ_N, and ρ_N refer to the Young's modulus, Poisson's ratio, and mass density of the non-piezoelectrically active ceramic material.

Initially, the output section electrode radius is assumed to be equal to or larger than the input section electrode radius, and the tertiary section electrode radius is assumed to be equal to the output section electrode radius. Therefore a corresponds to the input section electrode radius, and b corresponds to the output section and tertiary section electrode radius.

From a modelling perspective, the device is split into 3 distinct regions, such that the composition of the PT (and the electric fields within it) remain constant in the r (and θ) directions within each region.

Region 1: $0 < r < a$

Region 2: $a < r < b$

Region 3: $b < r < c$

Mason equivalent circuits are derived for each section, coupled together, simplified, and expanded in a Taylor series about the first radial resonance to obtain a lumped equivalent circuit. The process is therefore similar to that used for Rosen PTs [2-4], and radial mode transducers coupled to non-piezoelectric rings [5, 6]. Region 1 is modelled as a composite piezoelectric disc containing input section, output section, and tertiary section electrodes. Region 2 is modelled as composite piezoelectric ring containing only output section and tertiary section electrodes, and region 3 is modelled as a composite non-piezoelectric ring. Models for the 3 regions are derived using the same assumptions as the model in Chapter 2. The subscripts 1, 2, and 3 are used to indicate which region a particular quantity relates to. Hence, I_{out2} refers to the output section current that flows through the portion of the output section electrodes that are located in region 2.

The thickness fractions of each material will vary from region to region. For the device illustrated in Figure 3.1 and Figure 3.3, the thickness fractions are as follows

$$f_{C1}^{\ in} = \frac{n_{in} t_{in}}{t_{total}}$$

$$f_{C1}^{\ out} = f_{C2}^{\ out} = \frac{n_{out} t_{out}}{t_{total}}$$

$$f_{C1}^{\ ter} = f_{C2}^{\ ter} = \frac{n_{ter} t_{ter}}{t_{total}}$$

$$f_{E1} = \frac{n_E^{\ in} t_E^{\ in} + n_E^{\ out} t_E^{\ out} + n_E^{\ ter} t_E^{\ ter}}{t_{total}}$$

$$f_{E2} = \frac{n_E^{\ out} t_E^{\ out} + n_E^{\ ter} t_E^{\ ter}}{t_{total}}$$

$$f_{N1} = \frac{t_{inactive1} + t_{inactive2} + t_{inactive3} + t_{inactive4}}{t_{total}}$$

$$f_{N2} = \frac{\left(t_{inactive1} + t_{inactive2} + t_{inactive3} + t_{inactive4}\right) + n_{in} t_{in} + n_E^{\ in} t_E^{\ in}}{t_{total}}$$

$$f_{N3} = 1$$

where the subscript "N" is used as the identifier for the non-piezoelectrically active (i.e. unpoled) ceramic.

3.2 Mason equivalent circuit for the radial motion of a composite piezoelectric thin disc with three sets of electrodes

The Mason equivalent circuit for the radial motion of a composite piezoelectric thin disc with three sets of electrodes is derived using the method described in Chapter 2. The radial force and radial vibration velocity at the outer radius of the disc are termed F_{al} and v_{al} respectively, and defined as shown in Figure 3.4.

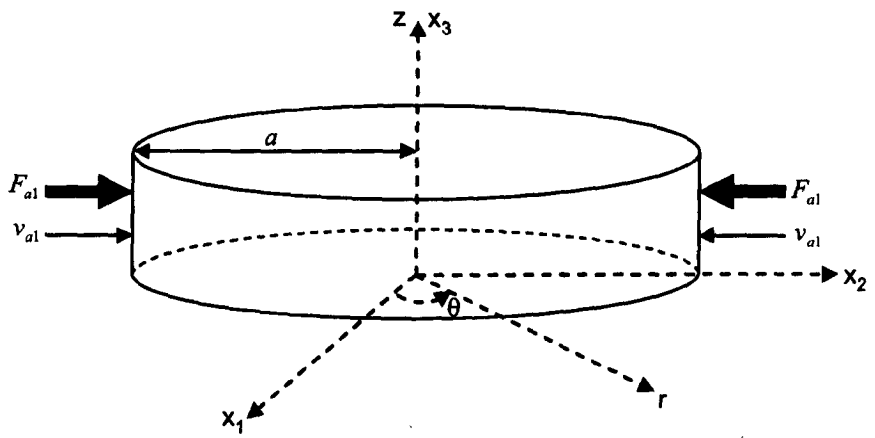

Figure 3.4: Composite piezoelectric thin disc with three sets of electrodes positioned in the Cartesian and cylindrical coordinate systems.

Since there are now 3 sets of electrodes, there are 3 'electrical' equations and 1 'mechanical' equation

$$I_{in1} = V_{in} j\omega C_{in1} - A_{in1} v_{a1} \tag{3.1}$$

$$I_{out1} = V_{out} j\omega C_{out1} - A_{out1} v_{a1} \tag{3.2}$$

$$I_{ter1} = V_{ter} j\omega C_{ter1} - A_{ter1} v_{a1} \tag{3.3}$$

$$F_{a1} = v_{a1} Z_{m1} + V_{in} A_{in1} + V_{out} A_{out1} + V_{ter} A_{ter1} \tag{3.4}$$

where

$$A_{in1} = \frac{2\pi a d_{31}^{\ in} n_{in}}{s_{11}^{E\,in}\left(1-\sigma_C^{E\,in}\right)} \tag{3.5}$$

$$A_{out1} = \frac{2\pi a d_{31}^{\ out} n_{out}}{s_{11}^{E\,out}\left(1-\sigma_C^{E\,out}\right)} \tag{3.6}$$

$$A_{ter1} = \frac{2\pi a d_{31}^{\ ter} n_{ter}}{s_{11}^{E\,ter}\left(1-\sigma_C^{E\,ter}\right)} \tag{3.7}$$

$$C_{in1} = \frac{\pi a^2 n_{in} \varepsilon_{33}^{T\,in}}{t_{in}}\left(1-k_p^{\ in^2}\right) \tag{3.8}$$

$$C_{out1} = \frac{\pi a^2 n_{out} \varepsilon_{33}^{T\,out}}{t_{out}} \left(1 - k_p{}^{out\,2}\right) \tag{3.9}$$

$$C_{ter1} = \frac{\pi a^2 n_{ter} \varepsilon_{33}^{T\,ter}}{t_{ter}} \left(1 - k_p{}^{ter\,2}\right) \tag{3.10}$$

$$Z_{m1} = \frac{t_{total}\, 2\pi \bar{Y}_{r1}}{j\omega} \left(\frac{J_0(\beta_1 a)\beta_1 a}{J_1(\beta_1 a)} + \bar{\sigma}_1 - 1 \right) \tag{3.11}$$

where

$$\bar{Y}_{r1} = f_{C1}{}^{in} \frac{1}{s_{11}^{E\,in}\left(1 - \sigma_C^{E\,in\,2}\right)} + f_{C1}{}^{out} \frac{1}{s_{11}^{E\,out}\left(1 - \sigma_C^{E\,out\,2}\right)} + f_{C1}{}^{ter} \frac{1}{s_{11}^{E\,ter}\left(1 - \sigma_C^{E\,ter\,2}\right)} + f_{N1} \frac{Y_N}{\left(1 - \sigma_N{}^2\right)} + f_{E1} \frac{Y_E}{\left(1 - \sigma_E{}^2\right)} \tag{3.12}$$

$$\bar{P}_1 = f_{C1}{}^{in} \frac{\sigma_C^{E\,in}}{s_{11}^{E\,in}\left(1 - \sigma_C^{E\,in\,2}\right)} + f_{C1}{}^{out} \frac{\sigma_C^{E\,out}}{s_{11}^{E\,out}\left(1 - \sigma_C^{E\,out\,2}\right)} + f_{C1}{}^{ter} \frac{\sigma_C^{E\,ter}}{s_{11}^{E\,ter}\left(1 - \sigma_C^{E\,ter\,2}\right)} + f_{N1} \frac{\sigma_N Y_N}{\left(1 - \sigma_N{}^2\right)} + f_{E1} \frac{\sigma_E Y_E}{\left(1 - \sigma_E{}^2\right)} \tag{3.13}$$

$$\bar{\sigma}_1 = \frac{\bar{P}_1}{\bar{Y}_{r1}} \tag{3.14}$$

$$\beta_1 = \frac{\omega}{\bar{v}_{r1}} \tag{3.15}$$

$$\bar{v}_{r1} = \sqrt{\frac{\bar{Y}_{r1}}{\bar{\rho}_1}} \tag{3.16}$$

$$\bar{\rho}_1 = f_{C1}{}^{in} \rho_C{}^{in} + f_{C1}{}^{out} \rho_C{}^{out} + f_{C1}{}^{ter} \rho_C{}^{ter} + f_{N1} \rho_N + f_{E1} \rho_E \,. \tag{3.17}$$

The equation of radial motion and radial vibration velocity are

$$\xi_r = \left(A_1 J_1(\beta_1 r) + B_1 Y_1(\beta_1 r)\right) e^{j\omega t} \tag{3.18}$$

$$v = \frac{\partial \xi_r}{\partial t} = j\omega \left(A_1 J_1(\beta_1 r) + B_1 Y_1(\beta_1 r)\right) e^{j\omega t} \tag{3.19}$$

where

$$A_1 = -\frac{v_{a1}}{j\omega J_1(\beta_1 a) e^{j\omega t}} \tag{3.20}$$

$$B_1 = 0 \,. \tag{3.21}$$

Equations (3.1) to (3.4) can be represented with the Mason equivalent circuit shown in Figure 3.5.

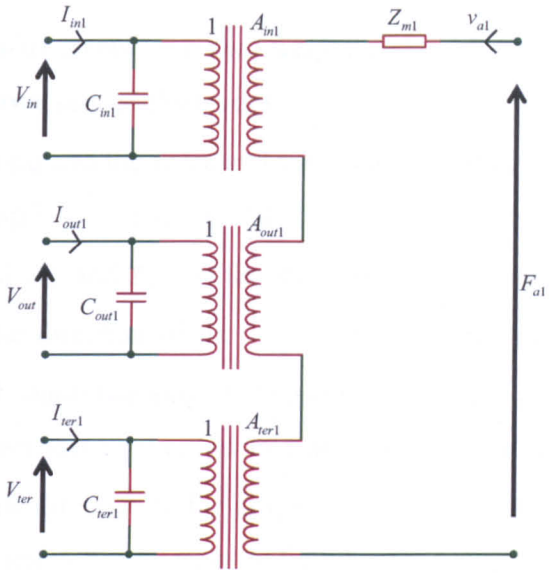

Figure 3.5: Mason equivalent circuit for the radial vibration of a composite piezoelectric thin disc with three sets of electrodes.

3.3 Mason equivalent circuit for the radial motion of a composite piezoelectric thin ring with two sets of electrodes

The structure of the ring and the force and vibration velocities are shown in Figure 3.6 and Figure 3.7. v_{a2} and v_{b2} are the radial vibration velocities at the inner and outer radius of the ring, and F_{a2} and F_{b2} are the radial forces at the inner and outer radius of the ring. Note that the direction of the F_{a2} arrow is shown pointing in the opposite direction to the radial coordinate axis. Although this is not the usual practice (see [2, 5-7]), the arrow is shown this way round to emphasise that the force F_{a2} is defined as positive in the opposite direction to the radial coordinate, and therefore in the opposite direction to the radial stress T_r. (T_r is, by definition, positive in the r direction).

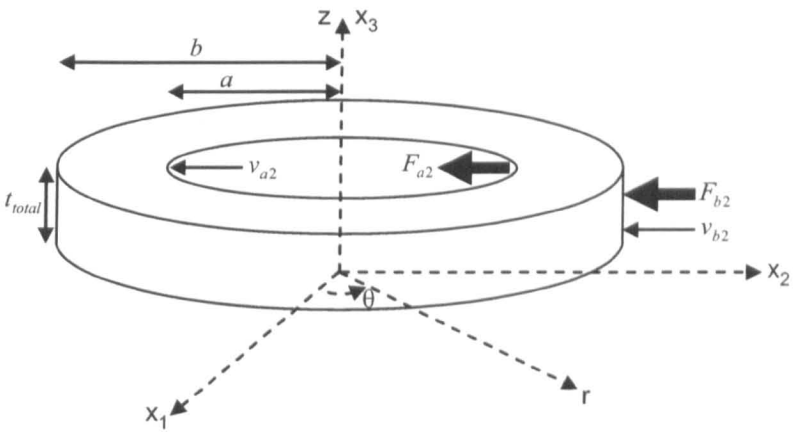

Figure 3.6: Dimensions, forces, and vibration velocities of the composite piezoelectric ring.

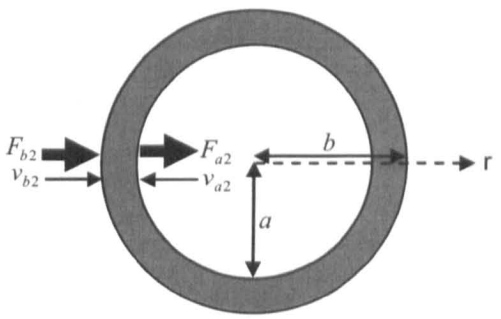

Figure 3.7: Aerial view of the composite piezoelectric ring.

A. Equation of motion

The equation of equilibrium for the radial motion of a thin ring is (since $T_z \approx 0$)

$$\frac{\partial T_r}{\partial r}+\frac{T_r-T_\theta}{r}=\rho\frac{\partial^2\xi_r}{\partial t^2}. \tag{3.22}$$

The average density of the composite ring is

$$\bar{\rho}_2=f_{C2}{}^{out}\rho_C{}^{out}+f_{C2}{}^{ter}\rho_C{}^{ter}+f_{N2}\rho_N+f_{E2}\rho_E. \tag{3.23}$$

The constitutive equations for the output section layers are

$$T_{rC}{}^{out}=\frac{1}{s_{11}^{E\,out}\left(1-\sigma_C^{E\,out\,2}\right)}\left(S_{rC}{}^{out}+\sigma_C^{E\,out}S_{\theta C}{}^{out}-d_{31}{}^{out}E_\kappa{}^{out}\left(1+\sigma_C^{E\,out}\right)\right) \tag{3.24}$$

$$T_{\theta C}{}^{out}=\frac{1}{s_{11}^{E\,out}\left(1-\sigma_C^{E\,out\,2}\right)}\left(S_{\theta C}{}^{out}+\sigma_C^{E\,out}S_{rC}{}^{out}-d_{31}{}^{out}E_\kappa{}^{out}\left(1+\sigma_C^{E\,out}\right)\right) \tag{3.25}$$

$$D_\kappa{}^{out}=d_{31}{}^{out}T_{rC}{}^{out}+d_{31}{}^{out}T_{\theta C}{}^{out}+\varepsilon_{33}^{T\,out}E_\kappa{}^{out} \tag{3.26}$$

where $E_\kappa{}^{out}$ and $D_\kappa{}^{out}$ are defined as shown in Figure 3.3 and described in Chapter 2. The constitutive equations for the tertiary section layers are

$$T_{rC}{}^{ter}=\frac{1}{s_{11}^{E\,ter}\left(1-\sigma_C^{E\,ter\,2}\right)}\left(S_{rC}{}^{ter}+\sigma_C^{E\,ter}S_{\theta C}{}^{ter}-d_{31}{}^{ter}E_\kappa{}^{ter}\left(1+\sigma_C^{E\,ter}\right)\right) \tag{3.27}$$

$$T_{\theta C}{}^{ter}=\frac{1}{s_{11}^{E\,ter}\left(1-\sigma_C^{E\,ter\,2}\right)}\left(S_{\theta C}{}^{ter}+\sigma_C^{E\,ter}S_{rC}{}^{ter}-d_{31}{}^{ter}E_\kappa{}^{ter}\left(1+\sigma_C^{E\,ter}\right)\right) \tag{3.28}$$

$$D_\kappa{}^{ter}=d_{31}{}^{ter}T_{rC}{}^{ter}+d_{31}{}^{ter}T_{\theta C}{}^{ter}+\varepsilon_{33}^{T\,ter}E_\kappa{}^{ter} \tag{3.29}$$

where $E_\kappa{}^{ter}=E_z{}^{ter}$ in the layers poled $\uparrow P$, whereas $E_\kappa{}^{ter}=-E_z{}^{ter}$ in the layers poled $\downarrow P$. Likewise, $D_\kappa{}^{ter}=D_z{}^{ter}$ in the layers poled $\uparrow P$, whereas $D_\kappa{}^{ter}=-D_z{}^{ter}$ in the layers poled $\downarrow P$. For the non-piezoelectrically active ceramic

$$T_{rN}=\frac{Y_N}{1-\sigma_N{}^2}\left(S_{rN}+\sigma_N S_{\theta N}\right) \tag{3.30}$$

$$T_{\theta N}=\frac{Y_N}{1-\sigma_N{}^2}\left(S_{\theta N}+\sigma_N S_{rN}\right). \tag{3.31}$$

For the electrode layers

$$T_{rE}=\frac{Y_E}{1-\sigma_E{}^2}\left(S_{rE}+\sigma_E S_{\theta E}\right) \tag{3.32}$$

$$T_{\theta E}=\frac{Y_E}{1-\sigma_E{}^2}\left(S_{\theta E}+\sigma_E S_{rE}\right). \tag{3.33}$$

The overall stresses in the composite ring are

$$\bar{T}_r=f_{C2}{}^{out}T_{rC}{}^{out}+f_{C2}{}^{ter}T_{rC}{}^{ter}+f_{N2}T_{rN}+f_{E2}T_{rE} \tag{3.34}$$

$$\bar{T}_\theta=f_{C2}{}^{out}T_{\theta C}{}^{out}+f_{C2}{}^{ter}T_{\theta C}{}^{ter}+f_{N2}T_{\theta N}+f_{E2}T_{\theta E}. \tag{3.35}$$

Since the strains are assumed constant with thickness, and $T_z=0$,

$$S_{rC}^{\ out} = S_{rC}^{\ ter} = S_{rN} = S_{rE} = \frac{\partial \xi_r}{\partial r} \tag{3.36}$$

$$S_{\theta C}^{\ out} = S_{\theta C}^{\ ter} = S_{\theta N} = S_{\theta E} = \frac{\xi_r}{r}. \tag{3.37}$$

Substituting (3.24), (3.25), (3.27), (3.28), (3.30) to (3.33), (3.36), and (3.37), into (3.34) and (3.35),

$$\overline{T}_r = \frac{\partial \xi_r}{\partial r}\overline{Y}_{r2} + \frac{\xi_r}{r}\overline{P}_2 - f_{C2}^{\ out}\frac{d_{31}^{\ out}E_\kappa^{\ out}\left(1+\sigma_C^{E^{out}}\right)}{s_{11}^{E^{out}}\left(1-\sigma_C^{E^{out2}}\right)} - f_{C2}^{\ ter}\frac{d_{31}^{\ ter}E_\kappa^{\ ter}\left(1+\sigma_C^{E^{ter}}\right)}{s_{11}^{E^{ter}}\left(1-\sigma_C^{E^{ter2}}\right)} \tag{3.38}$$

$$\overline{T}_\theta = \frac{\xi_r}{r}\overline{Y}_2 + \frac{\partial \xi_r}{\partial r}\overline{P}_2 - f_{C2}^{\ out}\frac{d_{31}^{\ out}E_\kappa^{\ out}\left(1+\sigma_C^{E^{out}}\right)}{s_{11}^{E^{out}}\left(1-\sigma_C^{E^{out2}}\right)} - f_{C2}^{\ ter}\frac{d_{31}^{\ ter}E_\kappa^{\ ter}\left(1+\sigma_C^{E^{ter}}\right)}{s_{11}^{E^{ter}}\left(1-\sigma_C^{E^{ter2}}\right)} \tag{3.39}$$

where effective Young's moduli have been defined

$$\overline{Y}_{r2} = f_{C2}^{\ out}\frac{1}{s_{11}^{E^{out}}\left(1-\sigma_C^{E^{out2}}\right)} + f_{C2}^{\ ter}\frac{1}{s_{11}^{E^{ter}}\left(1-\sigma_C^{E^{ter2}}\right)} + f_{N2}\frac{Y_N}{\left(1-\sigma_N^{\ 2}\right)} + f_{E2}\frac{Y_E}{\left(1-\sigma_E^{\ 2}\right)} \tag{3.40}$$

$$\overline{P}_2 = f_{C2}^{\ out}\frac{\sigma_C^{E^{out}}}{s_{11}^{E^{out}}\left(1-\sigma_C^{E^{out2}}\right)} + f_{C2}^{\ ter}\frac{\sigma_C^{E^{ter}}}{s_{11}^{E^{ter}}\left(1-\sigma_C^{E^{ter2}}\right)} + f_{N2}\frac{\sigma_N Y_N}{\left(1-\sigma_N^{\ 2}\right)} + f_{E2}\frac{\sigma_E Y_E}{\left(1-\sigma_E^{\ 2}\right)}. \tag{3.41}$$

Substituting (3.38) and (3.39) into (3.22), the wave equation is thus

$$\frac{\overline{Y}_{r2}}{\overline{\rho}_2}\left(\frac{\partial^2 \xi_r}{\partial r^2} + \frac{1}{r}\frac{\partial \xi_r}{\partial r} - \frac{\xi_r}{r^2}\right) = \frac{\partial^2 \xi_r}{\partial t^2}. \tag{3.42}$$

Assuming harmonic excitation, the solution for the equation of motion is

$$\xi_r = \left(A_2 J_1(\beta_2 r) + B_2 Y_1(\beta_2 r)\right)e^{j\omega t} \tag{3.43}$$

where the radial wave number is

$$\beta_2 = \frac{\omega}{\overline{v}_{r2}} \tag{3.44}$$

and the radial speed of sound in the ring is

$$\overline{v}_{r2} = \sqrt{\frac{\overline{Y}_{r2}}{\overline{\rho}_2}}. \tag{3.45}$$

The constants A_2 and B_2 are found in terms of the vibration velocity at the inner and outer radius of the ring. From (3.43), radial velocity is

$$v = \frac{\partial \xi_r}{\partial t} = j\omega\left(A_2 J_1(\beta_2 r) + B_2 Y_1(\beta_2 r)\right)e^{j\omega t}. \tag{3.46}$$

At the inner radius $(r = a)$, the radial velocity of a particle is v_{a2}, hence

$$v_{a2} = j\omega\left(A_2 J_1(\beta_2 a) + B_2 Y_1(\beta_2 a)\right)e^{j\omega t}. \tag{3.47}$$

At the outer radius $(r = b)$, the radial velocity of a particle is $-v_{b2}$, hence

$$-v_{b2} = j\omega\left(A_2 J_1(\beta_2 b) + B_2 Y_1(\beta_2 b)\right)e^{j\omega t}. \tag{3.48}$$

Note that the negative sign in (3.48) is due to v_{b2} being defined in the opposite direction to the radial coordinate (see Figure 3.6). Solving the simultaneous equations (3.47) and (3.48), the constants are

$$A_2 = \frac{1}{j\omega}\frac{v_{a2}Y_1(\beta_2 b) + v_{b2}Y_1(\beta_2 a)}{\left(Y_1(\beta_2 b)J_1(\beta_2 a) - J_1(\beta_2 b)Y_1(\beta_2 a)\right)}e^{-j\omega t} \tag{3.49}$$

$$B_2 = -\frac{1}{j\omega}\frac{v_{a2}J_1(\beta_2 b) + v_{b2}J_1(\beta_2 a)}{\left(Y_1(\beta_2 b)J_1(\beta_2 a) - J_1(\beta_2 b)Y_1(\beta_2 a)\right)}e^{-j\omega t} \tag{3.50}$$

Substituting (3.49) and (3.50) into (3.43), the equation of motion can be expressed as

$$\xi_r = \frac{1}{j\omega}\left(\frac{J_1(\beta_2 r)\left(v_{a2}Y_1(\beta_2 b) + v_{b2}Y_1(\beta_2 a)\right) - Y_1(\beta_2 r)\left(v_{a2}J_1(\beta_2 b) + v_{b2}J_1(\beta_2 a)\right)}{Y_1(\beta_2 b)J_1(\beta_2 a) - J_1(\beta_2 b)Y_1(\beta_2 a)}\right). \tag{3.51}$$

B. Electrical equations

For harmonic excitation, the current through a single output layer in the ring is

$$I_{out2}^{\ layer} = \frac{dQ}{dt} = j\omega Q = j\omega\int_a^b D_\kappa^{\ out} 2\pi r\, dr \tag{3.52}$$

Substituting (3.26), (3.24), (3.25), (3.36), and (3.37) into (3.52)

$$I_{out2}^{\ layer} = j\omega 2\pi\int_a^b\left(\frac{d_{31}^{\ out}\left(1+\sigma_C^{E\,out}\right)}{s_{11}^{E\,out}\left(1-\sigma_C^{E\,out\,2}\right)}\left(\frac{\partial\xi_r}{\partial r} + \frac{\xi_r}{r} - 2d_{31}^{\ out}E_\kappa^{\ out}\right) + \varepsilon_{33}^{T\,out}E_\kappa^{\ out}\right) r\, dr. \tag{3.53}$$

From Figure 3.3, $E_\kappa^{\ out}$ and $E_\kappa^{\ ter}$ are related to the voltages by

$$E_\kappa^{\ out} = \frac{V_{out}}{t_{out}} \tag{3.54}$$

$$E_\kappa^{\ ter} = \frac{V_{ter}}{t_{ter}}. \tag{3.55}$$

Substituting (3.51) into (3.53), evaluating, making use of the planar coupling factor, and using (3.54), results in

$$I_{out2}^{\ layer} = \frac{j\omega\pi\varepsilon_{33}^{T\,out}\left(b^2 - a^2\right)\left(1-k_p^{\ out\,2}\right)}{t_{out}}V_{out} - \frac{2\pi d_{31}^{\ out}}{s_{11}^{E\,out}\left(1-\sigma_C^{E\,out}\right)}\left(av_{a2} + bv_{b2}\right) \tag{3.56}$$

Since there are n_{out} layers connected electrically in parallel, $I_{out2} = n_{out}I_{out2}^{\ layer}$, and

$$I_{out2} = \frac{j\omega\pi\varepsilon_{33}^{T\,out}n_{out}\left(b^2 - a^2\right)\left(1-k_p^{\ out\,2}\right)}{t_{out}}V_{out} - \frac{2\pi d_{31}^{\ out}n_{out}}{s_{11}^{E\,out}\left(1-\sigma_C^{E\,out}\right)}\left(av_{a2} + bv_{b2}\right) \tag{3.57}$$

Repeating the process for the tertiary section layers,

$$I_{ter2} = \frac{j\omega\pi\varepsilon_{33}^{T\,ter} n_{ter}\left(b^2 - a^2\right)\left(1 - {k_p}^{ter\,2}\right)}{t_{ter}} V_{ter} - \frac{2\pi {d_{31}}^{ter} n_{ter}}{s_{11}^{E\,ter}\left(1 - \sigma_C^{E\,ter}\right)}\left(a v_{a2} + b v_{b2}\right). \tag{3.58}$$

C. Mechanical equations

The radial force acting (inwards) on the inner radius of the ring is

$$F_{a2} = -T_r\big|_{r=a} S_a \tag{3.59}$$

where the surface area on which the force acts is

$$S_a = 2\pi a t_{total}. \tag{3.60}$$

Substituting (3.60), (3.38), (3.36), (3.37), (3.51), (3.54), and (3.55) into (3.59), and making use of the Bessel function identity

$$x\left(Y_1(x)J_0(x) - J_1(x)Y_0(x)\right) = \frac{-2}{\pi} \tag{3.61}$$

where Y_0 is a Bessel function of the second kind and zero order, results in

$$\begin{aligned} F_{a2} = {} & v_{b2}\left(\frac{-4jt_{total}\overline{Y}_{r2}}{\omega\left(Y_1(\beta_2 b)J_1(\beta_2 a) - J_1(\beta_2 b)Y_1(\beta_2 a)\right)}\right) \\ & + v_{a2}\left(\frac{2j\pi t_{total}\left[\begin{array}{l}\left(\overline{P}_2 - \overline{Y}_{r2}\right)J_1(\beta_2 a)Y_1(\beta_2 b) + \left(\overline{Y}_{r2} - \overline{P}_2\right)Y_1(\beta_2 a)J_1(\beta_2 b) \\ + \overline{Y}_{r2}Y_1(\beta_2 b)J_0(\beta_2 a)\beta_2 a - \overline{Y}_{r2}J_1(\beta_2 b)Y_0(\beta_2 a)\beta_2 a\end{array}\right]}{\omega\left(Y_1(\beta_2 b)J_1(\beta_2 a) - J_1(\beta_2 b)Y_1(\beta_2 a)\right)}\right) \\ & + \frac{2\pi a n_{out} {d_{31}}^{out}}{s_{11}^{E\,out}\left(1 - \sigma_C^{E\,out}\right)} V_{out} + \frac{2\pi a n_{ter} {d_{31}}^{ter}}{s_{11}^{E\,ter}\left(1 - \sigma_C^{E\,ter}\right)} V_{ter} \end{aligned} \tag{3.62}$$

Likewise, the radial force acting (inwards) on the outer radius is

$$F_{b2} = -T_r\big|_{r=b} S_b \tag{3.63}$$

where the surface area on which the force acts is

$$S_b = 2\pi b t_{total}. \tag{3.64}$$

Substituting (3.64), (3.38), (3.36), (3.37), (3.51), (3.54), and (3.55) into (3.63), and making use of the identity (3.61),

$$\begin{aligned} F_{b2} = {} & v_{a2}\left(\frac{-4jt_{total}\overline{Y}_{r2}}{\omega\left(Y_1(\beta_2 b)J_1(\beta_2 a) - J_1(\beta_2 b)Y_1(\beta_2 a)\right)}\right) \\ & + v_{b2}\left(\frac{2j\pi t_{total}\left[\begin{array}{l}\left(\overline{P}_2 - \overline{Y}_{r2}\right)J_1(\beta_2 b)Y_1(\beta_2 a) + \left(\overline{Y}_{r2} - \overline{P}_2\right)Y_1(\beta_2 b)J_1(\beta_2 a) \\ + \overline{Y}_{r2}Y_1(\beta_2 a)J_0(\beta_2 b)\beta_2 b - \overline{Y}_{r2}J_1(\beta_2 a)Y_0(\beta_2 b)\beta_2 b\end{array}\right]}{\omega\left(Y_1(\beta_2 b)J_1(\beta_2 a) - J_1(\beta_2 b)Y_1(\beta_2 a)\right)}\right) \\ & + \frac{2\pi b n_{out} {d_{31}}^{out}}{s_{11}^{E\,out}\left(1 - \sigma_C^{E\,out}\right)} V_{out} + \frac{2\pi b n_{ter} {d_{31}}^{ter}}{s_{11}^{E\,ter}\left(1 - \sigma_C^{E\,ter}\right)} V_{ter} \end{aligned} \tag{3.65}$$

The key equations for the composite ring with multiple sets of electrodes are (3.57), (3.58), (3.62), and (3.65). If the simpler case of a single layer piezoelectric ring is considered (i.e. let $n_{out}=1$, $n_{ter}=0$, and $t_{out}=t_{total}$), then (3.57), (3.62), and (3.65) become mathematically equivalent to those in [5].

D. Equivalent circuit representation

Equations (3.62) and (3.65) are now rewritten as

$$F_{a2}=Av_{a2}+Bv_{b2}+\frac{2\pi an_{out}d_{31}^{\ out}}{s_{11}^{E\,out}\left(1-\sigma_C^{E\,out}\right)}V_{out}+\frac{2\pi an_{ter}d_{31}^{\ ter}}{s_{11}^{E\,ter}\left(1-\sigma_C^{E\,ter}\right)}V_{ter} \tag{3.66}$$

$$F_{b2}=Bv_{a2}+Cv_{b2}+\frac{2\pi bn_{out}d_{31}^{\ out}}{s_{11}^{E\,out}\left(1-\sigma_C^{E\,out}\right)}V_{out}+\frac{2\pi bn_{ter}d_{31}^{\ ter}}{s_{11}^{E\,ter}\left(1-\sigma_C^{E\,ter}\right)}V_{ter} \tag{3.67}$$

where

$$A=\frac{2j\pi t_{total}\left[\begin{array}{l}\left(\overline{P}_2-\overline{Y}_{r2}\right)J_1(\beta_2a)Y_1(\beta_2b)+\left(\overline{Y}_{r2}-\overline{P}_2\right)Y_1(\beta_2a)J_1(\beta_2b)\\+\overline{Y}_{r2}Y_1(\beta_2b)J_0(\beta_2a)\beta_2a-\overline{Y}_{r2}J_1(\beta_2b)Y_0(\beta_2a)\beta_2a\end{array}\right]}{\omega\left(Y_1(\beta_2b)J_1(\beta_2a)-J_1(\beta_2b)Y_1(\beta_2a)\right)} \tag{3.68}$$

$$B=\frac{-4jt_{total}\overline{Y}_{r2}}{\omega\left(Y_1(\beta_2b)J_1(\beta_2a)-J_1(\beta_2b)Y_1(\beta_2a)\right)} \tag{3.69}$$

$$C=\frac{2j\pi t_{total}\left[\begin{array}{l}\left(\overline{P}_2-\overline{Y}_{r2}\right)J_1(\beta_2b)Y_1(\beta_2a)+\left(\overline{Y}_{r2}-\overline{P}_2\right)Y_1(\beta_2b)J_1(\beta_2a)\\+\overline{Y}_{r2}Y_1(\beta_2a)J_0(\beta_2b)\beta_2b-\overline{Y}_{r2}J_1(\beta_2a)Y_0(\beta_2b)\beta_2b\end{array}\right]}{\omega\left(Y_1(\beta_2b)J_1(\beta_2a)-J_1(\beta_2b)Y_1(\beta_2a)\right)}. \tag{3.70}$$

With reference to (3.57), (3.58), (3.66), and (3.67), the following force factors and clamped capacitances are defined

$$A_{out2}=\frac{2\pi d_{31}^{\ out}n_{out}}{s_{11}^{E\,out}\left(1-\sigma_C^{E\,out}\right)} \tag{3.71}$$

$$C_{out2}=\frac{n_{out}\pi\varepsilon_{33}^{T\,out}\left(b^2-a^2\right)\left(1-k_p^{\ out\,2}\right)}{t_{out}} \tag{3.72}$$

$$A_{ter2}=\frac{2\pi d_{31}^{\ ter}n_{ter}}{s_{11}^{E\,ter}\left(1-\sigma_C^{E\,ter}\right)} \tag{3.73}$$

$$C_{ter2}=\frac{n_{ter}\pi\varepsilon_{33}^{T\,ter}\left(b^2-a^2\right)\left(1-k_p^{\ ter\,2}\right)}{t_{ter}} \tag{3.74}$$

where

$$k_p^{\ out}=\sqrt{\frac{2d_{31}^{\ out\,2}}{\varepsilon_{33}^{T\,out}s_{11}^{E\,out}\left(1-\sigma_C^{E\,out}\right)}} \tag{3.75}$$

$$k_p^{ter} = \sqrt{\frac{2d_{31}^{ter\,2}}{\varepsilon_{33}^{T\,ter} s_{11}^{E\,ter}\left(1-\sigma_C^{E\,ter}\right)}}. \tag{3.76}$$

Then, let

$$v_{a2}' = a v_{a2} \tag{3.77}$$

$$v_{b2}' = b v_{b2} \tag{3.78}$$

$$F_{a2}' = \frac{F_{a2}}{a} \tag{3.79}$$

$$F_{b2}' = \frac{F_{b2}}{b}. \tag{3.80}$$

Therefore (3.57), (3.58), (3.66), and (3.67) can be written as

$$I_{out2} = j\omega C_{out2} V_{out} - A_{out2}\left(v_{a2}' + v_{b2}'\right) \tag{3.81}$$

$$I_{ter2} = j\omega C_{ter2} V_{ter} - A_{ter2}\left(v_{a2}' + v_{b2}'\right) \tag{3.82}$$

$$F_{a2}' = \frac{A}{a^2} v_{a2}' + \frac{B}{ab} v_{b2}' + A_{out2} V_{out} + A_{ter2} V_{ter} \tag{3.83}$$

$$F_{b2}' = \frac{B}{ab} v_{a2}' + \frac{C}{b^2} v_{b2}' + A_{out2} V_{out} + A_{ter2} V_{ter}. \tag{3.84}$$

The equations (3.81) to (3.84) can be represented with the circuit of Figure 3.8, where

$$Z_{m2} = \frac{A}{a^2} - \frac{B}{ab} \tag{3.85}$$

$$Z_{m3} = \frac{B}{ab} \tag{3.86}$$

$$Z_{m4} = \frac{C}{b^2} - \frac{B}{ab}. \tag{3.87}$$

Using additional ideal transformers to implement (3.77) to (3.80), the Mason equivalent circuit for the composite ring with two sets of electrodes is shown in Figure 3.9.

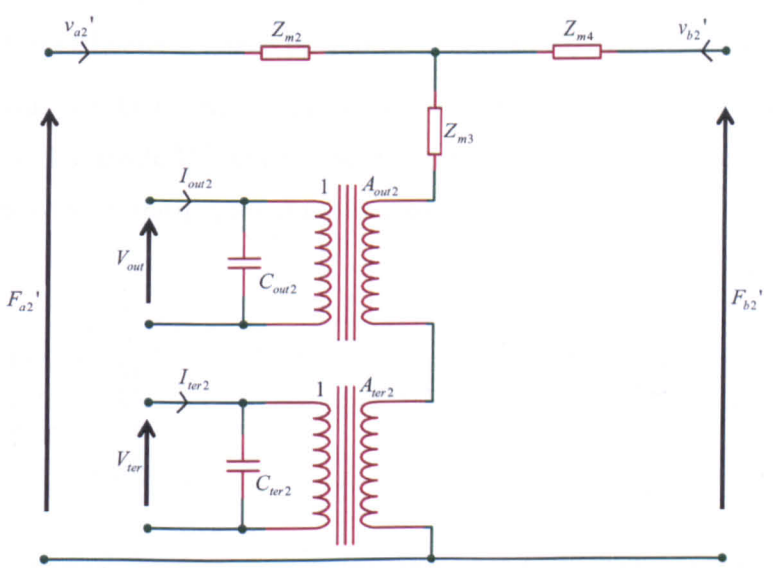

Figure 3.8: Equivalent circuit representation of (3.81) to (3.84).

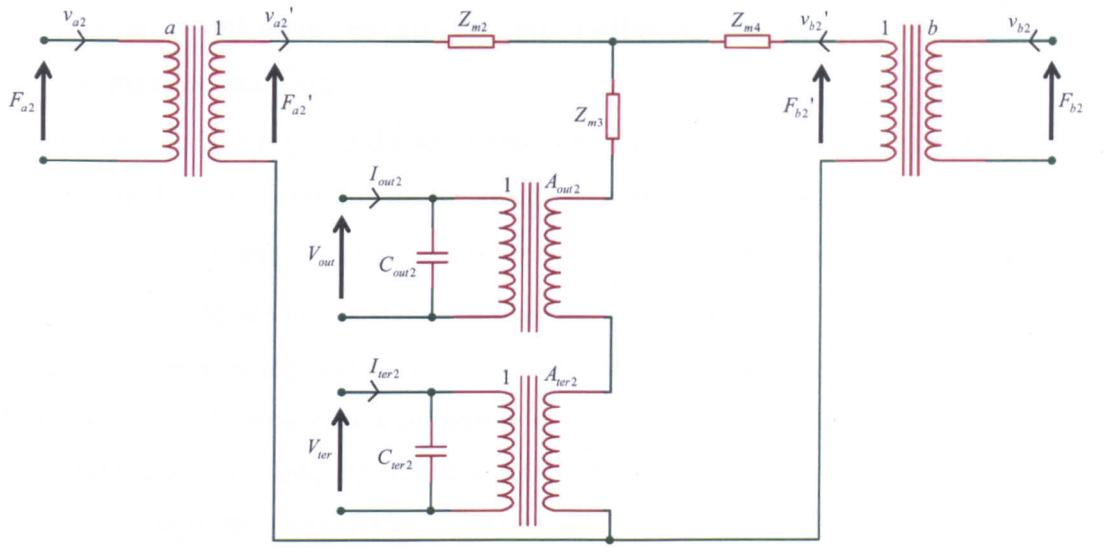

Figure 3.9: Mason equivalent circuit for the radial vibration of a thin composite ring with two sets of electrodes.

Whilst the circuit of Figure 3.9 is suitable for modelling region 2 of the disc type PT shown in Figure 3.3, it can also be used to obtain an equivalent circuit for a ring shaped radial mode Transoner-type PT. The boundary conditions for a ring shaped PT are $F_{b2} = 0$ and $F_{c2} = 0$, and applying these to Figure 3.9 results in the equivalent circuit shown in Figure 3.10. Interestingly, the mechanical branch current is the sum of v_a' and v_b'. Unlike the simple disc type PT discussed in Chapter 2, this means there is unlikely to be a convenient relationship between the mechanical branch current and the maximum vibration velocity within the ring. When the inner radius a tends to zero, the impedance Z_{m2} tends to infinity, v_{a2}' tends to zero, the motional current tends to v_{b2}', and the mechanical impedance becomes $Z_{m3} + Z_{m4}$. Comparing $Z_{m3} + Z_{m4}$ to a suitably adapted Z_{m1} from Chapter 2 (since the motional current was v_a rather than v_{b2}', and the outer radius was a rather than b), the two models are found to be consistent. Although the ring type radial mode PT will not be developed further in this thesis, the circuit of Figure 3.10 provides a starting point for its study.

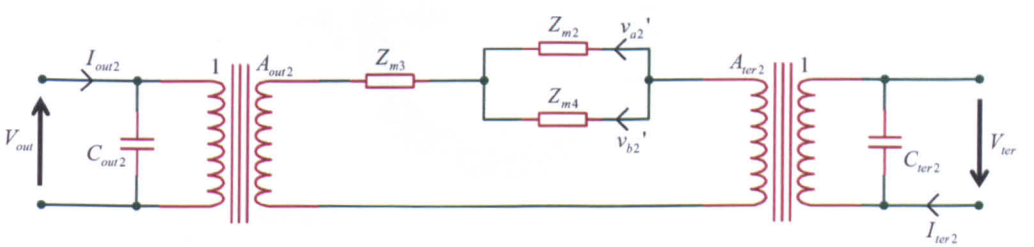

Figure 3.10: Equivalent circuit for the radial vibration of a ring shaped Transoner-type PT.

3.4 Mason equivalent circuit for the radial motion of a non-piezoelectric composite thin ring

The structure of the ring and the force and vibration velocities are shown in Figure 3.11 and Figure 3.12. v_{b3} and v_{c3} are the radial vibration velocities at the inner and outer radius of the ring, and F_{b3} and F_{c3} are the radial forces at the inner and outer radius of the ring. In the device layout shown in Figure 3.1 and Figure 3.3, the ring consists only of non-piezoelectrically active (i.e. unpoled) ceramic. However, the equations are formulated as if the ring were a composite in order to preserve generality (some co-fired and bonded devices have an alumina isolation layer, resulting in a composite outer ring). Although the connections between the internal and external electrodes run through a section of this ring, their effect is assumed negligible. Since the Mason equivalent circuit for a non-piezoelectric thin ring has previously been developed in [5, 6], only the key equations will be shown.

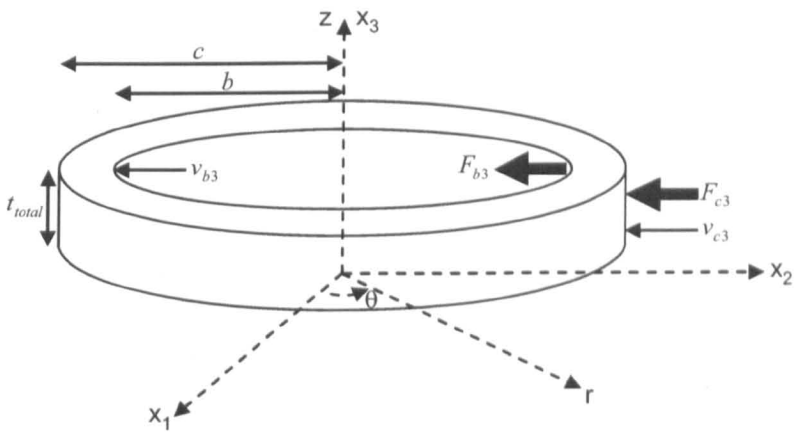

Figure 3.11: Dimensions, forces, and vibration velocities of the non-piezoelectric ring.

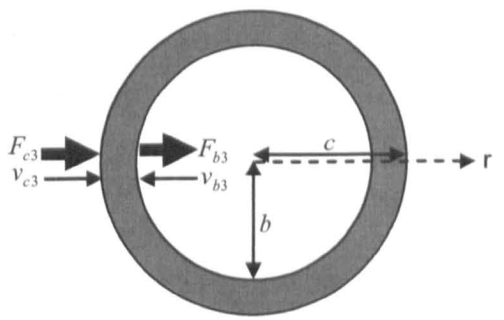

Figure 3.12: Aerial view of the non-piezoelectric ring.

The radial forces acting inward at the inner and outer radius of the ring are

$$F_{b3} = v_{b3}(Z_{m5} + Z_{m6}) + v_{c3}Z_{m6} \tag{3.88}$$

$$F_{c3} = v_{b3}Z_{m6} + v_{c3}(Z_{m6} + Z_{m7}) \tag{3.89}$$

where

$$Z_{m5} = \frac{2j\pi t_{total}\left[\begin{array}{l}(\bar{P}_3 - \bar{Y}_{r3})J_1(\beta_3 b)Y_1(\beta_3 c) + (\bar{Y}_{r3} - \bar{P}_3)Y_1(\beta_3 b)J_1(\beta_3 c) + \bar{Y}_{r3}Y_1(\beta_3 c)J_0(\beta_3 b)\beta_3 b \\ -\bar{Y}_{r3}J_1(\beta_3 c)Y_0(\beta_3 b)\beta_3 b + \dfrac{2\bar{Y}_{r3}}{\pi}\end{array}\right]}{\omega(Y_1(\beta_3 c)J_1(\beta_3 b) - J_1(\beta_3 c)Y_1(\beta_3 b))} \tag{3.90}$$

$$Z_{m6} = \frac{-4jt_{total}\bar{Y}_{r3}}{\omega(Y_1(\beta_3 c)J_1(\beta_3 b) - J_1(\beta_3 c)Y_1(\beta_3 b))} \tag{3.91}$$

$$Z_{m7} = \frac{2j\pi t_{total}\left[\begin{array}{l}(\bar{P}_3 - \bar{Y}_{r3})J_1(\beta_3 c)Y_1(\beta_3 b) + (\bar{Y}_{r3} - \bar{P}_3)Y_1(\beta_3 c)J_1(\beta_3 b) + \bar{Y}_{r3}Y_1(\beta_3 b)J_0(\beta_3 c)\beta_3 c \\ -\bar{Y}_{r3}J_1(\beta_3 b)Y_0(\beta_3 c)\beta_3 c + \dfrac{2\bar{Y}_{r3}}{\pi}\end{array}\right]}{\omega(Y_1(\beta_3 c)J_1(\beta_3 b) - J_1(\beta_3 c)Y_1(\beta_3 b))} \tag{3.92}$$

$$\bar{Y}_{r3} = f_{N3}\frac{Y_N}{(1-\sigma_N^2)} \tag{3.93}$$

$$\bar{P}_3 = f_{N3}\frac{\sigma_N Y_N}{(1-\sigma_N^2)} \tag{3.94}$$

$$\bar{\rho}_3 = f_{N3}\rho_N \tag{3.95}$$

$$\beta_3 = \frac{\omega}{\bar{v}_{r3}} \tag{3.96}$$

$$\bar{v}_{r3} = \sqrt{\frac{\bar{Y}_{r3}}{\bar{\rho}_3}}. \tag{3.97}$$

The equation of motion and radial vibration velocity of the non-piezoelectric ring are

$$\xi_r = (A_3 J_1(\beta_3 r) + B_3 Y_1(\beta_3 r))e^{j\omega t} \tag{3.98}$$

$$v = \frac{\partial \xi_r}{\partial t} = j\omega(A_3 J_1(\beta_3 r) + B_3 Y_1(\beta_3 r))e^{j\omega t} \tag{3.99}$$

where

$$A_3 = \frac{1}{j\omega}\frac{v_{b3}Y_1(\beta_3 c) + v_{c3}Y_1(\beta_3 b)}{(Y_1(\beta_3 c)J_1(\beta_3 b) - J_1(\beta_3 c)Y_1(\beta_3 b))}e^{-j\omega t} \tag{3.100}$$

$$B_3 = -\frac{1}{j\omega}\frac{v_{b3}J_1(\beta_3 c) + v_{c3}J_1(\beta_3 b)}{(Y_1(\beta_3 c)J_1(\beta_3 b) - J_1(\beta_3 c)Y_1(\beta_3 b))}e^{-j\omega t} \tag{3.101}$$

The Mason equivalent circuit for a thin composite ring in radial vibration is shown in Figure 3.13.

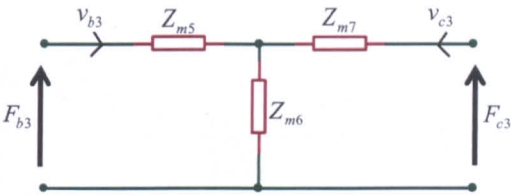

Figure 3.13: Mason equivalent circuit for a thin composite ring in radial vibration.

3.5 The complete equivalent circuit model for the radial mode Transoner PT

Radial force and vibration velocity are continuous at the region boundaries. From Figure 3.1, Figure 3.4, Figure 3.6, and Figure 3.11, it is therefore apparent that

$$F_{a1} = F_{a2},\ F_{b2} = F_{b3},\ v_{a1} = -v_{a2},\ v_{b2} = -v_{b3}. \tag{3.102}$$

Thus, using the equivalent circuit models from sections 3.2 to 3.4, a complete Mason equivalent circuit for the radial motion of the device shown in Figure 3.1 can be assembled, as shown in Figure 3.14.

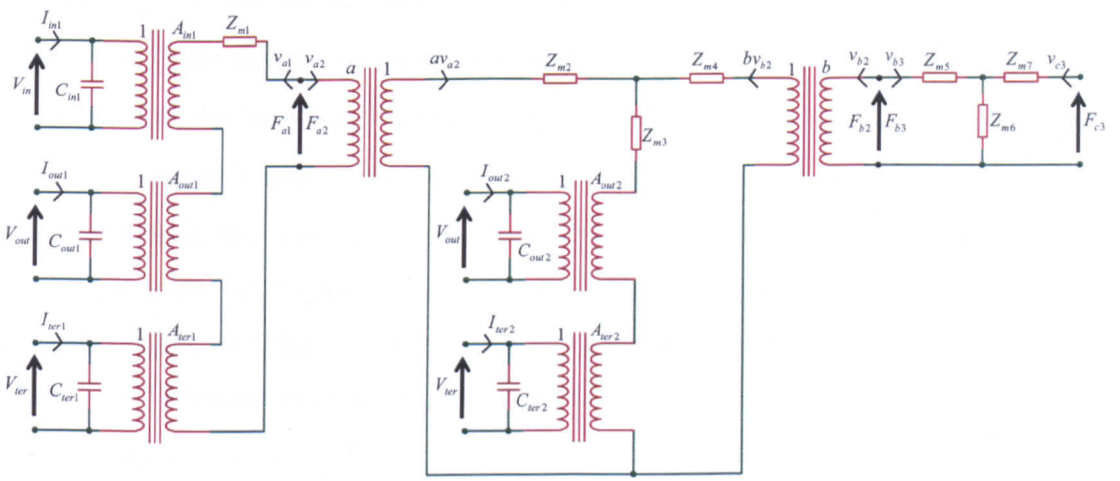

Figure 3.14: Mason equivalent circuit for the radial mode Transoner PT.

Since the outer radius of the device is free to vibrate, $F_c = 0$ (see Figure 3.2). Therefore $F_{c3} = 0$ (see Figure 3.11). Applying this boundary condition results in the circuit of Figure 3.15, where

$$Z_{m8} = Z_{m4} + \frac{1}{b^2}\left(Z_{m5} + \frac{Z_{m6}Z_{m7}}{Z_{m6} + Z_{m7}}\right). \tag{3.103}$$

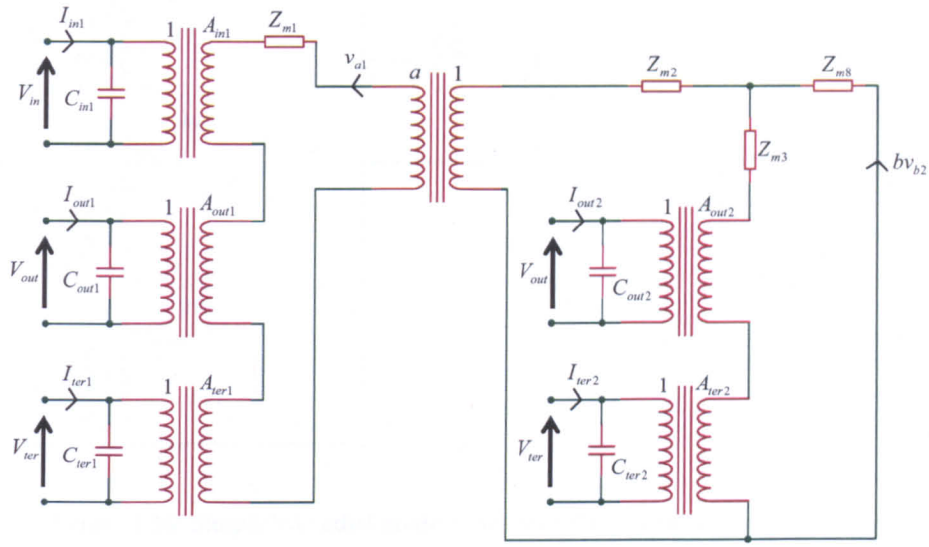

Figure 3.15: Mason equivalent circuit for the radial mode Transoner PT once the boundary condition $F_{c3} = 0$ is implemented.

The impedances Z_{m2}, Z_{m3}, and Z_{m8} are then referred across the $a:1$ transformer, and the $a:1$ and $A_{out2}:1$, and the $a:1$ and $A_{ter2}:1$ transformers combined to give the circuit of Figure 3.16. Note that the resulting turns ratios, $aA_{out2}:1$, and $aA_{ter2}:1$ are the same as the turns ratios of the output and tertiary sections in region 1, i.e. $A_{out1}:1$ and $A_{ter1}:1$ (see (3.71), (3.73), (3.6), and (3.7)). Since the voltages across C_{out1} and C_{out2} are equal, and the ideal transformer turns ratios into which they feed are equal, the two points marked with the * symbol in Figure 1.6 are at the same potential, and may therefore be joined. A similar argument holds for the two points marked with the # symbol. Thus, the circuit of Figure 3.16 simplifies to that shown in Figure 3.17, where

$$Z_1 = Z_{m1} + Z_{m2}a^2, \quad Z_2 = Z_{m8}a^2, \quad Z_3 = Z_{m3}a^2. \tag{3.104}$$

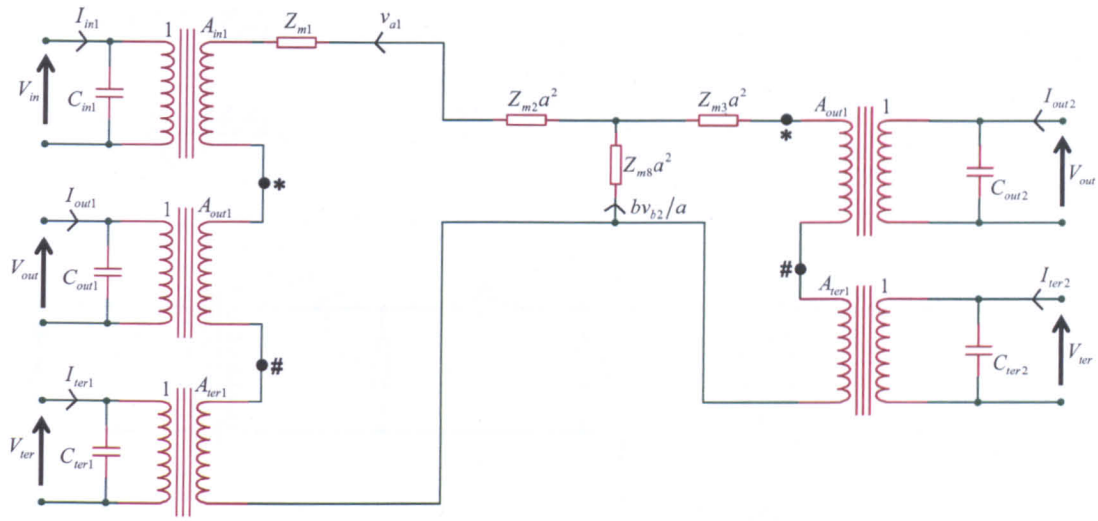

Figure 3.16: Simplified radial mode Transoner PT equivalent circuit, stage 1.

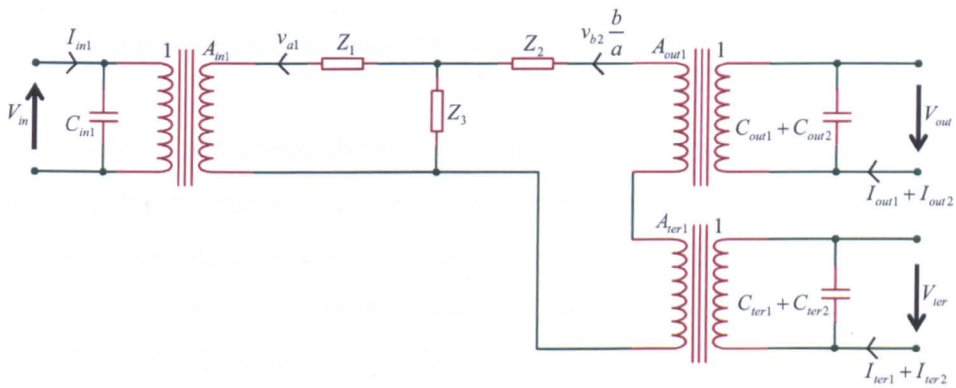

Figure 3.17: Simplified radial mode Transoner PT equivalent circuit, stage 2.

The circuit of Figure 3.17 can be used to simulate the electrical behaviour of a radial mode Transoner PT when it is operating in the vicinity of any radial resonance (i.e. first radial resonance, second radial resonance, etc), providing there is no interference from other vibration modes in the region of interest. However, this circuit cannot be simulated in SPICE because of the mathematical form of the impedances, and therefore cannot be simulated together with the rest of the components in a converter (e.g. the half-bridge, rectifier, etc). Simplifications are therefore made to allow the behaviour of the PT to be modelled with a lumped equivalent circuit.

The 'T' network in Figure 3.17 can be converted to a 'π' network, as shown in Figure 3.18, where

$$Z_a = \frac{Z_1 Z_2 + Z_1 Z_3 + Z_2 Z_3}{Z_2} \tag{3.105}$$

$$Z_b = \frac{Z_1Z_2 + Z_1Z_3 + Z_2Z_3}{Z_1} \tag{3.106}$$

$$Z_c = \frac{Z_1Z_2 + Z_1Z_3 + Z_2Z_3}{Z_3}. \tag{3.107}$$

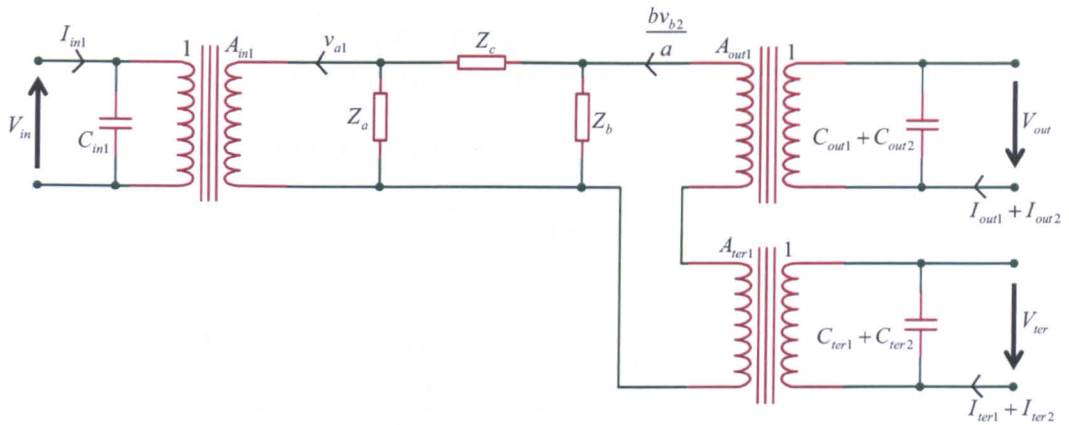

Figure 3.18: π network representation of the equivalent circuit of a radial mode Transoner PT.

In order to allow further simplification, the effective Young's modulus, Poisson's ratio, and average density are assumed to be approximately equal in the three regions. In practice, the third region is usually made as small as possible, and devices where the input (or output) section electrode radius is made smaller than the output (or input) section will usually have only 1 or 2 layers in the input (or output) section. Therefore the loss of accuracy that will occur by making this assumption is likely to be small. Hence, let

$$\overline{Y}_{r1} \approx \overline{Y}_{r2} \approx \overline{Y}_{r3} = \overline{Y}_r \tag{3.108}$$

$$\overline{P}_1 \approx \overline{P}_2 \approx \overline{P}_3 = \overline{P} \tag{3.109}$$

$$\overline{\rho}_1 \approx \overline{\rho}_2 \approx \overline{\rho}_3 = \overline{\rho}. \tag{3.110}$$

Thus,

$$\overline{\upsilon}_{r1} \approx \overline{\upsilon}_{r2} \approx \overline{\upsilon}_{r3} = \overline{\upsilon}_r \tag{3.111}$$

$$\beta_1 \approx \beta_2 \approx \beta_3 = \beta \tag{3.112}$$

and

$$\overline{\upsilon}_r = \sqrt{\frac{\overline{Y}_r}{\overline{\rho}}} \tag{3.113}$$

$$\beta = \frac{\omega}{\overline{\upsilon}_r}. \tag{3.114}$$

Substituting (3.108) to (3.112) into (3.105), (3.106), and (3.107), and making extensive use of the identity shown in (3.61), Z_a, Z_b, and Z_c become

$$Z_a = \frac{\left(\frac{-4jJ_1(\beta c)^2 Y_1(\beta b)\overline{Y}_r^{\,2}\pi t_{total} a}{\omega J_1(\beta a)}\left(1-\frac{J_1(\beta b)Y_1(\beta c)}{J_1(\beta c)Y_1(\beta b)}\right)\left(\frac{\beta c J_0(\beta c)}{J_1(\beta c)}+\frac{\overline{P}}{\overline{Y}_r}-1\right)\right)}{\left(\begin{array}{l}\pi b\left(\overline{P}-\overline{Y}_r\right)\left(J_1(\beta b)^2 Y_1(\beta c)^2+Y_1(\beta b)^2 J_1(\beta c)^2\right)\\ -2\pi b\left(\overline{P}-\overline{Y}_r\right)J_1(\beta b)Y_1(\beta b)Y_1(\beta c)J_1(\beta c)\\ +2a\overline{Y}_r\left(Y_1(\beta b)J_1(\beta a)-J_1(\beta b)Y_1(\beta a)\right)\\ +\pi bc\beta\overline{Y}_r\left(Y_1(\beta b)J_1(\beta c)-Y_1(\beta c)J_1(\beta b)\right)\left(J_0(\beta c)Y_1(\beta b)-J_1(\beta b)Y_0(\beta c)\right)\\ +\pi ac\beta\overline{Y}_r\left(Y_1(\beta b)J_0(\beta c)-J_1(\beta b)Y_0(\beta c)\right)\left(J_1(\beta a)Y_1(\beta c)-J_1(\beta c)Y_1(\beta a)\right)\\ +\pi a\left(\overline{P}-\overline{Y}_r\right)\left(J_1(\beta a)Y_1(\beta c)-J_1(\beta c)Y_1(\beta a)\right)\left(Y_1(\beta b)J_1(\beta c)-J_1(\beta b)Y_1(\beta c)\right)\end{array}\right)} \tag{3.115}$$

$$Z_b = \frac{\left(\frac{4jJ_1(\beta c)^2 Y_1(\beta b)\overline{Y}_r^{\,2} t_{total} a^2}{b\omega}\left(\frac{J_1(\beta b)Y_1(\beta c)}{J_1(\beta c)Y_1(\beta b)}-1\right)\left(\frac{\beta c J_0(\beta c)}{J_1(\beta c)}+\frac{\overline{P}}{\overline{Y}_r}-1\right)\right)}{\left(\begin{pmatrix}Y_1(\beta c)J_1(\beta b)\\ -J_1(\beta c)Y_1(\beta b)\end{pmatrix}(aJ_1(\beta a)-bJ_1(\beta b))\begin{pmatrix}\left(\overline{P}-\overline{Y}_r\right)\left(J_1(\beta b)Y_1(\beta c)-Y_1(\beta b)J_1(\beta c)\right)\\ +\overline{Y}_r\beta c\left(J_1(\beta b)Y_0(\beta c)-Y_1(\beta b)J_0(\beta c)\right)\end{pmatrix}\right)} \tag{3.116}$$

$$Z_c = \frac{\left(\frac{4jaJ_1(\beta c)^2 Y_1(\beta b)\overline{Y}_r^{\,2} t_{total}}{b\omega J_1(\beta a)}\left(\frac{J_1(\beta b)Y_1(\beta c)}{J_1(\beta c)Y_1(\beta b)}-1\right)\left(\frac{\beta c J_0(\beta c)}{J_1(\beta c)}+\frac{\overline{P}}{\overline{Y}_r}-1\right)\right)}{\left(\begin{pmatrix}\left(\overline{P}-\overline{Y}_r\right)\left(J_1(\beta b)Y_1(\beta c)-Y_1(\beta b)J_1(\beta c)\right)\\ +\overline{Y}_r\beta c\left(J_1(\beta b)Y_0(\beta c)-Y_1(\beta b)J_0(\beta c)\right)\end{pmatrix}\left(J_1(\beta c)Y_1(\beta b)-J_1(\beta b)Y_1(\beta c)\right)\right)} \tag{3.117}$$

Note that notation of the form $J_1(\beta c)^2$ should be taken to mean $(J_1(\beta c))^2$. Unlike the impedances in the T network representation, Z_a, Z_b, and Z_c in the π representation all become zero at the same frequencies, which are the short circuit resonant frequencies of the device (i.e. the frequencies at which the input impedance tends to zero when the output and tertiary terminals are short circuited). From the numerators of Z_a, Z_b, and Z_c, this occurs when

$$\frac{\beta c J_0(\beta c)}{J_1(\beta c)}+\overline{\sigma}-1=0 \tag{3.118}$$

where $\overline{\sigma}$ is the effective Poisson's ratio of the device

$$\overline{\sigma}=\frac{\overline{P}}{\overline{Y}_r}. \tag{3.119}$$

As expected, (3.118) demonstrates that the short circuit resonant frequencies are determined by the outer radius of the device, c. The impedances in the π representation are now represented using the first two terms of their Taylor series taken about the first short circuit resonant frequency. Let R be the first positive value of βc that satisfies (3.118). The first short circuit radial resonant frequency is thus

$$\omega_{rsc}=\frac{R\overline{v}_r}{c}. \tag{3.120}$$

Using only the first two terms of the Taylor series of Z_a, Z_b, and Z_c taken about the first short circuit radial resonant frequency,

$$Z_a \approx \frac{-4j\Delta\omega a c^2 t_{total}\overline{Y}_r J_1(R)\left(R^2+\overline{\sigma}^2-1\right)}{R^2\overline{v}_r{}^2\left(Y_1(R)(\overline{\sigma}-1)+RY_0(R)\right)J_1\left(\frac{Ra}{c}\right)\left(bJ_1\left(\frac{Rb}{c}\right)-aJ_1\left(\frac{Ra}{c}\right)\right)} \tag{3.121}$$

$$Z_b \approx \frac{-4j\Delta\omega a^2 c^2 t_{total}\overline{Y}_r J_1(R)\left(R^2+\overline{\sigma}^2-1\right)}{R^2\overline{v}_r{}^2 b\left(Y_1(R)(\overline{\sigma}-1)+RY_0(R)\right)J_1\left(\frac{Rb}{c}\right)\left(aJ_1\left(\frac{Ra}{c}\right)-bJ_1\left(\frac{Rb}{c}\right)\right)} \tag{3.122}$$

$$Z_c \approx \frac{4j\Delta\omega a c^2 t_{total}\overline{Y}_r J_1(R)\left(R^2+\overline{\sigma}^2-1\right)}{R^2\overline{v}_r{}^2 b\left(Y_1(R)(\overline{\sigma}-1)+RY_0(R)\right)J_1\left(\frac{Rb}{c}\right)J_1\left(\frac{Ra}{c}\right)}. \tag{3.123}$$

where $\Delta\omega = \omega - \omega_{rsc}$. Next, the network transformation from page 240 of [7] is applied to the circuit of Figure 3.18, resulting in the circuit of Figure 3.19, where

$$Z_R = Z_a + Z_c = \frac{4j\Delta\omega t_{total}\, a^2 c^2 \overline{Y}_r J_1(R)\left(R^2+\overline{\sigma}^2-1\right)}{R^2\overline{v}_r{}^2 b\left(RY_0(R)+Y_1(R)(\overline{\sigma}-1)\right)J_1\left(\frac{Rb}{c}\right)\left(aJ_1\left(\frac{Ra}{c}\right)-bJ_1\left(\frac{Rb}{c}\right)\right)} \tag{3.124}$$

$$N_\alpha = \frac{Z_a + Z_c}{Z_a} = \frac{aJ_1\left(\frac{Ra}{c}\right)}{bJ_1\left(\frac{Rb}{c}\right)} \tag{3.125}$$

$$Z_Q = \frac{Z_c(Z_a+Z_c)}{Z_a} = \frac{4j\Delta\omega t_{total}\, a^2 c^2 \overline{Y}_r J_1(R)\left(R^2+\overline{\sigma}^2-1\right)}{\overline{v}_r{}^2 R^2 b^2\left(Y_1(R)(\overline{\sigma}-1)+RY_0(R)\right)\left(J_1\left(\frac{Rb}{c}\right)\right)^2} \tag{3.126}$$

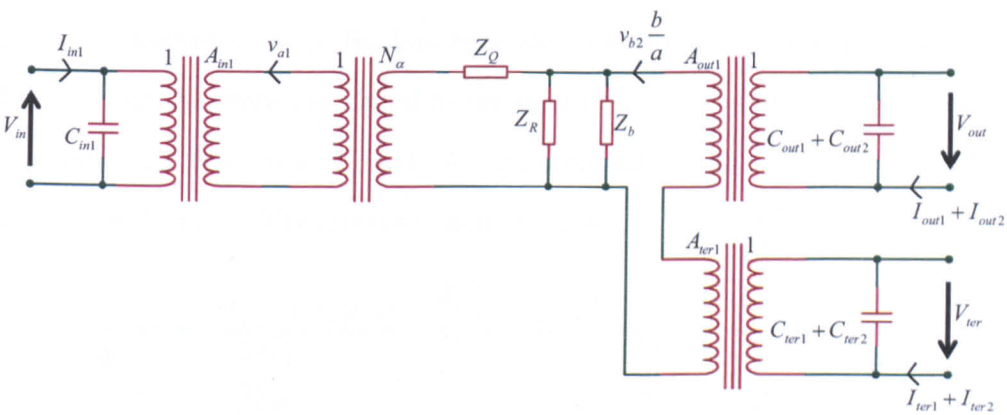

Figure 3.19: Radial mode Transoner PT equivalent circuit after the application of the network theorem from [7].

Since $Z_R + Z_b = 0$ and $Z_R Z_b \neq 0$, the parallel combination of Z_R and Z_b is an open circuit, i.e.

$$\frac{Z_R Z_b}{Z_R + Z_b} = \infty. \tag{3.127}$$

A similar self-cancelling was observed with the equivalent circuit impedances of a radial mode ring-dot filter in [8]. Combining the $1:A_{in1}$ and $1:N_\alpha$ turns ratios, the equivalent circuit becomes that shown in Figure 3.20.

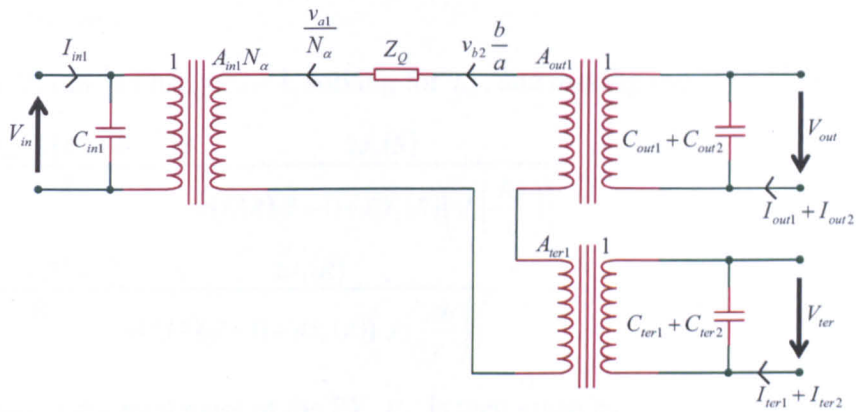

Figure 3.20: Equivalent circuit after noting that $Z_R // Z_b = \infty$.

At this point, the equivalent current through the remaining mechanical impedance is $v_{b2}(b/a)$. However, from a design perspective, it is useful to know what the maximum vibration velocity within the device is going to be. It will be shown later that when the radius of the larger set of electrodes is slightly smaller than the outer radius of the device, the maximum vibration velocity of the device is approximately the vibration velocity at $r = b$. Therefore it is convenient to make the tank current in the equivalent circuit v_{b2} instead of $v_{b2}(b/a)$. Back-to-back ideal transformers with turns ratios $1:(b/a)$ and $(b/a):1$ are therefore introduced to the right of Z_Q. Z_Q is then referred across the $1:(b/a)$ ratio, the ratios $1:A_{in1}N_\alpha$ and $1:(b/a)$ combined, and the ratio $(b/a):1$ combined into $A_{out1}:1$ and $A_{ter1}:1$. The resulting circuit is shown in Figure 3.21.

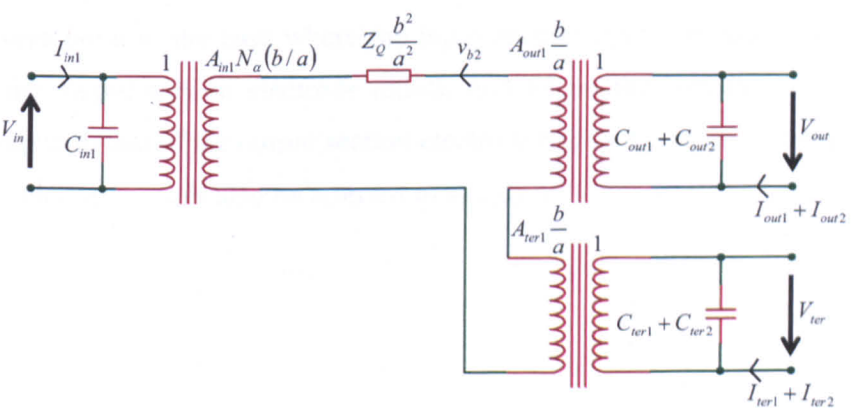

Figure 3.21: Radial mode Transoner PT equivalent circuit with the tank current scaled to v_b.

Finally, the remaining mechanical impedance is modelled with a series LC circuit. The first two terms in the Taylor series of the impedance of an LC circuit, taken about its resonant frequency $\omega_{rsc} = 1/(L_m C_m)$, are

$$Z_{L_m C_m} = 0 + 2jL_m \Delta\omega . \tag{3.128}$$

Equating (3.128) with $Z_Q(b^2/a^2)$, solving for L_m, and making use of (3.113)

$$\begin{aligned} L_m &= \frac{\pi c^2 t_{total} \bar{\rho}\left(R^2 + \bar{\sigma}^2 - 1\right)}{R^2} \frac{2J_1(R)}{\pi\left(Y_1(R)(\bar{\sigma} - 1) + RY_0(R)\right)\left(J_1\left(\frac{Rb}{c}\right)\right)^2} \\ &= Mass \frac{\left(R^2 + \bar{\sigma}^2 - 1\right)}{R^2} \frac{2J_1(R)}{\pi\left(Y_1(R)(\bar{\sigma} - 1) + RY_0(R)\right)\left(J_1\left(\frac{Rb}{c}\right)\right)^2} \end{aligned} \tag{3.129}$$

where $Mass$ is the total mass of the PT. C_m is then given by

$$C_m = \frac{1}{\omega_{rsc}{}^2 L_m} = \frac{1}{t_{total}\pi\bar{Y}_r\left(R^2 + \bar{\sigma}^2 - 1\right)} \frac{\pi\left(Y_1(R)(\bar{\sigma} - 1) + RY_0(R)\right)\left(J_1\left(\frac{Rb}{c}\right)\right)^2}{2J_1(R)} \tag{3.130}$$

and a mechanical loss resistance is introduced as

$$R_m = \frac{\omega_{rsc} L_m}{\bar{Q}_m} = \frac{\pi c t_{total} \bar{Y}_r\left(R^2 + \bar{\sigma}^2 - 1\right)}{\bar{Q}_m \bar{v}_r R} \frac{2J_1(R)}{\pi\left(Y_1(R)(\bar{\sigma} - 1) + RY_0(R)\right)\left(J_1\left(\frac{Rb}{c}\right)\right)^2} \tag{3.131}$$

where $\bar{Q}_m$ is the effective mechanical quality factor of the composite device.

A. Summary of the proposed lumped equivalent circuit model

The newly proposed lumped equivalent circuit model for the radial mode Transoner PT is shown in Figure 3.22 and summarised in (3.132) to (3.140). Note that (3.132) to (3.140) correspond to the case where the input section electrode radius is less than or equal to the output section electrode radius, and where the tertiary section electrode radius is equal to that of the output section electrode radius. From this point forward, the vibration velocity v_{b2} will also be referred to simply as v_b.

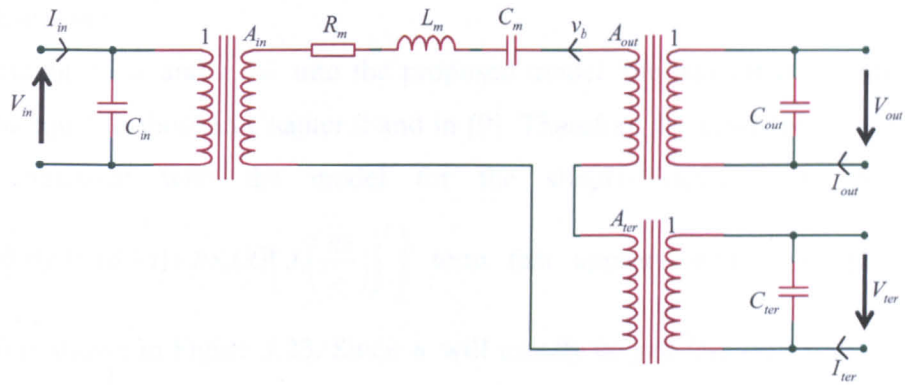

Figure 3.22: Lumped equivalent circuit for the radial mode Transoner PT with three sets of electrodes.

$$C_{in} = C_{in1} = \frac{\pi a^2 n_{in} \varepsilon_{33}^{T\,in}}{t_{in}}\left(1 - k_p^{\,in^2}\right) = \frac{\pi a^2 n_{in}^{\,2} \varepsilon_{33}^{T\,in}}{t_{in}^{total}}\left(1 - k_p^{\,in^2}\right) \tag{3.132}$$

$$C_{out} = C_{out1} + C_{out2} = \frac{\pi b^2 n_{out} \varepsilon_{33}^{T\,out}}{t_{out}}\left(1 - k_p^{\,out^2}\right) = \frac{\pi b^2 n_{out}^{\,2} \varepsilon_{33}^{T\,out}}{t_{out}^{total}}\left(1 - k_p^{\,out^2}\right) \tag{3.133}$$

$$C_{ter} = C_{ter1} + C_{ter2} = \frac{\pi b^2 n_{ter} \varepsilon_{33}^{T\,ter}}{t_{ter}}\left(1 - k_p^{\,ter^2}\right) = \frac{\pi b^2 n_{ter}^{\,2} \varepsilon_{33}^{T\,ter}}{t_{ter}^{total}}\left(1 - k_p^{\,ter^2}\right) \tag{3.134}$$

$$A_{in} = A_{in1} N_\alpha \frac{b}{a} = \frac{2\pi a n_{in} d_{31}^{\,in}}{s_{11}^{E\,in}\left(1 - \sigma_C^{E\,in}\right)} \frac{J_1\left(\frac{Ra}{c}\right)}{J_1\left(\frac{Rb}{c}\right)} \tag{3.135}$$

$$A_{out} = A_{out1} \frac{b}{a} = \frac{2\pi b n_{out} d_{31}^{\,out}}{s_{11}^{E\,out}\left(1 - \sigma_C^{E\,out}\right)} \tag{3.136}$$

$$A_{ter} = A_{ter1} \frac{b}{a} = \frac{2\pi b n_{ter} d_{31}^{\,ter}}{s_{11}^{E\,ter}\left(1 - \sigma_C^{E\,ter}\right)} \tag{3.137}$$

$$L_m = \frac{\pi c^2 t_{total} \overline{\rho}\left(R^2 + \overline{\sigma}^2 - 1\right)}{R^2} \frac{2J_1(R)}{\pi\left(Y_1(R)(\overline{\sigma} - 1) + RY_0(R)\right)\left(J_1\left(\frac{Rb}{c}\right)\right)^2} \tag{3.138}$$

$$C_m = \frac{1}{t_{total} \pi \overline{Y}_r \left(R^2 + \overline{\sigma}^2 - 1\right)} \frac{\pi\left(Y_1(R)(\overline{\sigma} - 1) + RY_0(R)\right)\left(J_1\left(\frac{Rb}{c}\right)\right)^2}{2J_1(R)} \tag{3.139}$$

$$R_m = \frac{\pi c t_{total} \overline{Y}_r \left(R^2 + \overline{\sigma}^2 - 1\right)}{\overline{Q}_m \overline{\upsilon}_r R} \frac{2J_1(R)}{\pi\left(Y_1(R)(\overline{\sigma} - 1) + RY_0(R)\right)\left(J_1\left(\frac{Rb}{c}\right)\right)^2} \tag{3.140}$$

where t_{in}^{total}, t_{out}^{total}, and t_{ter}^{total} are the total thicknesses of piezoelectrically active ceramic in the input, output and tertiary sections. Hence, $t_{in}^{total} = n_{in} t_{in}$, $t_{out}^{total} = n_{out} t_{out}$, and $t_{ter}^{total} = n_{ter} t_{ter}$.

B. Discussion

Substituting $b = a$ and $c = a$ into the proposed model, the equivalent circuit formulas become equal to those in Chapter 2 and in [9]. Therefore the newly proposed model is fully consistent with the model for the simpler devices. A plot of the $2J_1(R)/\left(\pi(Y_1(R)(\overline{\sigma}-1)+RY_0(R))\left(J_1\left(\frac{Rb}{c}\right)\right)^2\right)$ term that appears in (3.138), (3.139), and (3.140) is shown in Figure 3.23. Since b will usually be just less than c, it can be seen from this figure that the effect of this term on L_m, C_m, and R_m will usually be very small. However, if b is made much less than c, L_m will become extremely large whilst C_m will become commensurately small.

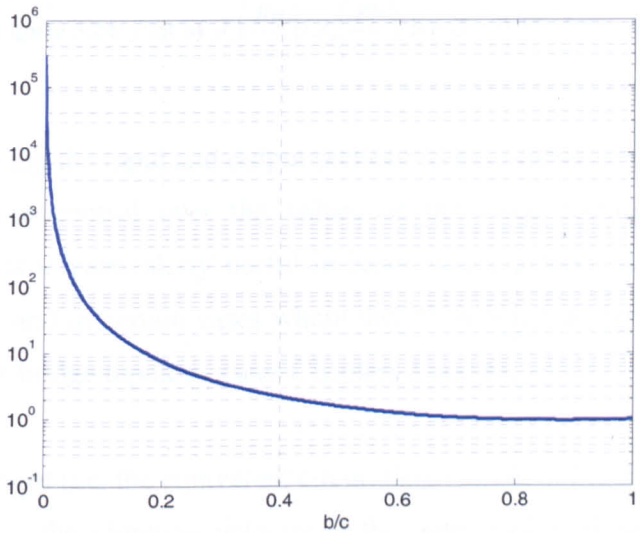

Figure 3.23: Plot of the function $2J_1(R)/\left(\pi(Y_1(R)(\overline{\sigma}-1)+RY_0(R))\left(J_1\left(\frac{Rb}{c}\right)\right)^2\right)$ **for** $\overline{\sigma} = 0.35$**. (For** $\overline{\sigma} = 0.35$**,** R **is** 2.0795**).**

From (3.132) to (3.137), the clamped capacitances are seen to remain in proportion to the square of the electrode radius, and the force factors that correspond to the sections with electrode radius b remain in proportion to the electrode radius. However, the force factor of the section with the smaller electrode radius becomes proportional to $J_1\left(\frac{Ra}{c}\right)/J_1\left(\frac{Rb}{c}\right)$. This function is plotted for the case where $b/c = 0.95$ (i.e. where b is slightly less than c) in Figure 3.24, and for the most part, its value is less than 1. Therefore if a is decreased whilst b and c remain constant, the force factor of this section will decrease with increasing rapidity. It will be shown in Chapter 6 that this function has important consequences for the design of PTs for inductor-less converters.

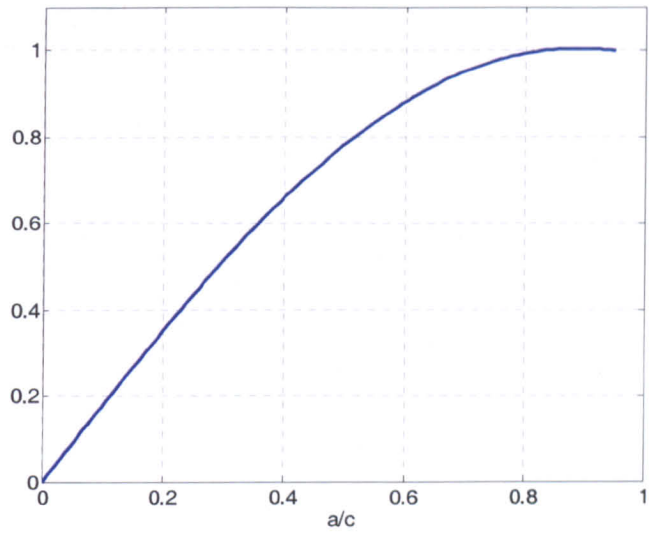

Figure 3.24: Plot of $J_1\left(\frac{Ra}{c}\right)/J_1\left(\frac{Rb}{c}\right)$ for $\overline{\sigma}=0.35$, $b/c=0.95$.

In practice, allowing the input and output sections to have different electrode radii gives the designer more control over the values of the force factors and the clamped capacitances. This is particularly useful in cases where a large step-up or step-down ratio is required, and in certain cases where the PT is being designed for use with the inductor-less half-bridge topology (sees Chapters 5 and 6).

The motional current (i.e. the equivalent circuit tank current in Figure 3.32) in the newly proposed model is the vibration velocity at the outer radius of the larger of the two electrode radii, instead of the vibration velocity at the outer radius of the device (as it was in the model described in Chapter 2). The relationship between v_{b3} and v_{c3} is obtained by substituting $F_{c3}=0$ into (3.89)

$$\frac{v_{c3}}{v_{b3}}=\frac{-Z_{m6}}{(Z_{m6}+Z_{m7})}=\frac{2\overline{Y}_{r3}}{\pi\left(\begin{array}{l}(\overline{P}_3-\overline{Y}_{r3})(J_1(\beta_3 c)Y_1(\beta_3 b)-Y_1(\beta_3 c)J_1(\beta_3 b))\\+\overline{Y}_{r3}\beta_3 c(Y_1(\beta_3 b)J_0(\beta_3 c)-J_1(\beta_3 b)Y_0(\beta_3 c))\end{array}\right)}. \tag{3.141}$$

After substituting (3.114) and $\overline{v}_r=c\omega_{rsc}/R$ (from (3.120)) into (3.141), and observing the approximations in (3.108) to (3.114), a plot of v_{c3}/v_{b3} against b/c for several values of ω/ω_{rsc} can be generated, as shown in Figure 3.25. Since b/c will usually be greater than 0.85, it can be seen from this figure that the difference between v_{b3} and v_{c3} will usually be negligible. Therefore a measurement of the vibration velocity at the outer

radius of the PT (taken with a laser vibrometer) should correspond very closely with the tank current in Figure 3.22.

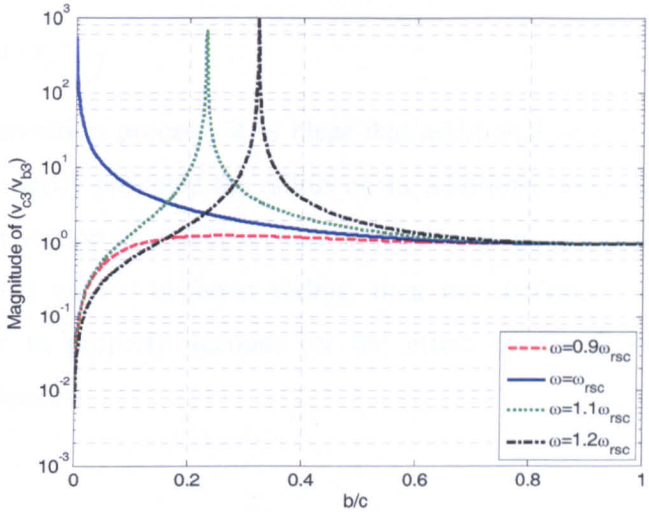

Figure 3.25: Magnitude of v_{c3}/v_{b3} against b/c for several ω/ω_{rsc}.

For the simpler case where the tertiary section layers are not present, the lumped equivalent circuit reduces to that shown in Figure 3.26, and the expressions in (3.132) to (3.140) apply. If the input section radius is made greater than or equal to the radius of the output section, then a becomes the radius of the output section electrodes, b becomes the radius of the input section electrodes, and the equivalent circuit formula are obtained by swapping all the "in" and "out" identifiers (both subscript and superscript) in (3.132) to (3.140).

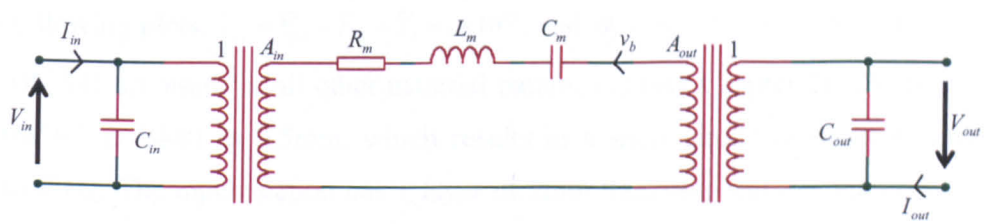

Figure 3.26: The lumped equivalent circuit for a radial mode Transoner PT with two sets of electrodes.

For the case where the radius of the tertiary section is made equal to the smaller of the other two electrode radii, the equivalent circuit remains as shown in Figure 3.22, but A_{ter} and C_{ter} become

$$A_{ter} = \frac{2\pi a n_{ter} d_{31}^{\ ter}}{s_{11}^{E\,ter}\left(1-\sigma_C^{E\,ter}\right)} \frac{J_1\left(\frac{Ra}{c}\right)}{J_1\left(\frac{Rb}{c}\right)} \tag{3.142}$$

$$C_{ter} = \frac{\pi a^2 n_{ter} \varepsilon_{33}^{T\,ter}}{t_{ter}}\left(1-k_p^{\ ter^2}\right). \tag{3.143}$$

Reviewing the derivation process, it is clear that additional sets of electrodes can be incorporated very easily provided the radius of the additional sets is equal to the radius of either the input section or output section electrodes. However, if an additional set of electrodes is added with a different radius, then the derivation would have to be repeated in order to properly account for the effect on the force factors and the mechanical impedances.

3.6 Comparison between the full and simplified equivalent circuits

In order to reduce the equivalent circuit representation of Figure 3.18 to the form shown in Figure 3.22, each of the mechanical impedances was represented by the first two terms of its Taylor series, taken about the first radial resonance, and then equated to a similar expansion of the impedance of a series LC combination. The effect of this simplification on the predicted input impedance, gain, and vibration velocity characteristics are now examined for a device which has an input section radius less than or equal to the output section radius (i.e. a corresponds to the input section radius, and b corresponds to the output section radius), and which has no tertiary section. In the following plots, $\bar{Y}_{r1} = \bar{Y}_{r2} = \bar{Y}_{r3} = \bar{Y}_r = 1\times10^{11}$, and $\bar{\sigma}_1 = \bar{\sigma}_2 = \bar{\sigma}_3 = \bar{\sigma} = 0.35$. The properties of APC841 are used for all other material parameters (see Chapter 2). The outer radius of the PT is taken as 9.5mm, which results in a short circuit resonant frequency of 129.24kHz. The input section has 1 layer of 2mm thickness and the output section has two layers, each of 1mm thickness. The output is terminated with a purely resistive load of $1/(\omega_{rsc} C_{out})$, where ω_{rsc} is the short circuit resonant frequency. The simulated characteristics of a device with 1) $a = b = c = 9.5$ mm, 2) $a = b = 9$ mm, $c = 9.5$ mm, 3) $a = 4$ mm, $b = 9$ mm, $c = 9.5$ mm, and 4) $a = 2$ mm, $b = 3$ mm, $c = 9.5$ mm are shown in Figures 3.27, 3.28, 3.29, and 3.30 respectively. The devices are assumed to be lossless.

Graphs a) and b) show the magnitude of the PT input impedance against frequency, and the magnitude of the ratio of the output voltage to input voltage against frequency,

respectively, when calculated using the full π network representation (i.e. (3.105) to (3.107)), the Taylor series approximations of the π network (i.e. (3.121) to (3.123)), and the lumped equivalent circuit. Note that the Taylor series approximation of the π network is not mathematically identical to the lumped equivalent circuit because only the first two terms of the Taylor series of the impedance of the series LC branch correspond; the LC branch impedance also has higher order Taylor series terms which are not present in the $Z_Q b^2/a^2$ impedance that results from the 2-term Taylor series approximation of the π network. The plots of graphs a) and b) were calculated using standard AC network analysis on the appropriate equivalent circuits. Graph c) shows the magnitude of v_{c3}/v_{b3} against frequency, which was calculated using (3.141). Graph d) shows the magnitude of v_{b2}/v_{a1} against frequency. For the plot that is based on the full π network, this was calculated using the magnitude of

$$\frac{v_{b2}}{v_{a1}} = \left(\frac{a}{b}\right) \frac{Z_a Z_b \left(j - R_L \omega (C_{out1} + C_{out2})\right)}{\begin{pmatrix} -Z_a Z_b R_L \omega (C_{out1} + C_{out2}) + jZ_a Z_b + jZ_a R_L A_{out1}{}^2 \\ -Z_c Z_b R_L \omega (C_{out1} + C_{out2}) + jZ_c Z_b + jR_L A_{out1}{}^2 (Z_b + Z_c) \end{pmatrix}} \tag{3.144}$$

(obtained from a version of Figure 3.18 that has been adapted for the case where there is no tertiary section). For the Taylor approximation of the π network and the lumped equivalent circuit plot, this was calculated using the magnitude of

$$\frac{v_{b2}}{v_{a1}} = \frac{a}{bM_a} = \frac{J_1\left(\frac{Rb}{c}\right)}{J_1\left(\frac{Ra}{c}\right)} \tag{3.145}$$

(obtained from an adapted version of Figure 3.21). Note that (3.144) is specific to the case where the output section electrode radius is greater than or equal to the input section electrode radius. Graphs e), f), and g) show the vibration velocities that occur for a 1V input voltage. These were calculated from the appropriate equivalent circuits using AC network analysis. Graph h) shows the magnitude of the vibration velocity as a function of the radial coordinate, normalised to the vibration velocity at $r = c$. This was calculated in a piecewise fashion. The vibration velocities at the region boundaries are known in terms of v_{c3} via (3.141), (3.144), and (3.102). The magnitude of the vibration velocity in region 3 can then be plotted using (3.99), (3.100), and (3.101), region 2 using (3.46), (3.49), and (3.50), and region 1 using (3.19), (3.20), and (3.21). The vibration velocity is plotted at the short circuit resonant frequency, the frequency of maximum gain, the capacitive frequency at which the gain drops by -3dB from the maximum, and the inductive frequencies at which the gain drops by -3dB and -10dB from the maximum. Note that the shape of the magnitude of the radial displacement

profile (i.e. $|\xi_r|$ against r) is identical to the shape of the vibration velocity profile because the magnitude of the radial velocity is simply a scaled version of the magnitude of the displacement (see (3.18) and (3.19), (3.43) and (3.46), (3.98) and (3.99)).

In Figure 3.27, where a=b=c=9.5mm, the gain, input impedance, and vibration velocity simulations from the lumped equivalent circuit and Taylor approximation of the π network are very close to those from the full π network. Figure 3.28 corresponds to the case of a typical co-fired or co-fired and bonded device where the electrode radii are equal to one another, and the outer radius is made slightly larger than the electrode radius. Here, the lumped equivalent circuit and Taylor approximation of the π network are shown to be in close agreement with the full π network representation, and the difference between v_{b3} and v_{c3} is extremely small. As the difference between input section and output section electrode radius is increased, the accuracy of the lumped equivalent circuit and the Taylor approximation of the π network begins to decrease. The case of a considerable difference in electrode radii is shown in Figure 3.29, and as expected, there is a large difference between v_{b2} and v_{a1}. From (3.145) and Figure 3.29d, it can be seen that the relationship between v_{b2} and v_{a1} becomes independent of frequency in the lumped equivalent circuit and Taylor representations. Whilst this is shown to be inaccurate, it is interesting to note from Figure 3.29e and Figure 3.29f that both representations still provide a good estimate of the absolute values of v_{a1} and v_{b2}. The dimensions used in the Figure 3.29 simulation are loosely based on a specification from industry.

Unlike the device dimensions used in the simulations for Figures 3.27 to 3.29, the dimensions used in the simulation for Figure 3.30 are not of practical interest because they would result in very low power density (see Section 3.7). However, it is shown to illustrate some interesting device behaviours and the limitations of the proposed lumped equivalent circuit model. In the simulation of Figure 3.30, the vast majority of the device consists of a non-piezoelectric ring. Whilst the gain and input impedance characteristics are reasonably well modelled by the lumped and Taylor equivalent circuits in the vicinity of resonance, the gain is shown to drop to zero at a particular frequency, and this behaviour is not modelled at all by the approximations. The frequency at which the gain drops to zero (149.55kHz) coincides with the point at which v_{b2} approaches zero, and conceptually this agrees with the schematic of Figure 3.22; if

the current v_{b2} is zero, there can be no output voltage (note that the load is purely resistive so there cannot be a resonance occurring between the clamped output capacitance and the load), and hence no gain. The device continues to vibrate at this frequency, however, the vibration velocity profile (shown in Figure 3.30h) is such that $v_{b2} = 0$, and this is caused by the impedances of the non-piezoelectric ring becoming such that $Z_{m5} + \frac{Z_{m6}Z_{m7}}{Z_{m6} + Z_{m7}} = \infty$ (see Figure 3.14 and Figure 3.15).

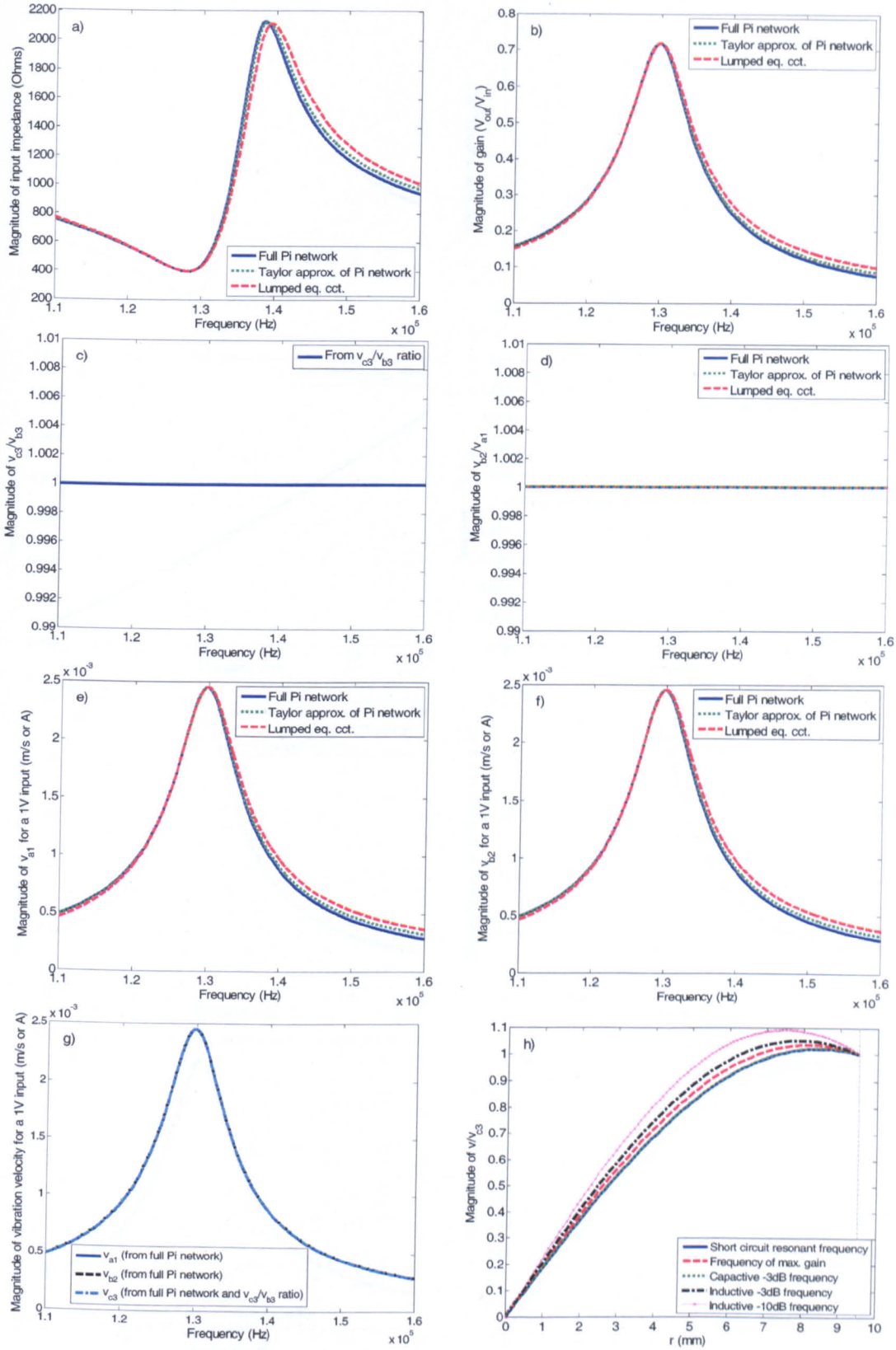

Figure 3.27: Simulated input impedance, gain, and vibration velocity characteristics of a PT with $a = b = c = 9.5$ mm.

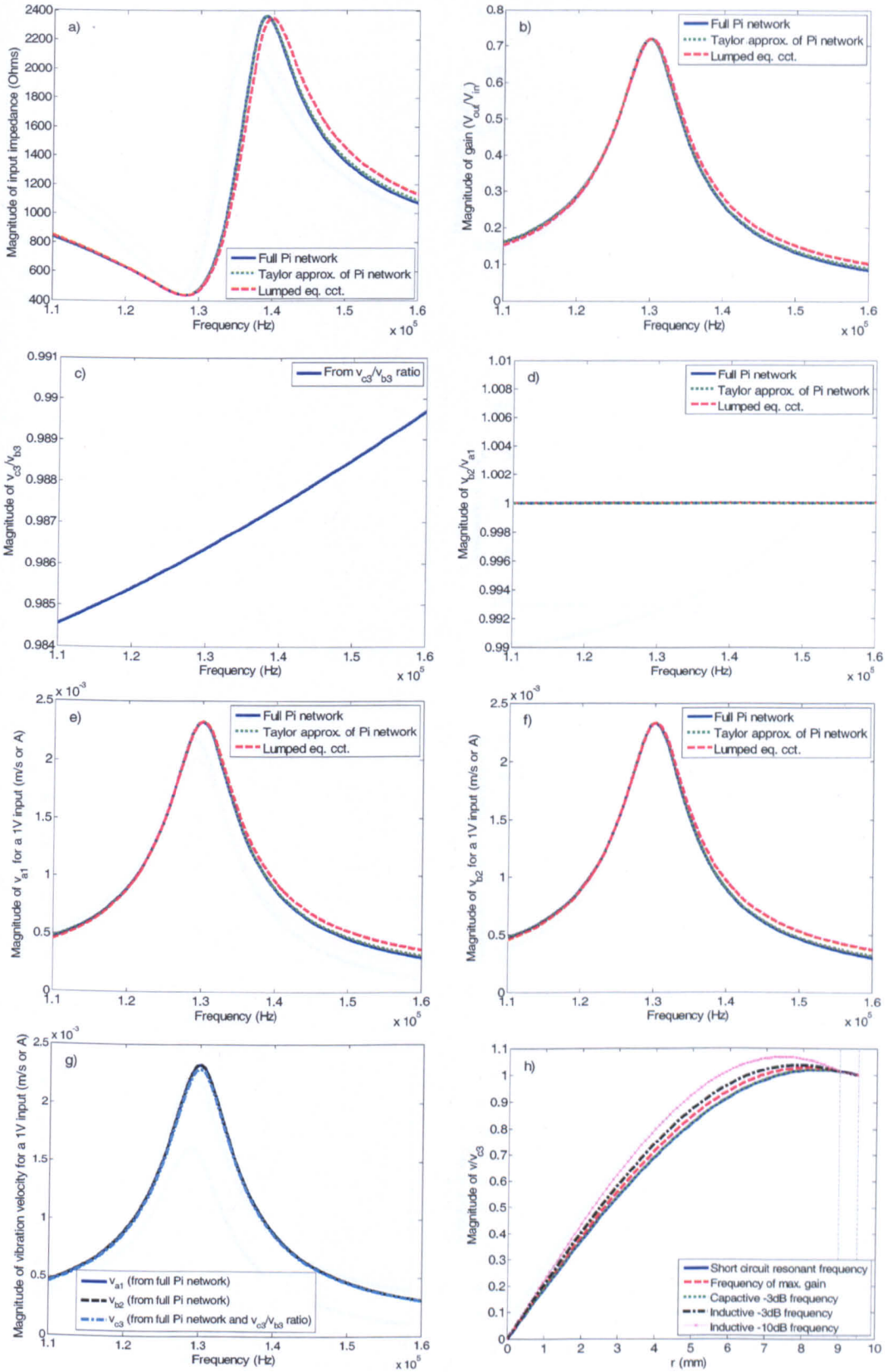

Figure 3.28: Simulated input impedance, gain, and vibration velocity characteristics of a PT with $a = b = 9$ mm, $c = 9.5$ mm.

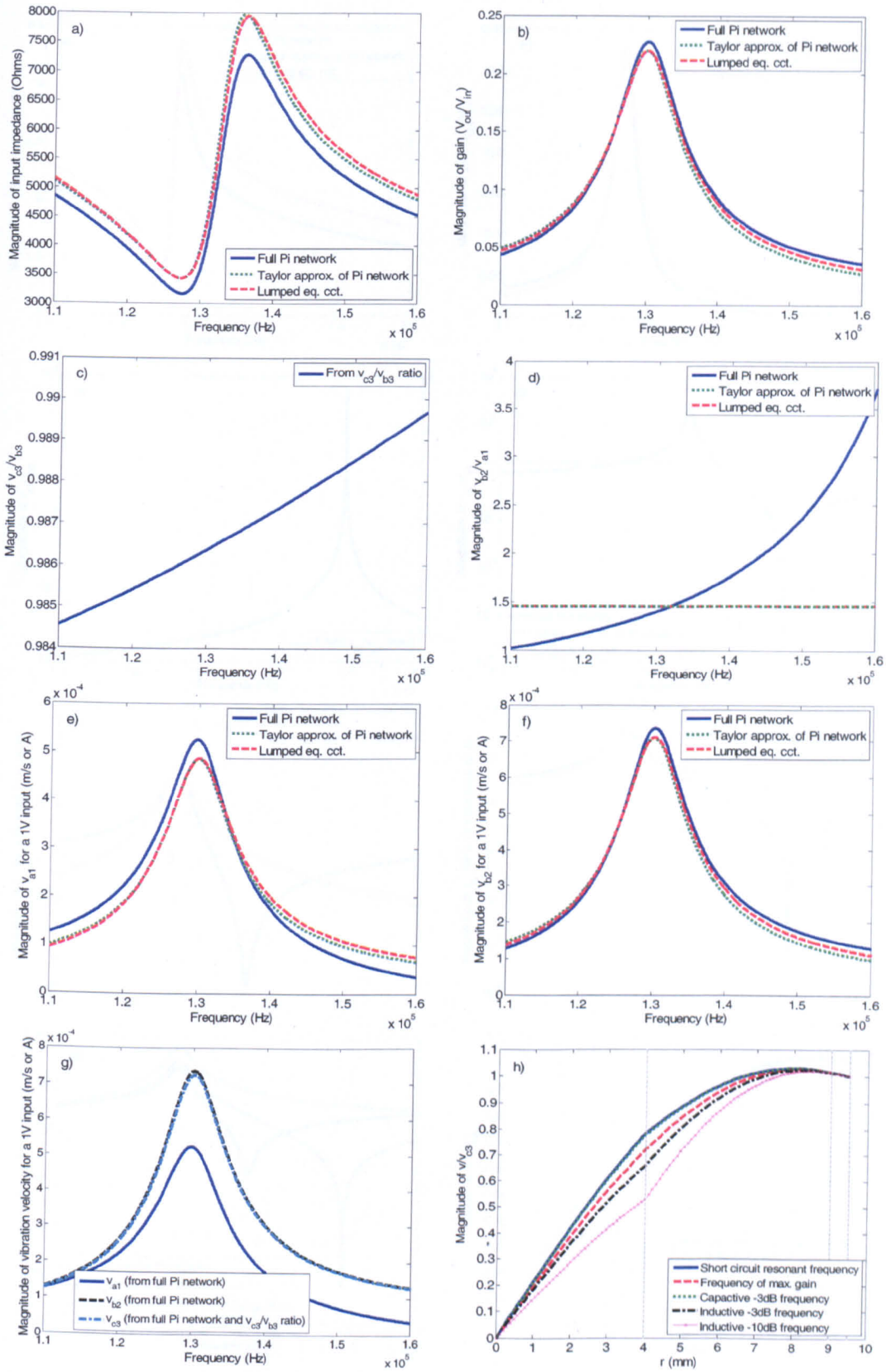

Figure 3.29: Simulated input impedance, gain, and vibration velocity characteristics of a PT with $a = 4$ mm, $b = 9$ mm, $c = 9.5$ mm.

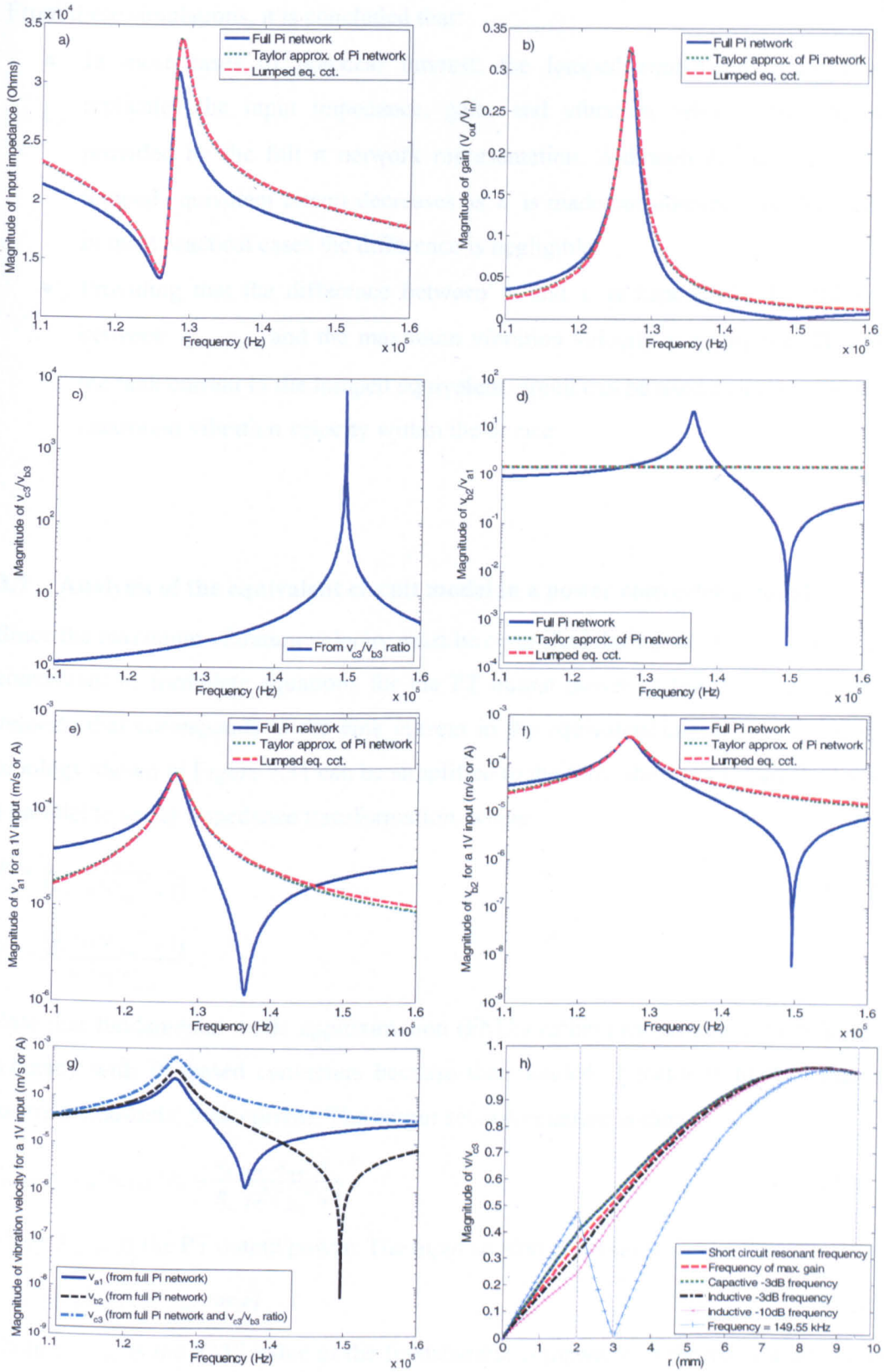

Figure 3.30: Simulated input impedance, gain, and vibration velocity characteristics of a PT with $a = 2$ mm, $b = 3$ mm, $c = 9.5$ mm.

From these simulations, it is concluded that:

- In most cases of practical interest, the lumped equivalent circuit closely replicates the input impedance, gain, and vibration velocity characteristics provided by the full π network representation. Although the accuracy of the lumped equivalent circuit decreases as a is made considerably smaller than b, in most practical cases the difference is negligible.
- Providing that the difference between b and c is kept small, the difference between v_{b3}, v_{c3}, and the maximum vibration velocity is negligible. Therefore the tank current in the lumped equivalent circuit can be used as a measure of the maximum vibration velocity within the device.

3.7 Analysis of the equivalent circuit model in a power converter context

Since the maximum vibration velocity must be controlled during the design of a PT, it is convenient to formulate equations for the PT output power in terms of the vibration velocity that corresponds to the tank current in the equivalent circuit. The AC-output topology shown in Figure 3.31 can be simplified to the form shown in Figure 3.32 using a parallel to series impedance transformation, where

$$R_s = \frac{R_L}{\left(R_L{}^2\omega^2 C_{out}{}^2 + 1\right)} \tag{3.146}$$

$$C_s = \frac{\left(R_L{}^2\omega^2 C_{out}{}^2 + 1\right)}{R_L{}^2\omega^2 C_{out}}. \tag{3.147}$$

Note that fundamental mode approximation (FMA) techniques provide a high level of accuracy with PT-based converters because their loaded Q factor is high enough to ensure a sinusoidal tank current. The output section equation is then

$$P_{out,PT} = A_{out}{}^2 v_{b,RMS}{}^2 R_s = \frac{v_{b,RMS}{}^2 A_{out}{}^2 R_L}{R_L{}^2\omega^2 C_{out}{}^2 + 1} \tag{3.148}$$

where $P_{out,PT}$ is the PT output power. The input section equation is

$$P_{in,PT} = |A_{in}| v^1_{Cin,RMS} v_{b,RMS} \cos(\phi) \tag{3.149}$$

where $v^1_{Cin,RMS}$ is the RMS value of the fundamental component of the voltage across the PT input capacitance, ϕ is the phase angle of the tank impedance (which is comprised of R_m, L_m, C_m, A_{out}, C_s, and R_s), and $P_{in,PT}$ is the input power to the PT. Note that the modulus sign is used in (3.149) because the force factors of a radial mode Transoner PT

are actually negative because d_{31} is usually treated as being a negative quantity (see the force factor formula (3.135), (3.136), and (3.137), and also in Chapter 2, and d_{31} in any piezoelectric material datasheet).

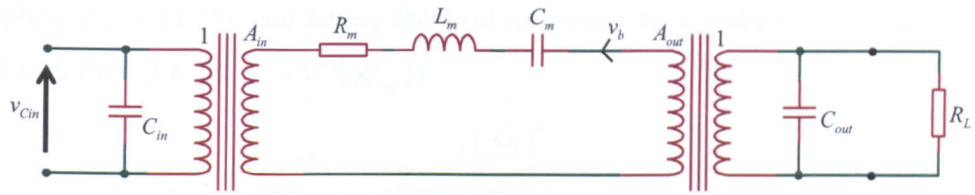

Figure 3.31: PT equivalent circuit as part of an AC-output converter.

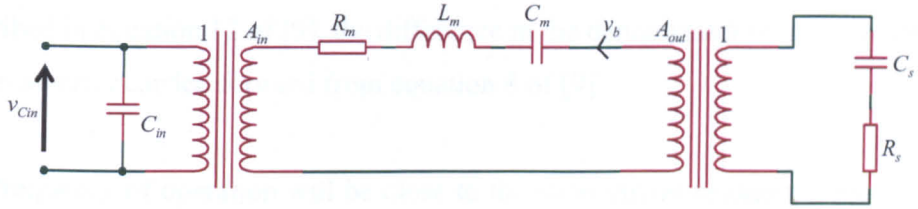

Figure 3.32: Simplified equivalent circuit for the AC-output topology.

A. The effect of the output section variables on output power

The variables that affect the power density of the output section are now examined. Whilst (3.133) and (3.136) could be substituted into (3.148), v_b would no longer correspond to the maximum vibration velocity in the device if the radius of the output section electrodes was made considerably smaller than the outer radius. Therefore we reverse the "in" and "out" sections in (3.132) to (3.140) and consider the case where the output section electrode radius is less than or equal to the input section electrode radius. Thus, b corresponds to the radius of the input section and a corresponds to the radius of the output section. The radius of the input section is then considered to be fixed and very close to c, meaning that v_b can be treated as the maximum vibration velocity in the device, regardless of the size of the output section electrodes. For this scenario, A_{out} and C_{out} become

$$C_{out} = \frac{\pi a^2 n_{out}{}^2 \varepsilon_{33}^{T\,out}}{t_{out}^{total}}\left(1 - k_p{}^{out\,2}\right) \tag{3.150}$$

$$A_{out} = \frac{2\pi a d_{31}^{\ out} n_{out}}{s_{11}^{E\,out}\left(1-\sigma_C^{E\,out}\right)} \frac{J_1\left(\frac{Ra}{c}\right)}{J_1\left(\frac{Rb}{c}\right)}. \tag{3.151}$$

Substituting (3.150) and (3.151) into (3.148), making use of the formula for planar coupling factor (3.75), and letting the load resistance be a multiple M of the matched load condition (i.e. let $R_L = M/(\omega C_{out})$)

$$P_{out,PT} = \frac{v_{b,RMS}^{\ 2} t_{out}^{total} \pi}{\omega s_{11}^{E\,out}\left(1-\sigma_C^{E\,out}\right)} \frac{k_p^{\ out\,2}}{\left(1-k_p^{\ out\,2}\right)} \frac{2M}{\left(M^2+1\right)} \frac{J_1\left(\frac{Ra}{c}\right)^2}{J_1\left(\frac{Rb}{c}\right)^2}. \tag{3.152}$$

For the case where $a = b = c$ and $M = 1$, (3.152) becomes very similar to the result described in equation 12 of [9]; the difference in the denominator terms is believed to be due to an error carried forward from equation 8 of [9].

The frequency of operation will be close to the short circuit resonant frequency, which in turn is inversely proportional to the outer radius of the device. Substituting $\omega = \omega_f \frac{R\overline{v}_r}{c}$ into (3.152)

$$P_{out,PT} = \frac{v_{b,RMS}^{\ 2} t_{out}^{total} \pi c}{\omega_f R \overline{v}_r s_{11}^{E\,out}\left(1-\sigma_C^{E\,out}\right)} \frac{k_p^{\ out\,2}}{\left(1-k_p^{\ out\,2}\right)} \frac{2M}{\left(M^2+1\right)} \frac{J_1\left(\frac{Ra}{c}\right)^2}{J_1\left(\frac{Rb}{c}\right)^2} \tag{3.153}$$

where ω_f is the ratio of the operating frequency to the short circuit resonant frequency, and will usually be around 1.05 to 1.1 when the PT is delivering full power. Neglecting the thickness of the electrodes in the output section, the volume of the output section is $\pi c^2 t_{out}^{total}$ (note that the region of non-piezoelectric ceramic that lies between the outer radius of the output section electrodes and the outer radius of the device is deemed to be included in this). The power density of the output section is therefore

$$P_{density\_output\_section} = \frac{P_{out,PT}}{\pi c^2 t_{out}^{total}} = \frac{v_{b,RMS}^{\ 2}}{\omega_f c R \overline{v}_r s_{11}^{E\,out}\left(1-\sigma_C^{E\,out}\right)} \frac{k_p^{\ out\,2}}{\left(1-k_p^{\ out\,2}\right)} \frac{2M}{\left(M^2+1\right)} \frac{J_1\left(\frac{Ra}{c}\right)^2}{J_1\left(\frac{Rb}{c}\right)^2}. \tag{3.154}$$

Like [9], it can be concluded from (3.154) that the power density of the output section (and therefore of the whole device, see later) is strongly dependent on the planar coupling factor of the output section $k_p^{\ out}$, and the vibration velocity v_b (which, when b is close to c, has been shown to be the maximum vibration velocity within the device).

Equation (3.154) indicates that power density is proportional to the square of the vibration velocity v_b. Hence, it is advantageous to use the largest value possible. However, as the maximum vibration velocity within a resonator increases, the temperature rises and the mechanical quality factor decreases (i.e. the losses increase) (see the discussion in Chapter 1 and [10-17]). Therefore the largest value of the maximum vibration velocity that occurs within the device that can be used is dictated by the need to ensure that the device remains thermally stable. The tendency for the temperature of a piezoelectric material to increase as vibration velocity increases is highly dependent on the composition of the material itself. Therefore considerable research has gone in to the development of materials that remain thermally stable at high vibration velocity. However, because the tendency for a PT to generate heat is governed by the nature of the piezoelectric material used within it, *and* the construction of the device (i.e. the bonding agents, the isolation layers, the number of internal electrode layers used, the ability of the PT to radiate heat (i.e. its surface area to volume ratio, the uniformity of the temperature distribution, whether in forced or natural convection), etc), the maximum vibration velocity that can be used in a particular PT is, at least to some extent, likely to be a function of both the piezoelectric material *and* the construction of the device itself. Hence, if a PT is badly constructed (e.g. with very thick layers of bonding agent), the maximum vibration velocity that can be used will be low, regardless of how good the piezoelectric material is. The maximum vibration velocity is a key PT design parameter [18] and is often treated as a figure of merit for piezoelectric materials [13].

As expected, (3.153) indicates that using a load resistance and output capacitance such that the matched load condition ($M = 1$) is observed in the vicinity of resonance will maximise the output power for a given vibration velocity. It will be shown in Chapter 4 that the maximum output power that can be obtained for a given vibration velocity is also highly dependent on the output topology (i.e. whether a simple resistive load as analysed here, or a rectifier of some description). Unless some form of additional matching network is used, the highest output power is always achieved with a simple resistive load.

Equation (3.154) suggests that the maximum power density is not dependent upon the number of layers. In general, increasing the number of layers within a piezoelectric

device decreases Q_m [19] and therefore increases heat generation. This is related back into (3.154) via the vibration velocity, because the lower $\overline{Q}_m$ means that a lower vibration velocity will result in the same amount of heat generation. However, increasing the number of electrodes within the device tends to increase thermal conduction, thereby allowing the generated heat to be dissipated more effectively. The overall relationship is therefore quite complicated and is affected by the thickness and composition of the electrode material. The number of layers required in the input section is dictated by the DC link voltage, the converter topology (with-inductor, inductor-less, or class-E), the tank impedance phase angle ϕ, the electrode and outer radii (a, b, and c), the maximum PT input power required, and the maximum vibration velocity. The number of layers required in the output section is dictated by the load resistance, the maximum output power required, the maximum vibration velocity, the electrode and outer radii (a, b, and c), the extent to which the output capacitance and load resistance are matched (or the output capacitance, rectifier and load resistance in the case of DC-output topologies), the output topology (AC-output or DC-output), and the choice of rectifier topology in the case of DC-output (see Chapter 4).

Since power density decreases as the outer radius is increased (see (3.154)), it would initially appear advantageous to make all radial mode Transoner PTs as thick as possible, so as to achieve the required output power whilst keeping the outer radius as small as possible. However, it should be remembered that the equivalent circuit model was derived under the assumption that the device is "thin" and that $T_z \approx 0$. As the ratio of the outer radius to total device thickness is decreased, this assumption becomes increasingly inaccurate, therefore there is no guarantee that making a PT very thick will always result in higher power density. The final limit will come from the need to keep the ratio of the radius to total thickness large enough to prevent interference between the first thickness and first radial vibration modes.

The appearance of c in the denominator of (3.154) succinctly demonstrates why a single PT will only ever be suitable for use in relatively low power, point-of-use applications. However, it also suggests that using many smaller PTs to achieve a particular converter specification may allow for very much higher power densities to be achieved. Of particular note is a 0.2W PT shown in [20] with a claimed power density of 250W/cm^3. Although there are likely to be considerable mounting and control issues

to overcome, not least the need to ensure equal power sharing between the devices, this is a good justification for research into multi-PT converter strategies.

The appearance of R in the denominator of (3.154) indicates the importance of operating at the first radial resonance. Operation at the second radial resonance would correspond to R being the second positive value of βc that satisfies (3.118), and would therefore decrease power density (for $\bar{\sigma} = 0.35$, the first and second positive values of R that satisfy (3.118) are 2.0795 and 5.3989 respectively). Operating at the second resonance also presents other difficulties, such as the need for a larger outer radius to total device thickness ratio in order to prevent interference from the thickness vibration mode, which in turn will result in a larger c and hence lower power density.

Finally, the effect of the electrode radii is considered. The function $J_1\left(\frac{Ra}{c}\right)^2 / J_1\left(\frac{Rb}{c}\right)^2$ is plotted in Figure 3.33 for the case where $\bar{\sigma} = 0.35$ and $b = 0.95c$. Whilst a very small increase in power density can be achieved by making $a = 0.88c$ compared to $a = b = 0.95c$, the overall trend is for power density to decrease as a/c is decreased. Thus, it is concluded that to maximise power density, the output section electrode radius should be kept close to the outer radius of the device.

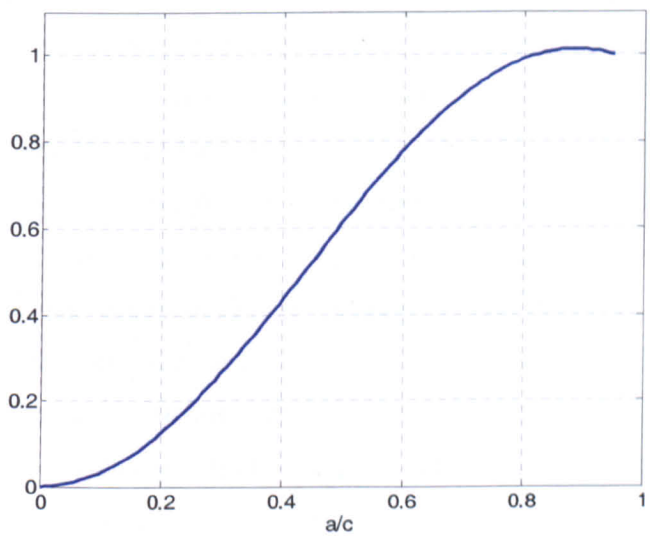

Figure 3.33: Plot of $J_1\left(\frac{Ra}{c}\right)^2 / J_1\left(\frac{Rb}{c}\right)^2$ for $\bar{\sigma} = 0.35$ (i.e. $R = 2.0795$) and $b = 0.95c$. The peak value is 1.0128 at a/c=0.883.

B. The effect of the input section variables on output power

Here, it is most convenient to consider the case where the input section electrodes are less than or equal to the radius of the output section electrodes, and the output section electrodes are close to the outer radius of the device. Substituting (3.135) into (3.149) and assuming high efficiency operation ($P_{out,PT} \approx P_{in,PT}$)

$$P_{out,PT} = \frac{2\pi a d_{31}^{\ in} n_{in}}{s_{11}^{E\,in}\left(1-\sigma_C^{E\,in}\right)} \frac{J_1\left(\frac{Ra}{c}\right)}{J_1\left(\frac{Rb}{c}\right)} v_{Cin,RMS}^{1} v_{b,RMS} \cos(\phi). \tag{3.155}$$

However, this shows only a dependence on the electrode radii and the outer radius of the device, not on the total thickness of the input section. Therefore the equivalent circuit model provides no direct relationship between the volume of the input section (defined as $\pi c^2 t_{in}^{total}$, neglecting the thickness of the electrodes) and the maximum output power of the PT. Crucially though, the equivalent circuit models were derived on the assumption of constant radial strain in the thickness direction; therefore the equivalent circuit formulas are only valid when this assumption is valid. In reality, if the input section is made too small in comparison to the rest of the device, then it will not be able to induce a radial vibration in the output section, and no output will be obtained. For the same reason, if the feedback layer (which is proportionally very small) in a piezoelectric device is connected to an impedance analyser, the response is often simply a flat line. Therefore it is incumbent on the PT designer to ensure that the input section is large enough in comparison to the rest of the device for a radial strain to be properly and efficiently induced in the output section. Identifying the point at which further reductions in input section size have a detrimental impact on the overall power density of a device is not straightforward because the degradation will initially be a gradual process, and will be seen as a reduction in the maximum output power that can be obtained for a particular temperature rise – something that is not easy to predict from analytical or finite element simulations. One strategy that can help obtain a more uniform strain profile in the thickness direction is to split the input (or output) section into two parts and sandwich the output (or input) section between them. This also helps to suppress bending modes (which can cause interference with the desired radial mode).

For the case where $a = b = c$, the total input section thickness must therefore be at least a certain minimum size compared to the total thickness of the rest of the device. However, once this condition is met, (3.153) and (3.155) suggest that it is highly unlikely that any further increase in maximum output power will be achieved by making further increases

in the input section thickness. Considering devices that were optimized for the with-inductor topology, where no stipulation is placed on the total input section thickness by the need to keep C_{in} small enough to achieve inductor-less ZVS, it is likely that this point is reached when the total thickness of the input section is somewhat smaller than the total thickness of the rest of the device. For example, the ratio of the total input section thickness to the thickness of the rest of the device is just 0.66 in the T1-15W devices.

When the input section electrode radius is made smaller than the outer radius, the required input section thickness relative to the rest of the device is likely to change. That is, for a given set of output section dimensions and a given outer radius, it is likely that the minimum thickness of input section that is required to efficiently induce a radial vibration in the output section will increase as the radius of the input section electrodes is decreased. Thus, for a given outer radius, reducing the input section electrode radius will increase the total volume of input section ($\pi c^2 t_{in}^{total}$) required to properly establish a radial vibration in the output section, and will therefore decrease the overall power density of the device.

C. Summary of the design choices that will maximise overall PT power density

Guidelines for maximising the power density of a radial mode Transoner PT are summarised below. It should be noted that no consideration is given to the need to meet topology-specific requirements (such as a low enough C_{in} for ZVS in the case of the inductor-less topology) or the need to meet a particular converter specification (such as a specific output power, input voltage, load resistance, etc); this list is purely for obtaining maximum power density when driving the PT with a sinusoidal AC-input.

- The input and output section electrode radii should be equal to one another and as close to the outer radius as possible.
- The outer radius should be kept relatively small (i.e. the ratio c/t_{total} should be large enough to avoid interference from the thickness mode, but not so large that power density is unnecessarily compromised, see (3.154)).
- The input section should be made just large enough to efficiently induce a radial vibration in the output section.

- The AC-output topology should be used, and the load resistance and output capacitance should be such that the matched load condition $(M = 1)$ is observed in the vicinity of resonance (see Chapter 4).
- A piezoelectric material that has high k_p, high Q_m, and is capable of operating at high vibration velocities in a thermally stable manner, should be used.
- Piezoelectrically inactive layers should be kept to a minimum.

3.8 Practical design considerations that affect power density

The converter topology, converter specification, and externally imposed dimension restrictions can often require design choices to be made that compromise PT power density. A discussion of why the with-inductor topology is largely able to avoid such compromises is presented here. The inductor-less topology is discussed in Chapters 5 and 6.

A. Half-bridge with-inductor topology

The half-bridge with-inductor topology is shown with the full PT lumped equivalent circuit in Figure 3.34. Generally, when designing a PT for the with-inductor topology, the size of the input capacitance does not need to be controlled. As the total input section thickness is decreased (which does not affect A_{in}), the input capacitance increases. This usually results in a smaller external inductor being required, which is advantageous. Furthermore, achieving ZVS with this topology is not usually difficult, particularly if MOSFETs with a low output capacitance are used. Therefore the main concern with the input section of a with-inductor device is achieving the required A_{in} and ensuring that a radial vibration is efficiently induced in the output section.

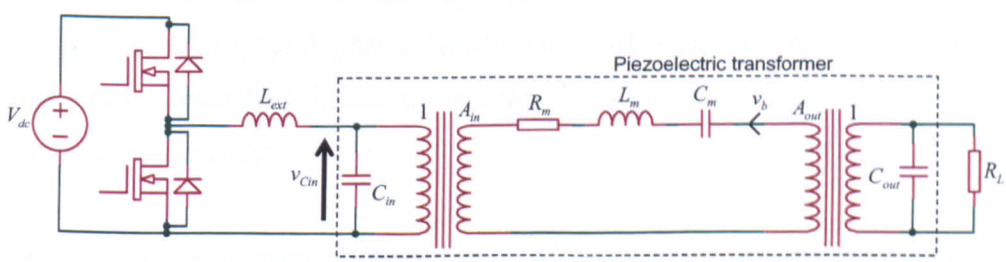

Figure 3.34: The half-bridge with-inductor PT-based topology.

Consider (3.149) and Figure 3.34. Assume high efficiency operation ($P_{out,PT} \approx P_{in,PT}$), and assume that the maximum vibration velocity that can be used has been determined. The value of $v^1_{Cin,RMS}$ will depend upon the $L_{ext}C_{in}$ filter, the resonant tank (including the load), the DC link voltage, and the operating frequency. However, regardless of its value, it can be seen that once the maximum input power and maximum permissible $v_{b,RMS}$ are specified, there are still two variables in (3.149) that are left unspecified, ϕ and A_{in}. Therefore the required value of A_{in} can be adjusted by changing the value of ϕ at which maximum power is to be delivered. This is extremely useful because it means that, regardless of the required converter specification, A_{in} can be sized such that the input section electrode radius is approximately equal to the outer radius of the PT. Furthermore, since there is no stipulation on the size of C_{in}, the total thickness of the input section can then be chosen such that it is just large enough to efficiently induce a radial vibration in the output section, thereby maximising the power density of the device. Some researchers have stated that designing a conventional converter to deliver its rated power at a power factor well below unity should be avoided because it increases the currents, voltages, and losses within the converter (see Chapter 3 of [21]). However, such arguments are less valid for PT-based converters because of the two force factors and the desire to use the largest vibration velocity possible in order to reduce the output section (and by extension, the input section) volume. Furthermore, it is shown in Chapter 4 that maximum PT efficiency is actually achieved above resonance, and remains high as the phase angle of the tank is increased and the input voltage is increased so as to maintain constant output power. Therefore the conclusion for with-inductor PT design is that, regardless of the converter specification, the radius of the input section electrodes should be made approximately equal to the outer radius, and the total input section thickness should be made just large enough to properly induce a radial vibration in the output section. Virtually all converter specifications should still be achievable with these stipulations because the phase angle can be used to provide the required extra degree of freedom in (3.149), and the input capacitance does not need to be controlled. In short, the designer is free to design the input section to maximise power density.

Since an optimal input section design can be achieved regardless of the outer radius, the designer is free to choose the outer radius to suit the output section. The only caveat

being the need for the ratio of the outer radius to the total device thickness to be large enough to prevent interference from the first thickness mode. Therefore the outer radius can be made just larger than the output section electrode radius. The output section electrode radius and the total thickness of the output section can then be set to obtain the required output power (see (3.153)), and to ensure the required A_{out} and C_{out} can be achieved with an integer number of output section layers. Because any converter specification can be achieved with an equal input and output section electrode radius, and the input section thickness need only be large enough to efficiently induce a vibration in the output section, it is concluded that the requirements of the with-inductor topology do not compromise PT power density.

B. Externally imposed restrictions on device dimensions

To maximise the overall power density of the converter, it is important that no single component is considerably taller than the others because that component will end up defining the overall form factor of the converter. Therefore a converter manufacturer will often specify a maximum total thickness for the PT. Ideally (from a PT power density perspective), the rest of the converter and its layout should be designed around the PT, rather than the other way around. Nevertheless, it is common for a maximum thickness to be specified, and the impact this has on PT power density depends on the converter topology.

In the case of a with-inductor design, specifying a restrictive maximum total thickness means that a larger radius must be used to obtain the required power level (see (3.153), remembering that enough space must be left for the input section to be large enough to efficiently induce a radial vibration in the output section). The use of a larger radius decreases power density as indicated by the presence of c in the denominator of (3.154). However, there is no further penalty involved because an optimally designed input section where the electrode radius is approximately equal to the outer radius can always be achieved with this topology, regardless of the required converter specification. The effect of dimension restrictions on the inductor-less topology can be more severe, and will be discussed further in Chapter 6.

3.9 The centre-tapped rectifier problem

A conventional resonant converter will often incorporate a (magnetic) transformer with two (approximately) identical output windings. This allows a centre-tapped rectifier configuration to be used [22]. Compared to a full-bridge or half-wave configuration, the centre-tapped rectifier has a higher efficiency, particularly in converters with a low output voltage [22].

The connection of a capacitively smoothed centre-tapped rectifier to the lumped equivalent circuit from Section 3.5 can be modelled as shown in Figure 3.35. If the rectifier is working, the currents through the diodes will have a DC component (i.e. a non-zero average value). The current through the resonant tank of a PT is sinusoidal because of its high Q factor, and cannot have a DC component because of the blocking action of the series tank capacitance (C_m in Figure 3.22). Furthermore, the capacitances C_{out} and C_{ter} present an open circuit to DC. Consider the node marked 'A'. Since $i_1 + i_2 + i_3 = 0$, it is therefore apparent that no mechanism exists to allow for a DC component to be present on the currents through the rectifier diodes. Hence in practice, the tank current flows only through the capacitances C_{out} and C_{ter}, the rectifier diodes do not conduct, and no output voltage is obtained. If inductors were placed in parallel with C_{out} and C_{ter}, then a path for the DC component is created and the rectifier would work. However, this will increase the cost and size of the converter, and these additional inductors are not required if a magnetic transformer is used instead (due to the magnetising inductance). If a centre-tapped approach is being considered for a PT-based converter, then the current doubler configuration should also be considered because it requires a similar component count.

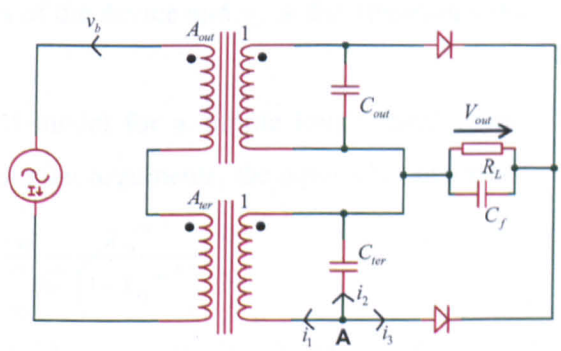

Figure 3.35: Equivalent circuit model of a PT connected to a capacitively smoothed centre-tapped rectifier configuration. The PT would be designed such that A_{out}=A_{ter} and C_{out}=C_{ter}.

Because the force factor ratios in the PT equivalent circuit have no parasitic parallel inductance, there is the possibility of using some rectifier topologies that are not suitable for use with a conventional transformer, such as that proposed in Figure 3.36. The advantage of this rectifier is that only 1 diode is required, the average current through which is equal to the load current. The down-side is that, unlike the centre-tapped rectifier, only an inductively smoothed version is possible. This rectifier could only be implemented with a conventional transformer by placing an additional DC-blocking capacitor between the transformer and the rectifier to prevent the magnetising inductance short-circuiting the DC component of the current that has to flow through the diode.

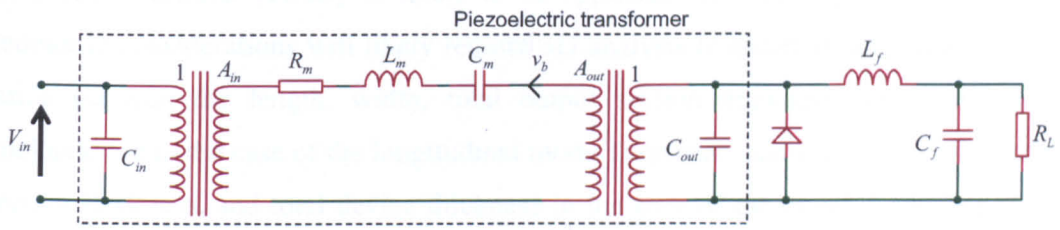

Figure 3.36: Rectifier topology that relies on there being no inductance in parallel with the rectifier input.

3.10 Comparison between radial and longitudinal Transoner PTs

In the case of a simple radial mode Transoner of the type discussed in Chapter 2 operating in the AC-output topology with a matched load, (3.154) becomes

$$P_{density\_output\_section} = \frac{v_{a,RMS}^{\ 2}}{\omega_f a R \overline{\upsilon}_r s_{11}^{E\,out}\left(1-\sigma_C^{E\,out}\right)} \frac{k_p^{\ out\,2}}{\left(1-k_p^{\ out\,2}\right)} \tag{3.156}$$

where a is the radius of the device and v_a is the vibration velocity at the outer radius.

An equivalent circuit model for a simple longitudinal mode Transoner is derived in Appendix A. Using similar arguments, the equivalent expression to (3.156) is

$$P_{density\_output\_section} = \frac{2v_{1,RMS}^{\ 2}}{l\omega_f s_{11}^{E\,out}\pi\overline{\upsilon}_l} \frac{k_{31}^{\ out\,2}}{\left(1-k_{31}^{\ out\,2}\right)}. \tag{3.157}$$

v_1 is the longitudinal vibration velocity at either end of the device, which is also the maximum vibration velocity that occurs anywhere within the device. $\overline{\upsilon}_l$ is the effective longitudinal speed of sound, and l is the length of the device. Note that just as the

power density of a radial mode Transoner is predicted to decrease with increasing radius, the power density of a longitudinal Transoner is predicted to decrease with increasing length.

The factor $k_p^{out\,2}/\left(1-k_p^{out\,2}\right)$ is much larger than $k_{31}^{out\,2}/\left(1-k_{31}^{out\,2}\right)$ for most piezoelectric ceramics that are suitable for use in PTs (typically around 4 times larger). However, it can also be seen that there are other differences between (3.156) and (3.157). Furthermore, there are many other factors to consider when trying to compare the power densities, including geometric considerations, the size of input section required to efficiently establish a vibration in the output section, and whether the same value of maximum vibration velocity is likely to be applicable to both types of device. The geometric considerations will likely require 3D analysis to ascertain what the optimum ratios between the length, width, total output section thickness, and total device thickness are in the case of the longitudinal mode Transoner, and the radius, total output section thickness, and total device thickness in the case of the radial mode Transoner. Thus, although the models presented here provide a starting point, a detailed comparison of power density it not made here. The purpose of this section is to show the form that the dependence on the appropriate coupling factor takes in each case, and to show that, whilst radial mode Transoner PTs do tend to achieve higher power densities than longitudinal mode Transoner PTs, there are several other factors at play besides the obvious numerical difference in the applicable coupling factors.

3.11 Summary

A new equivalent circuit model for the disc-shaped radial mode Transoner PT has been presented. Unlike previous models, this incorporates many of the features that are currently found in commercially produced radial mode Transoner PTs, such as unequal electrode radius in the input and output sections, an outer radius that extends past the electrode radii, and multiple sets of electrodes that are of the same radius. A lumped element representation has been given, and has been shown to provide a good approximation to the 'full' model, though it was also shown that the accuracy does start to decrease if one set of electrodes is made considerably larger in radius than the other, or if the radius of the non-piezoelectric ring section is made much larger than the electrode radii. Since the maximum vibration velocity was shown to occur near the

outer radius of the device, only the final lumped equivalent circuit representation need be considered during the design phase if one of the sets of electrodes extends close to the outer radius.

Unfortunately, the cost of producing a one-off co-fired PT meant that the new model could not be verified experimentally. It is hoped, however, that the new model will allow those within the PT industry to better predict the effects of their design choices, and as a consequence, maximise the power density of their designs.

3.12 References

[1] S. Nittayarumphong, F. Bisogno, M. Radecker, A. V. Carazo, A. Riedlhammer, and H. Guldner, "High efficiency control methods for class-E resonant converter for step-down applications using Piezoelectric Transformers (PT)," presented at European Conference on Power Electronics and Applications, 2007.

[2] H. W. Katz, *Solid State Magnetic and Dielectric Devices*: John Wiley & Sons, Inc. New York, 1959.

[3] C. A. Rosen, "Ceramic Transformers and Filters," *Proceedings of the Electronic Components Symposium (1956)*, pp. 205-211, 1956.

[4] C. A. Rosen, "Analysis and design of ceramic transformers and filter elements," PhD thesis, Syracuse University, USA, 1956.

[5] S. Lin, "Study on the radial composite piezoelectric ceramic transducer in radial vibration," *Ultrasonics*, vol. 46, pp. 51-59, 2007.

[6] S. Lin, "Radial vibration of the combination of a piezoelectric ceramic disk and a circular metal ring," *Smart Materials and Structures*, vol. 16, pp. 469-476, 2007.

[7] D. A. Berlincourt, D. R. Curran, and H. Jaffe, "Piezoelectric and Piezomagnetic Materials and Their Function in Transducers," in *Physical Acoustics: Principles and Methods*, vol. I part A, W. P. Mason, Ed.: Academic Press, New York, 1964.

[8] E. C. Munk, "The Equivalent Electrical Circuit For Radial Modes Of A Piezoelectric Ceramic Disc With Concentric Electrodes," *Philips Research Reports*, vol. 20, pp. 170-189, 1965.

[9] M. Yamamoto, Y. Sasaki, A. Ochi, T. Inoue, and S. Hamamura, "Step-Down Piezoelectric Transformer for AC-DC Converters," *Japanese Journal of Applied Physics, Part 1*, vol. 40, pp. 3637-3642, 2001.

[10] M. Umeda, S. Takahashi, Y. Sasaki, K. Nakamura, and S. Ueha, "Vibration stress and temperature dependence of piezoelectric resonators with lead-zirconate-titanate ceramics," *Electronics and Communications in Japan, Part II: Electronics*, vol. 83, pp. 1-7, 2000.

[11] S. Takahashi, M. Yamamoto, and Y. Sasaki, "Nonlinear Piezoelectric Effect in Ferroelectric Ceramics," *Japanese Journal of Applied Physics, Part 1*, vol. 37, pp. 5292-5296, 1998.

[12] K. Uchino, A. Joshi, Y.-H. Chen, and Yoshikawa, "High Power Characterization of Piezoelectric Materials," *Journal of Electroceramics*, vol. 2, pp. 33-40, 1998.

[13] K. Uchino, "High Power Piezoelectrics," in *Advanced Piezoelectric Materials: Science and Technology*, K. Uchino, Ed.: Woodhead Publishing Ltd, 2010.

[14] M. Katsuno, Y. Fuda, and M. Tamura, "High-Power Ceramic Materials for Piezoelectric Transformers," *Electronics and Communications in Japan, Part 3*, vol. 82, pp. 86-92, 1999.

[15] S. Hirose, S. Takahashi, M. Aoyagi, and Y. Tomikawa, "High-Power Characteristics of Piezoelectric Materials," presented at Ninth IEEE International Symposium on Applications of Ferroelectrics, 1995.

[16] S. Takahashi and S. Hirose, "Vibration-Level Characteristics for Iron-Doped Lead-Zirconate-Titanate Ceramic," *Japanese Journal of Applied Physics, Part 1*, vol. 32, pp. 2422-2425, 1993.

[17] S. Takahashi and S. Hirose, "Vibration-Level Characteristics of Lead-Zirconate-Titanate Ceramics," *Japanese Journal of Applied Physics, Part 1*, vol. 31, pp. 3055-3057, 1992.

[18] A. V. Carazo, "Piezoelectric Converters for DC/DC and AC/DC applications," presented at Portable Power Developer's Conference, 2005.

[19] Y. Sasaki, M. Umeda, S. Takahashi, M. Yamamoto, A. Ochi, and T. Inoue, "High-power Characteristics of Multilayer Piezoelectric Ceramic Transducers," *Japanese Journal of Applied Physics, Part 1*, vol. 40, 2001.

[20] I. Kartashev, T. Vontz, and H. Florian, "Regimes of piezoelectric transformer operation," *Measurement Science and Technology*, vol. 17, pp. 2150-2158, 2006.

[21] A. J. Gilbert, "Analysis, Design and Control of LCC Resonant Power Converters," PhD thesis, The University of Sheffield, UK, 2007.

[22] M. K. Kazimierczuk and D. Czarkowski, *Resonant Power Converters*: John Wiley & Sons Inc, 1995.

Chapter 4 - Effect of the output topology on PT power density

4.1 Introduction

To date, relatively few publications have considered the effect of the output topology (i.e. whether AC-output or a rectifier of some description) on PT power density.

A comparison of the current doubler and voltage doubler (referred to here as the half-wave capacitively smoothed) rectifiers was made in [1, 2]. However, it is the present author's opinion that the model for the current doubler rectifier used in [1, 2] is not correct. It is stated on page 1449 of [1] that the current doubler can result in the effective capacitance at the PT output becoming less than the PT's clamped output capacitance, thereby indicating that the current doubler can appear inductive-resistive to the PT. When the present author adapted the model from [3] for use with the current doubler, it was found that the current doubler never appears inductive to the PT. Fig. 10 in [1] shows the relative output power of one rectifier compared to the other for a given level of power dissipation in the PT. Numerically, the results from Fig. 10 differ from those presented in this chapter, and it is believed that the difference is caused by an error in the current doubler model used in [1].

The use of full-bridge capacitively smoothed and current doubler rectifiers with PTs was also discussed in [4], however, the purely resistive rectifier models that were employed were not detailed enough to show the effect on maximum PT output power. A similar comment applies to the current doubler model used in [5]. The full-bridge capacitively smoothed and half-wave capacitively smoothed topologies are discussed in the context of PTs in [6], but the effect on PT power density is not considered.

This chapter considers the effect of 5 different output topologies on the output power of a given PT and, more generally, on PT power density. The analysis is made from the perspective of vibration velocity, and uses rectifier models that fully account for the shape of the voltage waveform across the PT output capacitance and its relationship to the equivalent circuit tank current.

The correlation between the maximum vibration velocity within a piezoelectric material and the temperature rise that occurs is well established [7-14]. As vibration velocity increases, the mechanical quality factor of the material decreases, causing greater power dissipation in the material and an increase in temperature [7-10, 12, 15, 16] (see also discussion in Chapter 1). Since the tank current in the (full) radial mode Transoner equivalent circuit (see Figures 2.7, 3.22, and 3.26) is approximately equal to the maximum vibration velocity within the PT (assuming the set of electrodes with the largest radius extends close to the outer radius of the device), it is to be expected that the tank current, and the vibration velocity that it represents, is closely related to the temperature rise of the PT.

PTs are nearly always thermally limited. In other words, the maximum output power of a given PT in a given topology operating at a given frequency with a given load is nearly always limited by the need to prevent excessive temperature rise. Since the temperature rise will be closely related to the vibration velocity, specifying a maximum allowable temperature rise effectively specifies an approximate maximum level of vibration velocity. Thus, in order to achieve high PT power density, it is crucially important that a PT is loaded in a way that maximises the output power obtained for a given vibration velocity, because this is expected to maximise the output power that can be obtained for the specified maximum allowable temperature rise. This is essentially what the matched load resistance $R_L = 1/(\omega C_{out})$ does in the AC-output topology – it maximises the output power obtained for a given tank current (and therefore for a given vibration velocity).

The purpose of this chapter is to

1. Reinforce the concept of the tank current (and therefore vibration velocity) being directly related to the (minimum) temperature rise seen with a given PT.
2. Demonstrate that, for a given PT, DC-output topologies result in a lower maximum PT output power for a given level of tank current compared to the AC-output topology.
3. Consider the implications of 1) and 2) from a design perspective using the radial mode Transoner equivalent circuit models developed in Chapters 2 and 3.
4. Determine the effect of the rectifier topology on the number of layers required in the output section of a radial mode Transoner PT for a given converter specification.

To the author's knowledge, this is the first time that the concepts of vibration velocity, rectifier operation, and equivalent circuit modelling have been brought together to elucidate the challenges posed by PT design for DC-output converters.

4.2 Output topology analysis

The 5 output topologies to be considered are shown in Figure 4.1. Since the loaded Q factor of a PT is high enough to ensure that the tank current in the lumped equivalent circuit is sinusoidal, fundamental mode approximation (FMA) can be applied. The 5 topologies are initially modelled with the circuits shown in Figure 4.2, where a sinusoidal current source is used to represent the tank current. Then, using FMA, all 5 topologies can be modelled with the circuit of Figure 4.3.

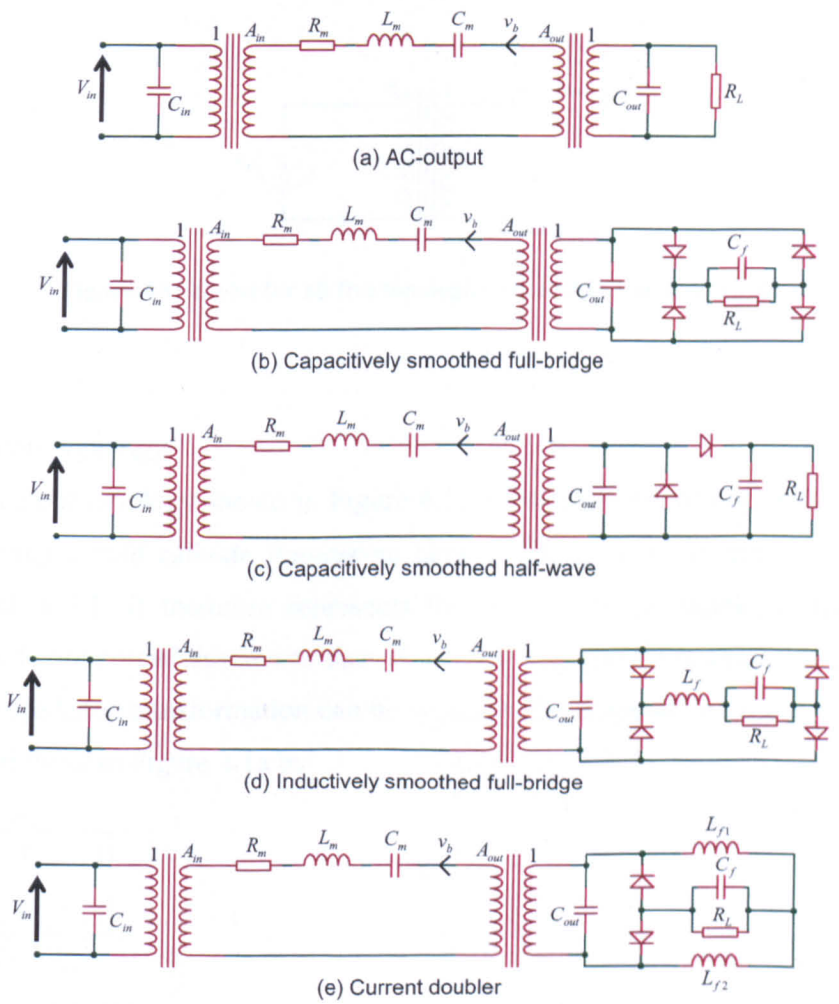

Figure 4.1: Radial mode Transoner equivalent circuit, shown with five different output topologies.

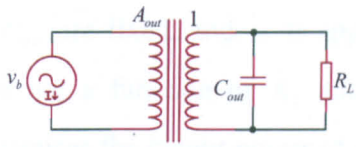

(a) Model for AC-output

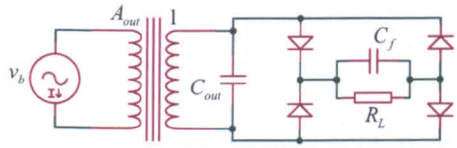

(b) Model for capacitively smoothed full-bridge

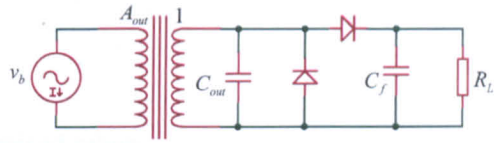

(c) Model for capacitively smoothed half-wave

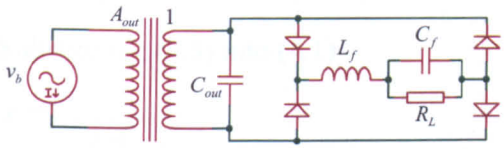

(d) Model for inductively smoothed full-bridge

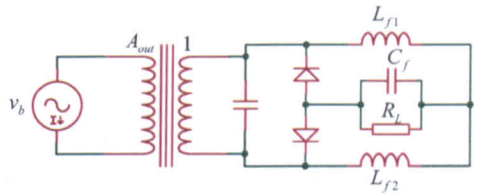

(e) Model for current doubler

Figure 4.2: Models for the five PT output topologies.

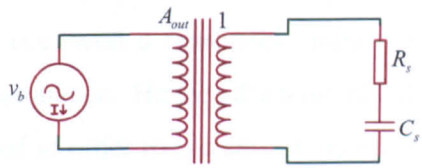

Figure 4.3: Model for all five topologies once FMA has been applied.

A. AC-output topology

The AC-output topology shown in Figure 4.1a is basically the arrangement that occurs when driving a cold cathode fluorescent lamp (CCFL), or a conventional fluorescent lamp, with a PT. It therefore represents the only PT-based topology that has seen widespread commercial success to date. Since the tank current is sinusoidal, a series to parallel impedance transformation can be applied. The elements in Figure 4.3 are given in terms of those in Figure 4.1a by

$$R_s = \frac{R_L}{\left(R_L{}^2\omega^2 C_{out}{}^2 + 1\right)} \tag{4.1}$$

$$C_s = \frac{\left(R_L{}^2\omega^2 C_{out}{}^2 + 1\right)}{R_L{}^2\omega^2 C_{out}}. \tag{4.2}$$

From Figure 4.3, PT output power is given by

$$P_{out,PT} = A_{out}{}^2 v_{b,RMS}{}^2 R_s . \tag{4.3}$$

For a given PT, A_{out} and C_{out} are fixed, and ω is approximately fixed (we make the assumption here that ω is not a function of R_L and hence treat it as a constant). Therefore the load that maximises the output power of a given PT for a given v_b is the load that maximises R_s. Differentiating (4.1) with respect to R_L,

$$\frac{\partial R_s}{\partial R_L} = \frac{\left(1 - R_L{}^2 \omega^2 C_{out}{}^2\right)}{\left(R_L{}^2 \omega^2 C_{out}{}^2 + 1\right)^2} . \tag{4.4}$$

From the stationary points of (4.4), R_s is maximised when

$$R_L = \frac{1}{\omega C_{out}} . \tag{4.5}$$

Substituting (4.5) into (4.1)

$$R_s{}^{\max} = \frac{1}{2\omega C_{out}} . \tag{4.6}$$

Hence, the maximum output power from a given PT for a given tank current when using the AC-output topology is proportional to $1/(2\omega C_{out})$. Note that, for a given PT, ω may be thought of as being approximately fixed, because power transfer through the PT can only be achieved sensibly (i.e. with a reasonable input voltage and good efficiency) when operating close to resonance. Hence, dramatically decreasing the frequency at which a given PT is operated in order to increase R_s is *not* a way to increase maximum output power, and results in poor efficiency (see Figure 4.6 in Section 4.3).

B. DC-output full-bridge capacitively smoothed topology

When considering the DC-output topologies, it is vital that the rectifier models are based on an analysis that fully accounts for the shape of the voltage waveform across the parallel capacitance C_{out}. If a simple resistance-only model is used, the effect of the rectifier on PT output power will be missed. The rectifier models utilized in this chapter are based on those presented in [3, 17] and shown in full in Appendix B. For the capacitively smoothed full-bridge rectifier, the elements in Figure 4.3 are given by

$$R_s = \frac{8R_L\left(1 + 2V_{df}\right)}{\left(\pi + 2R_L C_{out}\omega\left(1 + 2V_{df}\right)\right)^2} \tag{4.7}$$

$$C_s = \frac{\pi C_{out}\left(\pi + 2\omega R_L C_{out}\left(1+2V_{df}\right)\right)^2}{\left(\begin{array}{l}\left(2\omega R_L C_{out}\left(1+2V_{df}\right)+\pi\right)^2 \cos^{-1}\left(\dfrac{\pi - 2\omega R_L C_{out}\left(1+2V_{df}\right)}{\pi + 2\omega R_L C_{out}\left(1+2V_{df}\right)}\right) \\ +\left(4\omega R_L C_{out}\sqrt{\pi}\left(1+2V_{df}\right) - 2\pi^{3/2}\right)\sqrt{2\omega R_L C_{out}\left(1+2V_{df}\right)}\end{array}\right)} \tag{4.8}$$

where V_{df} is the ratio of the on-state voltage drop across a single rectifier diode (which is assumed to be constant) to the voltage across the load resistance. Note that V_{df} is regarded as a constant (see discussion in Appendix B), and hence not a function of R_L. For a given PT, V_{df}, and v_b, the total PT output power (i.e. the sum of the power dissipated in the load resistance and the power dissipated in the rectifier diodes) will be maximised when R_s is maximised. Differentiating (4.7) with respect to R_L and considering the stationary points, R_s is maximised when

$$R_L = \frac{\pi}{2\omega C_{out}\left(1+2V_{df}\right)}. \tag{4.9}$$

Substituting (4.9) into (4.7),

$$R_s^{\max} = \frac{1}{\pi\omega C_{out}}. \tag{4.10}$$

Comparing (4.10) to (4.6), the maximum size of R_s for this topology is $2/\pi = 0.637$ times that of the AC-output case. Therefore the maximum PT output power that can be obtained for a given level of tank current from a given PT with a full-bridge capacitively smoothed rectifier is only 0.637 times that which can be achieved from the same PT using the AC-output topology.

For a given PT and a given maximum allowable temperature rise, the maximum level of vibration velocity that can be used is approximately fixed. Therefore the maximum thermally limited output power that can be achieved from a given PT with a full-bridge capacitively smoothed rectifier is expected to be only 0.637 times that which could be achieved from the same PT with the AC-output topology. The use of this rectifier therefore results in a considerable drop in the maximum (thermally limited) power density of a given PT.

In [3], Forsyth showed that the inductively smoothed rectifier increases the apparent size of the parallel capacitance in an LCC series-parallel converter. Similar behaviour also occurs with the capacitively smoothed topologies. Substituting (4.9) into (4.8),

$$C_s = 2C_{out}. \tag{4.11}$$

Applying a series to parallel transformation to (4.10) and (4.11) results in an effective parallel capacitance of

$$C_{out\_effective} = \frac{2\pi^2 C_{out}}{(\pi^2+4)} = 1.423 C_{out} \tag{4.12}$$

and an effective parallel resistance of

$$R_{parallel\_equivalent} = \frac{(\pi^2+4)}{4\pi\omega C_{out}} = \frac{1.104}{\omega C_{out}}. \tag{4.13}$$

Thus, it can be seen that the rectifier significantly increases the apparent capacitance at the PT output.

C. DC-output half-wave capacitively smoothed topology

An equivalent circuit model for this topology was derived by adapting the method from [17] (see Appendix B). The elements in Figure 4.3 are given by

$$R_s = \frac{8R_L(1+2V_{df})}{(2\pi + R_L\omega C_{out}(1+2V_{df}))^2} \tag{4.14}$$

$$C_s = \frac{\pi C_{out}(2\pi + \omega R_L C_{out}(1+2V_{df}))^2}{\left((\omega R_L C_{out}(1+2V_{df})+2\pi)^2 \cos^{-1}\left(\frac{2\pi - \omega R_L C_{out}(1+2V_{df})}{2\pi + \omega R_L C_{out}(1+2V_{df})}\right) + \left(2\omega R_L C_{out}\sqrt{\pi}(1+2V_{df}) - 4\pi^{3/2}\right)\sqrt{2\omega R_L C_{out}(1+2V_{df})}\right)} \tag{4.15}$$

The load which maximises R_s, and therefore maximises PT output power for a given PT, V_{df}, and v_b is

$$R_L = \frac{2\pi}{\omega C_{out}(1+2V_{df})}. \tag{4.16}$$

Substituting (4.16) into (4.14),

$$R_s^{\max} = \frac{1}{\pi\omega C_{out}}. \tag{4.17}$$

Like the full-bridge capacitively smoothed topology, the maximum PT output power that can be obtained for a given tank current from a given PT with a half-wave capacitively smoothed rectifier is only $2/\pi = 0.637$ times that which can be achieved from the same PT using the AC-output topology.

D. DC-output full-bridge inductively smoothed topology

Unlike the capacitively smoothed topologies, this rectifier has two modes of operation [3], named "continuous" and "discontinuous" (with reference to the voltage across the

parallel capacitance), or "non-overlapping" and "overlapping" (with reference to whether both pairs of diagonally opposite diodes conduct at the same time). Initially, let us suppose that maximum R_s is obtained in the continuous mode. From [3] and Appendix B, R_s and C_s for this mode are given by

$$R_s = \frac{8R_L(1+2V_{df})}{\pi^2\left(\omega^2 C_{out}{}^2 R_L{}^2(1+2V_{df})^2+1\right)} \tag{4.18}$$

$$C_s = \frac{C_{out}\pi^2\left(\omega^2 C_{out}{}^2 R_L{}^2(1+2V_{df})^2+1\right)}{\left(\pi^2\omega^2 C_{out}{}^2 R_L{}^2(1+2V_{df})^2+\pi^2-8\right)}. \tag{4.19}$$

Note that a key assumption of this model is that the filter inductor, L_f, is large enough to ensure that its current ripple can be neglected. From (4.18), the load which maximises PT output power for a given PT, V_{df}, and v_b is

$$R_L = \frac{1}{\omega C_{out}(1+2V_{df})}. \tag{4.20}$$

Substituting (4.20) into (4.18)

$$R_s{}^{\max} = \frac{4}{\pi^2\omega C_{out}}. \tag{4.21}$$

It is then necessary to check that the load in (4.20) does in fact result in the continuous mode of operation, and to check that a higher output power cannot be achieved in the discontinuous mode.

From [3] and Appendix B, the rectifier will be in the continuous mode provided that

$$2 < \pi\omega C_{out} R_L(1+2V_{df}). \tag{4.22}$$

Substituting (4.20) into (4.22), it can be seen that this condition is satisfied. Thus, (4.20) is the load that maximises PT output power in the continuous mode. Before considering the discontinuous mode, we define a load factor, M, as the ratio between the actual load resistance and the load resistance that maximises PT output power in the continuous mode. Hence, the load resistance can be expressed as

$$R_L = \frac{M}{\omega C_{out}(1+2V_{df})}. \tag{4.23}$$

Substituting (4.23) into (4.22), it can be seen that the boundary between the continuous and discontinuous modes of rectifier operation is $M = 2/\pi = 0.637$. Thus, the rectifier will be in the continuous mode when $M > 2/\pi$. From [3] and Appendix B, R_s and C_s for the discontinuous mode are given by

$$R_s = \frac{\left(2\sin(\alpha+\beta)\sin(\alpha)-\cos^2(\alpha)-\cos^2(\alpha+\beta)+2\right)}{\pi\omega C_{out}} \tag{4.24}$$

$$C_s = \frac{C_{out}\pi}{(\pi - 2\sin(\alpha+\beta)\cos(\alpha) - \cos(\alpha)\sin(\alpha) - \cos(\alpha+\beta)\sin(\alpha+\beta) - \beta)} \tag{4.25}$$

where α and β must be numerically determined using the simultaneous equations

$$\cos(\alpha+\beta) + (\beta-\pi)\sin(\alpha+\beta) + \cos(\alpha) = 0 \tag{4.26}$$

$$\pi\omega C_{out}(1+2V_{df})R_L + \frac{2(\beta-\pi)\cos(\alpha+\beta) + (\beta^2+\pi^2-2-2\beta\pi)\sin(\alpha+\beta) - 2\sin(\alpha)}{2\sin(\alpha+\beta)} = 0. \tag{4.27}$$

Substituting (4.23) into (4.27) gives

$$(2\pi M + \beta^2 - 2 - 2\beta\pi + \pi^2)\sin(\alpha+\beta) + 2(\beta-\pi)\cos(\alpha+\beta) - 2\sin(\alpha) = 0 \tag{4.28}$$

and results in α and β becoming dependent only upon M. (4.24) can be written as

$$R_s = \frac{G}{\omega C_{out}} \tag{4.29}$$

where

$$G = \frac{(2\sin(\alpha+\beta)\sin(\alpha) - \cos^2(\alpha) - \cos^2(\alpha+\beta) + 2)}{\pi}. \tag{4.30}$$

Now, since α and β depend only upon M, G can be plotted against M using (4.26), (4.28), and (4.30), as shown in Figure 4.4.

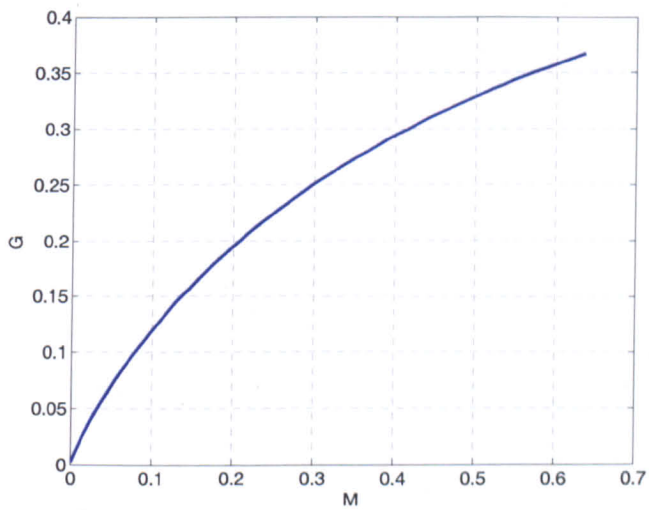

Figure 4.4: G against M for the discontinuous mode. Note that from (4.3) and (4.29), PT output power for a given PT and a given v_b is proportional to G.

The range of M in Figure 4.4 is 0 to $2/\pi$, such that it covers the entire region of discontinuous mode operation. Since the peak value of G in Figure 4.4 is 0.367 (and occurs at $M = 2/\pi$, the boundary between continuous and discontinuous operation), it can be seen by comparing (4.29) to (4.21) that maximum PT output power does indeed occur in the continuous mode (since $4/\pi^2 = 0.405$, which is greater than 0.367), and does so at the load specified in (4.20).

Comparing (4.21) to (4.10) and (4.6), it can be seen that the full-bridge inductively smoothed rectifier results in a maximum R_s that is $8/\pi^2 = 0.811$ times the maximum R_s for the AC-output case. Hence, the maximum PT output power that can be achieved for a given PT, V_{df}, and tank current, lies approximately mid-way between the AC-output and the DC-output capacitively smoothed topologies. Although this topology allows greater output power to be obtained than the capacitively smoothed topologies, the cost, losses, and space required for the inductor L_f must not be forgotten.

E. DC-output current doubler topology

Compared to the other three DC-output topologies, the current doubler has the advantage of a single rectifier diode conducting the full load current at any one time (in the continuous mode), thereby reducing the total rectifier diode losses. It is therefore most suitable for use in low output voltage applications. An equivalent circuit model for this topology was derived by adapting the method from [3], and can be found in Appendix B. Like the full-bridge inductively smoothed rectifier, the current doubler has two modes of operation; continuous and discontinuous. In the continuous mode, the elements in Figure 4.3 are given by

$$R_s = \frac{32R_L(1+V_{df})}{\pi^2\left(16\omega^2 C_{out}{}^2 R_L{}^2(1+V_{df})^2+1\right)} \tag{4.31}$$

$$C_s = \frac{C_{out}\pi^2\left(16\omega^2 C_{out}{}^2 R_L{}^2(1+V_{df})^2+1\right)}{\left(\pi^2\left(16\omega^2 C_{out}{}^2 R_L{}^2(1+V_{df})^2+1\right)-8\right)}. \tag{4.32}$$

From (4.31), the load which maximises PT output power for a given PT, V_{df}, and v_b is

$$R_L = \frac{1}{4\omega C_{out}(1+V_{df})}. \tag{4.33}$$

Substituting (4.33) into (4.31)

$$R_s{}^{max} = \frac{4}{\pi^2\omega C_{out}}. \tag{4.34}$$

The equations for operation in the discontinuous mode are given in Appendix B. Like the full-bridge inductively smoothed topology, it can be shown that maximum PT output power is obtained in the continuous mode. Note that the boundary between the continuous and discontinuous modes of rectifier operation is $M = 2/\pi = 0.637$ when M is defined as the ratio between the actual load resistance and the load resistance that maximises PT output power in the continuous mode, i.e.

$$R_L = \frac{M}{4\omega C_{out}\left(1+V_{df}\right)}. \tag{4.35}$$

Hence, the current doubler rectifier will be in the continuous mode of operation when $M > 2/\pi$. Note that (4.34) is identical to (4.21), just as (4.17) is identical to (4.10). The maximum PT output power that can be achieved with the current doubler for a given PT, V_{df}, and tank current is therefore $8/\pi^2 = 0.811$ times that which can be achieved with the AC-output topology.

Table 4.1 summarises the results from this section. Also included is the efficiency of each rectifier, as it is modelled by the analyses on which the RC rectifier models are based.

Topology	Optimum load condition	Maximum series equivalent resistance, R_s^{max}	Maximum PT output power that can be obtained for a given PT, V_{df}, and v_b, relative to the AC-output topology	Rectifier efficiency (as modelled by the RC equivalent circuit analyses)
AC-output	$R_L = \frac{1}{\omega C_{out}}$	$R_s^{max} = \frac{1}{2\omega C_{out}}$	1	N/A
DC-output full-bridge capacitively smoothed	$R_L = \frac{\pi}{2\omega C_{out}\left(1+2V_{df}\right)}$	$R_s^{max} = \frac{1}{\pi\omega C_{out}}$	$\frac{2}{\pi}$	$\frac{1}{\left(1+2V_{df}\right)}$
DC-output half-wave capacitively smoothed	$R_L = \frac{2\pi}{\omega C_{out}\left(1+2V_{df}\right)}$	$R_s^{max} = \frac{1}{\pi\omega C_{out}}$	$\frac{2}{\pi}$	$\frac{1}{\left(1+2V_{df}\right)}$
DC-output full-bridge inductively smoothed	$R_L = \frac{1}{\omega C_{out}\left(1+2V_{df}\right)}$	$R_s^{max} = \frac{4}{\pi^2\omega C_{out}}$	$\frac{8}{\pi^2}$	$\frac{1}{\left(1+2V_{df}\right)}$
DC-output current doubler	$R_L = \frac{1}{4\omega C_{out}\left(1+V_{df}\right)}$	$R_s^{max} = \frac{4}{\pi^2\omega C_{out}}$	$\frac{8}{\pi^2}$	$\frac{1}{\left(1+V_{df}\right)}$

Table 4.1: Optimum load condition and relative maximum PT output power of the five different output topologies.

4.3 Experimental verification

The preceding section clearly shows that, for a given PT and a given tank current, the AC-output topology will achieve higher PT output power than the DC-output inductively smoothed topologies, which in turn will achieve higher PT output power than the capacitively smoothed topologies. The temperature rise of a given PT will be closely related to the maximum vibration velocity within the PT. Thus, a given PT

operating with a given level of tank current would be expected to have a higher maximum output power when operated in the AC-output topology than in a DC-output topology, but undergo approximately the same rise in temperature in both cases. To verify this, the output power and temperature rise of a T1-15W non-isolated radial mode Transoner PT was measured under various loading conditions.

Power tests on a PT are usually performed using a purely sinusoidal input signal [18, 19]. Using a sinusoid is preferable to the trapezoid generated by a half-bridge inductor-less stage (see Chapters 1 and 5) because

- The trapezoid contains harmonics which, depending on frequency, could affect the efficiency of the PT by exciting other vibration modes.
- The inductor-less topology can only be used sensibly at inductive frequencies. At capacitive frequencies, ZVS is not possible, and large amounts of electro-magnetic interference (EMI) are generated by the current spike caused by the PT input capacitance trying to instantly charge up to the DC-link voltage when the high-side MOSFET turns on, and trying to instantly discharge to 0V when the low-side MOSFET turns on.
- The PT must be capable of inductor-less ZVS in the first place.

Furthermore, using a sinusoid is preferable to the quasi-sinusoid generated by the half-bridge with-inductor topology because

- The shape of the PT input voltage waveform tends to change with frequency and load condition, meaning the harmonic content is not constant.

Using a purely sinusoidal input voltage waveform ensures that the harmonic content at the PT input remains approximately constant, and that any changes in PT efficiency (and therefore in output power capability) are due solely to the output topology. The usual practice is to use a sinusoidal signal generator and a power amplifier [18, 19]. Since a commercial power amplifier capable of delivering the required voltage level and frequency was not available, a simple class B amplifier was designed (see Appendix C). This amplifier was capable of delivering a 43V RMS sinusoid at 150kHz into an 110 ohm load with no harmonics having an amplitude greater than -42.2dB of the fundamental. A toroidal magnetic transformer with a step-up ratio of 55:230 was then used to boost the maximum output to 180V RMS. In practice, it was found that a larger voltage could be obtained when the toroidal transformer was connected to the PT,

probably because of a resonance occurring between the inductances of the toroidal transformer and the input capacitance of the PT.

Constant output power tests were performed on the PT. For each load condition, the steady-state temperature rise (PT temperature - ambient temperature) was recorded over a range of frequencies, so as to capture the most efficient point. Since the characteristics of a PT change with heat, the input voltage had to be adjusted so as to maintain a constant output power. To facilitate this, the test rig illustrated in Figure 4.5 was constructed. A PC running MATLAB was used to communicate with the oscilloscope and signal generator via RS232. PT temperature was measured using a thermocouple placed on a small piece of mica, pressed lightly into contact with the centre of the PT (i.e. at the nodal point). Another thermocouple was used to measure the ambient temperature. Both thermocouples were connected to a USB temperature interface, and the results read directly into MATLAB. The load was constructed from ceramic, low-inductance resistors (BPC series by BI Technologies).

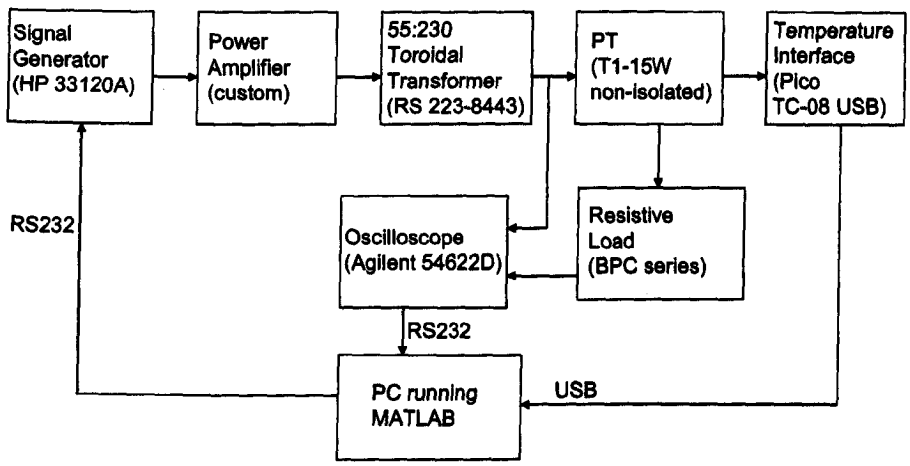

Figure 4.5: Block diagram of test-rig for temperature and power measurements. AC-output scenario is shown (i.e. no rectifier between PT and load).

A MATLAB script was used to automate the test procedure. For a particular load, the signal generator was set to the desired frequency. The amplitude of the sinusoidal signal generator output was then adjusted until the voltage across the load reached the required level for the required output power. The PT temperature, ambient temperature, and the voltage across the load resistance were then monitored. As the voltage across the load changed, the signal generator output voltage was adjusted, thereby maintaining constant output voltage, and therefore constant output power. Once the PT temperature had reached steady-state, the voltage across the load, the PT input voltage, and the PT and

ambient temperatures were recorded. The signal generator was then set to the next frequency, and the process repeated. When moving in 1kHz increments, it was found to take approximately 20 to 25 minutes for steady-state to be reached each time the frequency was incremented. The tests were performed using the device referred to in Table 2.3 in Chapter 2 as "device 5".

A. AC-output tests

The optimum load resistance was calculated using (4.5) to be around 960Ω at the frequency of maximum efficiency, which was determined in preliminary tests to be around 128kHz. Therefore the lowest temperature rise for a given output power should occur with this load. For the AC-output topology, the output power of the PT is

$$P_{out,PT} = A_{out}{}^2 v_{b,RMS}{}^2 R_s = \frac{v_{b,RMS}{}^2 A_{out}{}^2 R_L}{R_L{}^2 \omega^2 C_{out}{}^2 + 1}. \tag{4.36}$$

Since the electrodes and ceramic all have the same radius in the T1-15W, $v_b = v_a$. The experimentally measured values of C_{out} and A_{out} for device 5 in Table 2.3 of Chapter 2 were 1.30nF and 0.922 respectively. Using (4.36) and the experimentally measured values of C_{out} and A_{out}, 12W into 960Ω at 128kHz should result in $v_{b,RMS} = 0.172$ m/s (or A).

Loads of 460Ω and 2004Ω were also chosen because, from (4.36), they should require the same tank current of $v_{b,RMS} = 0.194$ m/s (or A) to deliver 12W (assuming the frequency of operation remains ≈128kHz). Note that this is slightly higher than the 0.172 m/s required for 12W with the 960Ω load. Therefore the 460Ω and 2004Ω loads should have similar temperature versus frequency profiles to one another (albeit over slightly different frequency ranges because the gain versus frequency characteristics at these two loads are different), and result in a temperature rise slightly greater than the 960Ω load. The reason that there are two different loads that require the same tank current to deliver the same power at the same frequency is that a plot of (4.1) against R_L is convex.

There is some uncertainty in the value of A_{out} that was used in these calculations because it was inferred from the mass of the device, rather than being directly measured. However, because of the nature of the experiments and the form of (4.36) and (4.40), it

is not necessary to know exactly what the vibration velocity is in each case. In other words, regardless of the actual value of A_{out}, the 460Ω and 2004Ω loads would still be expected to require the same tank current to deliver 12W at 128kHz, and this value of tank current would still be slightly larger than that required to deliver 12W at 128kHz with the 960Ω load.

Profiles of temperature rise against frequency for the 960Ω, 460Ω, and 2004Ω loads in the AC-output topology are shown in Figure 4.6. The input voltage required (at steady-state) for a 12W output against frequency is shown in Figure 4.7. As expected, the 460Ω and 2004Ω loads have a similar profile, with a minimum temperature rise of 17.0°C and 18°C respectively. The 960Ω load results in a minimum temperature rise of 14.8°C. The similarity between the temperature profiles of the 460Ω and 2004Ω loads confirms the applicability of (4.36) and the ω and C_{out} values that were used with it. It is therefore reasonable to assume that 960Ω is approximately the most efficient load for this PT in this topology. One possible reason for the difference between the 460Ω and 2004Ω results is the dielectric loss in the output section; dissipating 12W in the 460Ω load requires 74.3V RMS across the PT output capacitance, whereas the 2004Ω requires 155.1V RMS. Since dielectric loss is proportional to the square of the voltage, one would expect 4.36 times greater output section dielectric loss with the 2004Ω load. Note that the input voltages required by the two loads are broadly similar (see Figure 4.7), so any difference in input section dielectric losses is likely to be much smaller than the difference in the output section dielectric losses.

Spikes in the temperature rise profile of Figure 4.6 occur at 123kHz and 134kHz. Such spikes are not uncommon with PTs, and examples can be found in the efficiency versus frequency plots shown in [20, 21]. (Note that the shape of an efficiency versus frequency plot at constant output power will be the inverse of a temperature rise versus frequency plot at constant output power). Comparing Figure 4.6 and Figure 4.7, it can be seen that maximum efficiency clearly occurs above resonance, and similar behaviour has previously been noted in other works, e.g. [20]. Note that the resonant frequency is the frequency at which the lowest input voltage is required to obtain the 12W output.

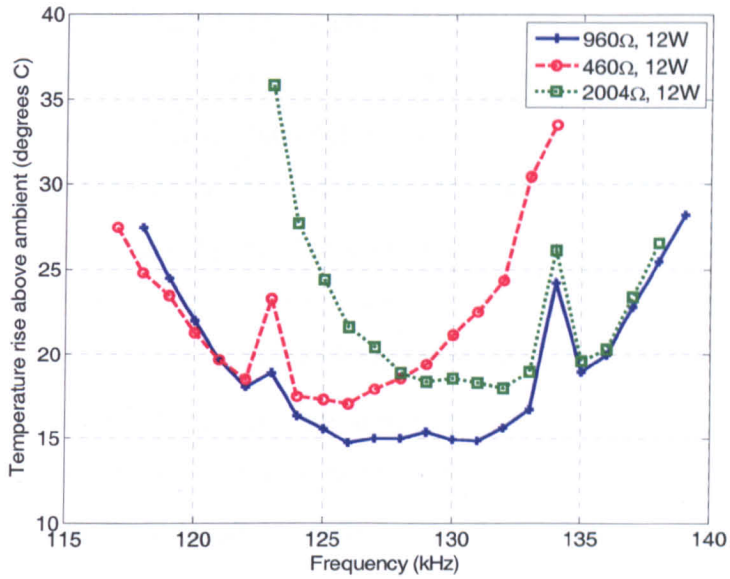

Figure 4.6: Steady-state PT temperature rise (i.e. PT temperature – ambient temperature) against frequency for the AC-output topology at 12W constant output power.

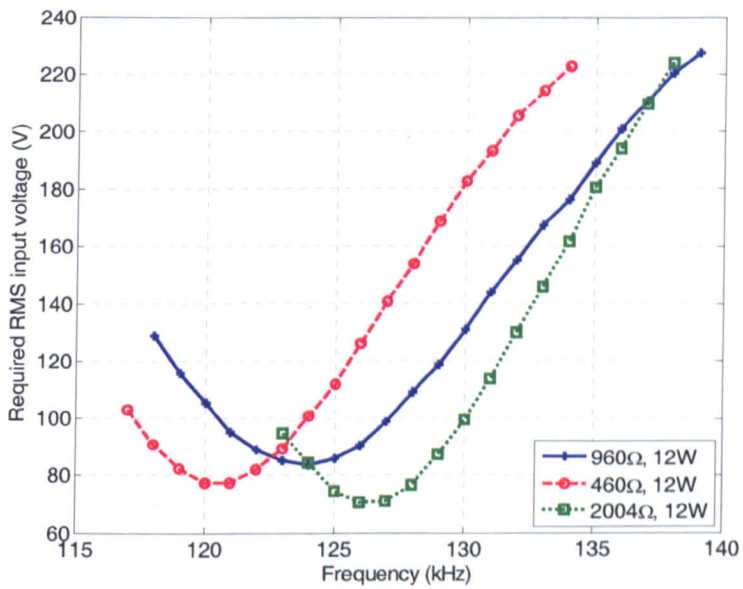

Figure 4.7: Required PT input voltage (at steady-state) against frequency for the AC-output topology at 12W constant output power.

The possible effects of dielectric loss are now considered. The equivalent series resistance of a capacitor is given by

$$R_{ESR} = \frac{\tan(\delta)}{\omega C} \tag{4.37}$$

where $\tan(\delta)$ is the applicable loss tangent (also known as the dissipation factor, DF), and C is the capacitance. For reference, the $\tan(\delta)$ of APC841 material (measured at room temperature and low excitation level) is stated as 0.0039 in [22], though it must be

remembered that dielectric losses are dependent on both temperature [22] and electric field strength [10, 23]. Detailed texts such as [10, 23] draw a distinction between the loss tangent that applies to ε^T and to ε^S, and indeed between all the "intensive" and "extensive" loss tangents. The loss tangents associated with ε^T and ε^S are referred to as $\tan(\delta')$ and $\tan(\delta)$ respectively in [10, 23]. However, many manufacturer's datasheets do not elaborate on how their figures for dielectric loss tangent were measured, and therefore do not distinguish between $\tan(\delta)$ and $\tan(\delta')$. In this discussion we refer to the applicable loss tangent simply as "$\tan(\delta)$". However, since the clamped capacitances of the radial mode Transoner PT are given in terms of ε^T, strictly speaking the quantity of interest for this device would be $\tan(\delta')$, rather than $\tan(\delta)$, when using the terminology of [10, 23]. Using a series to parallel transformation, the equivalent parallel resistance of a capacitor at a frequency ω is [24]

$$R_{EPR} = \frac{1}{\tan(\delta)\omega C} + \frac{\tan(\delta)}{\omega C} \tag{4.38}$$

which, providing $\tan(\delta)$ is small, is well approximated by [24]

$$R_{EPR} \approx \frac{1}{\tan(\delta)\omega C}. \tag{4.39}$$

In the experiments, as the frequency was adjusted, the voltage across the output capacitance was kept constant. Since the R_{EPR} of the output capacitance will decrease as frequency is increased (see (4.39)), it would be expected that the dielectric loss in the output section would increase with frequency. Therefore dielectric loss in the output section does not appear to explain why peak efficiency occurs above resonance.

The R_{EPR} of the input section would also be expected to decrease as frequency is increased. However, one would expect the overall change in dielectric loss in the input section to be dominated by the changing input voltage, because the loss is proportional to the square of the RMS of the input voltage. Since the required input voltage has to be increased as frequency is moved away from resonance (see Figure 4.7), the input section dielectric loss would be expected to be minimum at (or slightly below, given the frequency dependence of the R_{EPR}) resonance. Given that mechanical losses are expected to remain constant in the constant output power tests (see below), one would expect PT temperature rise to be minimum at (or slightly below) resonance, and to increase with increasing rapidity as frequency is moved away from resonance and the input voltage is increased. Therefore we conclude that dielectric loss in the input section does not appear to explain why peak efficiency occurs above resonance.

Mechanical losses are modelled by the series resistance R_m in the PT equivalent circuit. Since the tank current should remain constant as frequency is adjusted in the constant output power tests, the mechanical losses due to a constant-valued loss resistance would be expected to be constant. It is therefore concluded that the change in temperature rise (and therefore efficiency) with frequency shown in Figure 4.6 cannot be accurately modelled with the equivalent circuit shown in Figure 4.8 if the dielectric loss factor and mechanical loss resistance are taken to be constant. In Chapters 2 and 3, a value of R_m was estimated based on an average $\overline{Q}_m$. However, the results in Figure 4.6 and Figure 4.7 suggest that no single value of R_m will accurately model the loss characteristics, which is partly why relatively little time was spent considering it analytically in Chapters 2 and 3. It has been shown by many authors that the Q_m of a piezoelectric resonator changes with temperature and vibration velocity (see discussion in Chapter 1). However, Figure 4.6 and Figure 4.7 suggest that $\overline{Q}_m$ and/or $\tan(\delta)$ must be dependent on other factors as well if the circuit of Figure 4.8 is to accurately model the losses. In [20], an equivalent circuit with additional loss resistances was introduced to try and account for the frequency of maximum efficiency occurring above the resonant frequency.

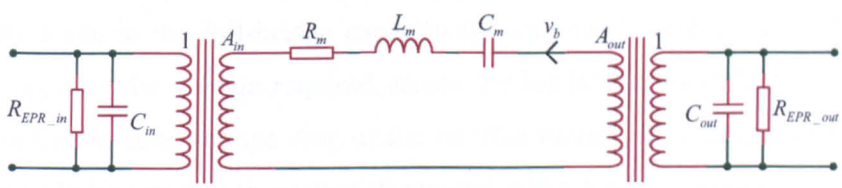

Figure 4.8: Radial mode Transoner PT lumped equivalent circuit with dielectric loss resistances. R_{EPR_in} and R_{EPR_out} are the equivalent parallel resistances modelling the dielectric losses in the input and output section respectively.

B. DC-output tests

The DC-output full-bridge capacitively smoothed rectifier is now considered. Given the theory in Section 4.2, a PT output power of $12\left(\frac{2}{\pi}\right) = 7.64$ W when operating in a DC-output capacitively smoothed topology would be expected to produce a similar tank current (and therefore vibration velocity) and temperature rise to an output power of 12W from the AC-output topology, assuming the optimum (i.e. most efficient) loads are used in each case. The optimum load for the full-bridge capacitively smoothed topology

was calculated using (4.9) to be around 1510Ω at the frequency at which maximum efficiency occurs (which was again found in preliminary experiments to be around 128kHz). For this topology

$$P_{out,PT} = A_{out}{}^2 v_{b,RMS}{}^2 R_s = \frac{A_{out}{}^2 v_{b,RMS}{}^2 8R_L\left(1+2V_{df}\right)}{\left(\pi + 2R_L C_{out}\omega\left(1+2V_{df}\right)\right)^2} \tag{4.40}$$

where $P_{out,PT}$ is the sum of the power dissipated in the load and the power dissipated in the rectifier. As expected, (4.40) indicates that 1510Ω at 7.64W at 128kHz requires $v_{b,RMS} = 0.172$ m/s (or A) (again, using $C_{out} = 1.30$ nF and $A_{out} = 0.922$ from Chapter 2). Note that V_{df} is assumed to be approximately zero because the voltage across the load resistance was much larger than the on-state voltage drop of a single rectifier diode. From (4.40), loads of 550Ω and 4164Ω should require $v_{b,RMS} = 0.194$ m/s (or A) to deliver 7.64W at ≈128kHz. Thus, 1510Ω at 7.64W in this topology should cause a similar temperature rise to 960Ω at 12W in the AC-output topology because they require the same tank current. Likewise, 550Ω and 4164Ω at 7.64W in this topology should correspond to 460Ω and 2004Ω at 12W in the AC-output topology. Note that this correspondence should occur regardless of any error in the value of A_{out}.

Figure 4.9 shows the profile of temperature rise with frequency for the 1510Ω, 550Ω, and 4164Ω loads in the full-bridge capacitively smoothed topology at 7.64W output. Note that because the voltage required across the loads to deliver this power is much higher than the on-state voltage drop of the rectifier diodes, the output power of the PT was assumed to be equal to the power dissipated in the load resistance. Also shown for comparison is the profile of the 1510Ω load at 12W output. Figure 4.10 shows the input voltage required (at steady-state) at each frequency.

The minimum temperature rise with the 1510Ω, 550Ω, and 4164Ω loads at 7.64W was 13.1°C, 16.0°C, and 17.5°C respectively. It is therefore reasonable to assume that 1510Ω is approximately the most efficient load for this PT in this topology. The difference in temperatures that occurred with the 4164Ω and 550Ω loads is likely to be due to the difference in dielectric losses in the output section as a result of the difference in voltages required across the output capacitance.

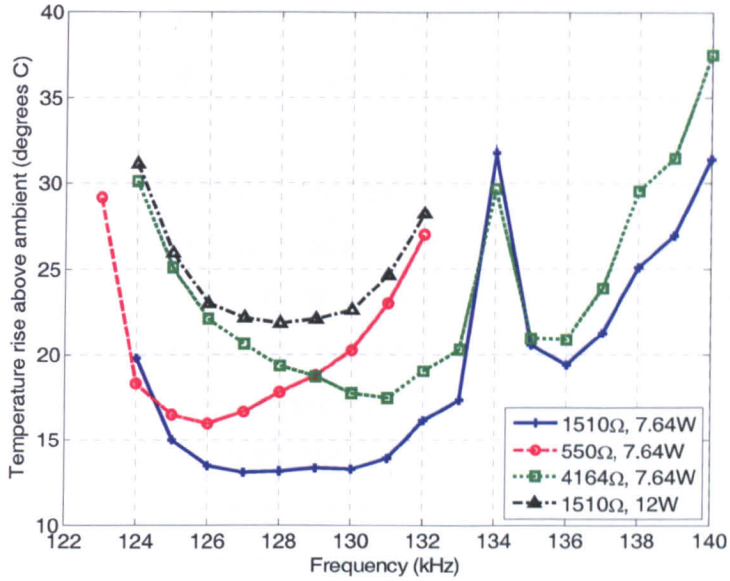

Figure 4.9: Steady-state PT temperature rise (i.e. PT temperature – ambient temperature) against frequency for the DC-output full-bridge capacitively smoothed topology at constant PT output power.

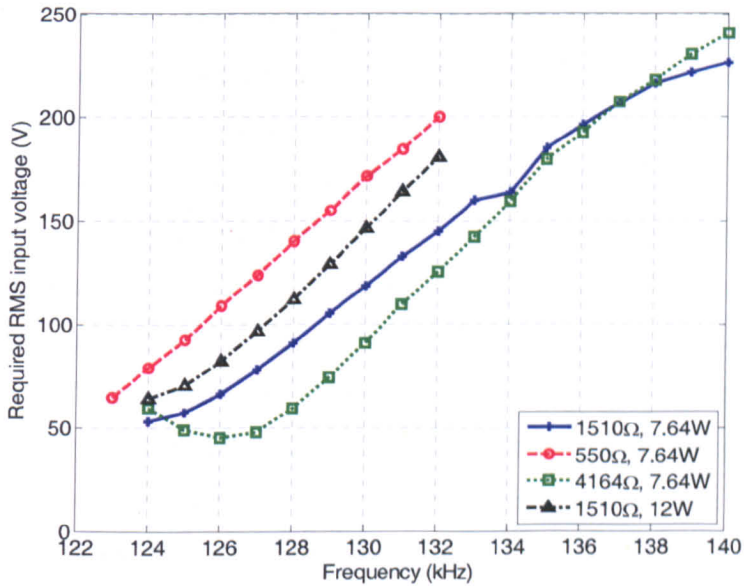

Figure 4.10: Required PT input voltage (at steady-state) against frequency for the DC-output full-bridge capacitively topology.

Comparing the 960Ω at 12W in the AC-output case to the 1510Ω at 7.64W in the DC-output capacitively smoothed topology, there is a difference in minimum temperature rise of 1.7°C (about 13% difference). The correlation between the 550Ω DC, 4164Ω DC, 460Ω AC, and 2004Ω AC temperature rises is also good, particularly when comparing the 550Ω DC to the 460Ω AC, and the 4164Ω DC to the 2004Ω AC (i.e.

comparing the loads with the lower C_{out} voltage to one another, and comparing the loads with the higher C_{out} voltage to one another).

From these results it is concluded that the tank current (and hence the vibration velocity) alone is a reasonably good indicator of the minimum temperature rise that will occur in a given PT (objective 1 in the introduction). It is also confirmed that, for a given PT and a given level of tank current, the full-bridge capacitively smoothed rectifier results in a maximum PT output power that is, approximately, only $2/\pi$ times that which can be achieved with the AC-output topology (objective 2 in the introduction). From these two conclusions, and the other results in Section 4.2, it directly follows that the maximum thermally limited output power of a given PT is considerably lower when a DC-output topology is used compared to an AC-output topology.

Finally, the spike that occurs at 134kHz in Figure 4.9 is noticeably larger than that in Figure 4.6. In both the AC-output and DC-output topologies, the voltage waveform across the PT input was sinusoidal. In the AC-output topology, the voltage waveform across the PT output is also sinusoidal. However, due to the way in which the full-bridge capacitively smoothed rectifier operates when connected to LCC type resonant converter topologies, the voltage waveform across the PT output is not sinusoidal in the DC-output full-bridge capacitively smoothed case (see [17, 25] for further information). Since, from the PT's perspective, the difference in PT output voltage waveform is the only apparent difference between operation in the AC-output topology and operation in the DC-output full-bridge capacitively smoothed topology, it *may* be that the larger temperature spike in the DC-output case was, in part, due to the additional harmonic content present in the voltage waveform across the PT output. This is, however, pure conjecture, and further investigation is required with other devices to see if frequencies at which there are temperature spikes with the AC-output topology always result in larger spikes with the DC-output topology, or whether there is another cause.

4.4 Implications for PT design

It has been shown that a given PT will always achieve a lower maximum output power when it is used with the DC-output topologies shown in Figure 4.1, compared to the

AC-output topology, because less output power is obtained for a given level of vibration velocity, and the vibration velocity is closely related to the minimum PT temperature rise. The scenario of a *given electrical specification* rather than a *given PT* is now considered.

The optimum load conditions in (4.5), (4.9), (4.16), (4.20), and (4.33), apply to both a "given PT" scenario, and a "given specification" scenario (where R_L and V_{df} are considered to be fixed). To demonstrate this, consider a radial mode Transoner PT in the AC-output topology. Let the output section electrode radius be approximately equal to the outer radius of the PT, and the input section electrode radius be less than or equal to the output section electrode radius. v_b is then approximately the peak vibration velocity occurring anywhere within the device, and b is the radius of the electrodes in the output section. From Chapter 3, the appropriate formula for A_{out} and C_{out} are

$$A_{out} = \frac{2\pi b n_{out} d_{31}^{\ out}}{s_{11}^{E\,out}\left(1-\sigma_C^{E\,out}\right)} \tag{4.41}$$

$$C_{out} = \frac{\pi b^2 n_{out}^{\ 2} \varepsilon_{33}^{T\,out}}{t_{out}^{total}}\left(1-k_p^{\ out^2}\right). \tag{4.42}$$

Substituting (4.41) and (4.42) into (4.36) and making use of the standard formula for planar coupling factor results in

$$P_{out,PT} = \frac{2v_{b,RMS}^{\ 2}\pi^2 b^2 \varepsilon_{33}^{T\,out} k_p^{\ out^2} n_{out}^{\ 2} R_L t_{out}^{total^2}}{s_{11}^{E}\left(1-\sigma_C^{E\,out}\right)\left(R_L^{\ 2}\omega^2\pi^2 b^4 n_{out}^{\ 4}\left(k_p^{\ out}-1\right)^2\left(k_p^{\ out}+1\right)^2 \varepsilon_{33}^{T\,out^2} + t_{out}^{total^2}\right)}. \tag{4.43}$$

If the thickness of the electrodes is assumed negligible, then the power density of the output section is

$$P_{density\_output\_section} = \frac{P_{out,PT}}{\pi c^2 t_{out}^{total}} = \frac{2v_{b,RMS}^{\ 2}\pi b^2 \varepsilon_{33}^{T\,out} k_p^{\ out^2} n_{out}^{\ 2} R_L t_{out}^{total}}{c^2 s_{11}^{E}\left(1-\sigma_C^{E\,out}\right)\left(R_L^{\ 2}\omega^2\pi^2 b^4 n_{out}^{\ 4}\left(k_p^{\ out}-1\right)^2\left(k_p^{\ out}+1\right)^2 \varepsilon_{33}^{T\,out^2} + t_{out}^{total^2}\right)}. \tag{4.44}$$

Taking the partial differential of (4.44) with respect to n_{out}, equating it to zero, and solving for n_{out}, (4.44) is maximised when

$$n_{out} = \frac{\sqrt{t_{out}^{total}}}{b\sqrt{\pi R_L \omega \varepsilon_{33}^{T\,out}\left(1-k_p^{\ out^2}\right)}}. \tag{4.45}$$

Substituting (4.45) into (4.42) results in

$$C_{out} = \frac{1}{\omega R_L}, \tag{4.46}$$

which is the same (4.5). Thus, the relationship therefore holds "for a given PT", and "for a given R_L". Likewise, (4.9), (4.16), (4.20), and (4.33) apply to both scenarios.

Substituting (4.45) and $\omega = \omega_f \frac{R\overline{v}_r}{c}$ (see Chapter 3) into (4.44),

$$P_{density\_output\_section} = \frac{{v_{b,RMS}}^2 {k_p}^{out^2}}{cs_{11}^E \omega_f R\overline{v}_r \left(1-\sigma_C^{E^{out}}\right)\left(1-{k_p}^{out^2}\right)}. \tag{4.47}$$

Repeating this process for the capacitively smoothed DC-output topologies results in

$$P_{density\_output\_section} = \frac{{v_{b,RMS}}^2 {k_p}^{out^2}}{cs_{11}^E \omega_f R\overline{v}_r \left(1-\sigma_C^{E^{out}}\right)\left(1-{k_p}^{out^2}\right)}\left(\frac{2}{\pi}\right). \tag{4.48}$$

Likewise, for the inductively smoothed topologies

$$P_{density\_output\_section} = \frac{{v_{b,RMS}}^2 {k_p}^{out^2}}{cs_{11}^E \omega_f R\overline{v}_r \left(1-\sigma_C^{E^{out}}\right)\left(1-{k_p}^{out^2}\right)}\left(\frac{8}{\pi^2}\right). \tag{4.49}$$

If the assumption is made that the maximum vibration velocity that can be used (due to thermal considerations) is independent of the PT design and determined only by the piezoelectric material, then it is clear from (4.47) to (4.49) that, for a given outer radius, a capacitively smoothed DC-output design will achieve $2/\pi$ times the maximum PT power density of an AC-output design, and an inductively smoothed DC-output design will achieve $8/\pi^2$ times the maximum PT power density of an AC-output design.

As discussed in Chapter 3, the maximum vibration velocity that can be used is also dependent on various design factors. Thus, whilst it is fairly clear that a given PT with a capacitively smoothed and inductively smoothed rectifier will achieve $2/\pi$ and $8/\pi^2$ times the output power that could be achieved with the AC-output topology, the same can only be said from a more general design perspective (where R_L is fixed) if the maximum vibration velocity that can be used is assumed to be independent of the PT design.

When designing a PT, the maximum vibration velocity that can be used is often assumed approximately constant for the first design iteration [26]. Therefore to a similar level of approximation, the $2/\pi$ and $8/\pi^2$ factors should hold.

4.5 Thermal behaviour of a PT at high power levels

The thermal behaviour of the T1-15W Transoner PT is now shown at high output power levels. The PT was operated in the AC-output topology with a load resistance of 960Ω at a frequency of 130kHz. The difference between the steady-state PT temperature and the ambient temperature is shown as a function of PT output power in Figure 4.11. At low power levels the temperature rise is proportional to output power. Once the output power reaches 14W the characteristic begins to change, and as the output power exceeds 18W the increase in temperature with PT output power begins to look exponential.

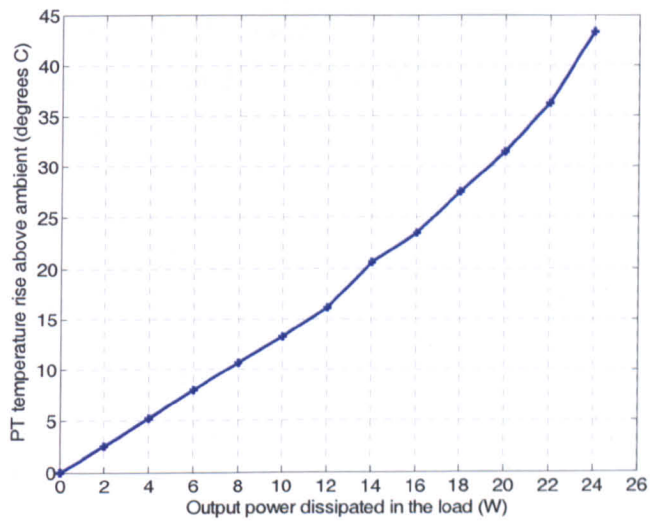

Figure 4.11: PT temperature rise (i.e. PT temperature – ambient temperature) against PT output power, recorded using the AC-output topology at 130kHz with a 960Ω load. The ambient temperature remained between 22.5 and 24°C throughout the experiment.

When the output power was increased from 24W to 26W, the PT temperature initially rose relatively slowly. Once the PT temperature exceeded about 95°C (72°C above ambient) there was a definite change in behaviour and the temperature rose extremely rapidly. The experiment was discontinued once the PT temperature exceeded 150°C as the device was clearly in a state of thermal runaway. Since operation at 26W resulted in thermal runaway, no temperature could be obtained for this point. The rate of change of temperature with output power (i.e. the gradient of Figure 4.11) is therefore essentially infinite at 26W.

The transient temperature behaviour as the PT approaches thermal runaway is shown in Figure 4.12. Note that Figure 4.12 shows the absolute PT temperature, not the difference between the PT temperature and the ambient temperature. In this experiment, the T1-15W PT was operated in the AC-output configuration with a 2004Ω load at

122kHz whilst maintaining 12W constant output power. It can be seen that the initial trajectory of the temperature rise appears to be approximately first order, and the rate of change of temperature with time is decreasing with time. However, somewhere between 75°C and 85°C this begins to change. By the time 88°C is reached the rate of change of temperature with time is clearly increasing with time, indicating a thermal runaway condition. The rate of temperature increase becomes extremely rapid once 95°C is reached. It has been shown in [15] (and many others) that the Q_m of a piezoelectric material decreases as temperature increases. Furthermore, the dielectric loss tangent $\tan(\delta)$ of the APC841 material used in the T1-15W increases with temperature [22]. Therefore both mechanical and dielectric losses increase with temperature, causing a further increase in temperature, and it is this mechanism that that is likely to cause the thermal runaway condition.

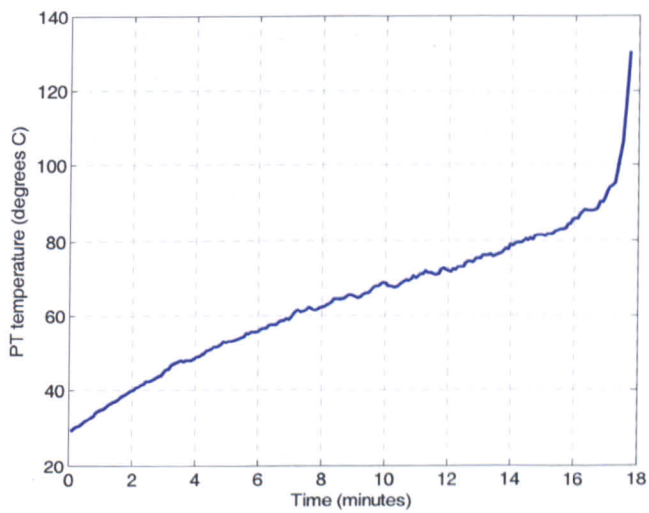

Figure 4.12: Transient temperature profile of the T1-15W PT with a 2004Ω load in the AC-output topology operating at 122kHz with 12W constant output power. The ambient temperature was approximately 24.5°C.

The results from this section reinforce the concept that the maximum output power of a PT is thermally limited, and therefore reinforce the importance of the results described in Sections 4.2, 4.3, and 4.4.

4.6 Effect of the rectifier topology on output section layer number

When choosing a rectifier for a PT-based converter, an important consideration is the number of layers that will be required to achieve the optimum load condition (see

column 2 of Table 4.1) and required output power. Consider the full-bridge capacitively smoothed topology. The power dissipated in the load resistance, P_{out}, is given in terms of the total PT output power as

$$P_{out} = \frac{P_{out,PT}}{(1+2V_{df})} = \frac{A_{out}{}^2 v_{b,RMS}{}^2 R_s}{(1+2V_{df})} \tag{4.50}$$

where the rectifier efficiency as described by the analyses on which the RC rectifier models are based has been used (see Table 4.1). When the optimum load condition is used, $R_s = R_s{}^{max}$. Substituting (4.10) into (4.50)

$$P_{out} = \frac{A_{out}{}^2 v_{b,RMS}{}^2}{(1+2V_{df})\pi\omega C_{out}}. \tag{4.51}$$

Solving (4.9) for C_{out} and substituting into (4.51), and then solving for A_{out}

$$A_{out} = \left(\frac{1}{\sqrt{2}}\right)\frac{\pi\sqrt{P_{out}}}{v_{b,RMS}\sqrt{R_L}}. \tag{4.52}$$

Repeating this process for the half-wave capacitively smoothed, full-bridge inductively smoothed, and current doubler topologies gives

$$A_{out} = \left(\sqrt{2}\right)\frac{\pi\sqrt{P_{out}}}{v_{b,RMS}\sqrt{R_L}} \tag{4.53}$$

$$A_{out} = \left(\frac{1}{2}\right)\frac{\pi\sqrt{P_{out}}}{v_{b,RMS}\sqrt{R_L}} \tag{4.54}$$

$$A_{out} = \left(\frac{1}{4}\right)\frac{\pi\sqrt{P_{out}}}{v_{b,RMS}\sqrt{R_L}} \tag{4.55}$$

respectively. From Chapter 3, A_{out} is proportional to bn_{out} (assuming that the output section radius is larger than or equal to the input section radius). Therefore it can be seen that for a given output power level, vibration velocity, load resistance, output section electrode radius, and outer radius, the half-wave capacitively smoothed topology requires 2 times as many output section layers as the full-bridge capacitively smoothed topology, the full-bridge inductively smoothed requires $\sqrt{2}/2 = 0.707$ times as many layers as the full-bridge capacitively smoothed topology, and the current doubler requires $\sqrt{2}/4 = 0.354$ times as many layers as the full-bridge capacitively smoothed topology. Since (4.52) to (4.55) show that the number of layers required increases with decreasing load resistance, and since a high number of layers tends to reduce $\overline{Q}_m$ (and therefore increase heat generation) and make the device more difficult to fabricate, the inductively smoothed topologies (and the current doubler in particular) are the most suitable when designing for low impedance loads.

4.7 Summary

The choice of output topology has been shown to have an important effect on the maximum output power that can be obtained from a given PT. The DC-output topologies considered in this chapter all result in lower PT power density than the AC-output topology, and this will make it harder for PTs to compete with their magnetic counterparts in DC-output applications where power density is the main consideration. Since it was shown that the inductively smoothed topologies achieve higher PT power density than the capacitively smoothed, there is a trade off between the use of an inductively smoothed topology to increase PT power density, and the increase in cost and size that the inductor brings.

It may be productive for other researchers to consider trying to develop new rectifier topologies that do not suffer the decrease in power density. One strategy that appeared to work (i.e. that allowed a higher maximum output power to be obtained for a given level of equivalent circuit tank current with a given PT) in simulation was to deliberately undersize the filter inductance(s) in the inductively smoothed topologies, such that the inductor current(s) had a substantial ripple, or even became discontinuous. However, this approach has not yet been investigated practically.

Compared to ferrites, "high-power" piezoelectric materials are somewhat less developed. The theory from Chapters 2, 3, and 4 certainly suggests that the development of piezoelectric materials that are capable of operating at high vibration velocities in a thermally stable manner will allow PTs to achieve much higher power densities. Materials capable of operating at 1m/s have been demonstrated in [27], but these have yet to be employed in commercial devices. If such materials are realised, and power density increases, then the fact that the existing range of rectifiers result in lower PT power density than the AC-output topology may become much less of an issue because the power density of the PT would still be substantially higher than that of a conventional transformer in some applications. High temperature stability is an area where ferrites currently have a distinct advantage; conventional converters that operate with a ferrite temperature of 90°C are readily available, whereas 20 or 30°C above ambient is usually treated as the maximum for PTs made with today's piezoelectric

ceramics. This inability to operate in a thermally stable manner at high temperatures is important, because the time rate of heat transfer (units: watts) away from the PT due to convection is proportional to the temperature difference between the PT and the surrounding air (see Newton's law of cooling, page 19 of [28], or page 4 of [29]). Hence, heat generated by the PT losses is removed much less effectively when the maximum temperature difference between the PT and its surroundings is heavily constrained.

4.8 References

[1] G. Ivensky, S. Bronstein, and S. Ben-Yaakov, "A Comparison of Piezoelectric Transformer AC/DC Converters with Current Doubler and Voltage Doubler Rectifiers," *IEEE Transactions on Power Electronics*, vol. 19, pp. 1446-1453, 2004.

[2] S. Bronstein, "Piezoelectric Transformers in Power Electronics," PhD thesis, Ben-Gurion University of the Negev, Israel, 2005.

[3] A. J. Forsyth, G. A. Ward, and S. V. Mollov, "Extended fundamental frequency analysis of the LCC resonant converter," *IEEE Transactions on Power Electronics*, vol. 18, pp. 1286-1292, 2003.

[4] T. Yamane, S. Hamamura, T. Zaitsu, T. Ninomiya, M. Shoyama, and Y. Fuda, "Efficiency Improvement of Piezoelectric-Transformer DC-DC Converter," presented at IEEE Power Electronics Specialists Conference (PESC), 1998.

[5] S. Choi, T. Kim, and B. H. Cho, "Design of half-bridge piezo-transformer converters in the AC adapter applications," presented at Conference Proceedings - IEEE Applied Power Electronics Conference and Exposition - APEC, 2005.

[6] Y.-P. Liu, D. Vasic, F. Costa, W.-J. Wu, and C. K. Lee, "Design Considerations of Piezoelectric Transformers with Voltage-Mode Rectifiers for DC/DC Converter Application," presented at IEEE Industrial Electronics Conference (IECON), 2008.

[7] M. Umeda, S. Takahashi, Y. Sasaki, K. Nakamura, and S. Ueha, "Vibration stress and temperature dependence of piezoelectric resonators with lead-zirconate-titanate ceramics," *Electronics and Communications in Japan, Part II: Electronics*, vol. 83, pp. 1-7, 2000.

[8] S. Takahashi, M. Yamamoto, and Y. Sasaki, "Nonlinear Piezoelectric Effect in Ferroelectric Ceramics," *Japanese Journal of Applied Physics, Part 1*, vol. 37, pp. 5292-5296, 1998.

[9] K. Uchino, A. Joshi, Y.-H. Chen, and Yoshikawa, "High Power Characterization of Piezoelectric Materials," *Journal of Electroceramics*, vol. 2, pp. 33-40, 1998.

[10] K. Uchino, "High Power Piezoelectrics," in *Advanced Piezoelectric Materials: Science and Technology*, K. Uchino, Ed.: Woodhead Publishing Ltd, 2010.

[11] M. Katsuno, Y. Fuda, and M. Tamura, "High-Power Ceramic Materials for Piezoelectric Transformers," *Electronics and Communications in Japan, Part 3*, vol. 82, pp. 86-92, 1999.

[12] S. Hirose, S. Takahashi, M. Aoyagi, and Y. Tomikawa, "High-Power Characteristics of Piezoelectric Materials," presented at Ninth IEEE International Symposium on Applications of Ferroelectrics, 1995.

[13] S. Takahashi and S. Hirose, "Vibration-Level Characteristics for Iron-Doped Lead-Zirconate-Titanate Ceramic," *Japanese Journal of Applied Physics, Part 1*, vol. 32, pp. 2422-2425, 1993.

[14] S. Takahashi and S. Hirose, "Vibration-Level Characteristics of Lead-Zirconate-Titanate Ceramics," *Japanese Journal of Applied Physics, Part 1*, vol. 31, pp. 3055-3057, 1992.

[15] Y. Sasaki, M. Umeda, S. Takahashi, M. Yamamoto, A. Ochi, and T. Inoue, "High-power Characteristics of Multilayer Piezoelectric Ceramic Transducers," *Japanese Journal of Applied Physics, Part 1*, vol. 40, 2001.

[16] M. Umeda, K. Nakamura, and S. Ueha, "Effects of Vibration Stress and Temperature on the Characteristics of Piezoelectric Ceramics under High Vibration Amplitude Levels Measured by Electrical Transient Responses," *Japanese Journal of Applied Physics, Part 1*, vol. 38, pp. 5581-5585, 1999.

[17] M. P. Foster, H. I. Sewell, C. M. Bingham, D. A. Stone, and D. Howe, "Methodologies for the design of LCC voltage-output resonant converters," *IEE Proceedings - Electric Power Applications*, vol. 153, pp. 559-567, 2006.

[18] S. Ural, S. Tuncdemir, Y. Zhuang, and K. Uchino, "Development of a High Power Piezoelectric Characterization System and Its Application for Resonance/Antiresonance Mode Characterization," *Japanese Journal of Applied Physics*, vol. 48, 2009.

[19] Y. Zhuang, S. Ural, R. Gosain, S. Tuncdemir, A. Amin, and K. Uchino, "High Power Piezoelectric Transformers with Pb(Mg1/3Nb2/3)O3-PbTiO3 Single Crystals," *Applied Physics Express*, vol. 2, pp. 121402-1 to 121402-2, 2009.

[20] K. Sakurai, K. Ohnishi, and Y. Tomikawa, "Presentation of a New Equivalent Circuit of a Piezoelectric Transformer under High-Power Operation," *Japanese Journal of Applied Physics, Part 1*, vol. 38, pp. 5592-5597, 1999.

[21] T. Ezaki, S. Manuspiya, P. Moses, K. Uchino, and A. V. Carazo, "Piezoelectric Transformers For A High Power Module," *Materials Technology*, vol. 19, pp. 79-83, 2004.

[22] L. Burianova, M. Prokopova, M. Pustka, and J. Nosek, "Characterization of the hard APC841 ceramics, report no. 2," Technical University of Liberec, supplied by American Piezo Ceramics, 2005.

[23] K. Uchino and S. Hirose, "Loss Mechanisms in Piezoelectrics: How to Measure Different Losses Seperately," *IEEE Transactions on Ultrasonics, Ferroelectrics, and Frequency Control*, vol. 48, pp. 307-321, 2001.

[24] E. M. Baker, "Design of Radial Mode Piezoelectric Transformers for Lamp Ballast Applications," MSc thesis, Virginia Polytechnic Institute and State University, USA, 2002.

[25] A. J. Forsyth and S. V. Mollov, "Simple equivalent circuit for the series-loaded resonant converter with voltage boosting capacitor," *IEE Proceedings - Electric Power Applications*, vol. 145, pp. 301-306, 1998.

[26] A. V. Carazo, "Piezoelectric Converters for DC/DC and AC/DC applications," presented at Portable Power Developer's Conference, 2005.

[27] Z. Zhu, G. Li, B. Li, Q. Yin, and K. Jiang, "The influence of Yb and Nd substituents on high-power piezoelectric properties of PMS-PZT ceramics," *Ceramics International*, vol. 34, pp. 2067-2072, 2008.

[28] J. H. Lienhard IV and J. H. Lienhard V, *A Heat Transfer Textbook (Fourth Edition)*: Dover Publications, 2011.

[29] K.-F. V. Wong, *Intermediate Heat Transfer*: Marcel Dekker, Inc., 2003.

Chapter 5 - Analysis of inductor-less zero-voltage-switching piezoelectric transformer based converters

5.1 Introduction

This chapter analyses the requirements for achieving zero-voltage-switching (ZVS) with the half-bridge inductor-less PT-based converter topology.

When a PT is used with a half-bridge inverter, an additional inductor is usually placed in series with the PT input, as shown in Chapter 1. This is primarily done to ensure that the MOSFETs in the half-bridge operate with ZVS, but also reduces the harmonic content of the PT input voltage compared to the mid-point of the half-bridge. However, since inductors are relatively expensive and bulky, there has been considerable effort by several research teams to remove this component [1-6].

The lumped equivalent circuit model for a PT is topologically similar to a conventional LCC series-parallel converter, but with an additional capacitance across the PT input. When used in the inductor-less topology, such as the AC-output variant shown in Figure 5.1, the output capacitance of the MOSFETs is augmented by the input capacitance of the PT, C_{in}. Since the former is of the order of tens to hundreds of pF, whereas the latter is often several nF, the amount of charge that must be delivered by the tank current i_{L1} during the dead-time in order for the next MOSFET in the switching sequence to turn on under ZVS conditions is much greater than that required by a conventional discrete resonant converter. A much larger dead-time must also be used in order to provide sufficient time for this charge to be delivered. Therefore inductor-less converters will typically be operated further above resonance than their conventional counterparts because the maximum dead-time (the time between one MOSFET being turned off and the other MOSFET being turned on) that can be used is dictated by the time between the low-side MOSFET (i.e. S_2 in Figure 5.1) turning off and the tank current crossing zero, which in turn is partly dictated by the phase angle at which the tank is operated. Since the total capacitance across the half-bridge is considerable, the voltage across the MOSFETs is heavily snubbed during turn-off. Therefore ZVS turn-off is easily obtained, and the primary concern throughout the rest of this chapter is the need for ZVS turn-on.

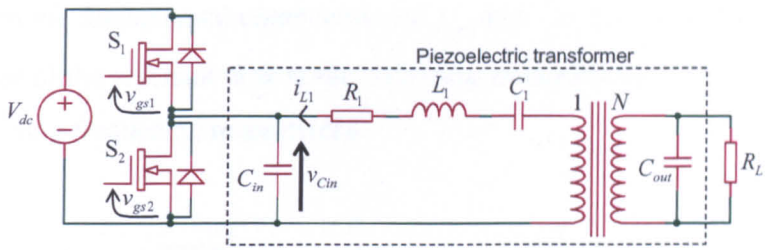

Figure 5.1: Inductor-less PT-based AC-output converter.

If the PT input capacitance is too large, the tank current will not be able to supply sufficient charge during the dead-time and ZVS will not be achieved. Since the total capacitance across the half-bridge is much larger compared to a discrete converter, the power dissipation that occurs in the MOSFET switches if ZVS is not achieved is also much greater. Whilst reducing the PT input capacitance will allow inductor-less ZVS to be achieved more readily, it will also decrease power density because the size of the input section must be increased, and this increase does not alter the theoretical, thermally-limited, maximum output power of the PT (this will be shown in Chapter 6). Therefore the PT input capacitance should be sized such that ZVS can be obtained over the required load and frequency range, but without compromising power density any further than is necessary.

This chapter describes the development of an analytical model for the ZVS condition in inductor-less PT-based converters. This is shown to offer accuracy comparable to a SPICE simulation and forms the basis for a numerical determination of the design criteria that ensure ZVS. Design charts are then presented for achieving inductor-less ZVS with any type of PT in 5 different topologies, thereby greatly reducing the need for iterative design and simulation. Note that the model and the design charts are applicable to any type of PT that can be modelled with the standard PT equivalent circuit (shown in the dotted box in Figure 5.1).

5.2 Inductor-less PT-based converter operation

The voltage and current waveforms for an AC-output inductor-less converter that is operating with a matched load ($R_L = 1/\omega C_{out}$) are shown in Figure 5.2. The input capacitance has been sized such that ZVS can only just be achieved when the optimum

frequency and dead-time for ZVS are used. The quantities ϕ and ω refer to the phase angle between the fundamental components of v_{Cin} and $-i_{L1}$ (i.e. ϕ is the phase angle of the impedance of the resonant tank at the switching frequency of the converter), and the angular switching frequency, respectively.

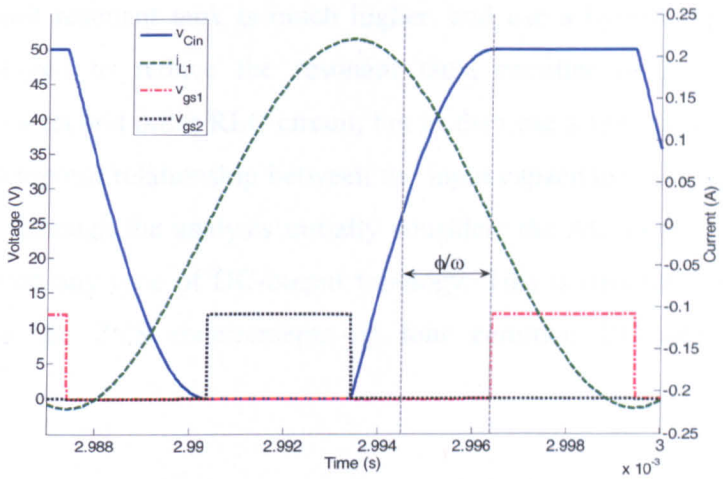

Figure 5.2: SPICE simulation of the steady-state voltage and current waveforms for a converter that can only just achieve ZVS.

It can be seen from Figure 5.2 that the dead-time required to achieve ZVS takes up a large proportion of the total switching period. As the tank current changes considerably during this time, the constant current assumption that is used to analyse discrete converters [7], and which has subsequently been applied to PTs [1, 3, 6], is not accurate for this type of converter.

Whilst the relationship between the tank current and the fundamental component of the input capacitance voltage is immediately known through knowledge of the tank impedance, the time between the zero-crossing of the tank current and the MOSFET switching signals is not. Therefore it is difficult to ascertain the correct time limits over which to integrate the tank current in order to find the change in input capacitance voltage during the dead-time when using a frequency domain approach. In [4], the period over which to integrate was taken as twice the phase shift between the fundamental components of v_{Cin} and $-i_{L1}$, but as Figure 5.2 suggests, this is likely to give an overly optimistic result.

To address the aforementioned issues, a novel, largely time domain analysis of the half-bridge inductor-less PT-based converter is presented. Whilst time-domain approaches

have been applied to discrete converter analysis in [8-11], these are necessarily topology specific (either DC-output capacitively smoothed or DC-output inductively smoothed) because fundamental mode approximation (FMA) cannot be applied due to the low Q factor and non-sinusoidal tank current that is often associated with conventional discrete converters. The approach taken here is to capitalise on the fact that the Q factor of a PTs equivalent circuit resonant tank is much higher, and use a hybrid approach whereby FMA is employed to reduce the resonant tank, rectifier (if present), and load combination to a second order RLC circuit, but to then use a time-domain analysis that preserves the temporal relationship between the input capacitance voltage and the tank current. Thus, although the analysis initially considers the AC-output topology, it can also be used with any type of DC-output topology. This is demonstrated in the latter sections where the ZVS requirements of four common DC-output variants are presented.

5.3 Analysis

The following analysis assumes that the behaviour of the PT is dominated by the vibration mode that corresponds to the switching frequency, and that the influence of the dielectric losses is negligible.

ZVS will occur if the voltage across the input capacitance is equal to the DC link voltage (or clamped by the high-side body diode to just above the DC link voltage) when the high-side MOSFET (i.e. S_1 in Figure 5.1) is switched on, and equal to 0V (or clamped by the low-side body diode to just below 0V) when the low-side MOSFET is switched on. Since the dead-times and on-times of the MOSFETs are equal, ZVS in one MOSFET implies ZVS in the other. Therefore to evaluate when ZVS can be achieved, an expression to calculate the voltage across the input capacitance at the end of the dead-time prior to the high-side MOSFET turning on is developed as a function of the PT equivalent circuit components, switching frequency, and dead-time.

Since the loaded Q factor of the resonant tank in a PT-based converter is greater than 2.5, the tank current is considered to be sinusoidal [7]. Since FMA can then be applied to both AC-output and DC-output variants of the inductor-less topology, the ZVS

behaviour of both variants can be modelled with the circuit shown in Figure 5.3. The total effective capacitance at the PT input is

$$C_{eff} = C_{in} + 2C_{oss} \tag{5.1}$$

where C_{oss} is the effective value of the output capacitance of a single MOSFET. For the AC-output topology shown in Figure 5.1, the circuit elements in Figure 5.3 are given by

$$R_x = R_1 + \frac{R_L}{N^2\left(R_L{}^2\omega^2 C_{out}{}^2 + 1\right)} \tag{5.2}$$

$$C_x = \frac{C_1 N^2\left(R_L{}^2\omega^2 C_{out}{}^2 + 1\right)}{C_1 R_L{}^2\omega^2 C_{out} + N^2\left(R_L{}^2\omega^2 C_{out}{}^2 + 1\right)}. \tag{5.3}$$

At any point in the switching cycle, the circuit of Figure 5.3 will be in one of 6 possible modes, equivalent circuits for which are shown in Figure 5.4. Schematically modes 1 and 4 are identical, though mode 1 is used to denote the case where i_{L1} is positive and mode 4 the case where i_{L1} is negative.

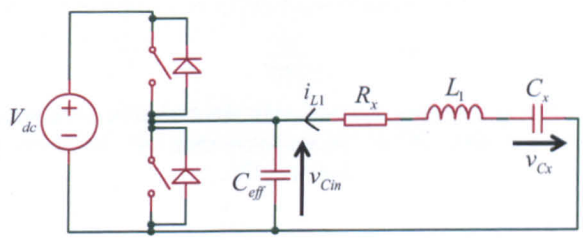

Figure 5.3: Simplified circuit for modelling the ZVS behaviour of both AC-output and DC-output inductor-less PT-based converters.

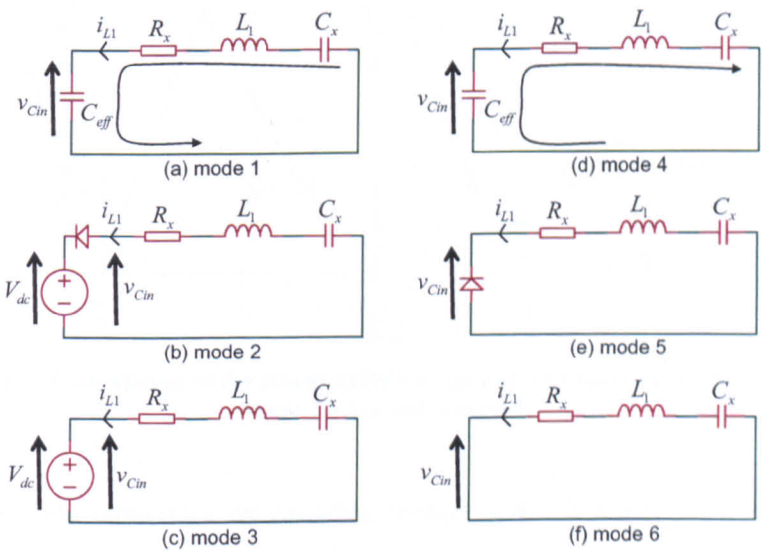

Figure 5.4: Equivalent circuits for inductor-less PT-based converter operation.

The mode sequence and steady-state voltage and current waveforms for a converter where ZVS is achieved and the MOSFET body diodes conduct is shown in Figure 5.5. t_d and T refer to the dead-time and switching period respectively. When ZVS is only just achieved, as shown in Figure 5.2, modes 2 and 5 are omitted and the sequence is 1-3-4-6. When ZVS is not achieved, and the phase angle of the tank impedance is inductive, the mode sequence is also usually 1-3-4-6, as shown in Figure 5.6.

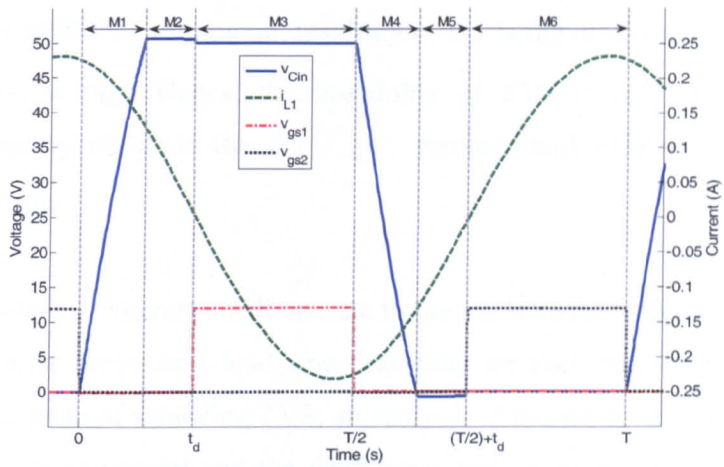

Figure 5.5: SPICE simulation of the steady-state voltage and current waveforms for a converter where ZVS is easily achieved. The abbreviations M1 to M6 refer to modes 1 to 6 described in Figure 5.4.

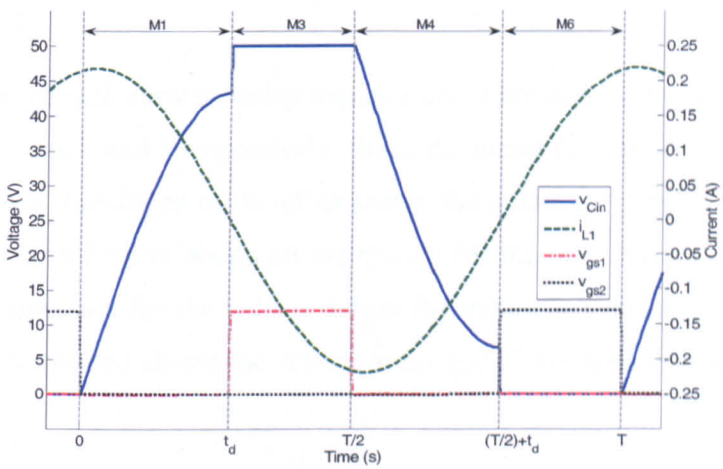

Figure 5.6: SPICE simulation of the steady-state voltage and current waveforms for a converter where ZVS is not achieved.

Several other mode sequences are possible, including 4-5-3-1-2-6, 1-2-4-5-3-4-5-1-2-6, 1-4-3-4-1-6, 1-4-5-3-4-1-2-6, and 4-3-1-6 when the frequency is such that the phase angle of the tank is capacitive, and 1-2-4-5-3-4-5-1-2-6, 1-2-4-3-4-5-1-6, 1-4-3-4-1-6, 1-4-5-3-4-1-2-6, 4-1-3-1-4-6, and 4-5-1-3-1-2-4-6 when the frequency is such that the

phase angle of the tank is inductive. The sequence 1-4-5-3-4-1-2-6 can occur when the tank impedance phase angle is inductive or capacitive.

ZVS can only be achieved when the switching frequency is such that the phase angle of the impedance of the resonant tank is inductive because i_{L1} must be positive just prior to the high-side MOSFET turning on. If the phase angle is capacitive, then the relationship between i_{L1} and the fundamental component of v_{Cin} is such that i_{L1} is negative just prior to the high-side MOSFET turning on, resulting in C_{eff} being discharged (or the low-side body diode conducting). Hence, the possibility of ZVS is only present when the switching frequency results in the R_x, L_1, C_x resonant tank exhibiting predominately inductive behaviour.

Since an inductor-less converter will operate in the mode sequence shown in Figure 5.6 when the converter, frequency, load, and dead-time are such that the converter is just below, or on the point of achieving ZVS, an analysis of this mode sequence is made. As the tank current is sinusoidal and the dead-times and on-times of the MOSFETs are equal, only modes 1 and 3 need be considered in order to obtain a solution for the tank current and input capacitance voltage during mode 1 when the converter is in steady-state.

Expressions for the tank current during modes 1 and 3 are derived in terms of the initial conditions of modes 1 and 3 respectively. Since the initial conditions for one mode are related to the final conditions of the other mode, the unknown initial conditions in the two modes can be solved to obtain an expression for the tank current during mode 1. Obtaining an expression for the voltage across the input capacitance during mode 1 is then relatively simple and allows the voltage at the end of the dead-time to be found.

A. Analysis of mode 1

With reference to Figure 5.6, mode 1 begins at $t = 0$ and ends at $t = t_d$, where t_d is the dead-time between one MOSFET turning off and the other turning on. Applying Kirchhoff's voltage law to Figure 5.4a, the governing equation for the equivalent circuit of mode 1 is

$$\frac{1}{C_{eff}}\int_0^t i_{L1}(t)dt + v_{Cin}(0) + i_{L1}(t)R_x + L_1\frac{di_{L1}(t)}{dt} + \frac{1}{C_x}\int_0^t i_{L1}(t)dt + v_{Cx}(0) = 0 \tag{5.4}$$

where $v_{Cin}(0)$ and $v_{Cx}(0)$ are the voltages across the PT input capacitance and C_x capacitance at $t=0$. Note that $v_{Cin}(0)=0$ because the low-side MOSFET has been on during the previous mode. Differentiating (5.4) with respect to t results in the following second order homogeneous differential equation

$$\frac{1}{C_{eff}}i_{L1}(t) + R_x\frac{di_{L1}(t)}{dt} + L_1\frac{d^2i_{L1}(t)}{dt^2} + \frac{1}{C_x}i_{L1}(t) = 0. \tag{5.5}$$

The solution to (5.5) is of the form

$$i_{L1}(t) = B_1e^{\alpha_1 t} + B_2e^{\beta_1 t} \tag{5.6}$$

where

$$\alpha_1 = \frac{-C_{eff}C_xR_x + \sqrt{C_{eff}{}^2C_x{}^2R_x{}^2 - 4C_{eff}C_x{}^2L_1 - 4C_{eff}{}^2C_xL_1}}{2C_{eff}C_xL_1} \tag{5.7}$$

$$\beta_1 = \frac{-C_{eff}C_xR_x - \sqrt{C_{eff}{}^2C_x{}^2R_x{}^2 - 4C_{eff}C_x{}^2L_1 - 4C_{eff}{}^2C_xL_1}}{2C_{eff}C_xL_1}. \tag{5.8}$$

The constants B_1 and B_2 are then found in terms of the voltages and currents at the beginning of the mode. Substituting $t=0$ into (5.6),

$$i_{L1}(0) = B_1 + B_2. \tag{5.9}$$

Substituting (5.6) into (5.4), and setting $t=0$,

$$v_{Cin}(0) + R_x(B_1 + B_2) + L_1(B_1\alpha_1 + B_2\beta_1) + v_{Cx}(0) = 0. \tag{5.10}$$

Since $v_{Cin}(0)=0$, solving the simultaneous equations (5.9) and (5.10) for B_1 and B_2 yields

$$B_1 = \frac{i_{L1}(0)R_x + i_{L1}(0)\beta_1L_1 + v_{Cx}(0)}{L_1(\beta_1 - \alpha_1)} \tag{5.11}$$

$$B_2 = \frac{i_{L1}(0)R_x + i_{L1}(0)\alpha_1L_1 + v_{Cx}(0)}{L_1(\alpha_1 - \beta_1)}. \tag{5.12}$$

The tank current and C_x voltage at the end of mode 1 are then found in terms of the initial conditions of mode 1. Substituting $t=t_d$ into (5.6), and making use of (5.11) and (5.12),

$$i_{L1}(t_d) = K_1i_{L1}(0) + K_2v_{Cx}(0) \tag{5.13}$$

where

$$K_1 = \frac{(R_x + \alpha_1L_1)e^{\beta_1t_d} - (R_x + \beta_1L_1)e^{\alpha_1t_d}}{L_1(\alpha_1 - \beta_1)} \tag{5.14}$$

$$K_2 = \frac{e^{\beta_1t_d} - e^{\alpha_1t_d}}{L_1(\alpha_1 - \beta_1)}. \tag{5.15}$$

The voltage across C_x during mode 1 is given by

$$v_{Cx}(t) = \frac{1}{C_x}\int_0^t i_{L1}(t)dt + v_{Cx}(0) \tag{5.16}$$

therefore substituting (5.6), (5.11), and (5.12) into (5.16), evaluating, and setting $t = t_d$,

$$v_{Cx}(t_d) = K_3 i_{L1}(0) + K_4 v_{Cx}(0) \tag{5.17}$$

where

$$K_3 = \frac{\left(\left(R_x\alpha_1 + L_1\alpha_1^2\right)e^{\beta_1 t_d} - \left(R_x\beta_1 + \beta_1^2 L_1\right)e^{\alpha_1 t_d} + L_1\left(\beta_1^2 - \alpha_1^2\right) + R_x\left(\beta_1 - \alpha_1\right)\right)}{C_x L_1\alpha_1\beta_1\left(\alpha_1 - \beta_1\right)} \tag{5.18}$$

$$K_4 = \frac{\alpha_1\left(e^{\beta_1 t_d} - 1\right) - \beta_1\left(e^{\alpha_1 t_d} - 1\right) + C_x L_1\alpha_1\beta_1\left(\alpha_1 - \beta_1\right)}{C_x L_1\alpha_1\beta_1\left(\alpha_1 - \beta_1\right)}. \tag{5.19}$$

B. Analysis of mode 3

With reference to Figure 5.6, mode 3 begins at $t = t_d$ and ends at $t = T/2$, where T is the switching period. From Figure 5.4c, the governing equation for mode 3 is

$$V_{dc} + i_{L1}(t)R_x + L_1\frac{di_{L1}(t)}{dt} + \frac{1}{C_x}\int_{t_d}^t i_{L1}(t)dt + v_{Cx}(t_d) = 0 \tag{5.20}$$

where $v_{Cx}(t_d)$ is the voltage across C_x at the beginning of mode 3. Differentiating (5.20) with respect to t, the differential equation for mode 3 is

$$R_x\frac{di_{L1}(t)}{dt} + L_1\frac{d^2 i_{L1}(t)}{dt^2} + \frac{1}{C_x}i_{L1}(t) = 0. \tag{5.21}$$

From the solution to (5.21), the current during mode 3 is of the form

$$i_{L1}(t) = B_3 e^{\alpha_2 t} + B_4 e^{\beta_2 t} \tag{5.22}$$

where

$$\alpha_2 = \frac{-C_x R_x + \sqrt{C_x^2 R_x^2 - 4C_x L_1}}{2C_x L_1} \tag{5.23}$$

$$\beta_2 = \frac{-C_x R_x - \sqrt{C_x^2 R_x^2 - 4C_x L_1}}{2C_x L_1}. \tag{5.24}$$

The constants B_3 and B_4 can be found in terms of the initial voltages and currents at the start of mode 3,

$$B_3 = \frac{i_{L1}(t_d)R_x + i_{L1}(t_d)\beta_2 L_1 + v_{Cx}(t_d) + V_{dc}}{L_1 e^{\alpha_2 t_d}\left(\beta_2 - \alpha_2\right)} \tag{5.25}$$

$$B_4 = \frac{i_{L1}(t_d)R_x + i_{L1}(t_d)\alpha_2 L_1 + v_{Cx}(t_d) + V_{dc}}{L_1 e^{\beta_2 t_d}\left(\alpha_2 - \beta_2\right)}. \tag{5.26}$$

The current though L_1 and the voltage across C_x at the end of mode 3 can be found in terms of the initial conditions of mode 3 as

$$i_{L1}\left(\frac{T}{2}\right) = K_5 i_{L1}(t_d) + K_6 v_{Cx}(t_d) + K_6 V_{dc} \tag{5.27}$$

$$v_{Cx}\left(\frac{T}{2}\right) = K_7 i_{L1}(t_d) + K_8 v_{Cx}(t_d) + K_9 V_{dc} \tag{5.28}$$

where

$$K_5 = \frac{(R_x + L_1\alpha_2)e^{\beta_2\left(\frac{T}{2}-t_d\right)} - (R_x + \beta_2 L_1)e^{\alpha_2\left(\frac{T}{2}-t_d\right)}}{L_1(\alpha_2 - \beta_2)} \tag{5.29}$$

$$K_6 = \frac{e^{\beta_2\left(\frac{T}{2}-t_d\right)} - e^{\alpha_2\left(\frac{T}{2}-t_d\right)}}{L_1(\alpha_2 - \beta_2)} \tag{5.30}$$

$$K_7 = \frac{\left(L_1\alpha_2^{\,2} + R_x\alpha_2\right)e^{\beta_2\left(\frac{T}{2}-t_d\right)} - R_x(\alpha_2 - \beta_2) - \left(\beta_2^{\,2}L_1 + R_x\beta_2\right)e^{\alpha_2\left(\frac{T}{2}-t_d\right)} - L_1\left(\alpha_2^{\,2} - \beta_2^{\,2}\right)}{C_x L_1\alpha_2\beta_2(\alpha_2 - \beta_2)} \tag{5.31}$$

$$K_8 = \frac{\beta_2\left(1 - e^{\alpha_2\left(\frac{T}{2}-t_d\right)}\right) - \alpha_2\left(1 - e^{\beta_2\left(\frac{T}{2}-t_d\right)}\right) + C_x L_1\alpha_2\beta_2(\alpha_2 - \beta_2)}{C_x L_1\alpha_2\beta_2(\alpha_2 - \beta_2)} \tag{5.32}$$

$$K_9 = \frac{\beta_2\left(1 - e^{\alpha_2\left(\frac{T}{2}-t_d\right)}\right) - \alpha_2\left(1 - e^{\beta_2\left(\frac{T}{2}-t_d\right)}\right)}{C_x L_1\alpha_2\beta_2(\alpha_2 - \beta_2)}. \tag{5.33}$$

C. Solution for the initial conditions of mode 1

Since the dead-times and on-times of the MOSFETs are equal, the initial conditions of mode 1 are related to the final conditions of mode 3 by

$$i_{L1}(0) = -i_{L1}\left(\frac{T}{2}\right) \tag{5.34}$$

$$v_{Cx}(0) = -v_{Cx}\left(\frac{T}{2}\right) - V_{dc}. \tag{5.35}$$

Note that the $-V_{dc}$ term in (5.35) is due to the C_x capacitance blocking the DC component of v_{Cln} (hence the average value of v_{Cx} is $-V_{dc}/2$). Substituting (5.27) into (5.34) and (5.28) into (5.35) provides a second set of equations that relate the initial conditions of mode 1 to the final conditions of mode 1

$$i_{L1}(0) = -K_5 i_{L1}(t_d) - K_6 v_{Cx}(t_d) - K_6 V_{dc} \tag{5.36}$$

$$v_{Cx}(0) = -K_7 i_{L1}(t_d) - K_8 v_{Cx}(t_d) - K_9 V_{dc} - V_{dc}. \tag{5.37}$$

Then, by eliminating $i_{L1}(t_d)$ and $v_{Cx}(t_d)$ from the simultaneous equations (5.13), (5.17), (5.36), and (5.37), the initial conditions of the first mode are given by

$$i_{L1}(0)=\frac{V_{dc}\begin{pmatrix}K_5K_2K_9+K_5K_2+K_6K_4K_9+K_6K_4\\-K_6-K_6K_7K_2-K_6K_8K_4\end{pmatrix}}{\begin{pmatrix}1+K_5K_1+K_6K_3+K_7K_2+K_7K_2K_6K_3\\+K_8K_4+K_8K_4K_5K_1-K_5K_2K_8K_3-K_6K_4K_7K_1\end{pmatrix}} \tag{5.38}$$

$$v_{Cx}(0)=\frac{V_{dc}\begin{pmatrix}K_6K_7K_1+K_8K_3K_6-K_9-K_9K_5K_1\\-K_9K_6K_3-K_5K_1-K_6K_3-1\end{pmatrix}}{\begin{pmatrix}1+K_5K_1+K_6K_3+K_7K_2+K_7K_2K_6K_3\\+K_8K_4+K_8K_4K_5K_1-K_5K_2K_8K_3-K_6K_4K_7K_1\end{pmatrix}}. \tag{5.39}$$

Since a complete solution for the current during mode 1 has been obtained, the voltage across the input capacitance during mode 1 is given by

$$v_{Cin}(t)=\frac{1}{C_{eff}}\int_0^t i_{L1}(t)dt+v_{Cin}(0) \tag{5.40}$$

where $v_{Cin}(0)$ is zero. Substituting (5.6) into (5.40), followed by (5.11) and (5.12)

$$v_{Cin}(t)=\left(\frac{i_{L1}(0)R_x+i_{L1}(0)\beta_1L_1+v_{Cx}(0)}{L_1C_{eff}\alpha_1(\beta_1-\alpha_1)}\right)\left(e^{\alpha_1 t}-1\right)+\left(\frac{i_{L1}(0)R_x+i_{L1}(0)\alpha_1L_1+v_{Cx}(0)}{L_1C_{eff}\beta_1(\alpha_1-\beta_1)}\right)\left(e^{\beta_1 t}-1\right). \tag{5.41}$$

Hence, the voltage across the input capacitance at the end of the dead-time is given by

$$v_{Cin}(t_d)=\left(\frac{i_{L1}(0)R_x+i_{L1}(0)\beta_1L_1+v_{Cx}(0)}{L_1C_{eff}\alpha_1(\beta_1-\alpha_1)}\right)\left(e^{\alpha_1 t_d}-1\right)+\left(\frac{i_{L1}(0)R_x+i_{L1}(0)\alpha_1L_1+v_{Cx}(0)}{L_1C_{eff}\beta_1(\alpha_1-\beta_1)}\right)\left(e^{\beta_1 t_d}-1\right). \tag{5.42}$$

This is normalized with respect to the DC link voltage so that a value of 1 is obtained when ZVS is just achieved,

$$\tilde{v}_{Cin}(t_d)=\frac{v_{Cin}(t_d)}{V_{dc}}. \tag{5.43}$$

In effect, the above is an analysis of the converter if the MOSFET body diodes were not present. Therefore the result from (5.42) is only quantitative if the converter parameters, load, frequency, and dead-time in question are known to result in a mode sequence that does not include modes 2 and 5. This can be checked using (5.41). If (5.41) indicates that v_{Cin} remains $-V_{bd}<v_{Cin}<V_{dc}+V_{bd}$ throughout $0<t<t_d$ where V_{bd} is the MOSFET body diode on-state voltage drop, then $v_{Cin}(t_d)$ from (5.42) will be numerically accurate.

In cases where (5.41) indicates that $v_{Cin}<-V_{bd}$ at some point during $0<t<t_d$, and the phase angle of the tank is inductive, the mode sequence of the converter would actually be 1-4-5-3-4-1-2-6, 1-2-4-5-3-4-5-1-2-6, or 4-5-1-3-1-2-4-6. The first two sequences cannot result in ZVS because mode 1 or 2 does not immediately precede mode 3.

Furthermore, extensive SPICE simulation failed to find a scenario where, during the dead-time prior to the high-side MOSFET turning on, v_{Cin} could fall to $-V_{bd}$ and then subsequently rise all the way to V_{dc}. Thus, we believe 4-5-1-3-1-2-4-6 cannot result in ZVS either. From a practical perspective, 4-5-1-3-1-2-4-6 would never be used, not only because it cannot result in ZVS, but also because it typically requires a dead-time very close to half the switching period, thereby making it difficult to implement.

In cases where (5.41) indicates that $v_{Cin} > V_{dc} + V_{bd}$ at some point during $0 < t < t_d$, and the phase angle of the tank is inductive, the mode sequence of the converter would actually be 1-2-3-4-5-6, 1-2-4-3-4-5-1-6, or 1-2-4-5-3-4-5-1-2-6. The sequences 1-2-4-5-3-4-5-1-2-6 and 1-2-4-3-4-5-1-6 occur when the dead-time is too long in an otherwise ZVS capable converter, whilst 1-2-3-4-5-6 occurs when ZVS is achieved and the body diodes conduct and an appropriate dead-time is used. Thus, if (5.41) indicates that $v_{Cin} > V_{dc} + V_{bd}$ at some point during $0 < t < t_d$ and the phase angle of the tank is inductive, then the interpretation is that ZVS can be achieved with the converter, frequency, and load in question, though not necessarily with the dead-time in question.

If (5.42) indicates that $v_{Cin}(t_d) > V_{dc} + V_{bd}$, then ZVS can be achieved with the converter, frequency, and load in question, though not necessarily with the dead-time used in the calculation because the result is not numerically accurate due to modes 2 and 5 being entered. For example, certain combinations of converter, frequency, load, and dead-time result in the mode sequence 1-2-4-3-4-5-1-6 (which does not result in ZVS unless mode 4 is only entered extremely briefly prior to mode 3 commencing), but result in (5.42) indicating $v_{Cin}(t_d) > V_{dc} + V_{bd}$; in this situation, ZVS can be achieved with the converter, frequency, and load in question, but a shorter dead-time than that used in the calculation is required.

In practice, (5.42) will usually be evaluated with the dead-time (within the range $0 < t_d < T/2$) which maximises the result for a particular converter, frequency, and load. The result is then interpreted as follows:

- If $v_{Cin}(t_d) > V_{dc} + V_{bd}$, then $v_{Cin}(t_d)$ provides a qualitative measure of the margin by which ZVS is achieved if an appropriate dead-time is used.
- If $V_{dc} \le v_{Cin}(t_d) < V_{dc} + V_{bd}$, then $v_{Cin}(t_d)$ provides a quantitative measure of the margin by which ZVS is achieved.

- If $v_{Cin}(t_d) < V_{dc}$, and v_{Cin} remains above $-V_{bd}$ throughout $0 < t < t_d$, then $v_{Cin}(t_d)$ provides a quantitative measure of the margin by which ZVS is not achieved. (Since the dead-time is the one that maximises (5.42), the case of $v_{Cin}(t_d) < V_{dc}$ whilst also having v_{Cin} exceed V_{dc} at some point during $0 < t < t_d$ cannot occur).
- If $v_{Cin}(t_d) < V_{dc}$, and $v_{Cin} < -V_{bd}$ at some point during $0 < t < t_d$, then $v_{Cin}(t_d)$ provides a qualitative measure of the margin by which ZVS is not achieved.

The dead-time which maximises (5.42) is not necessarily the dead-time that would be used with the actual converter. However, evaluating (5.42) with the dead-time that maximises (5.42) for a particular converter, frequency, and load provides a definitive answer as to whether ZVS can be achieved with that converter, frequency, and load if an appropriate dead-time were used. This definitive answer is obtained using only (5.42) (i.e. there is no need to check whether $v_{Cin} < -V_{bd}$ or $v_{Cin} > V_{dc} + V_{bd}$ at some point during $0 < t < t_d$ using (5.41)); if (5.42) indicates that $v_{Cin}(t_d) \geq V_{dc}$ then ZVS can be achieved, if (5.42) indicates that $v_{Cin}(t_d) < V_{dc}$ then ZVS cannot be achieved. However, it must be remembered that the numerical result will not always be a quantitative measure of the margin by which ZVS is or is not achieved.

In summary, although the result from (5.42) is only numerically accurate for converters operating in certain mode sequences, the model can still be used to correctly assess whether ZVS can be achieved with a particular combination of converter, frequency, and load.

When design criteria for achieving ZVS are established in the latter sections, the model is used to find the relationships between the equivalent circuit component values that result in $v_{Cin}(t_d) = V_{dc}$ when using the frequency and dead-time that maximise (5.42). In these circumstances the mode sequence is always 1-3-4-6 and hence the results are always numerically accurate.

5.4 Model verification

To verify the accuracy of the new model, comparisons are made to SPICE simulations and experimental results from an AC-output converter running at constant frequency and constant dead-time. The SPICE model was based around voltage controlled switches (without diodes), rather than MOSFETs, because this allows the values for $v_{Cin}(t_d)$ to be compared in cases where ZVS would be achieved and the body diodes would otherwise conduct.

The converter was based around a Transoner T1-15W radial mode PT supplied by Micromechatronics Inc., USA. The equivalent circuit component values of the PT were measured with an Agilent 4294A impedance analyser as $C_{in} = 1.89\,\text{nF}$, $C_{out} = 1.28\,\text{nF}$, $L_1 = 10.70\,\text{mH}$, $C_1 = 166\,\text{pF}$, $R_1 = 8.54\,\Omega$, and $N = 0.934$. The MOSFETs used in the experimental converter were IRF510s, the combined parasitic output capacitance of which was estimated to be around 260pF for a DC link of 50V. The MOSFET timing signals were generated using a PIC® microcontroller.

$\tilde{v}_{Cin}(t_d)$ is shown in Figure 5.7 as a function of load resistance when switching at 120.5kHz with dead-time intervals of $t_d = 1.44\,\mu\text{s}$ and a DC link voltage of 50V. The model and SPICE predictions are extremely close to one another, whilst the predictions from the model are within 3.3% of the experimental results around $\tilde{v}_{Cin}(t_d) = 1$, and within 10.2% at $\tilde{v}_{Cin}(t_d) = 0.28$. The discrepancy between the simulated and experimental results is most likely due to changes in the equivalent circuit component values and the influence of other vibration modes. The equivalent circuit component values were measured at small signal levels with sinusoidal excitation. However, the excitation level in the converter is much larger, and this causes an increase in the PT losses. Furthermore, harmonics present in the voltage waveform across C_{in} will excite other modes of vibration within the PT, the effects of which are not included in the standard PT equivalent circuit. Since the harmonics become more pronounced as the margin by which ZVS is not obtained increases, it is to be expected that the accuracy of the model and SPICE predictions becomes worse when low values of $\tilde{v}_{Cin}(t_d)$ are obtained.

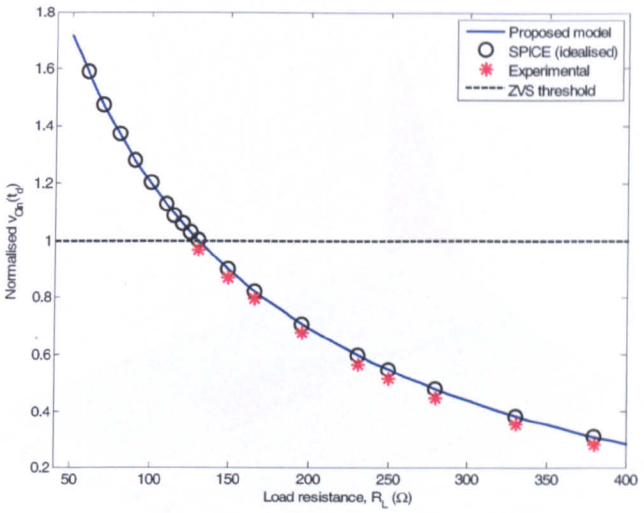

Figure 5.7 Change in $\tilde{v}_{Cin}(t_d)$ with load resistance for the T1-15W PT operating at 120.5kHz with 1.44μs dead-time intervals.

5.5 The ZVS profile of a PT

When analysing the ZVS capabilities of an inductor-less PT-based converter, it is useful to know the frequency and load range over which ZVS can be achieved, assuming that an appropriate dead-time is always used. By using numerical optimisation methods to find the value of dead-time within the range $0 < t_d < T/2$ that maximises $\tilde{v}_{Cin}(t_d)$ in (5.43) for each combination of load resistance and frequency, a profile of the inductor-less ZVS capabilities of a PT can be built up.

Figure 5.8 shows the ZVS profile of the T1-15W PT when used in the AC-output topology with $2C_{oss} = 260\,\text{pF}$. It can be seen that ZVS can only be achieved with very large or small load resistances. Operation with large and small load resistances is broadly similar from a ZVS perspective because the shape of the $R_L/\left(N^2\left(R_L{}^2\omega^2 C_{out}{}^2+1\right)\right)$ term in (5.2) is concave when plotted against R_L (the peak value occurring when $R_L = 1/(\omega C_{out})$). Hence the largest tank currents for a given input voltage and tank impedance phase angle are obtained with large and small load resistances.

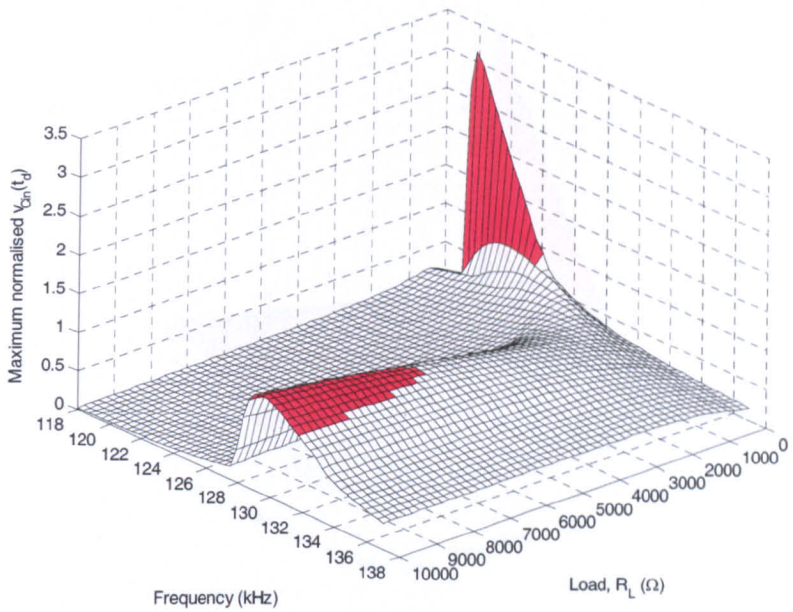

Figure 5.8: ZVS profile of T1-15W. The ZVS capable regions are shaded in red.

The efficiency and power density of a PT are maximised when the matched load $R_L = 1/(\omega C_{out})$ is used. Since the matched load for this PT is around 1kΩ, operating the T1-15W within the ZVS capable load regions will substantially reduce the maximum PT power density that can be achieved compared to operation at the matched load in a with-inductor topology.

Figure 5.9 shows the ZVS profile of another radial mode Transoner PT, termed T1-PP0361, in the AC-output topology with $2C_{oss} = 260\,\text{pF}$. The equivalent circuit component values of this device were measured as $C_{in} = 4.93\,\text{nF}$, $C_{out} = 2.70\,\text{nF}$, $L_1 = 4.48\,\text{mH}$, $C_1 = 891\,\text{pF}$, $R_1 = 4.34\,\Omega$, and $N = 2.21$. In contrast with the T1-15W device, ZVS can be achieved over a wide range of load and frequency ranges, including the matched load. The matched load for this PT is around 700Ω, and as the load resistance is increased or decreased from this value, the range of frequencies over which ZVS can be achieved tends to increase.

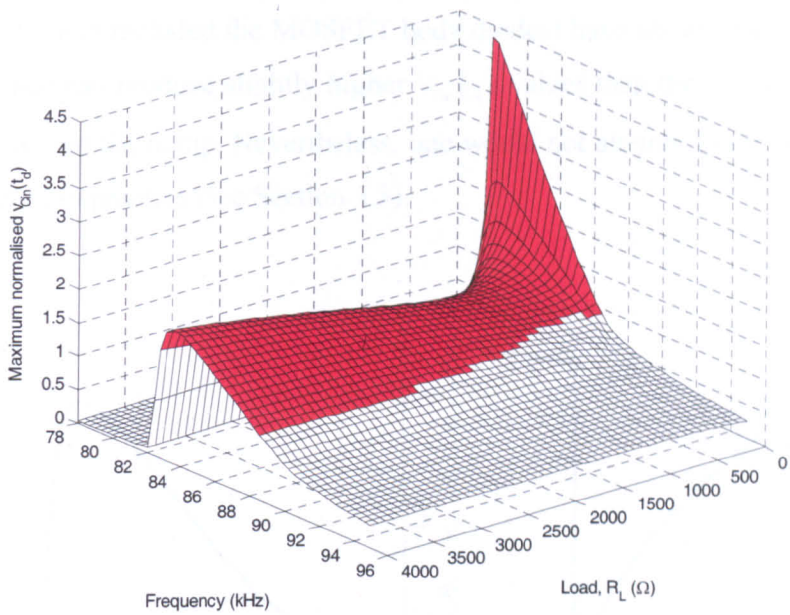

Figure 5.9: ZVS profile of T1-PP0361. ZVS capable regions are shaded in red.

In both Figure 5.8 and Figure 5.9 there is a 'bump' in the profile on the inductive side of resonance. This is most easily seen in Figure 5.9 by looking at the frequency just above the point at which ZVS is lost at each load resistance. The 'bump' is due to the dead-time which maximises (5.43) jumping to $T/2$ and then back again. To show this, a plot of maximum $\tilde{v}_{Cin}(t_d)$ against frequency, and the corresponding dead-time which maximises (5.43) against frequency, is shown in Figure 5.10 for the T1-PP0361 with $2C_{oss} = 260\,\text{pF}$ and $R_L = 4000\,\Omega$. The 'bump' region can clearly be seen in Figure 5.10 at around 89kHz, and corresponds to the region where the dead-time which maximises (5.43) is $T/2$. Plots of $\tilde{v}_{Cin}(t_d)$ against t_d for the T1-PP0361 with $2C_{oss} = 260\,\text{pF}$ and $R_L = 4000\,\Omega$ are shown at three different frequencies in Figure 5.11. The frequency 88.54kHz lies on the boundary of the region where inductor-less ZVS can be achieved with this load (see Figure 5.9 and Figure 5.10). The frequency 89.22kHz lies within the 'bump' region, and 89.90kHz lies beyond the 'bump' region. At 89.22kHz, it can be seen that the dead-time which maximises (5.43) becomes $T/2$. The mode sequence that actually occurs with $R_L = 4000\,\Omega$ at 89.22kHz with $t_d = T/2$ is 4-5-1-3-1-2-4-6, whereas the mode sequence that occurs when using the dead-time that maximises (5.43) at 88.54kHz and 89.90kHz is 1-3-4-6. Thus, the numerical results within the 'bump' region are not, strictly speaking, numerically accurate. Like the frequency and load combinations that result in ZVS being easily achieved (and the MOSFET body diodes therefore conducting), the results within the bump region serve as a qualitative indicator of the margin by which ZVS can or cannot be achieved. It is worth noting that SPICE

simulations (which included the MOSFET body diodes) have shown that the 4-5-1-3-1-2-4-6 sequence can produce slightly higher $\tilde{v}_{Cin}(t_d)$ values than the 1-3-4-6 sequence in the regions within the bump. Nevertheless, one would not attempt to use the 4-5-1-3-1-2-4-6 sequence in practice (see Section 5.3).

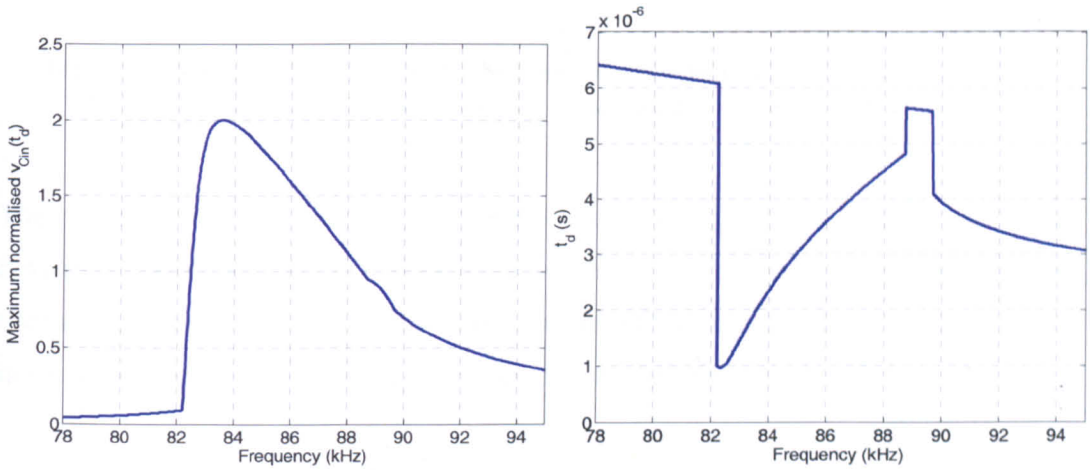

(a) (b)

Figure 5.10: a) The maximum $\tilde{v}_{Cin}(t_d)$, as calculated by (5.43), for the T1-PP0361 with $R_L = 4000\ \Omega$. b) The associated dead-time that maximises (5.43), for the T1-PP0361 with $R_L = 4000\ \Omega$.

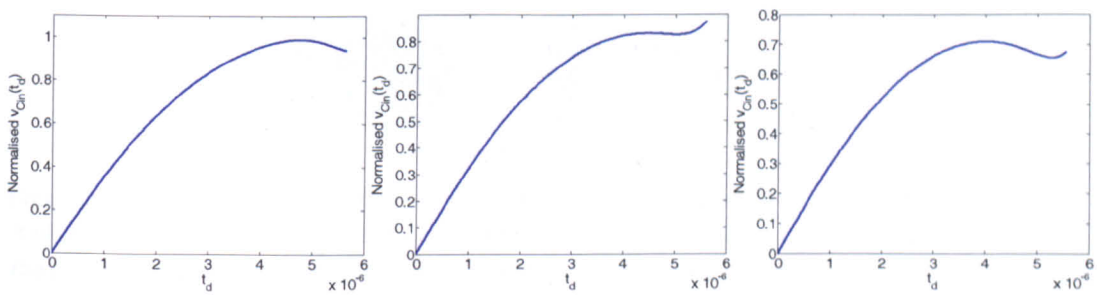

(a) (b) (c)

Figure 5.11: Plots of $\tilde{v}_{Cin}(t_d)$, as calculated by (5.43), against t_d, for the T1-PP0361 PT with $R_L = 4000\ \Omega$. t_d is shown over the range 0 to $T/2$ in each case. (a) Frequency = 88.54kHz. (b) Frequency = 89.22kHz. (c) Frequency = 89.90kHz.

Substituting $R_L = M/(\omega C_{out})$ into the model in Section 5.3, the maximum $\tilde{v}_{Cin}(t_d)$ that can be achieved when a free choice of frequency and dead-time is permitted (i.e. when frequency and dead-time are chosen so as to maximise $\tilde{v}_{Cin}(t_d)$ in (5.43)) can be plotted as a function of M, as shown in Figure 5.12. In both cases the lowest maximum $\tilde{v}_{Cin}(t_d)$ occurs at $M = 1$, indicating that the matched load condition is the most difficult to obtain ZVS with.

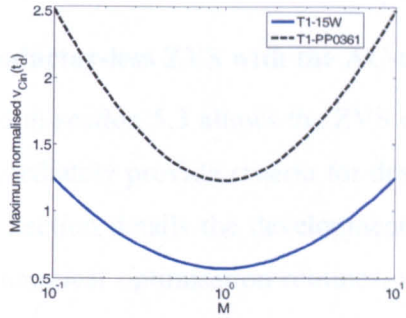

Figure 5.12: Maximum $\tilde{v}_{Cin}(t_d)$ that can be achieved when the frequency and dead-time that maximise $\tilde{v}_{Cin}(t_d)$ are used.

The geometry of T1-15W and T1-PP0361 is shown in Figure 5.13. Comparing the two devices, the input section of T1-PP0361 is twice as large as the output section, whereas the input section of T1-15W is 0.66 times the size of the output section. It will be shown in Chapter 6 that this is the principal reason for the difference in the ZVS profiles.

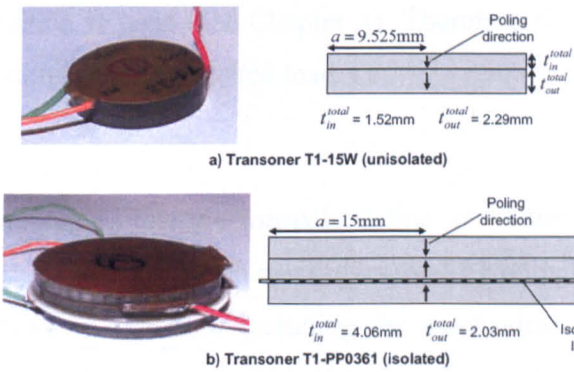

Figure 5.13: Geometric layout of T1-15W and T1-PP0361 radial mode Transoner PTs. a is the PT radius, t_{in}^{total} is the total thickness of active ceramic in the input section (the diagrams assume that the electrode thickness is negligible), and t_{out}^{total} is the total thickness of active ceramic in the output section.

5.6 Design criteria for inductor-less ZVS with the AC-output topology

Whilst the model developed in section 5.3 allows the ZVS capabilities of a given PT to be assessed, it does not immediately provide criteria for designing PTs that are capable of inductor-less ZVS. This section details the development of a normalisation scheme that, in conjunction with numerical optimisation routines, allows the key relationships between the equivalent circuit components and inductor-less ZVS capability to be identified.

The maximum output power of a given PT is nearly always limited by the need to prevent excessive PT temperature rise. Therefore the load which maximises PT efficiency is also the load which (for a given thermal limit) allows the greatest PT output power to be obtained (see Chapter 4). For a given tank current, PT output power and PT efficiency are theoretically maximised in the AC-output topology when the matched load condition is used (see Chapter 4). Therefore the load resistance is now represented as a multiple of the matched load, i.e.

$$R_L = \frac{M}{\omega C_{out}} \tag{5.44}$$

where M is the loading factor. We formally define M as the ratio of the actual load resistance to the load resistance which maximises total PT output power for a given tank current. Next, instead of explicitly including the mechanical loss resistance R_l, the effect of the mechanical losses is modelled by proportionally increasing the referred series equivalent resistance of R_L and C_{out} by a 'loss factor', ψ, that is given by the inverse of the efficiency of the PT. Thus, from (5.2) and (5.3), R_x and C_x become

$$R_x = \frac{\psi M}{\omega C_{out} N^2 \left(M^2 + 1\right)} \tag{5.45}$$

$$C_x = \frac{C_1 C_{out} N^2 \left(M^2 + 1\right)}{C_1 M^2 + C_{out} N^2 \left(M^2 + 1\right)}. \tag{5.46}$$

Since the efficiency of a PT will change considerably as the loading is changed, care must be taken to ensure that ψ is suitably chosen for the load condition in question (see Section 5.7). The phase angle of the tank impedance is given by

$$\phi = \tan^{-1}\left(\frac{\omega L_1 - \frac{1}{\omega C_x}}{R_x}\right). \tag{5.47}$$

Substituting (5.45) and (5.46) into (5.47), the angular frequency can be solved in terms of the phase angle to give

$$\omega = \sqrt{\frac{\left(C_{out}N^2 + C_1\psi M\tan(\phi) + C_1M^2 + C_{out}N^2M^2\right)}{L_1C_1C_{out}N^2\left(M^2+1\right)}}. \tag{5.48}$$

C_{eff} and C_1 are then normalized to the output capacitance referred across the ideal transformer turns ratio. Hence,

$$C_{eff} = YC_{out}N^2 \tag{5.49}$$

$$C_1 = XC_{out}N^2 \tag{5.50}$$

where X and Y are the normalisation factors. Substituting (5.49) and (5.50) into (5.45), (5.46), and (5.48), the equivalent resistance R_x, equivalent capacitance C_x and angular frequency for the AC-output topology can be expressed as

$$R_x = \frac{M\psi\sqrt{L_1X}}{\sqrt{C_{out}N^2\left(M^2+1\right)\left(1+\tan(\phi)X\psi M + M^2(1+X)\right)}} \tag{5.51}$$

$$C_x = \frac{C_{out}N^2X\left(M^2+1\right)}{XM^2+M^2+1} \tag{5.52}$$

$$\omega = \sqrt{\frac{1+X\psi M\tan(\phi)+M^2(X+1)}{L_1C_{out}N^2X\left(M^2+1\right)}}. \tag{5.53}$$

Finally, the dead-time is normalised to the switching period

$$t_d = t_{df}T \tag{5.54}$$

where the dead-time factor t_{df} is the fraction of the switching period that is occupied by each dead-time interval, and

$$T = \frac{2\pi}{\omega}. \tag{5.55}$$

The advantage of the normalisation scheme proposed in (5.49) to (5.55) is that, when substituted into the relevant equations from Section 5.3, $\tilde{v}_{Cln}(t_d)$ becomes dependent only on ϕ, X, Y, M, ψ, and t_{df}. Thus, not only has the dependency on C_{eff}, C_1, R_1, R_L, t_d, and T been removed (as would be directly expected from (5.49) to (5.55)), but so too has the dependency on L_1, C_{out}, and N. Thus, $\tilde{v}_{Cln}(t_d)$ becomes a function of 6 normalised variables instead of 9 un-normalised variables.

For a given X, M, and ψ, ZVS becomes easier to achieve as Y is decreased because this is equivalent to reducing C_{eff} whilst keeping R_1, L_1, C_1, N, C_{out}, and R_L constant.

We define Y_{max} to be the largest value of Y at which ZVS can just be achieved for a given X, M, and ψ, assuming a free choice of ϕ and t_{df} is permitted. Thus, Y_{max} is the value of Y that, for a given X, M, and ψ, results in $v_{Cin}(t_d) = V_{dc}$ when the ϕ and t_{df} that maximise (5.42) are used.

The relationship between the ZVS condition and Y, X, M, ϕ, and t_{df} is now shown when the mechanical losses are ignored (i.e. $\psi = 1$). Numerical optimisation routines from MATLAB and Maple were used to calculate Y_{max} over a range of X and M when $\psi = 1$. Plots of Y_{max} against X and M are shown in Figure 5.14, whilst plots of the t_{df} and ϕ that correspond to each Y_{max}, X, and M combination (i.e. the values t_{df} and ϕ that allow ZVS to be achieved at a particular Y_{max}, X, and M) are shown in Figure 5.15.

Figure 5.14 shows that for a given X, the lowest value of Y_{max} occurs at the matched load, $M = 1$. The value of Y_{max} at a given M changes very little with X, and Y_{max} increases rapidly as M is increased or decreased from unity. Figure 5.15 shows that when Y, X, and M are such that ZVS can only just be achieved (i.e. when Y_{max}), the phase angle and dead-time factor that allow ZVS to be achieved are always between 57° and 57.55°, and 0.228 and 0.25 respectively. Hence they are both insensitive to the relative sizes of Y_{max}, X, and M.

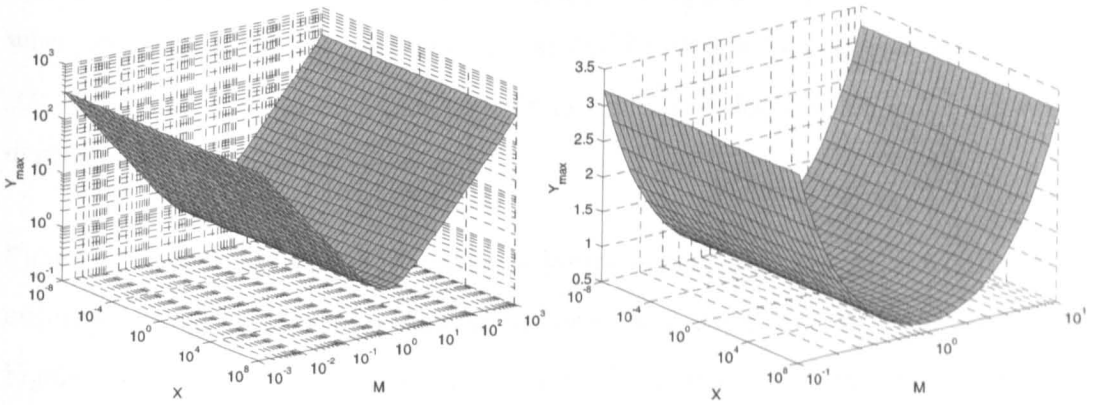

Figure 5.14: Change in Y_{max} with X and M when $\psi = 1$ for the AC-output topology.

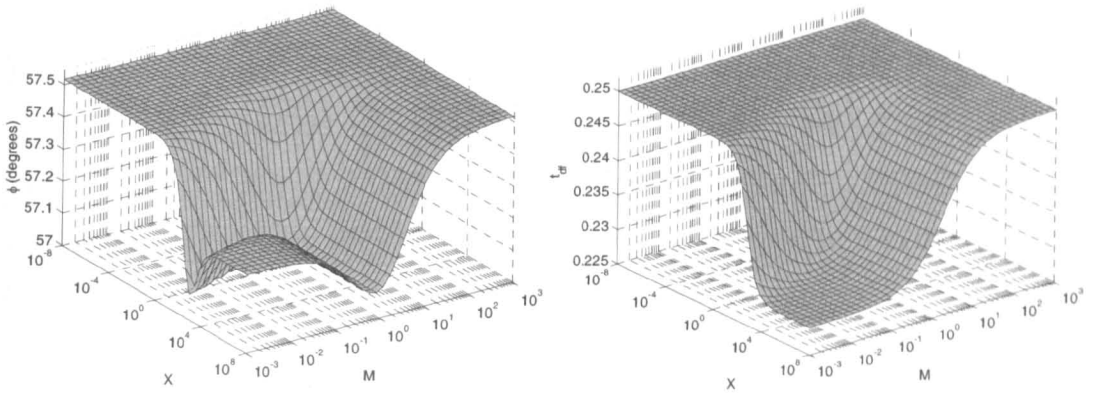

(a) (b)

Figure 5.15: The ϕ and t_{df} values that allow ZVS to be achieved with the AC-output topology when $\psi = 1$ and $Y = Y_{\max}$.

Since the lowest value of $Y_{\max}$ in Figure 5.14 is 0.6339, any PT with negligible losses, operating in the AC-output topology, will be able to achieve ZVS with any load resistance providing it is designed such that $C_{eff} < 0.6339 N^2 C_{out}$ and a free choice of frequency and dead-time is permitted. This figure is around 28% lower than that previously found in [4], and this is due to the reasons described in Section 5.2.

5.7 Consideration of mechanical losses

The 'loss factor' ψ is calculated from the inverse of the expected PT efficiency at a particular load condition. Thus, if a particular PT is expected to achieve 95% efficiency when operating at $M = 0.8$, then $\psi = 1.111$ should be used when calculating $Y_{\max}$ for this M. Note that in general, the efficiency of a given PT will decrease as M is increased or decreased away from unity.

Figure 5.16 shows a plot of $Y_{\max}$ against X for the load condition $M = 1$ at 5 different PT efficiency levels. It is shown that as the efficiency decreases, $Y_{\max}$ decreases. Like Figure 5.14, there is little change in $Y_{\max}$ with X. Indeed, the variation with X for a given M and ψ is so small that, for all practical purposes, $Y_{\max}$ can be assumed to be independent of X. It is therefore concluded that when a free choice of ϕ and t_{df} is permitted, the ability to obtain inductor-less ZVS is determined only by Y, M, and ψ. The phase angle and dead-time factor that allow ZVS to be achieved when $Y = Y_{\max}$ are shown as a function of X in Figure 5.17. There is little dependency on efficiency or X.

The efficiency of the T1-15W and T1-PP0361 devices is around 95% or better when operating with a matched load ($M=1$). Figure 5.16 indicates that $C_{eff} < 0.603N^2C_{out}$ is required for ZVS at this efficiency and load level. Comparing the equivalent circuit component values of the two devices to this relationship, it can be seen that the result from Figure 5.16 is consistent with Figures 1.8, 1.9, and 1.12.

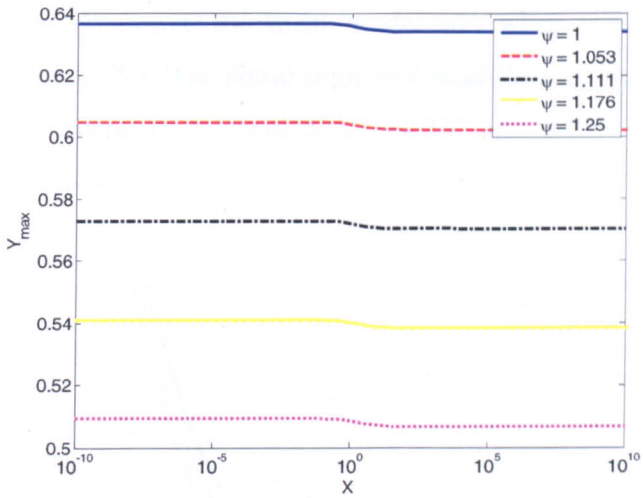

Figure 5.16: Variation in Y_{max} with X and ψ when $M=1$ for the AC-output topology.

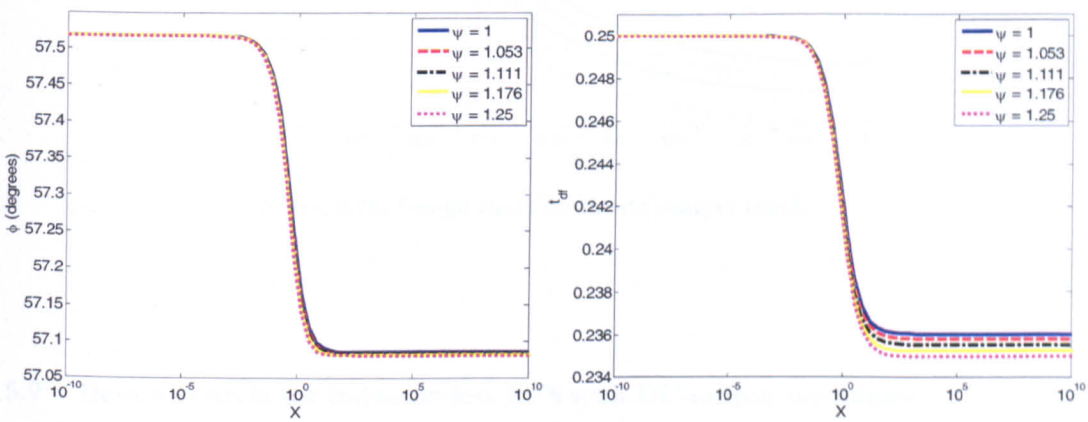

Figure 5.17: The ϕ and t_{df} values that allow ZVS to be achieved with the AC-output topology when $M=1$ and $Y=Y_{max}$.

5.8 Design chart for the AC-output topology

It has been shown that the only variables to affect Y_{max} are M and ψ. Therefore it is instructive to plot Y_{max} against M for several values of ψ, as shown in Figure 5.18. Although these plots were generated using $X = 0.1$, they apply to any X because the change in Y_{max} with X for a given M and ψ has been shown to be negligible. Thus, Figure 5.18 may be regarded as a design chart for determining Y_{max} for any type of PT (Rosen, radial mode Transoner, thickness mode, etc) when used in the AC-output topology shown in Figure 5.1. The phase angle and dead-time factor required to achieve ZVS with a device where $Y = Y_{max}$ are 57.3° ±0.25° and 0.239 ±0.011 for all load conditions and efficiencies.

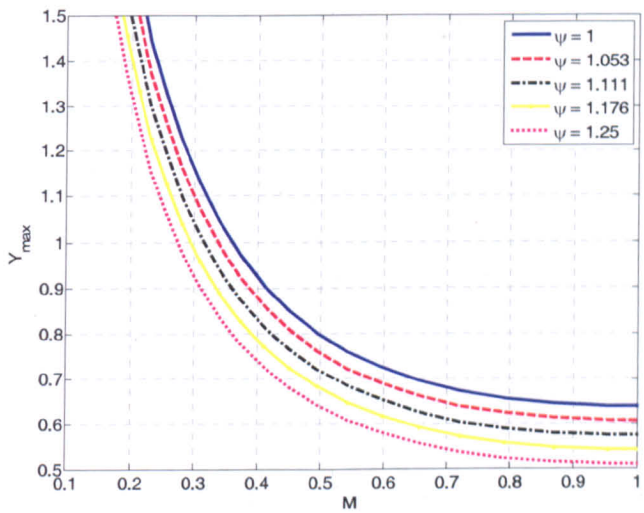

Figure 5.18: Design chart for the AC-output topology.

5.9 Design criteria for inductor-less ZVS with DC-output topologies

The ZVS model and normalisation scheme can be used in conjunction with equivalent circuit models of several rectifier topologies to investigate the design requirements for ensuring ZVS in DC-output converters. Schematics of the 4 topologies to be considered are shown in Figure 5.19.

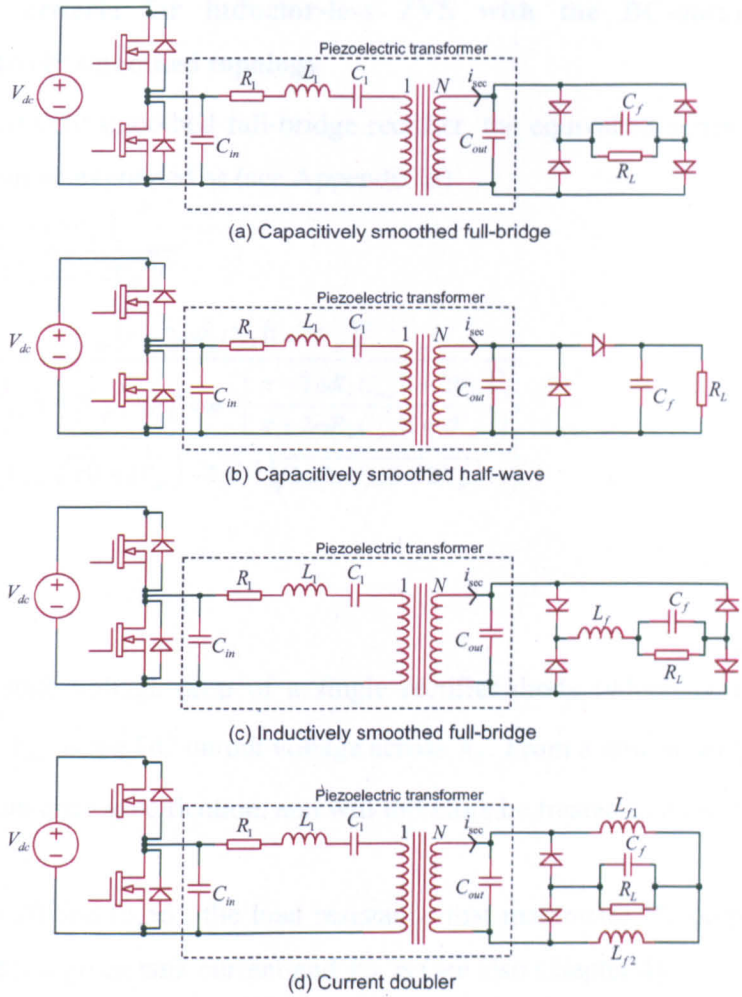

Figure 5.19: Four DC-output PT-based converters with no inductor at the PT input.

Since the tank current is sinusoidal, the PT output capacitance and rectifier stage in each of these converters can be modelled with a series resistor and capacitor as shown in Figure 5.20 and described in [12-15]. The specific rectifier models used in this Chapter may be found in Appendix B.

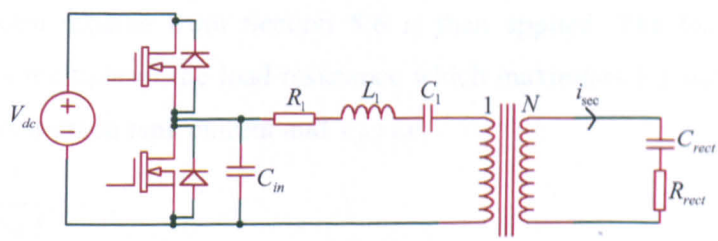

Figure 5.20: Inductor-less converter with an RC model of the rectifier.

5.10 Design criteria for inductor-less ZVS with the DC-output full-bridge capacitively smoothed topology

For the capacitively smoothed full-bridge rectifier, the equivalent series resistance and capacitance can be expressed as (see Appendix B)

$$R_{rect} = \frac{8R_L\left(1+2V_{df}\right)}{\left(\pi+2R_L C_{out}\omega\left(1+2V_{df}\right)\right)^2} \tag{5.56}$$

$$C_{rect} = \frac{\pi C_{out}\left(\pi+2\omega R_L C_{out}\left(1+2V_{df}\right)\right)^2}{\left(\begin{array}{l}\left(2\omega R_L C_{out}\left(1+2V_{df}\right)+\pi\right)^2\cos^{-1}\left(\dfrac{\pi-2\omega R_L C_{out}\left(1+2V_{df}\right)}{\pi+2\omega R_L C_{out}\left(1+2V_{df}\right)}\right) \\ +\left(4\omega R_L C_{out}\sqrt{\pi}\left(1+2V_{df}\right)-2\pi^{3/2}\right)\sqrt{2\omega R_L C_{out}\left(1+2V_{df}\right)}\end{array}\right)} \tag{5.57}$$

where

$$V_{df} = \frac{V_d}{V_{out}}. \tag{5.58}$$

V_d is the on-state voltage drop of a single rectifier diode (which is assumed to be constant), and V_{out} is the DC output voltage across R_L. From a design perspective, V_{df} is fixed by the converter specification, and will therefore be treated as a constant.

From Figure 5.20 and (5.56), the load resistance that maximises PT output power and PT efficiency for a given tank current and V_{df} is (see also Chapter 4)

$$R_L = \frac{\pi}{2C_{out}\omega\left(1+2V_{df}\right)}. \tag{5.59}$$

Note that if V_{df} is constant, then the efficiency of the rectifier is also approximately fixed. Thus, for a given tank current and V_{df}, power dissipation in the load resistance is maximised when the total PT output power is maximised. Therefore power dissipation in the load is also maximised by using (5.59).

The normalisation scheme from Section 5.6 is then applied. The load resistance is represented as a multiple of the load resistance which maximises PT output power and PT efficiency for a given tank current and V_{df}, i.e.

$$R_L = \frac{M\pi}{2C_{out}\omega\left(1+2V_{df}\right)}, \tag{5.60}$$

and R_x, C_x, and ω for the full-bridge capacitively smoothed PT-based converter become

$$R_x = \frac{4\psi M\sqrt{L_1 X}}{(M+1)\sqrt{\pi C_{out}N^2}\sqrt{\begin{pmatrix}2X\left(M^{3/2}-M^{0.5}\right)-X(M+1)^2\cos^{-1}\left(\frac{M-1}{M+1}\right)\\+X\left(\pi M^2+M(2\pi+4\psi\tan(\phi))+\pi\right)+\pi(M+1)^2\end{pmatrix}}} \tag{5.61}$$

$$C_x = \frac{\pi(M+1)^2 C_{out}N^2 X}{2X\left(M^{3/2}-M^{0.5}\right)+\pi(M+1)^2(1+X)-X(M+1)^2\cos^{-1}\left(\frac{M-1}{M+1}\right)} \tag{5.62}$$

$$\omega = \frac{\sqrt{\begin{pmatrix}2X\left(M^{3/2}-M^{0.5}\right)-X(M+1)^2\cos^{-1}\left(\frac{M-1}{M+1}\right)\\+X\left(\pi M^2+M(2\pi+4\psi\tan(\phi))+\pi\right)+\pi(M+1)^2\end{pmatrix}}}{(M+1)\sqrt{L_1 C_{out}N^2\pi X}} \tag{5.63}$$

where ψ is given by the inverse of the PT efficiency, not by the inverse of the combined efficiency of the PT and rectifier. Substituting (5.61), (5.62), (5.63), (5.49), (5.50), (5.54), and (5.55) into the model in Section 5.3, the relationship between the ZVS condition and Y_{max}, X, M, ϕ, t_{df}, and ψ can be studied. A plot of Y_{max} against X and M is shown in Figure 5.21 for the $\psi = 1$ case, whilst plots of the t_{df} and ϕ that correspond to each Y_{max}, X, and M combination are shown in Figure 5.22. Both Figure 5.21 and Figure 5.22 are very similar in shape to Figure 5.14 and Figure 5.15; the phase angle and dead-time factor that allow ZVS to be achieved when $Y = Y_{max}$ are once again always between 57.05° and 57.55°, and 0.228 and 0.25 respectively, the lowest value of Y_{max} occurs at $M = 1$, and very little change in Y_{max} occurs for a given M and ψ as X is varied. However, for the load conditions of interest, Y_{max} is considerably larger than it is for the AC-output topology.

Figure 5.23 shows Y_{max} against X at $M = 1$ for 5 different PT efficiency levels. Comparing Figure 5.23 to Figure 5.16, it can be seen that at $M = 1$, Y_{max} is around 1.57 times larger in the DC-output capacitively smoothed case. This is caused by the rectifier increasing the apparent size of C_{out} to the rest of the equivalent circuit (see Chapter 4), and similar behaviour was also noted with inductively smoothed rectifiers in [15].

In Chapter 4 it was shown that, for the DC-output full-bridge capacitively smoothed rectifier, at the load which maximises total PT output power for a given tank current (i.e. at $M = 1$), the equivalent parallel resistance of R_{rect} and C_{rect} (R_{rect} and C_{rect} are termed R_s and C_s in Chapter 4) is 1.104 times larger than $1/(\omega C_{out})$, and the equivalent

parallel capacitance of R_{rect} and C_{rect} is 1.423 times larger than C_{out}. It is therefore no surprise that (at $M=1$) inductor-less ZVS can be achieved at a higher value of Y with the DC-output full-bridge capacitively smoothed topology than it can with the AC-output topology. The significance of $Y_{\max}$ being larger in the DC-output capacitively smoothed case will be shown, in the context of the design of radial mode Transoner PTs, in Chapter 6.

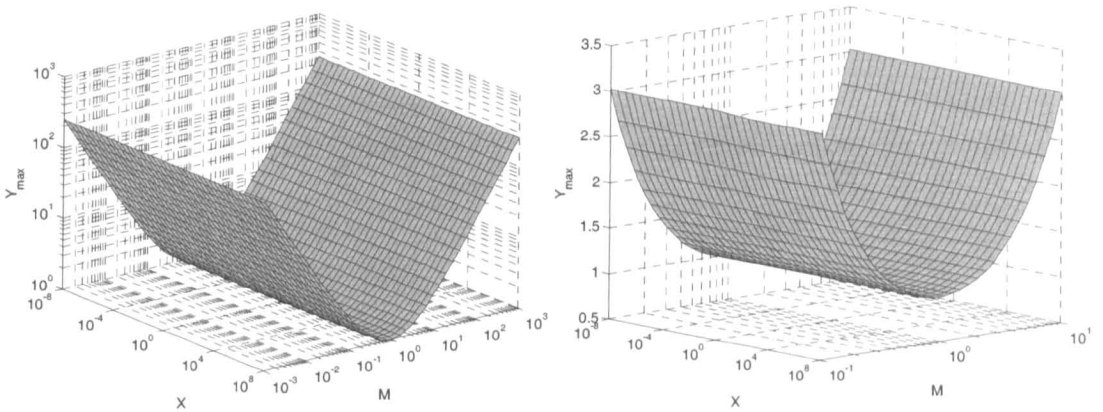

Figure 5.21: Change in $Y_{\max}$ with X and M when $\psi=1$ for the DC-output full-bridge capacitively smoothed topology.

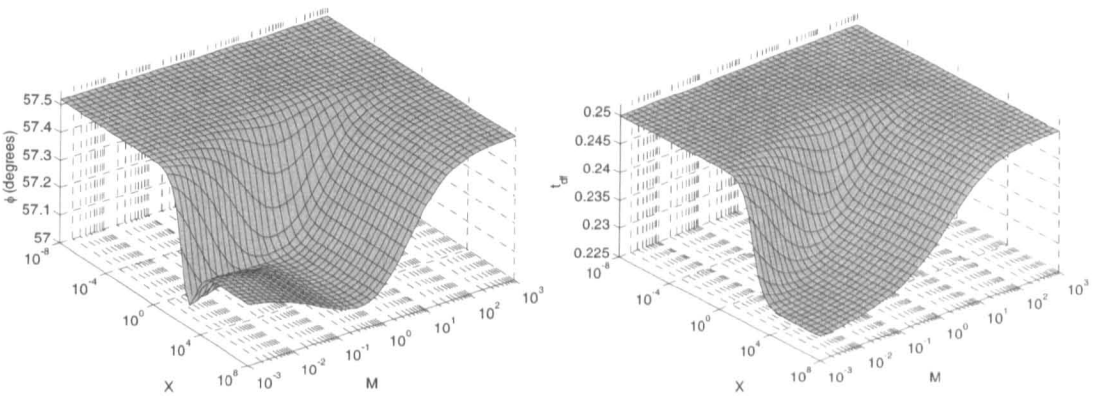

(a) (b)

Figure 5.22: The ϕ and t_{df} values that allow ZVS to be achieved with the DC-output full-bridge capacitively smoothed topology when $\psi=1$ and $Y=Y_{\max}$.

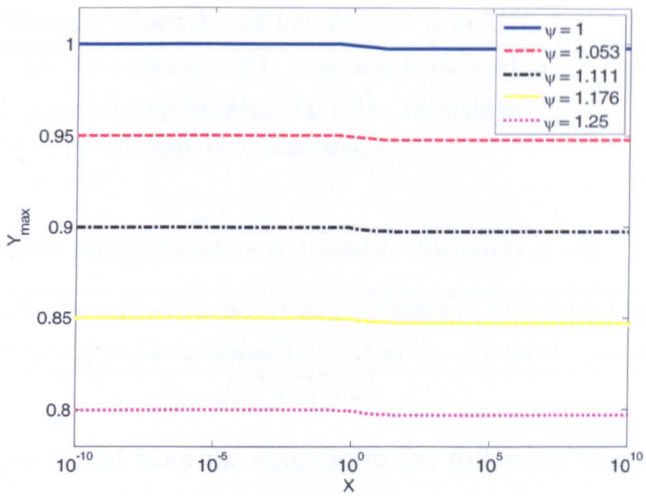

Figure 5.23: Change in Y_{max} with X and ψ at $M=1$ for the DC-output full-bridge capacitively smoothed topology.

5.11 Design criteria for inductor-less ZVS with the DC-output full-bridge inductively smoothed topology

To study the inductor-less ZVS requirements of the full-bridge inductively smoothed variant, the rectifier model shown in Appendix B is used. This is a modified version of the model presented in [15]. Representing the load as a multiple of the load resistance which maximises PT output power and PT efficiency for a given tank current and V_{df} (see Chapter 4),

$$R_L = \frac{M}{\omega C_{out}\left(1+2V_{df}\right)}. \tag{5.64}$$

The normalisation scheme is then applied. When the rectifier is operating in the "continuous" mode, the equations for R_x, C_x, and ω in terms of the normalised quantities are

$$R_x = \frac{8\psi M\sqrt{L_1 X}}{\pi\sqrt{C_{out}N^2\left(M^2+1\right)\left(\pi^2\left(X+1\right)\left(M^2+1\right)-8X\left(1-\psi M\tan(\phi)\right)\right)}} \tag{5.65}$$

$$C_x = \frac{C_{out}N^2X\pi^2\left(M^2+1\right)}{\pi^2\left(X+1\right)\left(M^2+1\right)-8X} \tag{5.66}$$

$$\omega = \frac{\sqrt{\pi^2\left(X+1\right)\left(M^2+1\right)-8X\left(1-\psi M\tan(\phi)\right)}}{\pi\sqrt{C_{out}N^2XL_1\left(M^2+1\right)}}. \tag{5.67}$$

When the rectifier is operating in the "discontinuous" mode, the equations are

$$R_x = \frac{\psi\left(2\sin(\alpha+\beta)\sin(\alpha)-\cos^2(\alpha+\beta)-\cos^2(\alpha)+2\right)\sqrt{L_1 X}}{\sqrt{\pi C_{out} N^2}\sqrt{\begin{matrix}\pi - X\cos(\alpha+\beta)\sin(\alpha+\beta)+2X\psi\tan(\phi)\sin(\alpha+\beta)\sin(\alpha)-X\beta+X\pi \\ +2X\psi\tan(\phi)-X\psi\tan(\phi)\cos^2(\alpha+\beta)-X\psi\tan(\phi)\cos^2(\alpha) \\ -2X\sin(\alpha+\beta)\cos(\alpha)-X\cos(\alpha)\sin(\alpha)\end{matrix}}} \tag{5.68}$$

$$C_x = \frac{C_{out} N^2 X\pi}{\pi - X\left(\cos(\alpha)\sin(\alpha)+\sin(\alpha+\beta)\cos(\alpha+\beta)+2\sin(\alpha+\beta)\cos(\alpha)+\beta-\pi\right)} \tag{5.69}$$

$$\omega = \frac{\sqrt{\begin{matrix}\pi - X\cos(\alpha+\beta)\sin(\alpha+\beta)+2X\psi\tan(\phi)\sin(\alpha+\beta)\sin(\alpha)-X\beta+X\pi+2X\psi\tan(\phi) \\ -X\psi\tan(\phi)\cos^2(\alpha+\beta)-X\psi\tan(\phi)\cos^2(\alpha)-2X\sin(\alpha+\beta)\cos(\alpha)-X\cos(\alpha)\sin(\alpha)\end{matrix}}}{\sqrt{C_{out} N^2 L_1 X\pi}} \tag{5.70}$$

where α and β are found from the solution to the following simultaneous equations (obtained by substituting (5.64) into (B.18) in Appendix B, and straight from (B.17) in Appendix B)

$$\cos(\alpha+\beta)+(\beta-\pi)\sin(\alpha+\beta)+\cos(\alpha)=0 \tag{5.71}$$

$$\left(2\pi M+\beta^2-2-2\beta\pi+\pi^2\right)\sin(\alpha+\beta)+2(\beta-\pi)\cos(\alpha+\beta)-2\sin(\alpha)=0\,. \tag{5.72}$$

The rectifier will be in the continuous mode of operation when $M > 2/\pi$ (see Chapter 4 and [15]). Otherwise it will be in the discontinuous mode.

Plots of Y_{max} against X and M for the $\psi = 1$ case, and the associated ϕ and t_{df} that correspond to each combination of Y_{max}, X, and M, are shown in Figure 5.24 and Figure 5.25 respectively. Again, there is little change in Y_{max} with X. The phase angle and dead-time factor that allow ZVS to be achieved when $Y = Y_{max}$ are always between 57.05° and 57.55°, and 0.228 and 0.25 respectively, and the lowest value of Y_{max} occurs at $M = 1$. Y_{max} is shown against X for the $M = 1$ case at 5 PT efficiency levels in Figure 5.26. Comparing Figures 5.16, 5.23, and 5.26, it can be seen that the ZVS requirements of this topology lie approximately mid-way between those of the AC-output topology and those of the DC-output full-bridge capacitive smoothed topology.

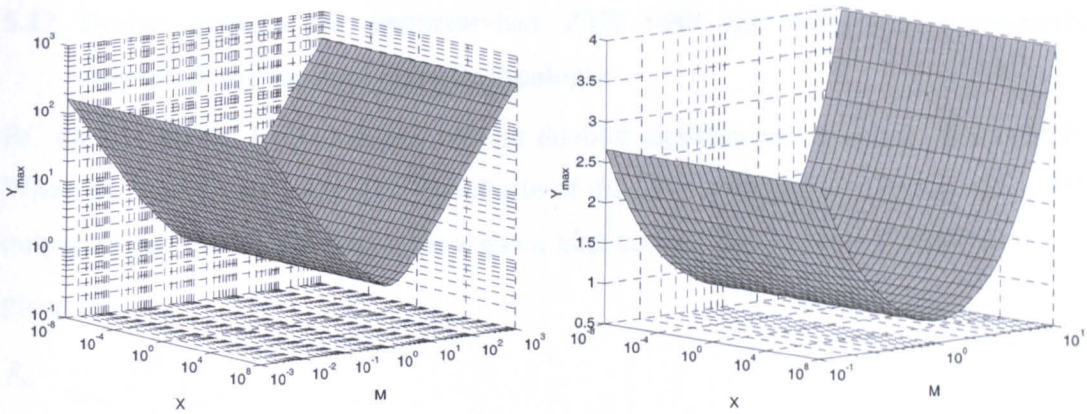

Figure 5.24: Change in Y_{max} with X and M when $\psi = 1$ for the DC-output full-bridge inductively smoothed topology.

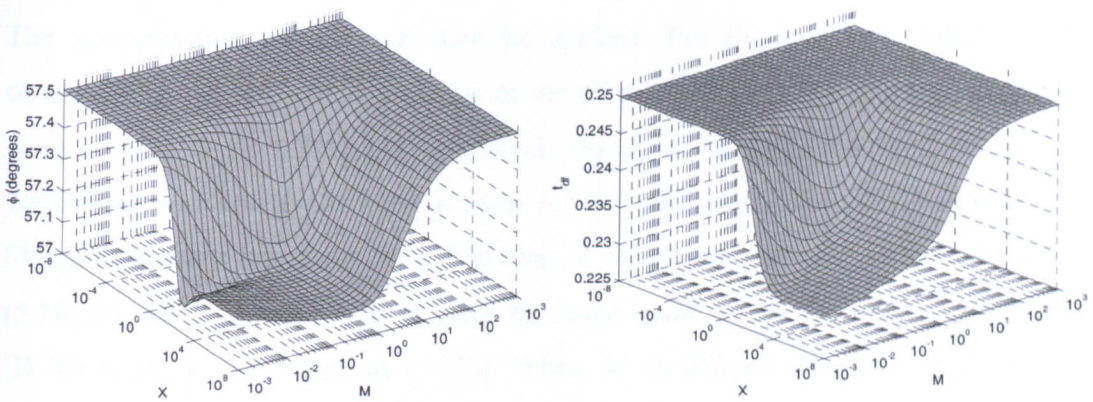

(a) (b)

Figure 5.25: The ϕ and t_{df} values that allow ZVS to be achieved with the DC-output full-bridge inductively smoothed topology when $\psi = 1$ and $Y = Y_{max}$.

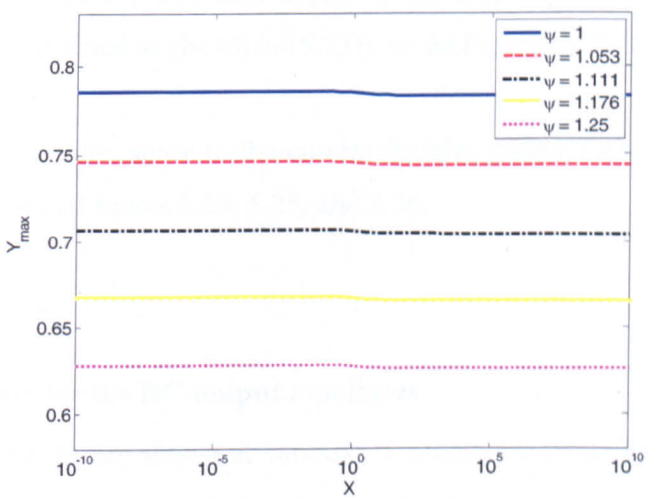

Figure 5.26: Change in Y_{max} with X and ψ at $M = 1$ for the DC-output full-bridge inductively smoothed variant.

5.12 Design criteria for inductor-less ZVS with the half-wave capacitively smoothed and current doubler topologies

RC models for the half-wave and current doubler rectifiers are shown in Appendix B. When the load is represented as a multiple of the load resistance which maximises PT output power and PT efficiency for a given tank current and V_{df} (see Chapter 4), R_L is given by

$$R_L = \frac{2\pi M}{\omega C_{out}(1+2V_{df})} \tag{5.73}$$

$$R_L = \frac{M}{4\omega C_{out}(1+V_{df})}, \tag{5.74}$$

for half-wave capacitively smoothed, and current doubler configurations, respectively. The normalisation scheme can then be applied. For the half-wave topology, the equations for R_x, C_x, and ω in terms of the normalised quantities become exactly the same as those for the full-bridge capacitively smoothed case, whilst those for the current doubler become exactly the same as those for the full-bridge inductively smoothed case (the simultaneous equations for calculating α and β are also the same; substituting (5.74) into (B.27) in Appendix B gives the same result as that shown in (5.72), whilst (B.26) is already the same as (5.71)). When M is defined as shown in (5.74), the current doubler rectifier will also be in the continuous mode of operation when $M > 2/\pi$ (see Chapter 4 and [15]). Otherwise it will be in the discontinuous mode.

Since (5.61), (5.62), and (5.63) also apply to the half-wave capacitively smoothed variant (when M is defined as shown in (5.73)), so do Figures 5.21, 5.22, and 5.23.

Since (5.65) to (5.72) also apply to the current doubler variant (when M is defined as shown in (5.74)), so do Figures 5.24, 5.25, and 5.26.

5.13 Design charts for the DC-output topologies

Plots of Y_{max} against M are shown at various PT efficiency levels for the 4 DC-output topologies at $X = 0.1$ in Figure 5.27 and Figure 5.28. Since there is negligible change in Y_{max} with X for a given M and ψ, these plots may be regarded as a set of design charts for determining Y_{max} for any type of PT when used in these topologies. The ϕ and t_{df}

that allow ZVS to be achieved when $Y = Y_{max}$ are 57.3° ±0.25° and 0.239 ±0.011 for all topologies at all load conditions and efficiencies.

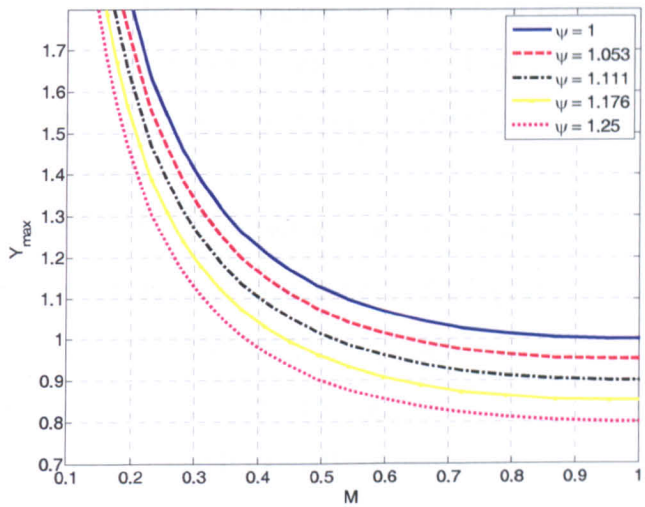

Figure 5.27: Design chart for the full-bridge capacitively smoothed and the half-wave capacitively smoothed topologies.

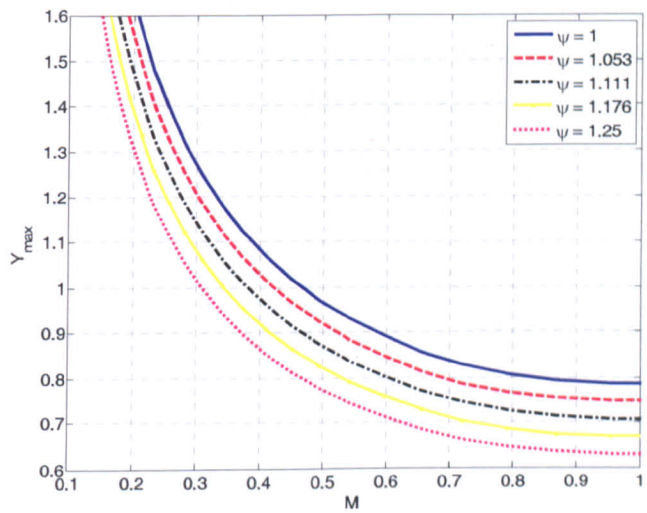

Figure 5.28: Design chart for the full-bridge inductively smoothed and current doubler topologies.

5.14 Summary

A new model for calculating the frequency and load range over which a given PT can achieve inductor-less ZVS when used in both AC-output and DC-output topologies has been presented. Unlike previously reported models, this has been shown to provide a level of accuracy comparable to SPICE simulation, and is therefore as accurate as the

standard lumped equivalent circuit PT model will allow. Good agreement was found between the model and experimental results from a PT-based converter.

Through the use of a normalisation scheme and numerical optimisation techniques, it has been demonstrated that, when a free choice of frequency and dead-time are permitted, the ability to achieve inductor-less ZVS depends only on

- M, the load condition.
- ψ, the inverse of the PT efficiency at that load condition.
- Y, the ratio between the total capacitance at the PT input and N^2C_{out}.

The maximum value of Y at which ZVS can be achieved for a given M and ψ has been shown to depend on the output topology (i.e. whether AC-output, DC-output capacitively smoothed, or DC-output inductively smoothed).

For a given output topology, Y_{max} (the maximum value of Y at which ZVS can just be achieved when a free choice of ϕ and t_{df} is permitted) decreases as M approaches unity and decreases as PT efficiency decreases. The tank impedance phase angle and dead-time factor that allow ZVS to be achieved when $Y = Y_{max}$ are 57.3° ±0.25° and 0.239 ±0.011 for all 5 topologies at all load conditions and efficiencies.

Design charts for determining Y_{max} for various M and ψ have been presented for all 5 topologies. Thus, if the M and ψ at which a PT is going to operate are known, the ability to achieve inductor-less ZVS can be ensured by designing the PT such that $Y < Y_{max}$.

This chapter has established the electrical criteria for achieving inductor-less ZVS in terms of the PT equivalent circuit components. Relating the electrical criteria to the physical criteria (i.e. device dimensions, electrode layout, etc) requires the use of models that are specific to a particular type of PT. The case of the radial mode Transoner PT is considered in the next chapter.

Insofar as the electrical characteristics of a PT are represented by the standard lumped equivalent circuit model, and the behaviour of the rectifiers are represented by the RC models described in Appendix B, the ZVS criteria established in this chapter apply to any type of PT (Rosen, radial mode Transoner, thickness mode, etc).

5.15 References

[1] R.-L. Lin, F. C. Lee, E. M. Baker, and D. Y. Chen, "Inductor-less piezoelectric transformer electronic ballast for linear fluorescent lamp," presented at IEEE Applied Power Electronics Conference and Exposition, 2001.

[2] R.-L. Lin, "Piezoelectric Transformer Characterization and Application of Electronic Ballast," PhD thesis, Virginia Polytechnic Institute and State University, USA, 2001.

[3] S. Bronstein and S. Ben-Yaakov, "Design considerations for achieving ZVS in a half bridge inverter that drives a piezoelectric transformer with no series inductor," presented at IEEE Applied Power Electronics Conference and Exposition, 2002.

[4] K. S. Meyer, M. A. E. Andersen, and F. Jensen, "Parameterized analysis of Zero Voltage Switching in resonant converters for optimal electrode layout of Piezoelectric Transformers," presented at IEEE Power Electronics Specialists Conference, 2008.

[5] E. M. Baker, W. Huang, D. Y. Chen, and F. C. Lee, "Radial mode piezoelectric transformer design for fluorescent lamp ballast applications," *IEEE Transactions on Power Electronics*, vol. 20, pp. 1213-1220, 2005.

[6] S. Bronstein, "Piezoelectric Transformers in Power Electronics," PhD thesis, Ben-Gurion University of the Negev, Israel, 2005.

[7] M. K. Kazimierczuk and D. Czarkowski, *Resonant Power Converters*: John Wiley & Sons Inc, 1995.

[8] U. Kirchenberger and D. Schroder, "Comparison of multiresonant half-bridge DC-DC converters for high voltage and high output power," presented at Industry Applications Society Annual Meeting, 1992.

[9] N. Frohleke, J. Kunze, A. Fiedler, and H. Grotstollen, "Contribution to the AC-analysis of resonant converters; analysis of the series-parallel resonant converter including effects of parasitics and lossless snubbers for optimized design," presented at Applied Power Electronics Conference and Exposition, 1992.

[10] J. A. Sabate, R. W. Farrington, M. M. Jovanovic, and F. C. Lee, "Effect of switch capacitance on zero-voltage switching of resonant converters," presented at IEEE Power Electronics Specialists Conference, 1992.

[11] J. A. Sabate, R. W. Farrington, M. M. Jovanovic, and F. C. Lee, "Effect of FET output capacitance on ZVS of resonant converters," *IEEE Transactions on Aerospace and Electronic Systems*, vol. 32, pp. 255-266, 1996.

[12] M. P. Foster, H. I. Sewell, C. M. Bingham, D. A. Stone, and D. Howe, "Methodologies for the design of LCC voltage-output resonant converters," *IEE Proceedings - Electric Power Applications*, vol. 153, pp. 559-567, 2006.

[13] J. G. Hayes and M. G. Egan, "Rectifier-compensated fundamental mode approximation analysis of the series parallel LCLC family of resonant converters with capacitive output filter and voltage-source load," presented at IEEE Power Electronics Specialists Conference, 1999.

[14] A. J. Forsyth and S. V. Mollov, "Simple equivalent circuit for the series-loaded resonant converter with voltage boosting capacitor," *IEE Proceedings - Electric Power Applications*, vol. 145, pp. 301-306, 1998.

[15] A. J. Forsyth, G. A. Ward, and S. V. Mollov, "Extended fundamental frequency analysis of the LCC resonant converter," *IEEE Transactions on Power Electronics*, vol. 18, pp. 1286-1292, 2003.

Chapter 6 - Analysis of inductor-less ZVS with radial mode Transoner PTs

6.1 Introduction

In the previous chapter, relationships were derived between the ZVS condition and the components in the standard PT equivalent circuit. As such, these relationships are applicable to any type of PT that can be modelled with this equivalent circuit. However, they do not show what the physical design requirements are for achieving inductor-less ZVS, or how these requirements affect power density.

In this chapter, the equivalent circuit models for the radial mode Transoner PT that were derived in Chapters 2 and 3 are used in conjunction with the results from Chapter 5 to determine the physical design requirements that apply specifically to this type of PT. The impact of these requirements on power density is assessed, guidelines for maximising power density are given, and comparisons between the inductor-less and with-inductor half-bridge topologies are made. Finally, the need for the PT designer to meet a particular set of converter specifications is considered.

6.2 Analysis of radial mode Transoner PTs with input and output section electrode radius equal to the outer radius

To make the analysis that follows as clear as possible, the simplest case of a radial mode Transoner PT where the input electrodes, output electrodes, and outer radius are all equal to one another is considered in its entirety first.

A. Relationship between the ZVS condition and device geometry

When the input section electrode radius, output section electrode radius, and outer radius are equal to one another, the equivalent circuit components are described by (2.68) to (2.84) in Chapter 2. Depending on the choice of MOSFETs, the contribution to C_{eff} from the parasitic MOSFET output capacitances may be neglected in many cases. With this approximation, substituting the equivalent circuit formula from Chapter 2 into

(5.49) yields the following relationship for Y in terms of the physical dimensions and material parameters

$$Y = \frac{t_{out}^{total}}{t_{in}^{total}} \frac{\varepsilon_{33}^{T\,in}\left(1-k_p{}^{in\,2}\right)d_{31}{}^{out\,2}s_{11}^{E\,in\,2}\left(1-\sigma_C{}^{in}\right)^2}{\varepsilon_{33}^{T\,out}\left(1-k_p{}^{out\,2}\right)d_{31}{}^{in\,2}s_{11}^{E\,out\,2}\left(1-\sigma_C{}^{out}\right)^2}. \tag{6.1}$$

Hence, for ZVS to be possible, the following condition must be observed

$$\frac{t_{out}^{total}}{t_{in}^{total}} \frac{\varepsilon_{33}^{T\,in}\left(1-k_p{}^{in\,2}\right)d_{31}{}^{out\,2}s_{11}^{E\,in\,2}\left(1-\sigma_C{}^{in}\right)^2}{\varepsilon_{33}^{T\,out}\left(1-k_p{}^{out\,2}\right)d_{31}{}^{in\,2}s_{11}^{E\,out\,2}\left(1-\sigma_C{}^{out}\right)^2} < Y_{\max}. \tag{6.2}$$

If there is negligible difference between the dielectric constant, coupling factor, mechanical compliance, Poisson's ratio, and piezoelectric coefficient in the input and output sections, then (6.1) reduces to

$$Y \approx \frac{t_{out}^{total}}{t_{in}^{total}}. \tag{6.3}$$

Therefore to a first approximation, it is the ratio of the total thickness of the output section layers to the total thickness of the input section layers that determines whether ZVS can be achieved for a given M, ψ, and output topology. From Figures 5.14, 5.16, 5.21, 5.23, 5.24, and 5.26, the size of input section required to obtained ZVS for a given topology with a given sized output section therefore increases as M approaches unity, and increases as PT efficiency decreases. In reality, the material parameters that apply to the input and output sections are often not the same. Nevertheless, it is clear from (6.1) that adjusting the ratio of t_{out}^{total} to t_{in}^{total} is the primary means of adjusting Y, and therefore of adjusting the ZVS capability.

Comparing Figures 5.18, 5.27, and 5.28, it can be seen from (6.2) that for a given M and ψ, the size of input section that is required for a given sized output section depends on the output topology (i.e. whether AC-output, DC-output capacitively smoothed, or DC-output inductively smoothed). The AC-output topology requires the largest input section, the DC-output capacitively smoothed topologies require the smallest, and the requirements of the inductively smoothed lie approximately mid-way between the two.

For the case where the input and output section electrode radii are equal, but smaller than the outer radius of the device, the results in (6.1) to (6.3) still apply because the $J_1\left(\frac{Ra}{c}\right)/J_1\left(\frac{Rb}{c}\right)$ term that appears in the force factor equations in Chapter 3 becomes

unity. Therefore making the outer radius larger than the electrode radius has no effect upon ZVS capability when the two electrode radii are equal.

B. Relationship between Y and power density (AC-output topology)

Neglecting isolation layers, electrode layers, and any other inactive layers, assuming that $2C_{oss} << C_{in}$, and assuming there is negligible difference between the material parameters that apply to the input and output sections, (6.3) can be used to express the volume of a PT in terms of Y

$$Volume = \pi a^2 \left(t_{out}^{total} + t_{in}^{total}\right) = \pi a^2 t_{out}^{total} \left(1 + \frac{1}{Y}\right). \tag{6.4}$$

Working on the assumption that the input section is large enough to efficiently induce a radial vibration in the output section (i.e. Y is not excessively large), and with reference to Figures 2.7 and 5.1, the output power of a PT in the AC-output topology can be written in terms of the vibration velocity as

$$P_{out,PT} = \frac{A_{out}{}^2 R_L v_{a,RMS}{}^2}{R_L{}^2 \omega^2 C_{out}{}^2 + 1}. \tag{6.5}$$

The maximum vibration velocity that can be used is assumed to be approximately constant for all radial mode designs operating at the first radial resonance, and dependent only on the piezoelectric material itself. Although there are many factors that influence heat generation in a PT design, and therefore the maximum vibration velocity that can be used, the maximum vibration velocity is often assumed constant for the first design iteration [1]. Substituting (5.44) and the appropriate formula from the model in Chapter 2 into (6.5), and making use of the formula for planar coupling factor,

$$P_{out,PT}^{\max} = \frac{2 v_{a,RMS}^{\max}{}^2 \pi k_p{}^{out\,2} t_{out}^{total}}{\omega s_{11}^{E\,out} \left(1 - \sigma_C^{E\,out}\right)\left(1 - k_p{}^{out\,2}\right)} \frac{M}{\left(M^2 + 1\right)}. \tag{6.6}$$

Since a PT will always be operated close to the chosen resonant frequency, ω may be regarded as inversely proportional to the outer radius. Substituting $\omega = \omega_f \frac{R\bar{v}_r}{a}$ (see Chapter 3) into (6.6),

$$P_{out,PT}^{\max} = \frac{2 a v_{a,RMS}^{\max}{}^2 \pi k_p{}^{out\,2} t_{out}^{total}}{\omega_f R \bar{v}_r s_{11}^{E\,out} \left(1 - \sigma_C^{E\,out}\right)\left(1 - k_p{}^{out\,2}\right)} \frac{M}{\left(M^2 + 1\right)}. \tag{6.7}$$

where ω_f is the ratio of the operating frequency to the short circuit resonant frequency, and will usually be around 1.05 to 1.1 when the PT is delivering full power. Dividing (6.7) by (6.4), the power density of a PT can be expressed in terms of Y as

$$P_{density} \propto \frac{v_{a,RMS}^{max\ 2} MY}{a(Y+1)(M^2+1)}. \tag{6.8}$$

For a given load condition M, it is therefore desirable from a power density perspective to use the largest value of Y possible. However, from the previous chapter, it is known that ZVS can only be achieved if Y is less than or equal to Y_{max}, and that for a given topology Y_{max} is a function only of M and ψ. Thus, (6.8) elucidates why the previous chapter concentrated on calculating the largest value of Y at which ZVS can be achieved assuming a free choice of frequency and dead-time; for a given M and ψ, the power density of a PT capable of inductor-less ZVS is maximised by designing such that $Y = Y_{max}$.

C. Relationship between load condition and power density (AC-output topology)

It was shown in the previous chapter that Y_{max} is dependent upon M. However, as (6.7) demonstrates, so too is the maximum output power of a PT. For a given set of output section dimensions, (6.7) indicates that the maximum output power of a PT is proportional to $M/(M^2+1)$, and is therefore theoretically maximum at $M=1$. Since the output power of a PT with a given set of output section dimensions is maximum at $M=1$, but the size of the input section required for a PT with that output section to achieve ZVS is largest when $M=1$ (see Figure 5.14 and (6.2)), it is not immediately clear what value of M will maximize the overall power density of a PT that is designed for inductor-less ZVS. From (6.8), the power density of a PT where Y has been set so as to maximise power density whilst also just allowing ZVS to be achieved can be expressed as

$$P_{density} \propto \frac{v_{a,RMS}^{max\ 2} MY_{max}}{a(Y_{max}+1)(M^2+1)}. \tag{6.9}$$

Hence for a given radius and a given piezoelectric material, PT power density is proportional to $MY_{max}/((M^2+1)(Y_{max}+1))$. This function is plotted in Figure 6.1 using data for the AC-output $\psi=1$, $X=0.1$ case. Since there is negligible change in Y_{max} with X, this plot applies to all values of X. Figure 6.1 indicates that the theoretical power density of a PT in the inductor-less AC-output topology will be maximized by designing

the PT such that the load into which maximum power is to be delivered coincides with the matched load condition $(M=1)$, even though this value of M requires the largest input section thickness to achieve ZVS.

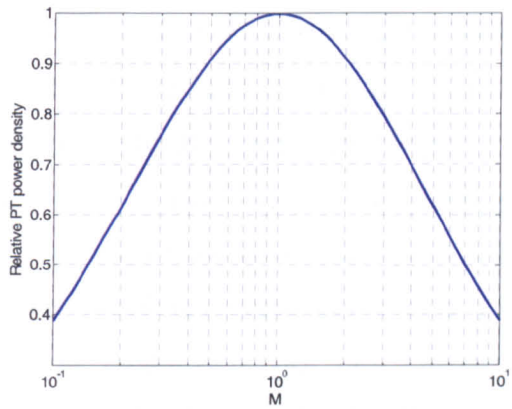

Figure 6.1: Change in relative power density with M for the AC-output topology when Y_{max} is calculated using $\psi=1$.

From a design perspective, the choice of M will also depend on many other factors, such as the tendency for Q_m to decrease as the number of layers is increased, geometric considerations, etc. However, given the shape of Figure 6.1, it is likely that power density will become increasingly compromised if a PT is designed such that maximum power is to be delivered at M values considerably above or below 1.

Taking into account the losses when calculating Y_{max} for use in (6.8) is not straightforward because in reality the way in which efficiency would change as the PT design were altered in order to change M (we are assuming here that R_L is fixed by the converter specification) depends on many factors. However, since there is a tendency for efficiency to decrease as M is moved away from unity, the decrease in power density that is shown in Figure 6.1 is likely to become even more pronounced at M values considerably above or below 1.

D. Relationship between load condition and power density (DC-output topologies)

Approximate relationships between PT power density, M, and Y_{max} for a radial mode Transoner device with a given radius and vibration velocity can be derived for the DC-output topologies using similar approximations. For the capacitively smoothed topologies, power density is found to be proportional to $MY_{max}/\left((M+1)^2(Y_{max}+1)\right)$, where

M is defined as shown in (5.60) for the full-bridge capacitively smoothed topology, or as shown in (5.73) for the half-wave capacitively smoothed topology. For the inductively smoothed topologies, power density is proportional to $MY_{max}/((M^2+1)(Y_{max}+1))$ when in the continuous mode, and $\pi Y_{max}(2\sin(\alpha+\beta)\sin(\alpha)-\cos^2(\alpha)-\cos^2(\alpha+\beta)+2)/(8(1+Y_{max}))$ when in the discontinuous mode, where M is defined as shown in (5.64) for the full-bridge inductively smoothed topology, or as shown in (5.74) for the current doubler topology. α and β are again found from the solution to (5.71) and (5.72). It should be noted that these formulas cannot be directly used to compare the power density of one inductor-less topology against another because the maximum output power of a given sized output section depends on the choice of output topology (see Chapter 4). Overall topology comparisons will be made in Section 6.5. Using the appropriate data sets for the change in Y_{max} with M at $X=0.1$, $\psi=1$, the anticipated change in overall PT power density with M is plotted for all 5 topologies in Figure 6.2. This figure applies to all values of X because the change in Y_{max} with X is negligible. It is concluded that, regardless of the topology, M should be kept close to unity for the load resistance into which maximum power is to be delivered. The change in shape that occurs for the inductively smoothed topologies in Figure 6.2 is caused by the rectifiers changing from the continuous to discontinuous modes of operation at $M=2/\pi$ (see Chapters 4 and 5, and [2]).

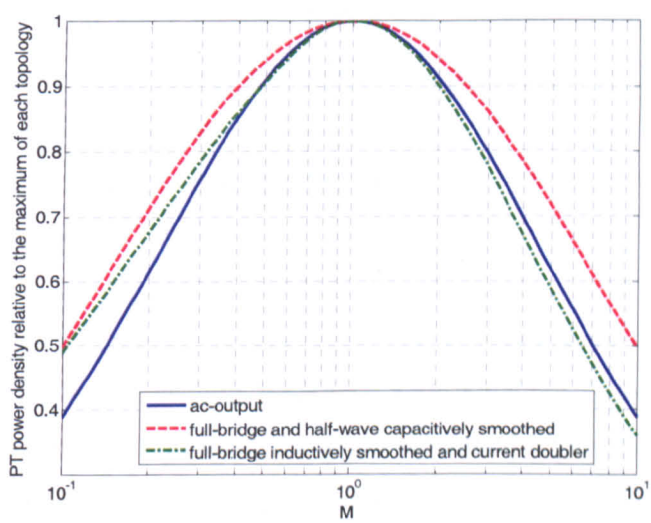

Figure 6.2: Change in relative power density with M when Y_{max} is calculated using $\psi=1$.

E. Comparison between with-inductor and inductor-less designs

From Figure 2.7, PT input power can be expressed in terms of the vibration velocity as

$$P_{in,PT} = |A_{in}| v^1_{Cin,RMS} v_{a,RMS} \cos(\phi) \tag{6.10}$$

where $v^1_{Cin,RMS}$ is the RMS value of the fundamental component of the voltage across the input capacitance and ϕ is the tank impedance phase angle. As discussed in Chapter 3, assuming $P_{out,PT} \approx P_{in,PT}$ and substituting the formula for A_{in} from Chapter 2 results only in a dependence on the radius and the number of layers in the input section, and not on the volume of the input section itself. However, because of the assumptions made in Chapters 2 and 3, the input section must be large enough compared to the rest of the device for a radial vibration to be efficiently induced in the output section. Considering devices that were optimised for the with-inductor topology, such as the Transoner T1-15W, this can be achieved with an input section that is much smaller than the rest of the device. In the case of the T1-15W, the total input section thickness is approximately 0.66 times the total thickness of the rest of the device.

A PT with a given set of output section dimensions, operating in the AC-output topology with a matched load and achieving 95% efficiency, would require a total input section thickness that was at least 1.57 times the total output section thickness if it were used in the inductor-less topology (see Figure 5.14 and (6.3)). In contrast, the same PT would require a much smaller input section if it were used in a with-inductor topology, e.g. 0.66 times the output section. Since both devices would have the same maximum theoretical output power (see (6.6)), it is therefore apparent that an inductor-less design will always achieve PT lower power density than a with-inductor design because it requires a proportionally larger input section which contributes nothing further to the theoretical maximum output power.

From (6.2), (6.3) and Figures 5.21 and 5.24, the DC-output capacitively smoothed topologies require an input section thickness approximately 1.05 times the output section at $M=1$, $\psi=1/0.95$, and the inductively smoothed topologies require an input section volume approximately 1.35 times the output section at $M=1$, $\psi=1/0.95$. Thus, all five variants have input section thickness requirements for ZVS at $M=1$ that are larger than that required to ensure a radial vibration is efficiently induced in the output section. Consequently, all five will achieve lower PT power density if they are designed for inductor-less operation compared to with-inductor operation. However, it is also

clear that the decrease in PT power density that will occur when moving from a with-inductor to an inductor-less design will be much less severe for the DC-output capacitively smoothed topologies than the AC-output topology. For a given set of output section dimensions, the DC-output topologies require a proportionally smaller input section to achieve ZVS than the AC-output topology. However, it is known from Chapter 4 that the maximum output power that can be achieved for a given vibration velocity and a given set of output section dimensions is highly dependent upon the output topology (i.e. whether AC-output, DC-output capacitively smoothed, or DC-output inductively smoothed). Therefore the previous statement does not imply that the inductor-less DC-output topologies achieve higher PT power density than the AC-output topology. Conclusions about PT power density in the various topologies are given in Section 6.5.

A further consideration is that, because the input section thickness required for an inductor-less design is greater than that for a with-inductor design, the design may have to be changed to a larger radius in order to prevent interference from the first thickness mode, and this may further reduce power density (see (6.8)). Although the power density of the PT itself will be lower when using an inductor-less design, a saving is then made by the removal of the inductor. Therefore in some cases, an inductor-less design may result in a converter with higher overall power density. Whilst the mechanical losses in an inductor-less design are likely to be greater than a with-inductor design, simply because the PT will be larger, the latter would obviously incur additional losses from the inductor. Hence there are many trade-offs between the with-inductor and inductor-less topologies.

6.3 Impact of unequal electrode radii on the ZVS condition and power density

The equivalent circuit model formulas in Chapter 3 depend on whether the input section electrode radius is smaller than the output section electrode radius, or vice versa. Therefore it is easiest to consider each case in turn.

A. Input section electrode radius less than or equal to output section electrode radius

For this case, the equivalent circuit components in Figure 5.1 are described by (3.132) to (3.140) in Chapter 3, where a is the radius of the input section electrodes and b is the radius of the output section electrodes. Substituting these into (5.49) and neglecting C_{oss} results in

$$Y = \frac{t_{out}^{total}}{t_{in}^{total}} \frac{J_1\left(\frac{Rb}{c}\right)^2}{J_1\left(\frac{Ra}{c}\right)^2} \frac{\varepsilon_{33}^{T\,in}\left(1-k_p{}^{in\,2}\right)d_{31}{}^{out\,2}s_{11}^{E\,in\,2}\left(1-\sigma_C{}^{in}\right)^2}{\varepsilon_{33}^{T\,out}\left(1-k_p{}^{out\,2}\right)d_{31}{}^{in\,2}s_{11}^{E\,out\,2}\left(1-\sigma_C{}^{out}\right)^2}. \tag{6.11}$$

Hence, for inductor-less ZVS,

$$t_{in}^{total} > \frac{t_{out}^{total}}{Y_{\max}} \frac{J_1\left(\frac{Rb}{c}\right)^2}{J_1\left(\frac{Ra}{c}\right)^2} \frac{\varepsilon_{33}^{T\,in}\left(1-k_p{}^{in\,2}\right)d_{31}{}^{out\,2}s_{11}^{E\,in\,2}\left(1-\sigma_C{}^{in}\right)^2}{\varepsilon_{33}^{T\,out}\left(1-k_p{}^{out\,2}\right)d_{31}{}^{in\,2}s_{11}^{E\,out\,2}\left(1-\sigma_C{}^{out}\right)^2}. \tag{6.12}$$

A plot of the function $J_1\left(\frac{Rb}{c}\right)^2 / J_1\left(\frac{Ra}{c}\right)^2$ is shown in Figure 6.3. From Figures 5.14, 5.16, 5.18, and Figure 6.3, and (6.12), it can be seen that the size of t_{in}^{total} (and hence the volume of the input section, $\pi c^2 t_{in}^{total}$) required to achieve ZVS:

- increases as M approaches unity (assumes ψ, a, b, c, t_{out}^{total} held constant)
- increases as PT efficiency decreases (assumes M, a, b, c, t_{out}^{total} held constant)
- decreases as a is increased (assumes ψ, M, b, c, t_{out}^{total} held constant)
- decreases as b is decreased (assumes ψ, M, a, c, t_{out}^{total} held constant)

(Note that a, b, and c are bounded: $a \le b \le c$)

Hence, for a given c, t_{out}^{total} (and hence a given output section volume), M, and ψ, the value of t_{in}^{total} (and hence the input section volume) required to obtain ZVS is minimised by making $a = b$. Once $a = b$, their size relative to c makes no difference to the ZVS behaviour, but does affect output power, and therefore power density.

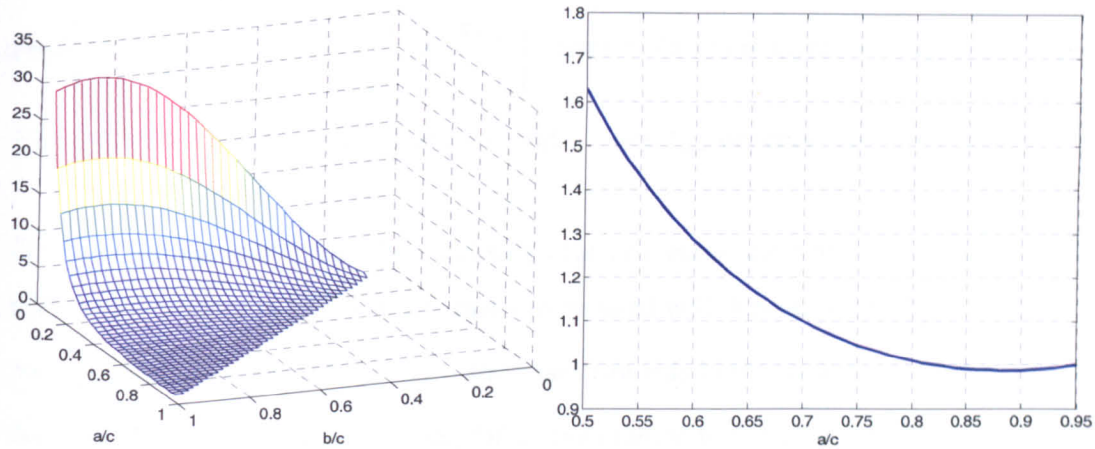

(a) (b)

Figure 6.3: Plots of the function $J_1\left(\frac{Rb}{c}\right)^2 / J_1\left(\frac{Ra}{c}\right)^2$. a) for $a \le b \le c$, b) for $a \le b$ when $b/c = 0.95$.

Substituting the appropriate formula from Chapter 3 into (6.5) and letting $\omega = \omega_f \frac{R\bar{\upsilon}_r}{c}$, the maximum output power of a PT in the AC-output configuration is

$$P_{out,PT}^{\max} = \frac{2v_{b,RMS}^{\max\ 2}\pi k_p^{\ out\,2} t_{out}^{total} c}{\omega_f R\bar{\upsilon}_r s_{11}^{E\,out}\left(1-\sigma_C^{E\,out}\right)\left(1-k_p^{\ out\,2}\right)}\frac{M}{\left(M^2+1\right)}. \tag{6.13}$$

Note that the vibration velocity is now $v_{b,RMS}$ instead of $v_{a,RMS}$. Neglecting isolation layers and any other inactive layers, assuming that $2C_{oss} << C_{in}$, and assuming there is negligible difference between the material parameters that apply to the input and output sections, the volume of a ZVS capable PT is given by

$$Volume = \pi c^2\left(t_{out}^{total} + t_{in}^{total}\right) = \pi c^2 t_{out}^{total}\left(1+\frac{J_1\left(\frac{Rb}{c}\right)^2}{Y_{\max}J_1\left(\frac{Ra}{c}\right)^2}\right) \tag{6.14}$$

where (6.11) has been used to define the t_{in}^{total} required for ZVS to just be achieved. Hence, from (6.13) and (6.14), the power density of such a PT is

$$P_{density} \propto \frac{v_{b,RMS}^{\max\ 2}}{c}\frac{k_p^{\ out\,2}}{\left(1-k_p^{\ out\,2}\right)}\frac{M}{\left(M^2+1\right)}\frac{1}{\left(1+\frac{J_1\left(\frac{Rb}{c}\right)^2}{Y_{\max}J_1\left(\frac{Ra}{c}\right)^2}\right)}. \tag{6.15}$$

It was shown in Figure 6.3 that $J_1\left(\frac{Rb}{c}\right)^2 / J_1\left(\frac{Ra}{c}\right)^2$ is minimised by making $a = b$, and that this minimum is independent of the value of $a = b$ and c. Since $Y_{\max}$ is always

positive, the $1/\left(1+J_1\left(\frac{Rb}{c}\right)^2/\left(Y_{\max}J_1\left(\frac{Ra}{c}\right)^2\right)\right)$ term in (6.15) is therefore maximised when $a=b$ and becomes independent of $a=b$ and c since $Y_{\max}$ depends only on M and ψ.

For a given maximum vibration velocity that can occur anywhere in the device, the maximum value of $v_{b,RMS}$ in (6.15) that can be used will depend on the ratio of b to c. As b is increased towards c, $v_{b,RMS}$ increases towards the maximum vibration velocity that occurs within the device. Thus, for a given material, the value of $v_{b,RMS}^{\max}$ that can be used in (6.15) is maximised when $b \approx c$. Since making $b \approx c$ has no effect on the $J_1\left(\frac{Rb}{c}\right)^2/J_1\left(\frac{Ra}{c}\right)^2$ term when $a=b$, it is therefore concluded that power density is maximised by making $a=b$, $b \approx c$, and keeping c relatively small. Although the difference between $v_{b,RMS}^{\max}$ and the maximum vibration velocity is small once b/c is greater than about 0.75, it is still advantageous to make $b \approx c$ because the mechanical losses will be lower (the non-piezoelectric ring in region 3 still contributes to R_m).

B. Output section electrode radius less than or equal to input section electrode radius

For this case, the equivalent circuit components in Figure 5.1 are described by (3.131) to (3.139), but with the "in" and "out" identifiers swapped around. a is the radius of the output section electrodes and b is the radius of the input section electrodes. Substituting these into (5.49) and neglecting C_{oss} results in

$$Y=\frac{t_{out}^{total}}{t_{in}^{total}}\frac{J_1\left(\frac{Ra}{c}\right)^2}{J_1\left(\frac{Rb}{c}\right)^2}\frac{\varepsilon_{33}^{T\,in}\left(1-k_p{}^{in\,2}\right)d_{31}{}^{out\,2}s_{11}^{E\,in\,2}\left(1-\sigma_C{}^{in}\right)^2}{\varepsilon_{33}^{T\,out}\left(1-k_p{}^{out\,2}\right)d_{31}{}^{in\,2}s_{11}^{E\,out\,2}\left(1-\sigma_C{}^{out}\right)^2}. \tag{6.16}$$

Hence, for inductor-less ZVS,

$$t_{in}^{total}>\frac{t_{out}^{total}}{Y_{\max}}\frac{J_1\left(\frac{Ra}{c}\right)^2}{J_1\left(\frac{Rb}{c}\right)^2}\frac{\varepsilon_{33}^{T\,in}\left(1-k_p{}^{in\,2}\right)d_{31}{}^{out\,2}s_{11}^{E\,in\,2}\left(1-\sigma_C{}^{in}\right)^2}{\varepsilon_{33}^{T\,out}\left(1-k_p{}^{out\,2}\right)d_{31}{}^{in\,2}s_{11}^{E\,out\,2}\left(1-\sigma_C{}^{out}\right)^2}. \tag{6.17}$$

A plot of the function $J_1\left(\frac{Ra}{c}\right)^2 / J_1\left(\frac{Rb}{c}\right)^2$ is shown in Figure 6.4. From Figures 5.14, 5.16, 5.18, and Figure 6.4, and (6.17), it can be seen that the size of t_{in}^{total} (and hence the volume of input section, $\pi c^2 t_{in}^{total}$) required to achieve ZVS:

- increases as M approaches unity (assumes ψ, a, b, c, t_{out}^{total} held constant)
- increases as PT efficiency decreases (assumes M, a, b, c, t_{out}^{total} held constant)
- decreases as a is decreased (assumes ψ, M, b, c, t_{out}^{total} held constant)
- decreases as b is increased (assumes ψ, M, a, c, t_{out}^{total} held constant)

(Again, a, b, and c are bounded: $a \le b \le c$).

Hence, for a given c, t_{out}^{total} (and hence a given output section volume), M, and ψ, the value of t_{in}^{total} (and hence the input section volume) required to obtain ZVS is minimised by maximising b and minimising a.

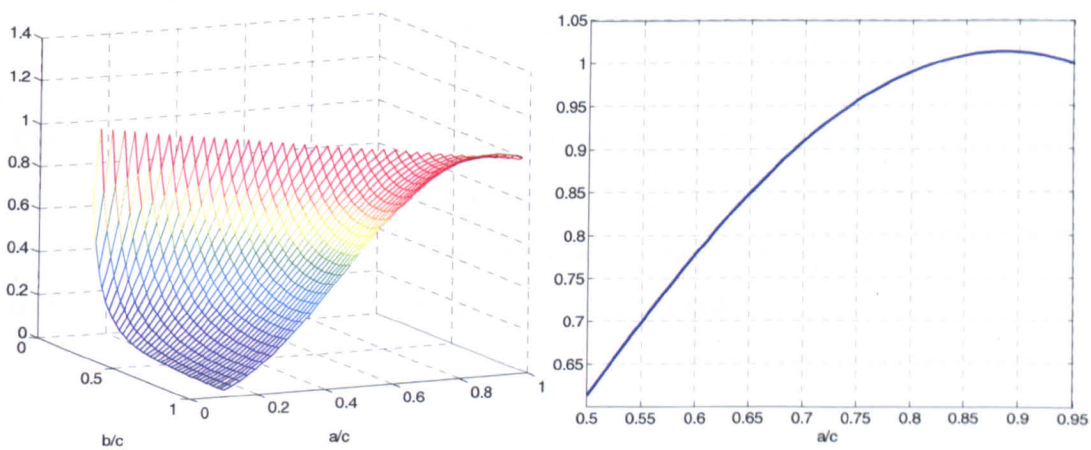

(a) (b)

Figure 6.4: Plots of the function $J_1\left(\frac{Ra}{c}\right)^2 / J_1\left(\frac{Rb}{c}\right)^2$. a) for $a \le b \le c$, b) for $a \le b$ when $b/c = 0.95$.

Substituting the appropriate formula from Chapter 3 into (6.5) and letting $\omega = \omega_f \frac{R\bar{\upsilon}_r}{c}$, the maximum output power of a PT in the AC-output configuration is

$$P_{out,PT}^{\max} = \frac{2v_{b,RMS}^{\max\ 2} \pi k_p^{\ out\ 2} t_{out}^{total} c}{\omega_f R\bar{\upsilon}_r s_{11}^{E\,out}\left(1-\sigma_C^{E\,out}\right)\left(1-k_p^{\ out\ 2}\right)} \frac{M}{\left(M^2+1\right)} \frac{J_1\left(\frac{Ra}{c}\right)^2}{J_1\left(\frac{Rb}{c}\right)^2}. \tag{6.18}$$

Using the previously described approximations, the volume of a PT capable of inductor-less ZVS is

$$Volume = \pi c^2 \left(t_{out}^{total} + t_{in}^{total} \right) = \pi c^2 t_{out}^{total} \left(1 + \frac{J_1\left(\frac{Ra}{c}\right)^2}{Y_{max} J_1\left(\frac{Rb}{c}\right)^2} \right) \tag{6.19}$$

where (6.16) has been used to define the t_{in}^{total} required for ZVS to just be achieved. Hence, from (6.18) and (6.19), PT power density is given by

$$P_{density} \propto \frac{v_{b,RMS}^{max\ 2}}{c} \frac{k_p{}^{out\,2}}{\left(1 - k_p{}^{out\,2}\right)} \frac{M}{\left(M^2+1\right)} \frac{1}{\left(\frac{J_1\left(\frac{Rb}{c}\right)^2}{J_1\left(\frac{Ra}{c}\right)^2} + \frac{1}{Y_{max}} \right)} \tag{6.20}$$

Again, it was shown in Figure 6.2 that $J_1\left(\frac{Rb}{c}\right)^2 / J_1\left(\frac{Ra}{c}\right)^2$ is minimised by making $a = b$, and that this minimum is independent of the value of $a = b$ and c. Since Y_{max} is always positive, the $1/\left(\left(J_1\left(\frac{Rb}{c}\right)^2 / J_1\left(\frac{Ra}{c}\right)^2 \right) + \frac{1}{Y_{max}} \right)$ term in (6.20) is therefore maximised when $a = b$ and becomes independent of $a = b$ and c since Y_{max} depends only on M and ψ.

This time, for a given material, the value of $v_{b,RMS}^{max}$ that can be used in (6.20) is dependent upon the ratio of the radius of the input section electrodes to the outer radius, and is maximised when $b \approx c$. Therefore it is again concluded that the power density of such devices is maximised by making $a = b$, $b \approx c$, and keeping c relatively small.

6.4 Guidelines for maximising the power density of PTs capable of inductor-less ZVS

In Sections 6.2 and 6.3, it has been shown that the power density of a radial mode Transoner PT that is designed to achieve inductor-less ZVS will be maximised if

- The load condition $M = 1$ is observed for the load into which maximum PT output power is to be delivered.
- The phase angle of the tank impedance is between 57.05° and 57.55° when operating with the load into which maximum PT output power is to be delivered.
- The ratio between C_{eff} and $N^2 C_{out}$ is equal to Y_{max} for the M and ψ that correspond to the load into which maximum PT output power is to be delivered.

- The input and output section electrode radii are equal to one another, and approximately equal to the outer radius of the device.
- The outer radius of the device is kept relatively small (but large enough that c/t_{total} is large enough to prevent interference from the first thickness mode)
- A piezoelectric material with a high planar coupling factor, which can operate at high vibration velocities in a thermally stable manner, is used.

Many of these guidelines are similar to those for the with-inductor topology (see Chapter 3). However, because there is a tank impedance phase angle that optimises power density (by minimising the size of the input section required to achieve inductor-less ZVS), it is harder to achieve a converter design that simultaneously meets these guidelines and also meets a particular converter specification.

For many converter specifications, it should be possible to find a design that adheres to the guidelines above. In step-down applications, A_{out} is relatively large, which in turn requires several layers to be used in the output section, whilst A_{in} is relatively small and may only require one layer (A_{out} is determined by $P_{out,PT} = A_{out}{}^2 v_{b,RMS}{}^2 R_s$, where R_s is the equivalent series resistance of the output topology, whilst A_{in} is determined by (3.149). Note that $\phi \approx 57.3°$ should be used in (3.149)). If the design is to be realised with $a = b \approx c$, then A_{in} effectively determines all three radii if the size of A_{in} is such that only a single layer is required. The need to have an integer number of layers may then result in A_{out} being slightly larger or smaller than the value required for M to equal 1 at the nominal load resistance, vibration velocity, and output power. However, because there are several output section layers, the deviation from $M = 1$ will be relatively small.

In cases where the desire to keep $a = b \approx c$ may result in an A_{out} that corresponds to an M of less than unity for the load into which maximum output power is to be delivered (due to the need for there to be an integer number of layers), the penalty in terms of power density will still be reasonably small (see Figure 6.2) provided the deviation from $M = 1$ is not too large. Thus, M can be thought of as a way of balancing the input and output section requirements so that a particular specification can be achieved with $a = b \approx c$. The alternative is to allow the input and output section electrode radii to be different; however, this will also have an impact on power density, as shown in Section 6.3.

If a very large step-down ratio is required, it may not be possible to simultaneously achieve an output section design that is capable of delivering the required output power whilst also having an outer radius that allows a small enough A_{in} to be achieved using a single layer input section with an electrode radius approximately equal to that outer radius. In other words, if A_{in} is allowed to dictate the input section electrode radius and the outer radius, the output section design may have to be so thick in order to achieve the required output power that interference will occur between the thickness and radial vibration modes. In these circumstances, there are two options:

1) Allow the input section electrode radius to be smaller than the output section electrode radius and outer radius (but keeping the output section electrode radius approximately equal to the outer radius).
2) Allow for a larger A_{in} to be used by operating at a ϕ larger than $\approx 57.3°$. Note that this *will* require a smaller Y to be used in order to achieve ZVS.

Both of these options will compromise power density. Note that the second option can be used in with-inductor PT designs without any impact on power density because the size of C_{in} does not need to be controlled (so there is no need to try and operate at $\phi = 57.3°$). However, for inductor-less designs, when ϕ is greater or less than $\approx 57.3°$, the value of Y required for inductor-less ZVS decreases, which in turn requires a larger input section to be used. The first option allows $\phi = 57.3°$ to be used at the nominal power, but also decreases power density because a larger input section is required when the input section electrode radius and output section electrode radius are not equal (see Section 6.3). However, both options allow the outer radius to be chosen such that the output section design is of reasonable proportions, and enable a design to be found that satisfies the electrical specifications. Note that using an M of less than 1 will not help in this situation because it would result in an even larger output section volume being required to meet the required output power.

Sometimes a converter manufacturer will specify a maximum component height which restricts the maximum total thickness of the PT. Depending on the other specifications (power level, etc), this can result in the PT requiring a larger outer radius than would otherwise be used. That is, a higher c/t_{total} ratio must be used. Not only does the use of a larger radius decrease power density (see (4.47), (4.48), and (4.49)) but it can also make it impossible to achieve the A_{in} that is commensurate to $\phi \approx 57.3°$ with an input section

electrode radius that is close to the outer radius in step-down applications. In other words, once a sufficient portion of the total thickness is allowed for the input section thickness, the required output power level can only be achieved with an output section that has a large electrode radius, and when the outer radius is then made just larger than this, a single input section layer with an electrode radius close to the outer radius results in A_{in} being too large for $\phi \approx 57.3°$ to coincide with the required power level, vibration velocity, and fundamental component of the half-bridge voltage waveform (see (3.149)). Again, there are two options, but both compromise power density:

1) Allow the input section electrode radius to be smaller than the output section electrode radius.
2) Allow for a larger A_{in} to be used by operating at a ϕ larger than $\approx 57.3°$.

It is therefore concluded that it can be more difficult to achieve a PT design that simultaneously achieves high power density and meets the required electrical specifications with an inductor-less design compared to a with-inductor design. Although there are many practical considerations that will affect the final choice of device dimensions and the associated equivalent circuit component values, the following is suggested as a starting point for achieving a high power density inductor-less PT design

- C_{out} is chosen such that M is close to 1 for the load into which maximum power is to be delivered.
- A_{out} is chosen such that the maximum allowable vibration velocity corresponds to the required maximum output power at the required load.
- A_{in} is chosen such that when $\phi = 57.3°$, the maximum vibration velocity corresponds to the chosen input voltage and maximum input power required.
- The upper limit for C_{eff} is then calculated from the design charts and the previously determined C_{out}, A_{out}, A_{in}, M, and an estimate of the expected PT efficiency.

A_{out}, A_{in}, C_{out}, and C_{eff} are then translated into a physical PT design using the equivalent circuit models in Chapters 2 and 3. However, because of the aforementioned issues, it may be necessary to adjust these values of A_{out}, A_{in}, C_{out}, and C_{eff} so that a physical design can be found that meets all the electrical specifications simultaneously.

6.5 Relative overall PT power density comparisons

Having studied the effect of the output topology on power density (Chapter 4), and the effect of the input topology (with-inductor or inductor-less) on power density (Chapters 3, 5, and 6), a comparison can now be made between the various half-bridge based topologies. Only devices where the input section electrode radius, output section electrode radius, and outer radius are all equal (i.e. the optimum case) will be considered. Furthermore, in each case it is assumed that the optimum load condition is always used ($M=1$). The results apply only to a given radius, and rely on making the assumption that the maximum vibration velocity that can be used is approximately constant across all designs.

We start by considering a radial mode Transoner device with a given set of output section dimensions. The volume of the output section is designated as 1. The input section volume is then calculated. For the with-inductor topologies, it is assumed that the input section volume must be approximately 0.66 times the volume of the output section in order for a radial vibration to be properly established in the output section. For the inductor-less topologies, the input section volume is defined by the need to obtain ZVS, assuming the PT is 95% efficient. The relative maximum PT output power of each topology is then calculated using the results from Chapter 4. Finally, a relative PT power density is obtained by dividing the relative maximum PT output power by the combined volume of the input and output sections. The results are shown in Table 6.1.

	With-inductor, AC-output	With-inductor, DC-output capacitively smoothed	With-inductor, DC-output inductively smoothed	Inductor-less, AC-output	Inductor-less, DC-output capacitively smoothed	Inductor-less, DC-output inductively smoothed
Output section volume	1	1	1	1	1	1
Input section volume	0.66	0.66	0.66	1.57	1.05	1.35
Relative PT output power	1	$2/\pi$	$8/\pi^2$	1	$2/\pi$	$8/\pi^2$
Relative PT power density	0.602	0.386	0.488	0.389	0.311	0.345

Table 6.1: Predicted relative PT power density when using the various half-bridge topologies.

From Table 6.1 it can be seen that, although the DC-output capacitively smoothed topologies require a much smaller input section for a given sized output section in order to achieve ZVS compared to the AC-output topology, the overall power density of this topology is still lower because less output power is obtained from a given sized output section with the capacitively smoothed topologies than with the AC-output topology.

A key conclusion of this work is that, for DC-output applications, the power density of a radial mode Transoner PT is maximised if it is used in the with-inductor topology with an inductively smoothed rectifier. For a given output topology, the with-inductor half-bridge achieves higher PT power density than the inductor-less topology, but requires an inductor. For a given input topology (i.e. with-inductor or inductor-less), an inductively smoothed rectifier achieves higher PT power density than the capacitively smoothed, but again requires an extra inductor. Hence, there is a trade-off with both the series inductor at the PT input and the inductor of the rectifier, between PT power density on the one hand, and the cost and size of the additional inductor(s) on the other.

If piezoelectric materials that can operate at high vibration velocity in a thermally stable manner are developed, then the decrease in power density that is incurred by the inductor-less DC-output capacitively smoothed topology may become far less of an obstacle to the introduction of PT-based DC-output converters because the power density will still be higher than their magnetic counterparts. However, until this happens, it is the author's opinion that PT-based DC-output converters will find it hard to compete directly with magnetic technology (and especially planar magnetics) in applications where power density is of utmost importance. There may, however, be other applications in which the specific merits of a completely inductor-less converter can be put to good use, such as converters for electromagnetically harsh environments.

6.6 Summary

Through an approximate analysis of the input section required for ZVS at a particular load condition, and the output power of a device of given radius at that load condition, it has been shown that the theoretical power density of an inductor-less radial mode Transoner PT is maximised by designing the PT such that the load condition $M=1$ corresponds to the load resistance into which maximum PT output power is to be delivered, even though this load condition requires the largest input section to achieve ZVS.

Inductor-less radial mode Transoner PTs have been shown to require a larger input section thickness than their with-inductor counterparts for a given set of output section dimensions. For the AC-output topology, this increase is substantial and results in considerably lower PT power density than the with-inductor topology. However, since the difference was found to be much smaller for the capacitively smoothed DC-output topologies, it is concluded that the inductor-less configuration is of greater benefit in converters where these topologies are used.

Guidelines for maximising the power density of radial mode Transoner PTs in inductor-less converters have been given, and the compromises that will sometimes be necessary in order to simultaneously meet all the requirements of certain converter specifications have been discussed.

6.7 References

[1] A. V. Carazo, "Piezoelectric Converters for DC/DC and AC/DC applications," presented at Portable Power Developer's Conference, 2005.

[2] A. J. Forsyth, G. A. Ward, and S. V. Mollov, "Extended fundamental frequency analysis of the LCC resonant converter," *IEEE Transactions on Power Electronics*, vol. 18, pp. 1286-1292, 2003.

Chapter 7 - Inductor-less PT-based DC-output capacitively smoothed converters with output voltage regulation

7.1 Introduction

The previous chapter has provided guidelines and design constraints for maximising the power density of inductor-less PT-based converters. This focused on the situation where a PT is designed to drive a specific load condition using the frequency and dead-time that most readily allow ZVS to be obtained. However, DC-DC converters are typically required to provide output voltage regulation from no-load up to the maximum specified load, and resonant converters often achieve this by frequency modulation. It is therefore important to assess the impact that output voltage regulation via frequency modulation has on the ZVS condition. This is addressed in the present chapter, where a focus is placed on the DC-output capacitively smoothed topology shown in Figure 7.1. Note that throughout this chapter, the vibration velocity that constitutes the tank current in the full lumped equivalent circuit is referred to as v_a (as per Chapter 2), however, the contents are equally applicable to devices where the tank current is v_b (as per Chapter 3).

Firstly, a method is presented for determining the optimum equivalent component values for a radial mode Transoner for a given converter specification such that the guidelines in the previous chapter are observed for the load into which maximum power is to be delivered. This is verified with an example design using SPICE simulation. Whilst ZVS will just be achieved at the maximum load, and PT power density will be maximised, it is not clear what will happen as the load resistance is increased and the switching frequency is dictated by the need to maintain constant output voltage. Therefore, a method for analysing the ZVS capability of voltage regulating converters is developed and applied to the example design. Conclusions are then drawn about the suitability of this topology for applications requiring voltage regulation, and how such converters should be designed.

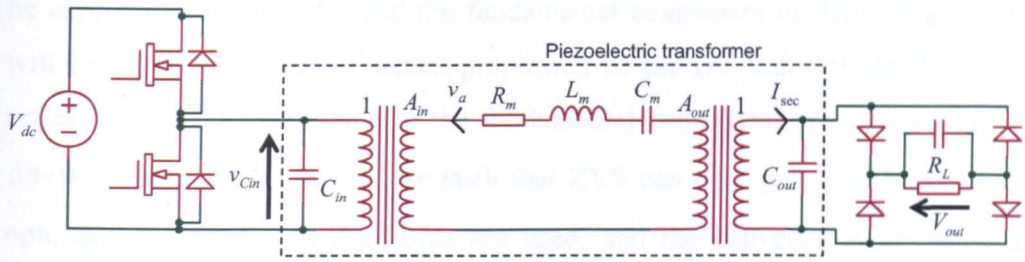

Figure 7.1: The inductor-less PT-based DC-output capacitively smoothed topology with a full-bridge rectifier. The full lumped equivalent circuit model of the PT is shown.

7.2 PT design method

The following method generates a theoretically optimum set of equivalent circuit component values based on the ZVS analysis in the previous chapter, and therefore represents a useful starting point for a practical PT design. The design is centred on the load into which maximum power is to be delivered.

The fixed electrical design specifications are:

- The load resistance into which maximum output power is to be delivered, R_L
- The associated maximum power to be delivered to that load resistance, P_{out}
- Required output voltage, V_{out}
- DC link voltage, V_{dc}
- On-state voltage drop of a single rectifier diode, V_d

The variables that must be decided by the PT designer are

- The maximum motional current (i.e. the maximum vibration velocity), v_a
- M, the desired loading factor when delivering maximum power
- ψ, the inverse of the expected PT efficiency at that loading factor
- L_m
- C_m

When a PT is designed such that ZVS is only just achieved when the optimum frequency and dead-time for ZVS are used, the phase angle and dead-time fraction that result in ZVS are always approximately 57.3° and 0.239 respectively. Therefore the shape of the voltage waveform across the input capacitance at this operating point will

be approximately constant, and the fundamental component of that voltage waveform will be an approximately constant proportion of the DC link voltage. Using Fourier series formula, the amplitude of the fundamental component of v_{Cin} was found to be $0.593V_{dc}$ when Y, M, and ψ are such that ZVS can only just be achieved when the optimum frequency and dead-time are used, and the converter is operating at that optimum frequency and dead-time.

The following quantities can be calculated directly from the design specification and remain fixed during the design process:

- The RMS of the fundamental component of v_{Cin}, $v^1_{Cin,RMS} = \dfrac{0.593V_{dc}}{\sqrt{2}}$.
- The efficiency of the full-bridge capacitively smoothed rectifier is approximately $\eta_{rect} = \dfrac{1}{1+2V_{df}}$. Therefore the total PT output power required is $P_{out,PT} = \dfrac{P_{out}}{\eta_{rect}} = P_{out}\left(1+2V_{df}\right)$.
- The total PT input power required is therefore $P_{in,PT} = \psi P_{out,PT}$.
- The ratio of the rectifier diode on-state voltage drop to the converter output voltage, $V_{df} = \dfrac{V_d}{V_{out}}$.

The circuit of Figure 7.1 is modelled with the circuits shown in Figure 7.2 (see Appendix B), Figure 7.3, and Figure 7.4 (see Chapter 5), depending on the type of calculation being performed and which model it is most convenient to use.

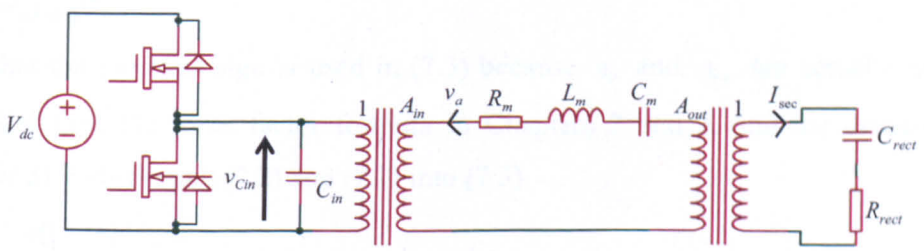

Figure 7.2: Full PT lumped equivalent circuit with RC rectifier model.

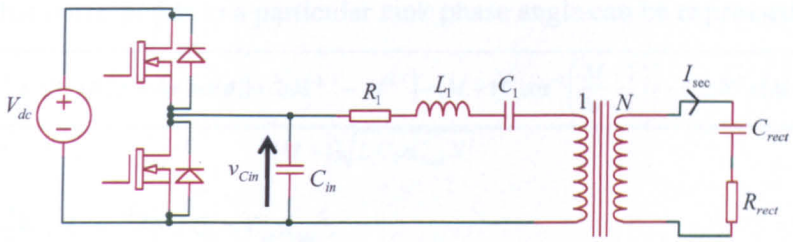

Figure 7.3: Simplified PT lumped equivalent circuit with RC rectifier model.

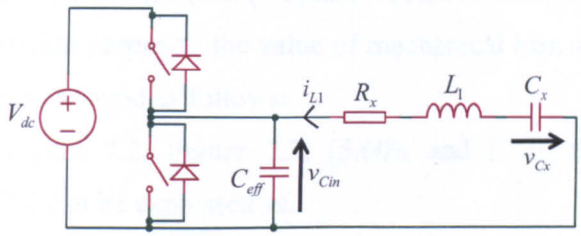

Figure 7.4: Simplified equivalent circuit of the form used for the ZVS analysis in Chapter 5.

The main design equations are derived as follows (and draw upon those developed in Chapter 5). Rearranging (5.60), the output capacitance can be expressed as

$$C_{out} = \frac{M\pi}{2R_L\omega(1+2V_{df})}. \tag{7.1}$$

From Appendix B, R_{rect} in Figure 7.2 is given by

$$R_{rect} = \frac{8R_L(1+2V_{df})}{(\pi + 2R_L C_{out}\omega(1+2V_{df}))^2} \tag{7.2}$$

From Figure 7.2, PT output power is given by $P_{out,PT} = v_{a,RMS}{}^2 A_{out}{}^2 R_{rect}$, hence

$$|A_{out}| = \frac{\sqrt{P_{out,PT}}}{v_{a,RMS}\sqrt{R_{rect}}}. \tag{7.3}$$

Note that the modulus sign is used in (7.3) because A_{in} and A_{out} are actually negative quantities (see the force factor formula in Chapters 2 and 3, and the discussion in Chapter 3). Substituting (7.2) and (7.1) into (7.3)

$$|A_{out}| = \frac{\pi(1+M)\sqrt{P_{out,PT}}}{v_{a,RMS}\sqrt{8R_L(1+2V_{df})}}. \tag{7.4}$$

From Figure 7.2, $P_{in,PT} = |A_{in}|v^1_{Cin,RMS}v_{a,RMS}\cos(\phi)$, where ϕ is the phase angle of the tank impedance. Thus,

$$|A_{in}| = \frac{P_{in,PT}}{v^1_{Cin,RMS}v_{a,RMS}\cos(\phi)}. \tag{7.5}$$

From (5.50) we have $X = C_1/(C_{out}N^2)$. Substituting this into (5.63), the angular frequency that corresponds to a particular tank phase angle can be expressed as

$$\omega = \frac{\sqrt{C_1\left[\pi(M^2+1)+M(2\pi+4\psi\tan(\phi))+2(M^{3/2}-M^{0.5})-(M+1)^2\cos^{-1}\left(\frac{M-1}{M+1}\right)\right]+C_{out}N^2\pi(M+1)^2}}{(M+1)\sqrt{L_1C_1\pi C_{out}N^2}} \quad (7.6)$$

where $N = \frac{A_{in}}{A_{out}}$, $L_1 = \frac{L_m}{A_{in}^2}$, $C_1 = C_m A_{out}^2$.

Closed-form equations for the required C_{out} and ω can be found by cross-substituting and solving the simultaneous equations (7.1) and (7.6), however, the result is too long to show here. For simulation purposes, the value of mechanical loss resistance that models the expected efficiency is found as follows:

With reference to Figure 7.2, Figure 7.3, (5.60), and (7.2), the equivalent series resistance in Figure 7.4 can be expressed as

$$R_x = R_1 + \frac{4M}{\pi\omega C_{out}N^2(M+1)^2}. \quad (7.7)$$

where $R_1 = \frac{R_m}{A_{in}^2}$. When expressed in terms of the lossfactor ψ (see Chapter 5), (7.7) becomes

$$R_x = \frac{4\psi M}{\pi\omega C_{out}N^2(M+1)^2}. \quad (7.8)$$

Therefore, by equating (7.7) and (7.8), a value for R_1 is obtained

$$R_1 = \frac{4M(\psi-1)}{\pi\omega C_{out}N^2(M+1)^2}, \quad (7.9)$$

and hence a figure for R_m is obtained from $R_m = R_1 A_{in}^2$.

The design process is summarised as follows:

1) Calculate A_{out}, A_{in}, and N using (7.4), (7.5), and $N = A_{in}/A_{out}$ respectively.
2) Calculate C_{out} and ω using (7.1) and (7.6), and $\phi = 57.3°$.
3) Find the upper limit for C_{eff} using the design charts in Chapter 5 and (5.49).
4) For simulation purposes, calculate the expected mechanical loss resistance R_m using (7.9).

The values of A_{in}, A_{out}, and N are not dependent on the values of L_m and C_m. The value of C_{out} (and therefore the upper limit for C_{eff} and C_{in}), however, is dependent on L_m and C_m (see (7.1) and (7.6)). From Chapters 2 and 3, the values of L_m and C_m are seen to

depend on the radius and total thickness of the PT. Hence, the value of C_{out} is dependent on the radius and total thickness. It was found, however, that the calculated value of C_{out} (using (7.1) and (7.6)) changed relatively little if the $L_m C_m$ product was kept constant. From the formula for L_m and C_m in Chapters 2 and 3, it can therefore be seen that the optimum value for C_{out} is strongly dependent on PT radius (because changing the radius will strongly change the $L_m C_m$ product), but only weakly dependent on the total thickness (because changing the total thickness does not affect the $L_m C_m$ product; the small change that does occur in C_{out} is due to the C_1 term that appears in the numerator of (7.6)). The dependency of C_{out} on radius, rather than total thickness, is consistent with (7.1), because all the terms except ω are fixed, and we know that the resonant frequency, and therefore the operating frequency, is mainly dictated by the outer radius. The method detailed above can therefore be regarded as a way of generating a theoretically ideal set of equivalent circuit component values for a given PT radius. Note that they are referred to as being "theoretically ideal" because they result in

1) The maximum allowable vibration velocity corresponding to the maximum required power level with the load resistance into which maximum power is to be delivered, thereby minimising the size of the output section required (for a given radius).

2) Inductor-less ZVS being achieved with the largest C_{eff} possible, thereby minimising the size of the input section required (for a given radius).

7.3 Theoretically optimum design example

The design method is now used to generate a set of theoretically optimum equivalent circuit component values for a converter with the following specifications:

$R_L = 10\,\Omega$

$V_{out} = 10\,\text{V}$

$P_{out} = 10\,\text{W}$

$V_d = 1\,\text{V}$

$V_{dc} = 100\,\text{V}$

The design variables are chosen as:

$v_{a,RMS} = 0.2\,\text{A}$ (or m/s)

$\psi = 1/0.95$

$M = 1$

$L_m = 10\,\text{mH}$

$C_m = 160\,\text{pF}$

The resulting equivalent circuit component values are:

$C_{out} = 155.8\,\text{nF}$

$|A_{in}| = 2.788$

$|A_{out}| = 11.11$

$R_m = 15.79\,\Omega$

$C_{eff} = 9.326\,\text{nF}$ (this is the upper limit beyond which inductor-less ZVS cannot be achieved)

The operating frequency is $f = 133.72\,\text{kHz}$

The dead-time factor is $t_{df} = 0.239$

Waveforms from an idealised SPICE simulation of this PT are shown in Figure 7.5. The motional branch current and output voltage meet the specification exactly, and ZVS is just achieved. In this figure, v_a appears to lag the fundamental component of v_{Cin}, even though v_a is defined in the direction shown in Figure 7.1, because A_{in} and A_{out} have been implemented in the simulation as being negative in accordance with d_{31} being negative (see Chapter 3). The phase angle of the impedance of the tank is, of course, inductive.

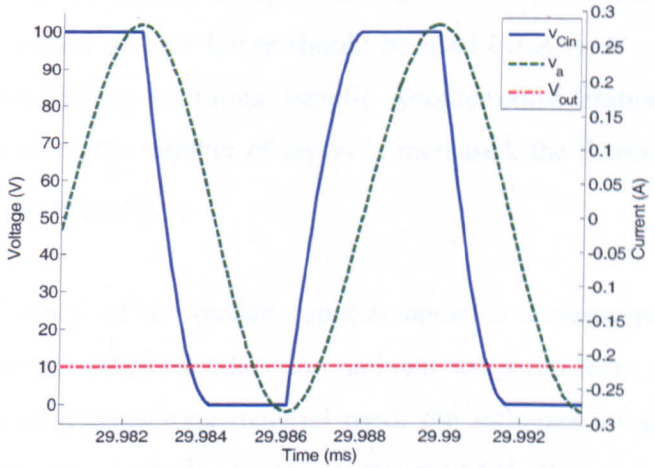

Figure 7.5: Simulated voltage and current waveforms for the design example (10Ω load).

7.4 Practical design considerations

The equivalent circuit component values from the design example could be translated into an approximate physical PT design using the models presented in Chapters 2 and 3. However, there are a great many practical considerations that affect the choice of the design variables ψ, M, maximum v_a, radius and total thickness.

In the design example, M was chosen to be 1, which would theoretically maximise the power density of the PT according to the relationships developed through Chapters 2, 3, and 4. However, the choice of M is also affected by the type of radial mode Transoner PT (i.e. whether purely bonded or co-fired), and the number of layers that the design is likely to require. If a purely bonded device is used, where the radius of the electrodes in the input and output section have to be equal to each other and to the radius of the ceramic, then decreasing M from 1 allows the required value of A_{out} to be adjusted such that the required values of A_{in} and A_{out} can be achieved simultaneously given the constraints that the electrode radius is the same in both sections and the number of layers in each section must be an integer. For both purely bonded and co-fired devices, M can also be used to trade-off the number of layers required in the output section for theoretical power density. Decreasing M from 1 reduces the number of layers required in the output section. Since the mechanical quality factor of a piezoelectric device decreases as the number of layers is increased [1], it may become beneficial to reduce M because the reduced number of layers reduces losses, allowing greater power to be transferred. Reducing the number of layers also makes the device easier to manufacture. Usually, only M values of 1 or lower should be used because $M > 1$ results in more layers being required for no additional benefit. Another consideration is that although Q_m tends to decrease as the number of layers is increased, the thermal conductivity of the device is likely to improve.

The expected efficiency of the device depends upon its dimensions, the number of layers in the input and output section, the ambient temperature in which it is to be operated, the type of piezoelectric material used, the influence of spurious vibration modes, and the way in which the device is mounted [2]. It is therefore difficult to accurately estimate without practical experience from other devices that are likely to have a similar composition to the one being designed.

The maximum vibration velocity is another property that is difficult to estimate with precision prior to the design commencing. Since power density is proportional to the square of the vibration velocity (see Chapter 3) it is essential that the design can operate at high vibration velocity.

The choice of outer radius and total thickness (and therefore L_m and C_m) requires consideration of the values of A_{in}, A_{out}, C_{out}, C_{in} to be achieved, the need to prevent interference from spurious modes such as bending and thickness, and the tendency for theoretical power density to decrease with radius (see Chapter 3). Usually the effect and location of other vibration modes can only be assessed with finite element analysis (FEA), however, one way of suppressing bending modes is to split the input section into two and place one on either side of the output section. It is crucial that the first radial resonance remains undisturbed.

Therefore, whilst the design method cannot, by itself, tell the designer what values of ψ, M, maximum v_a, radius and total thickness to use, it does tell them what values the equivalent circuit components should take as ψ, M, maximum v_a, and radius, are chosen and refined. It is therefore envisaged that the proposed design method would be used alongside the consideration of FEA, manufacturing tolerances and capabilities, material specifications, and experience from devices of similar specification. Specifically, its role is to ensure that the required electrical specifications are met in a manner which maximises power density.

7.5 Effect of output voltage regulation on ZVS

A theoretically optimum set of equivalent circuit component values has been generated such that maximum output power is delivered at $M = 1$ and $\phi = 57.3°$, and ZVS is just achieved at the load into which maximum power is to be delivered. In order to study the effect of using frequency modulation to achieve output voltage regulation in response to load changes, the following routine was developed to find the frequency required for a given load and converter to achieve a desired output voltage.

An initial value of ω is chosen. Ideally, the initial value of ω should be such that it will result in the impedance of the resonant tank being predominately inductive. Initial values for R_{rect} and C_{rect} are then calculated by substituting $V_d = 0$ into (B.1) and (B.2) (see Appendix B. Note that (B.1) and (B.2) become independent of I_{sec} when $V_d = 0$). R_x and C_x in Figure 7.4 are then calculated using

$$R_x = R_1 + \frac{R_{rect}}{N^2} \tag{7.10}$$

$$C_x = \frac{C_1 C_{rect} N^2}{C_1 + C_{rect} N^2}. \tag{7.11}$$

The maximum value of $v_{Cin}(t_d)$ and the dead-time at which it occurs is then calculated using (5.42). Note that only dead-times that result in the mode sequence 1-3-4-6 are to be permitted in cases where ZVS cannot be achieved ($v_{Cin}(t_d) < V_{dc}$), because this ensures that the description for $v_{Cin}(t)$ during the dead-time intervals (see (7.15) and (7.16)) that is subsequently used to calculate the fundamental component of v_{Cin} is correct. This was achieved by rejecting any dead-time values that did not result in $i_{L1}(0) > 0$.

If $v_{Cin}(t_d) \geq V_{dc}$, then ZVS can be achieved at this frequency, and (5.42) is then solved to find the (lowest) value of dead-time that results in $v_{Cin}(t_d) = V_{dc}$; again, this ensures that the value of dead-time that is subsequently used is known to result in the mode sequence 1-3-4-6, thereby ensuring that (7.15) and (7.16) are applicable. The RMS of the fundamental component of v_{Cin} is then found using Fourier series formula. Thus

$$v^1_{Cin,RMS} = \frac{\sqrt{a_1^2 + b_1^2}}{\sqrt{2}} \tag{7.12}$$

where

$$a_1 = \frac{2}{T}\left(\int_0^{t_d} v_{Cin\_M1}(t)\cos\left(\frac{2\pi t}{T}\right)dt + \int_{t_d}^{\frac{T}{2}} v_{Cin\_M3}(t)\cos\left(\frac{2\pi t}{T}\right)dt + \int_{\frac{T}{2}}^{\frac{T}{2}+t_d} v_{Cin\_M4}(t)\cos\left(\frac{2\pi t}{T}\right)dt + \int_{\frac{T}{2}+t_d}^{T} v_{Cin\_M6}(t)\cos\left(\frac{2\pi t}{T}\right)dt \right) \tag{7.13}$$

$$b_1 = \frac{2}{T}\left(\int_0^{t_d} v_{Cin\_M1}(t)\sin\left(\frac{2\pi t}{T}\right)dt + \int_{t_d}^{\frac{T}{2}} v_{Cin\_M3}(t)\sin\left(\frac{2\pi t}{T}\right)dt + \int_{\frac{T}{2}}^{\frac{T}{2}+t_d} v_{Cin\_M4}(t)\sin\left(\frac{2\pi t}{T}\right)dt + \int_{\frac{T}{2}+t_d}^{T} v_{Cin\_M6}(t)\sin\left(\frac{2\pi t}{T}\right)dt \right). \tag{7.14}$$

Using (5.41) from Chapter 5, the voltage across the input capacitance voltage during mode 1 is described by

$$v_{Cin\_M1}(t)=\left(\frac{i_{L1}(0)R_x+i_{L1}(0)\beta_1 L_1+v_{Cx}(0)}{L_1 C_{eff}\alpha_1(\beta_1-\alpha_1)}\right)\left(e^{\alpha_1 t}-1\right)+\left(\frac{i_{L1}(0)R_x+i_{L1}(0)\alpha_1 L_1+v_{Cx}(0)}{L_1 C_{eff}\beta_1(\alpha_1-\beta_1)}\right)\left(e^{\beta_1 t}-1\right). \quad (7.15)$$

Due to the symmetry of the v_{Cin} waveform, the voltage across the input capacitance voltage during mode 4 is

$$v_{Cin\_M4}(t)=V_{dc}-\left(\begin{array}{l}\left(\frac{i_{L1}(0)R_x+i_{L1}(0)\beta_1 L_1+v_{Cx}(0)}{L_1 C_{eff}\alpha_1(\beta_1-\alpha_1)}\right)\left(e^{\alpha_1\left(t-\frac{T}{2}\right)}-1\right)\\ +\left(\frac{i_{L1}(0)R_x+i_{L1}(0)\alpha_1 L_1+v_{Cx}(0)}{L_1 C_{eff}\beta_1(\alpha_1-\beta_1)}\right)\left(e^{\beta_1\left(t-\frac{T}{2}\right)}-1\right)\end{array}\right). \quad (7.16)$$

During mode 3 and mode 6 we have $v_{Cin\_M3}(t)=V_{dc}$ and $v_{Cin\_M6}(t)=0$ respectively. When calculating $v^1_{Cin,RMS}$, the dead-time that maximises $v_{Cin}(t_d)$ (whilst also resulting in $i_{L1}(0)>0$) is used if ZVS cannot be achieved, whereas the (lowest) dead-time that results in $v_{Cin}(t_d)=V_{dc}$ is used in cases where it can. This ensures that the dead-time will correspond to a mode sequence of 1-3-4-6. A value for $I_{sec,RMS}$ is then found using (see Figure 7.3)

$$I_{sec,RMS}=\frac{v^1_{Cin,RMS}}{N\sqrt{\left(R_1+\frac{R_{rect}}{N^2}\right)^2+\left(\omega L_1-\frac{1}{\omega C_1}-\frac{1}{\omega C_{rect}N^2}\right)^2}}. \quad (7.17)$$

R_{rect} and C_{rect} are then recalculated using (B.1) and (B.2), but with the correct V_d for the diodes in question and the newly calculated $\hat{I}_{sec}$ (which is simply $I_{sec,RMS}\sqrt{2}$). The ZVS capability and fundamental component are then recalculated using the new values for R_{rect} and C_{rect}, and a new value for $\hat{I}_{sec}$ is calculated. This process is repeated until no further change in $\hat{I}_{sec}$ occurs. Finally, the output voltage is found using (B.3). If V_{out} is greater than the desired output voltage, the frequency is increased and the whole process repeated. Conversely, if V_{out} is less than the desired value, the frequency is decreased (bringing the converter closer to resonance). Care must therefore be taken to ensure that the initial value of ω results in the tank impedance being inductive (note that ZVS would not be possible at capacitive frequencies anyway). The whole process is summarised in Figure 7.6.

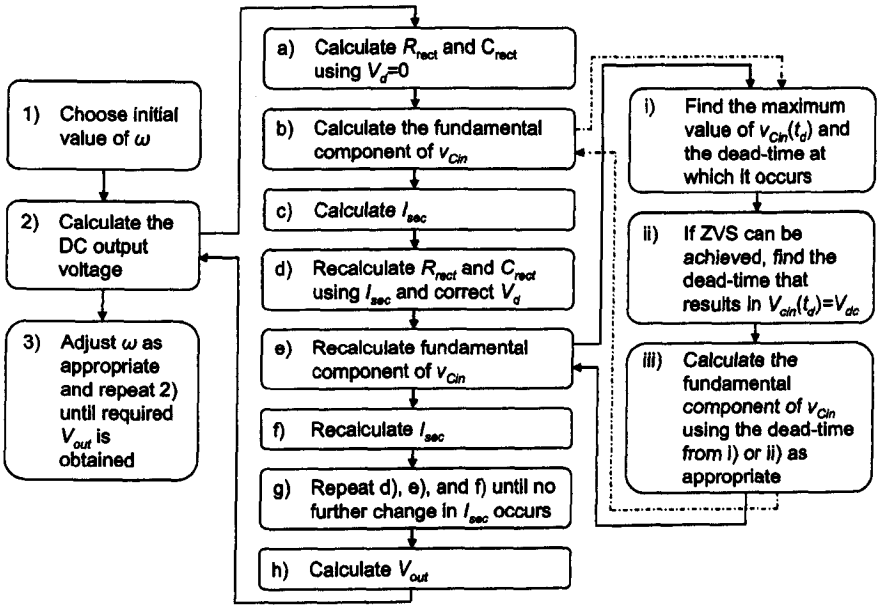

Figure 7.6: Method for calculating the frequency required for a particular output voltage.

Using this approach, the behaviour of the PT design from Section 7.3 is shown in Figure 7.7 as the output voltage is kept constant and the load resistance is increased. From Figure 7.7a it can be seen that very little change in the ZVS capability of the converter occurs as the load resistance is increased and the frequency is adjusted to maintain constant output voltage. A 1% decrease in C_{eff} would be more than sufficient to ensure that the maximum $\tilde{v}_{Cin}(t_d)$ remains above 1.0. The phase angle of the tank varies between 57.3° and 89.03°, as expected, because maximum power was designed to be delivered at 57.3° so as to maximise the size of C_{eff} and therefore minimise the size of the PT input section in accordance with the findings from Chapters 5 and 6.

Figure 7.7d shows that the dead-time fraction at which the converter must be operated increases considerably as the load resistance is increased and the phase angle of the tank is increased to maintain constant output voltage. Indeed, as the load resistance becomes negligible, over 90% of the switching period is spent with both MOSFETs turned off. The voltage and current waveforms for this situation are shown in Figure 7.8. The amplitude of the fundamental component of v_{Cin} is shown in Figure 7.7e. This decreases significantly as the load resistance is increased and the converter moves to a higher phase angle and dead-time fraction, and this is why the fundamental component had to be recalculated with each iteration during the analysis.

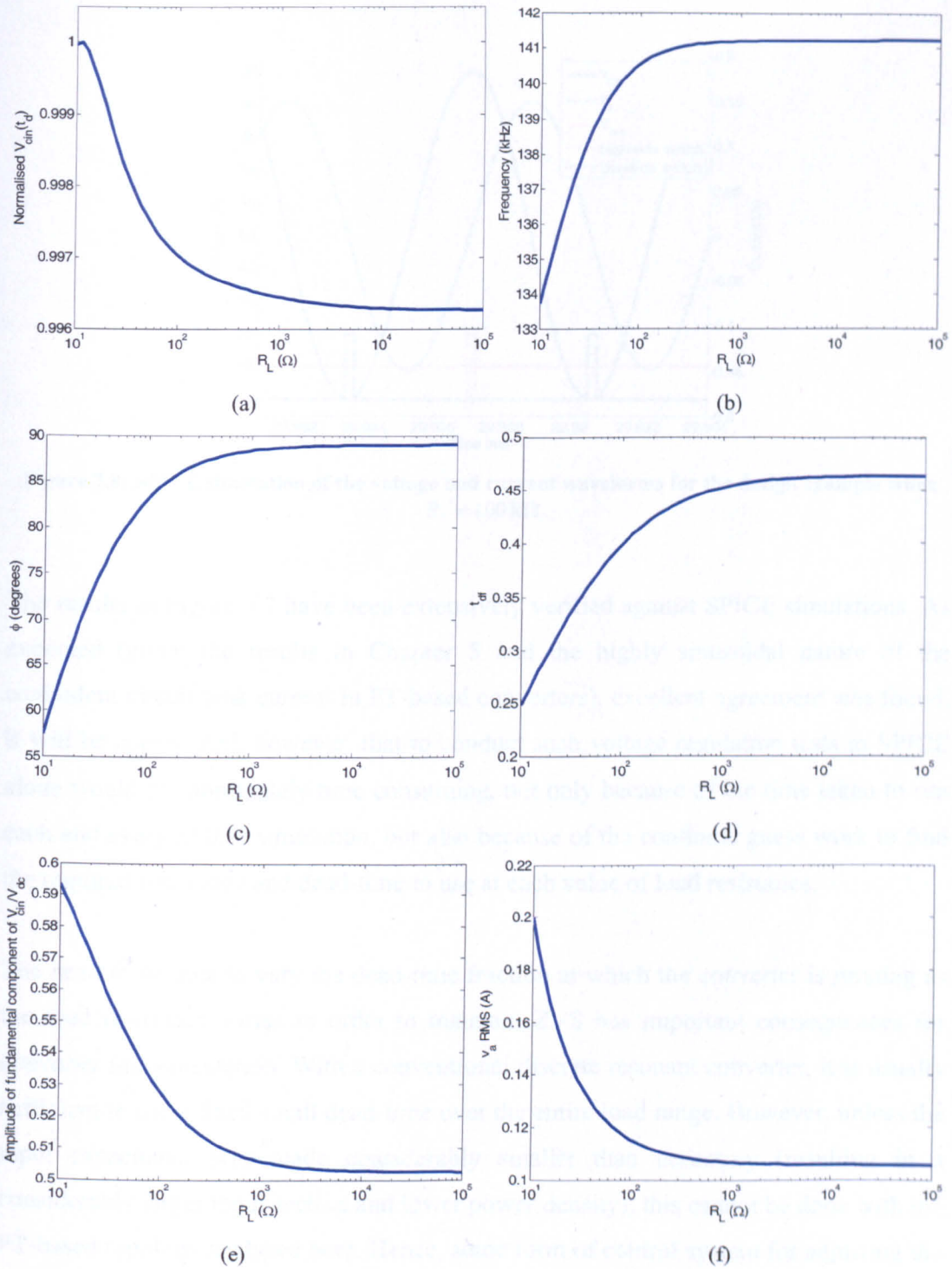

Figure 7.7: Converter behaviour when voltage regulating to maintain 10V output voltage. a) maximum $\widetilde{v}_{Cin}(t_d)$ at the frequency required for output voltage regulation against load resistance, b) frequency required (to maintain 10V output voltage) against load resistance, c) tank impedance phase angle against load resistance, d) dead-time factor at which the converter should be operated against load resistance, e) the amplitude of the fundamental component of the input capacitance voltage normalised to the dc link voltage, f) tank current against load resistance.

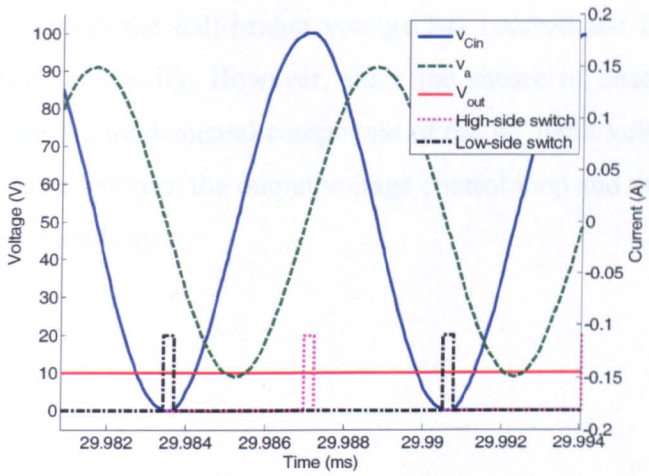

Figure 7.8: SPICE simulation of the voltage and current waveforms for the design example when $R_L = 100\,\mathbf{k\Omega}$.

The results in Figure 7.7 have been extensively verified against SPICE simulations. As expected (given the results in Chapter 5 and the highly sinusoidal nature of the equivalent circuit tank current in PT-based converters), excellent agreement was found. It will be appreciated, however, that to conduct such voltage regulation tests in SPICE alone would be inordinately time consuming, not only because of the time taken to run each and every SPICE simulation, but also because of the continual guess work to find the required frequency and dead-time to use at each value of load resistance.

The need to be able to vary the dead-time fraction at which the converter is running as the load resistance varies in order to maintain ZVS has important consequences for converter implementation. With a conventional discrete resonant converter, it is usually sufficient to use a fixed small dead-time over the entire load range. However, unless the input capacitance was made considerably smaller than necessary (resulting in a considerably larger input section and lower power density), this cannot be done with the PT-based topology analysed here. Hence, some form of control system for adjusting the dead-time would be required.

With regards to practical implementation, a key consideration is therefore how the control system would determine the value of dead-time to use. A fixed lookup table could be used to select the dead-time based on the switching frequency. However, since the equivalent circuit component values can change slightly as the PT heats up, as the PT ages, and from device to device variation, further investigation would be needed to

see if satisfactory ZVS performance could be obtained by this method. An alternative would be to detect when the half-bridge voltage has reached the DC link level and decide the dead-time on-the-fly. However, since the choice of dead-time can have a significant impact on the fundamental component of the PT input voltage, a method for preventing interference between the output voltage control loop and the automatic dead-time control may be necessary.

7.6 Summary

A method for generating theoretically optimum equivalent circuit component values for a radial mode Transoner PT-based DC-output full-bridge capacitively smoothed converter has been presented. The values are described as being optimum because they satisfy the criteria for maximising PT power density that were established in Chapters 5 and 6.

A method for analysing the ZVS capabilities of an inductor-less DC-output capacitively smoothed converter when frequency modulation is employed to provide output voltage regulation in response to load changes was then presented. Using this method, it was shown that if a PT is designed such that ZVS is just achieved at the load into which maximum output power is to be delivered, then the converter will also be able to maintain ZVS as the load resistance is increased and the output voltage is regulated though frequency modulation. This is good news in the sense that the total capacitance at the PT input (and therefore the size of the PT input section) does not need to be sized more conservatively in order to maintain ZVS during output voltage regulation compared to operation at the load into which maximum output power is to be delivered.

However, it was also shown that in order to maintain ZVS during output voltage regulation, the dead-time fraction t_{df} must be adjusted considerably, which means that a practical converter would require some form of dead-time control. Furthermore, since the choice of dead-time can substantially alter the fundamental component of the PT input voltage (and therefore the output voltage of the converter), it is concluded that the implementation of such control may not be straightforward.

7.7 References

[1] Y. Sasaki, M. Umeda, S. Takahashi, M. Yamamoto, A. Ochi, and T. Inoue, "High-power Characteristics of Multilayer Piezoelectric Ceramic Transducers," *Japanese Journal of Applied Physics, Part 1*, vol. 40, 2001.

[2] E. M. Baker, "Design of Radial Mode Piezoelectric Transformers for Lamp Ballast Applications," MSc thesis, Virginia Polytechnic Institute and State University, USA, 2002.

Chapter 8 - Conclusions and further work

8.1 Conclusions

The derivation of a Mason equivalent circuit for a simple radial mode Transoner was presented in Chapter 2. From this, it is concluded that the lumped equivalent circuit model of Yamamoto et al is correct, given the approximations made at the beginning of the chapter. Since good agreement was found between the model predictions and experiment, the model is an essential tool for quantitatively designing radial mode Transoner PTs to meet a particular electrical converter specification.

The new model presented in Chapter 3 more accurately reflects the way in which many devices are currently made in industry. It is concluded from this model that, as the radius of one set of electrodes is made smaller than the other, the clamped capacitance of the smaller set reduces in proportion to the square of the electrode radius (as one would intuitively expect), but that the associated force factor reduces in proportion to the electrode radius multiplied by a function that consists of the ratio of two Bessel functions. The nature of this function results in the force factor reducing more rapidly as the electrode radius is reduced than might otherwise have been expected. As a result, it is concluded that PT power density is maximised by making the input and output section electrode radii equal to one another, and approximately equal to the outer radius of the PT. However, it is also concluded in Chapter 6 that some converter specifications can only be achieved with the inductor-less topology by reducing the radius of one set of electrodes, or by delivering maximum output power at a non-optimal tank impedance phase angle. The former approach is the one currently used in industry.

Due to the form taken by the equivalent circuit when additional sets of electrodes are added to a radial mode PT, it was shown that the centre tapped rectifier configuration cannot be used with PTs unless additional inductors are included. Therefore, if the converter specification requires a particularly low output voltage, the current doubler rectifier should be considered.

A key conclusion from the work in Chapter 4 is that the maximum output power of a given PT is dependent on the output topology used. An AC-output topology will

achieve the highest thermally limited maximum output power, a DC-output capacitively smoothed topology will achieve the lowest, and an inductively smoothed topology will lie approximately half way in between. Hence, it is concluded that there is a clear trade off between using an inductively smoothed rectifier to increase PT power density, and the increase in cost and size incurred from the additional inductor(s). It was also shown in Chapter 4 that the number of layers required in the output section of a radial mode Transoner for a given output power level and load resistance is strongly dependent on the choice of rectifier topology. Therefore we conclude that in low output voltage applications, the current doubler configuration is advantageous because it reduces the rectifier diode losses (like a centre-tapped configuration), but also requires fewer layers to be used in the output section of the PT compared to the other topologies.

A new model of the ZVS condition in the inductor-less PT-based converter topology was presented in Chapter 5. Through the use of a normalisation scheme and numerical optimisation techniques, the requirements for achieving ZVS in 5 different topology variations were identified. The impact of these requirements on radial mode Transoner PT design was then assessed in Chapter 6. From these chapters, it is concluded that the input section of a radial mode Transoner PT has to be made larger when designing for the inductor-less topology compared to the with-inductor topology. It is also concluded that there is an optimal tank impedance phase angle and dead-time to switching period ratio that maximises the size of the input capacitance at which ZVS can be achieved and therefore minimises the size of the input section required. Furthermore, it was found that the input section requirements for achieving ZVS were dependent on the output topology, and that overall PT power density will be maximised by designing the PT such that the maximum required output power is to be delivered at the load condition which maximises PT output power for a given equivalent circuit tank current (i.e. $M = 1$), even though this load condition requires the largest input section to achieve ZVS.

Chapter 7 considered the use of the inductor-less PT-based DC-output full-bridge capacitively smoothed topology in applications that require output voltage regulation. It was shown that if a PT is designed such that ZVS is just achieved at the load resistance into which maximum output power is to be delivered, then ZVS can be maintained as the load resistance is increased and the frequency is adjusted to maintain constant output voltage. The resulting conclusion is that frequency modulation can be used to provide

output voltage regulation without compromising the ability of the converter to achieve ZVS, and that the input section design can be based around the ZVS and vibration velocity requirements at the load into which maximum power is to be delivered. However, since the dead-time needed to achieve ZVS was found to vary considerably with load, it is also concluded that some form of dead-time control would need to be implemented if this topology were used in a practical converter.

8.2 Further work

The newly proposed equivalent circuit model for the radial mode Transoner in Chapter 3 requires experimental verification. Because this will require many different specifications of co-fired PT to be manufactured and analysed, the cost of doing so is likely to be considerable. The proposed model is more likely to be proved or disproved, by industry, over an extended period of time during the development of PTs for various specialist applications. However, a comparative study between the proposed model and finite element analysis (FEA) would be a useful first step.

The results from Chapter 4 provide a clear impetus for the development of new rectifier topologies that allow a higher maximum output power to be achieved for a given level of equivalent circuit tank current with a given PT. In time, it may be proved mathematically that this is simply not possible. However, the advantage to be gained should it be proved otherwise means such an investigation is worthy of consideration.

The requirements for inductor-less ZVS have now been quantified. However, there are many practical questions regarding the implementation of inductor-less PT-based converters in DC-output applications that require output voltage regulation. Can a suitable method for adaptively controlling the dead-time be developed? Is it viable to use some form of fixed look-up table instead, or would the temperature dependence of the PT's characteristics and the production tolerances prevent this from being accurate enough?

This thesis has developed some of the models and analysis that are required for the design of radial mode Transoner PTs and inductor-less PT-based converters to meet a required set of electrical specifications in a way that maximises power density.

However, in many ways, the greatest challenges are now materials based. Improvements in piezoelectric materials and manufacturing techniques would, at least partially, address almost all the challenges identified in this thesis. The development of materials that have a high piezoelectric coupling factor, low losses, and which can operate at high vibration velocities in a thermally stable manner will result in commensurate increases in PT power density, and therefore mitigate the decreases caused by the use of an inductor-less converter topology, and the use of a DC-output topology. Developing these materials to a point where they are commercially viable should therefore be a priority, not least because they would also yield improvements in other related technologies, such as piezoelectric motors.

Appendix A - Longitudinal mode Transoner equivalent circuit

An equivalent circuit model for the longitudinal mode Transoner can be derived in a similar way to that shown in Chapter 2 for the radial mode Transoner. The device layout considered here is one where the input and output section layers are poled in the thickness direction. The electrodes run parallel to the direction of wave propagation (i.e. along the x_1 direction) in both sections, as shown in Figure A.1. The electrical connections are made to the longitudinal mode Transoner as shown in Figure A.2.

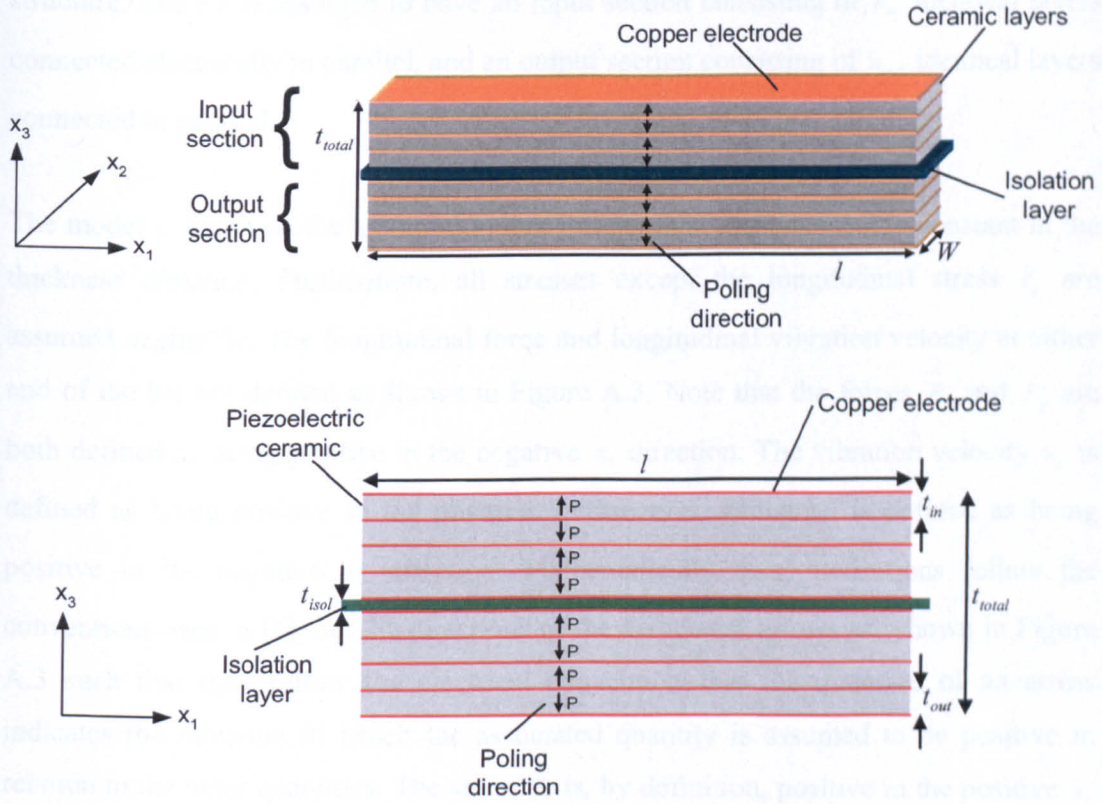

Figure A.1: Diagrams showing the construction of a purely bonded longitudinal mode Transoner PT.

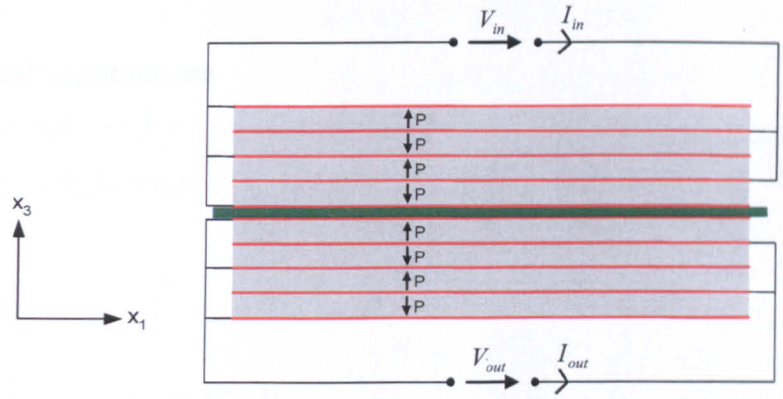

Figure A.2: Diagram of the electrical connections made to the purely bonded longitudinal mode Transoner.

Like Chapter 2, the equations here will be formulated for a simple purely bonded structure. The PT is assumed to have an input section consisting of n_{in} identical layers connected electrically in parallel, and an output section consisting of n_{out} identical layers connected in parallel.

The model is based on the assumption that longitudinal displacement is constant in the thickness direction. Furthermore, all stresses except the longitudinal stress T_1 are assumed negligible. The longitudinal force and longitudinal vibration velocity at either end of the bar are defined as shown in Figure A.3. Note that the forces F_1 and F_2 are both defined as being positive in the negative x_1 direction. The vibration velocity v_1 is defined as being positive in the positive x_1 direction, whilst v_2 is defined as being positive in the negative x_1 direction. Mathematically these definitions follow the conventions used in [1], but the directions of the associated arrows are shown in Figure A.3 such that they follow the electrical convention that the direction of an arrow indicates the direction in which the associated quantity is assumed to be positive in relation to the other quantities. The stress T_1 is, by definition, positive in the positive x_1 direction.

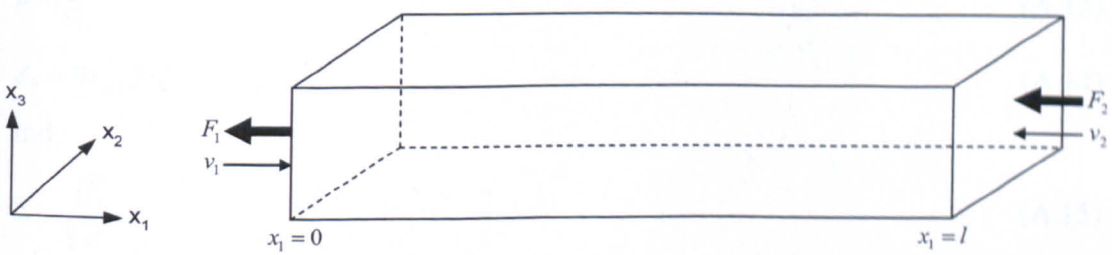

Figure A.3: Diagram showing the longitudinal force and longitudinal vibration velocity definitions.

The 'electrical' equations are

$$I_{in} = j\omega C_{in} V_{in} - A_{in}(v_1 + v_2) \tag{A.1}$$

$$I_{out} = j\omega C_{out} V_{out} - A_{out}(v_1 + v_2) \tag{A.2}$$

where

$$A_{in} = \frac{W d_{31}^{\ in} n_{in}}{s_{11}^{E\,in}} \tag{A.3}$$

$$C_{in} = \frac{W \varepsilon_{33}^{T\,in} n_{in} l}{t_{in}}\left(1 - k_{31}^{\ in^2}\right) = \frac{W \varepsilon_{33}^{T\,in} n_{in}^{\ 2} l}{t_{out}^{total}}\left(1 - k_{31}^{\ in^2}\right) \tag{A.4}$$

$$A_{out} = \frac{W d_{31}^{\ out} n_{out}}{s_{11}^{E\,out}} \tag{A.5}$$

$$C_{out} = \frac{W \varepsilon_{33}^{T\,out} n_{out} l}{t_{out}}\left(1 - k_{31}^{\ out^2}\right) = \frac{W \varepsilon_{33}^{T\,out} n_{out}^{\ 2} l}{t_{out}^{total}}\left(1 - k_{31}^{\ out^2}\right) \tag{A.6}$$

where

$$k_{31}^{\ in^2} = \frac{d_{31}^{\ in^2}}{s_{11}^{E\,in} \varepsilon_{33}^{T\,in}} \tag{A.7}$$

$$k_{31}^{\ out^2} = \frac{d_{31}^{\ out^2}}{s_{11}^{E\,out} \varepsilon_{33}^{T\,out}}. \tag{A.8}$$

The mechanical equations are

$$F_1 = -W t_{total} \overline{T}_1\Big|_{x_1=0} = Z_{l1} v_2 + Z_{l2} v_1 + A_{in} V_{in} + A_{out} V_{out} \tag{A.9}$$

$$F_2 = -W t_{total} \overline{T}_1\Big|_{x_1=l} = Z_{l1} v_1 + Z_{l2} v_2 + A_{in} V_{in} + A_{out} V_{out} \tag{A.10}$$

where

$$Z_{l1} = \frac{Z_0}{j \sin(\beta l)} \tag{A.11}$$

$$Z_{l2} = \frac{Z_0}{j \tan(\beta l)} \tag{A.12}$$

where

$$\beta = \frac{\omega}{\overline{v}_l} \tag{A.13}$$

$$Z_0 = W t_{total} \overline{\rho} \overline{v}_l \tag{A.14}$$

and

$$\overline{v}_l = \sqrt{\frac{\overline{Y}_l}{\overline{\rho}}}. \tag{A.15}$$

Here, β is the longitudinal wave number, $\overline{v}_l$ is the effective longitudinal speed of sound within the composite, $\overline{\rho}$ is the average density of the device, and $\overline{Y}_l$ is the effective Young's modulus of the device. For a purely bonded PT, $\overline{\rho}$ and $\overline{Y}_l$ would take the form

$$\overline{Y}_l = A_{fC}{}^{in}\frac{1}{s_{11}^{E\,in}} + A_{fC}{}^{out}\frac{1}{s_{11}^{E\,out}} + A_{fI}Y_I + A_{fE}Y_E \tag{A.16}$$

$$\overline{\rho} = A_{fC}{}^{in}\rho_C{}^{in} + A_{fC}{}^{out}\rho_C{}^{out} + A_{fI}\rho_I + A_{fE}\rho_E\,. \tag{A.17}$$

where the A_f symbols are the thickness fractions of the various materials. Y_I and Y_E are the Young's modulus of the isolation and electrode material respectively.

Equations (A.1), (A.2), (A.9), and (A.10) can be represented with the Mason equivalent circuit shown in Figure A.4.

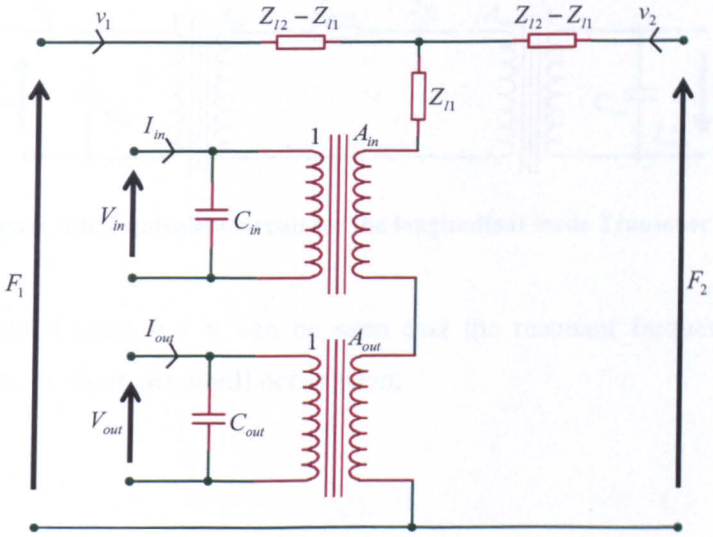

Figure A.4: Mason equivalent circuit for the longitudinal mode Transoner PT.

Since the device is free to vibrate, the longitudinal forces on either end of the bar will be zero. Hence,

$$F_1 = 0 \tag{A.18}$$

$$F_2 = 0\,. \tag{A.19}$$

Applying these boundary conditions to Figure A.4 results in the circuit of Figure A.5. Note that since the two $Z_{l2}-Z_{l1}$ branches appear in parallel with one another, the vibration velocities at either end of the bar are equal, i.e. $v_1 = v_2$.

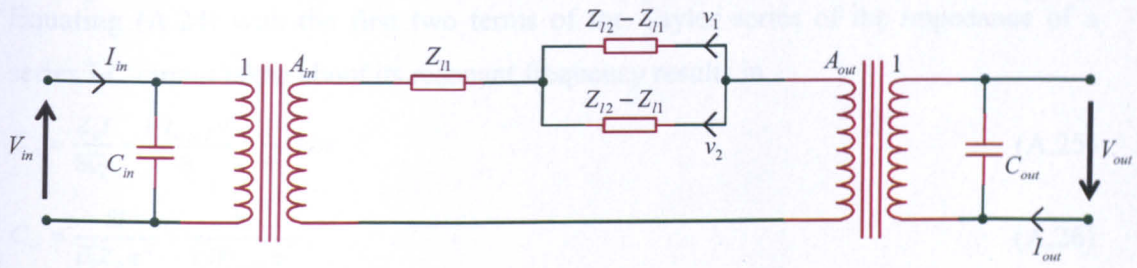

Figure A.5: The Mason equivalent circuit for the longitudinal mode Transoner PT after the boundary conditions for the force on either end of the bar have been applied.

Figure A.5 is then simplified to that shown in Figure A.6, where

$$Z_{mech} = Z_1 + \frac{(Z_{l2} - Z_{l1})}{2} = \frac{Z_0}{2j\tan\left(\frac{\beta l}{2}\right)}. \tag{A.20}$$

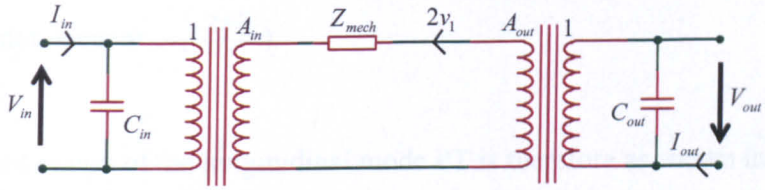

Figure A.6: Equivalent circuit for the longitudinal mode Transoner PT.

From (A.20) and Figure A.6 it can be seen that the resonant frequencies of the PT (when the output is short circuited) occur when

$$\frac{Z_0}{2j\tan\left(\frac{\beta l}{2}\right)} = 0 \tag{A.21}$$

and hence at the solutions to

$$\tan\left(\frac{\beta l}{2}\right) = \infty, \tag{A.22}$$

which are $\frac{\beta l}{2} = \frac{\pi}{2}, \frac{3\pi}{2}, \frac{5\pi}{2}, etc$. The first longitudinal (short circuit) resonant frequency is therefore

$$\omega_{rsc} = \frac{\pi \bar{v}_l}{l}. \tag{A.23}$$

Approximating Z_{mech} with the first two terms of its Taylor series taken about the first short circuit resonant frequency,

$$Z_{mech} \approx 0 + \frac{\Delta\omega j Z_0 l}{4\bar{v}_l}. \tag{A.24}$$

Equating (A.24) with the first two terms of the Taylor series of the impedance of a series LC circuit taken about its resonant frequency results in

$$L_m = \frac{Z_0 l}{8\overline{\upsilon}_l} = \frac{Wt_{total}\overline{\rho} l}{8} = \frac{1}{8} Mass \tag{A.25}$$

$$C_m = \frac{8l}{\overline{\upsilon}_l Z_0 \pi^2} = \frac{8l}{\overline{Y}_l Wt_{total} \pi^2}. \tag{A.26}$$

where $Mass$ is the total mass of the PT. Using the mechanical quality factor of the composite, $\overline{Q}_m$, to introduce a mechanical loss resistance

$$R_m = \frac{\omega_{rsc} L_m}{\overline{Q}_m} = \frac{\pi Z_0}{8\overline{Q}_m} = \frac{\pi Wt_{total}\overline{\rho}\overline{\upsilon}_l}{8\overline{Q}_m}. \tag{A.27}$$

Note that a longitudinal mode Transoner with the electrode layout analysed here should only be driven at the first longitudinal mode resonance (see the discussion on pages 226 to 228 of [2]). Indeed, the even longitudinal modes cannot be excited at all (note that (A.22) does not occur at $\omega = \frac{2\pi\overline{\upsilon}_l}{l}$).

The equivalent circuit of the longitudinal mode PT is therefore as shown in Figure A.7.

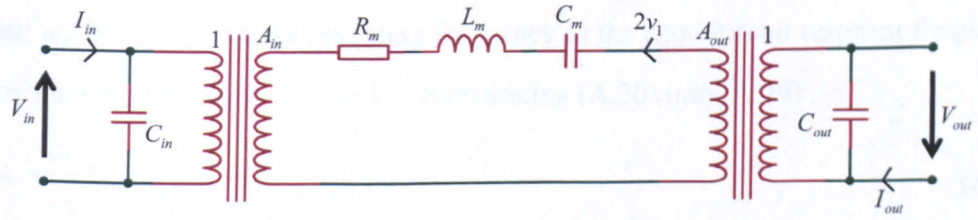

Figure A.7: Lumped equivalent circuit model for the longitudinal mode Transoner PT.

As a check, the model proposed above is compared to the result shown on pages 237 to 242 of [1] for a length expander bar with electric field perpendicular to length and which is free on one face. That is, we compare Figure A.7 to Figure 28 on page 242 of [1]. If both ends of the bar in [1] are free, rather than just one, then the electrical port with the voltage "F" in Figure 28 of [1] is short circuited. Comparing the model formula for this scenario to the case of a longitudinal mode PT with a single input layer and no output layers (i.e. so it becomes a length expander bar with electric field perpendicular to length), it can be seen that they are in complete agreement once the factor of 2 by which the force factor in Figure 28 of [1] is scaled by is taken into account. That is, the $2N$, L_1, C_1 in Figure 28 of [1] are fully equivalent to A_{in}, L_m, C_m in Figure A.7 when there are no output section layers present and only a single input section layer.

We then consider the case of a longitudinal mode PT being used in the AC-output topology, and the relationship between the output power and the output section variables. Using a similar method to that described in Chapter 3:

$$P_{out,PT} = A_{out}{}^2 (2v_{1,RMS})^2 R_s = \frac{4v_{1,RMS}{}^2 A_{out}{}^2 R_L}{R_L{}^2 \omega^2 C_{out}{}^2 + 1} \tag{A.28}$$

where R_s is the series equivalent resistance of the parallel combination of the load resistance R_L and the output capacitance C_{out}. The maximum vibration velocity within the device occurs at either end of the bar. Hence, v_1 is the largest longitudinal vibration velocity that occurs within the device. Substituting (A.5) and (A.6) into (A.28), assuming a matched load $\left(R_L = \frac{1}{\omega C_{out}}\right)$ is used, and making use of (A.8)

$$P_{out,PT} = \frac{2v_{1,RMS}{}^2}{\omega s_{11}^{E\,out}} \frac{Wt_{out}^{total}}{l} \frac{k_{31}{}^{out\,2}}{\left(1 - k_{31}{}^{out\,2}\right)}. \tag{A.29}$$

The operating frequency ω will be close to the short circuit resonant frequency ω_{rsc}. Let

$$\omega = \omega_f \omega_{rsc} = \omega_f \frac{\pi \bar{v}_l}{l} \tag{A.30}$$

where ω_f is the ratio of the operating frequency to the short circuit resonant frequency, and is likely to be around 1.05 to 1.1. Substituting (A.30) into (A.29)

$$P_{out,PT} = \frac{2v_{1,RMS}{}^2}{\omega_f s_{11}^{E\,out}} \frac{Wt_{out}^{total}}{\pi \bar{v}_l} \frac{k_{31}{}^{out\,2}}{\left(1 - k_{31}{}^{out\,2}\right)}. \tag{A.31}$$

The power density of the output section is therefore

$$P_{density\_output\_section} = \frac{P_{out,PT}}{l W t_{out}^{total}} = \frac{2v_{1,RMS}{}^2}{l \omega_f s_{11}^{E\,out} \pi \bar{v}_l} \frac{k_{31}{}^{out\,2}}{\left(1 - k_{31}{}^{out\,2}\right)}. \tag{A.32}$$

This result is then discussed in Chapter 3.

References

[1] D. A. Berlincourt, D. R. Curran, and H. Jaffe, "Piezoelectric and Piezomagnetic Materials and Their Function in Transducers," in *Physical Acoustics: Principles and Methods*, vol. I part A, W. P. Mason, Ed.: Academic Press, New York, 1964.

[2] H. W. Katz, *Solid State Magnetic and Dielectric Devices*: John Wiley & Sons, Inc. New York, 1959.

Appendix B - Rectifier models

The rectifier models used in Chapters 4, 5, and 7 are detailed below. Note that all 4 models rely on the current I_{sec} being sinusoidal, and are based on those in [1, 2].

A. Full-bridge capacitively smoothed rectifier

Following the method in [2], a sinusoidal current source feeding a capacitance in parallel with a full-bridge capacitively smoothed rectifier can be modelled with a series resistance and capacitance, as shown in Figure B.1.

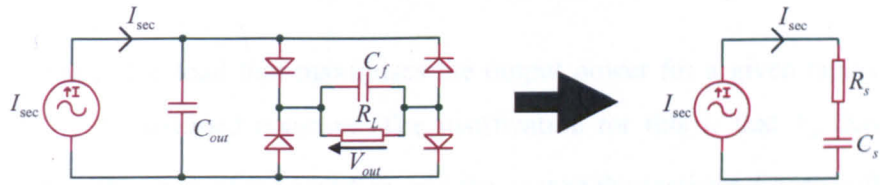

Figure B.1: Full-bridge capacitively smoothed rectifier topology and its equivalent circuit model.

The equivalent circuit elements are given by

$$R_s = \frac{8\left(R_L \hat{I}_{sec} + V_d \pi\right)\left(\hat{I}_{sec} - 2C_{out}\omega V_d\right)}{\left(\pi + 2R_L C_{out}\omega\right)^2 \hat{I}_{sec}^{\ 2}} \tag{B.1}$$

$$C_s = \frac{\hat{I}_{sec}^{\ 2}\pi C_{out}\left(\pi + 2\omega R_L C_{out}\right)}{\left(\begin{array}{l} -\hat{I}_{sec}^{\ 2}\left(\pi + 2\omega R_L C_{out}\right)\cos^{-1}\left(\dfrac{\left(\hat{I}_{sec}\left(2\omega R_L C_{out} - \pi\right) + 4\omega C_{out} V_d \pi\right)}{\hat{I}_{sec}\left(\pi + 2\omega R_L C_{out}\right)}\right) \\ + \dfrac{\left(\left(4R_L \omega C_{out} - 2\pi\right)\hat{I}_{sec} + 8C_{out}\omega V_d \pi\right)}{\left(\pi + 2R_L C_{out}\omega\right)}\sqrt{2\pi C_{out}\omega\left(\hat{I}_{sec} - 2C_{out}\omega V_d\right)\left(R_L \hat{I}_{sec} + V_d \pi\right)} \\ + \pi \hat{I}_{sec}^{\ 2}\left(\pi + 2R_L C_{out}\omega\right) \end{array}\right)} \tag{B.2}$$

$$V_{out} = \frac{2R_L\left(\hat{I}_{sec} - 2C_{out}\omega V_d\right)}{\left(\pi + 2R_L C_{out}\omega\right)} \tag{B.3}$$

where $\hat{I}_{sec}$ is the peak value (i.e. the amplitude) of the sinusoidal current I_{sec}. V_d is the on-state voltage drop of a single rectifier diode, and is assumed to independent of the current flowing through it. The difference between (B.2) and the formula that appears in [2] is due to a typo in [2]. A quantity V_{df} is then defined as

$$V_{df} = \frac{V_d}{V_{out}} \tag{B.4}$$

and allows (B.1), (B.2), and (B.3) to be rewritten as

$$R_s = \frac{8R_L\left(1+2V_{df}\right)}{\left(\pi+2R_LC_{out}\omega\left(1+2V_{df}\right)\right)^2} \tag{B.5}$$

$$C_s = \frac{\pi C_{out}\left(\pi+2\omega R_LC_{out}\left(1+2V_{df}\right)\right)^2}{\left(\begin{array}{l}\left(2\omega R_LC_{out}\left(1+2V_{df}\right)+\pi\right)^2\cos^{-1}\left(\dfrac{\pi-2\omega R_LC_{out}\left(1+2V_{df}\right)}{\pi+2\omega R_LC_{out}\left(1+2V_{df}\right)}\right)\\ +\left(4\omega R_LC_{out}\sqrt{\pi}\left(1+2V_{df}\right)-2\pi^{3/2}\right)\sqrt{2\omega R_LC_{out}\left(1+2V_{df}\right)}\end{array}\right)} \tag{B.6}$$

$$V_{out} = \frac{2R_L\hat{I}_{sec}}{\left(\pi+2R_LC_{out}\omega\left(1+2V_{df}\right)\right)} \tag{B.7}$$

The advantage of (B.5) and (B.6) is that they are not dependent on $\hat{I}_{sec}$. From a design perspective, V_{df} will be known immediately since the required output voltage is known and the available diodes (and hence V_d) are known.

When looking at the load that maximises the output power for a given tank current in Chapter 4, V_{df} is assumed constant. The justification for this is that V_{df} has a direct impact on the efficiency of the rectifier, and the cost of the rectifier diodes will increase as the desired V_d is decreased. Hence, if there is some minimum level of rectifier efficiency that must be achieved, and it is desirable not to exceed that level in order to minimise cost, then in effect the diodes must be chosen so as to meet that efficiency level, given the output voltage level, and this implies V_{df} is kept constant. In other words we assume that the specification of the diodes (i.e. their V_d) is always chosen so as to maintain a constant rectifier efficiency level, which results in V_{df} being constant.

B. Half-wave capacitively smoothed rectifier

Adapting the method in [2], a sinusoidal current source feeding a capacitance in parallel with a half-wave capacitively smoothed rectifier can be modelled with series resistance and capacitance as shown in Figure B.2.

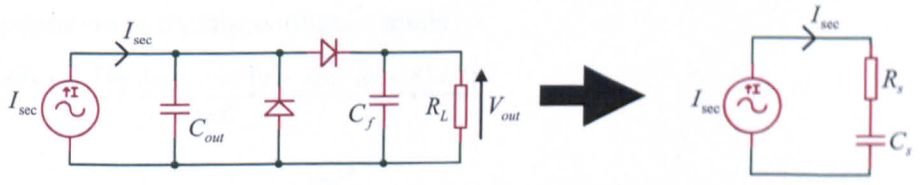

Figure B.2: Half-wave capacitively smoothed rectifier topology and its equivalent circuit model.

The equivalent circuit elements are given by

$$R_s = \frac{8R_L\left(1+2V_{df}\right)}{\left(2\pi + R_L\omega C_{out}\left(1+2V_{df}\right)\right)^2} \tag{B.8}$$

$$C_s = \frac{\pi C_{out}\left(2\pi + \omega R_L C_{out}\left(1+2V_{df}\right)\right)^2}{\left(\begin{array}{l}\left(\omega R_L C_{out}\left(1+2V_{df}\right)+2\pi\right)^2 \cos^{-1}\left(\dfrac{2\pi - \omega R_L C_{out}\left(1+2V_{df}\right)}{2\pi + \omega R_L C_{out}\left(1+2V_{df}\right)}\right) \\ +\left(2\omega R_L C_{out}\sqrt{\pi}\left(1+2V_{df}\right) - 4\pi^{3/2}\right)\sqrt{2\omega R_L C_{out}\left(1+2V_{df}\right)}\end{array}\right)} \tag{B.9}$$

$$V_{out} = \frac{2R_L\hat{I}_{sec}}{\left(2\pi + R_L C_{out}\omega\left(1+2V_{df}\right)\right)} \tag{B.10}$$

C. Full-bridge inductively smoothed rectifier

The model shown here for a sinusoidal current source feeding a capacitance in parallel with a full-bridge inductively smoothed rectifier (see Figure B.3) is based on that in [1], but adapted so as to include the effect of the on-state diode voltage drops. This rectifier has 2 modes of operation: "continuous" and "discontinuous" [1].

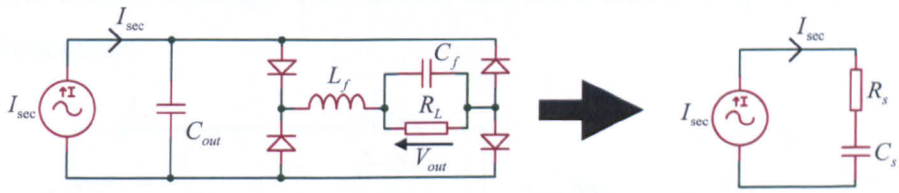

Figure B.3: Full-bridge inductively smoothed rectifier topology and its equivalent circuit model.

When operating in the continuous mode

$$R_s = \frac{8R_L\left(1+2V_{df}\right)}{\pi^2\left(\omega^2 C_{out}{}^2 R_L{}^2\left(1+2V_{df}\right)^2+1\right)} \tag{B.11}$$

$$C_s = \frac{C_{out}\pi^2\left(\omega^2 C_{out}{}^2 R_L{}^2\left(1+2V_{df}\right)^2+1\right)}{\left(\pi^2\omega^2 C_{out}{}^2 R_L{}^2\left(1+2V_{df}\right)^2+\pi^2-8\right)} \tag{B.12}$$

$$V_{out} = \frac{2R_L\hat{I}_{sec}}{\pi\sqrt{1+R_L{}^2 C_{out}{}^2\omega^2\left(1+4V_{df}+4V_{df}{}^2\right)}}. \tag{B.13}$$

When operating in the discontinuous mode

$$R_s = \frac{\left(2\sin(\alpha+\beta)\sin(\alpha)-\cos^2(\alpha)-\cos^2(\alpha+\beta)+2\right)}{\pi\omega C_{out}} \tag{B.14}$$

$$C_s = \frac{C_{out}\pi}{\left(\pi-2\sin(\alpha+\beta)\cos(\alpha)-\cos(\alpha)\sin(\alpha)-\cos(\alpha+\beta)\sin(\alpha+\beta)-\beta\right)} \tag{B.15}$$

$$V_{out} = \frac{\hat{I}_{sec}\left(2\sin(\alpha)-2(\beta-\pi)\cos(\alpha+\beta)-\left(\beta^2+\pi^2-2-2\beta\pi\right)\sin(\alpha+\beta)\right)}{2\pi\omega C_{out}\left(1+2V_{df}\right)} \tag{B.16}$$

where α and β must be numerically determined using the simultaneous equations

$$\cos(\alpha+\beta)+(\beta-\pi)\sin(\alpha+\beta)+\cos(\alpha)=0 \tag{B.17}$$

$$\pi\omega C_{out}(1+2V_{df})R_L+\frac{2(\beta-\pi)\cos(\alpha+\beta)+(\beta^2+\pi^2-2-2\beta\pi)\sin(\alpha+\beta)-2\sin(\alpha)}{2\sin(\alpha+\beta)}=0. \tag{B.18}$$

The rectifier will be in the continuous mode when

$$2<\pi\omega C_{out}R_L(1+2V_{df}). \tag{B.19}$$

Hence, the boundary between the continuous and discontinuous modes of rectifier operation occurs at $\pi\omega C_{out}R_L(1+2V_{df})=2$. Note that a key assumption of this model is that the ripple on the current through the filter inductor is negligible [1].

D. Current doubler rectifier

The model shown here for a sinusoidal current source feeding a capacitance in parallel with a current doubler rectifier (see Figure B.4) is based on that in [1], but adapted for the current doubler topology. This rectifier also has 2 modes of operation: continuous and discontinuous.

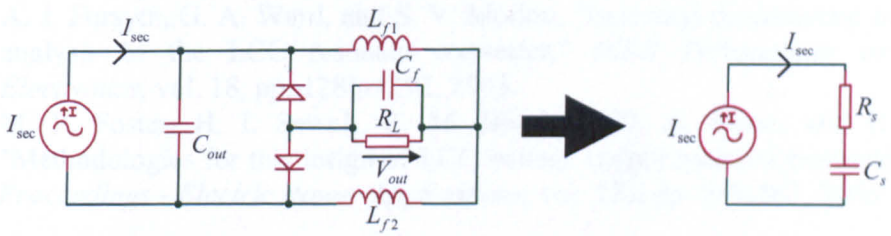

Figure B.4: Current doubler rectifier topology and its equivalent circuit model.

When operating in the continuous mode

$$R_s=\frac{32R_L(1+V_{df})}{\pi^2\left(16\omega^2C_{out}{}^2R_L{}^2(1+V_{df})^2+1\right)} \tag{B.20}$$

$$C_s=\frac{C_{out}\pi^2\left(16\omega^2C_{out}{}^2R_L{}^2(1+V_{df})^2+1\right)}{\left(\pi^2\left(16\omega^2C_{out}{}^2R_L{}^2(1+V_{df})^2+1\right)-8\right)} \tag{B.21}$$

$$V_{out}=\frac{4R_L\hat{I}_{sec}}{\pi\sqrt{1+16R_L{}^2C_{out}{}^2\omega^2\left(1+2V_{df}+V_{df}{}^2\right)}}. \tag{B.22}$$

When operating in the discontinuous mode

$$R_s=\frac{\left(2\sin(\alpha+\beta)\sin(\alpha)-\cos^2(\alpha)-\cos^2(\alpha+\beta)+2\right)}{\pi\omega C_{out}} \tag{B.23}$$

$$C_s=\frac{C_{out}\pi}{(\pi-2\sin(\alpha+\beta)\cos(\alpha)-\cos(\alpha)\sin(\alpha)-\cos(\alpha+\beta)\sin(\alpha+\beta)-\beta)} \tag{B.24}$$

$$V_{out} = \frac{\hat{I}_{sec}\left(2\sin(\alpha) - 2(\beta-\pi)\cos(\alpha+\beta) - \left(\beta^2+\pi^2-2-2\beta\pi\right)\sin(\alpha+\beta)\right)}{4\pi\omega C_{out}\left(1+V_{df}\right)} \tag{B.25}$$

where α and β must be numerically determined using the simultaneous equations

$$\cos(\alpha+\beta) + (\beta-\pi)\sin(\alpha+\beta) + \cos(\alpha) = 0 \tag{B.26}$$

$$\pi\omega C_{out}\left(1+V_{df}\right)R_L + \frac{2(\beta-\pi)\cos(\alpha+\beta) + \left(\beta^2+\pi^2-2-2\beta\pi\right)\sin(\alpha+\beta) - 2\sin(\alpha)}{8\sin(\alpha+\beta)} = 0. \tag{B.27}$$

Note that (B.23), (B.24), and (B.26) are identical to (B.14), (B.15), and (B.17), respectively, but that (B.25) and (B.27) are different to (B.16) and (B.18) respectively. The rectifier will be in the continuous mode when

$$0.5 < \pi\omega C_{out} R_L\left(1+V_{df}\right). \tag{B.28}$$

Hence, the boundary between the continuous and discontinuous modes of rectifier operation occurs at $\pi\omega C_{out} R_L\left(1+V_{df}\right) = 0.5$. Again, this model is assumes that the ripple on the currents through the filter inductors is negligible [1].

References

[1] A. J. Forsyth, G. A. Ward, and S. V. Mollov, "Extended fundamental frequency analysis of the LCC resonant converter," *IEEE Transactions on Power Electronics*, vol. 18, pp. 1286-1292, 2003.

[2] M. P. Foster, H. I. Sewell, C. M. Bingham, D. A. Stone, and D. Howe, "Methodologies for the design of LCC voltage-output resonant converters," *IEE Proceedings - Electric Power Applications*, vol. 153, pp. 559-567, 2006.

Appendix C - Amplifier schematic

A schematic diagram of the amplifier that was used to conduct the PT power tests described in Chapter 4 is shown in Figure C.1.

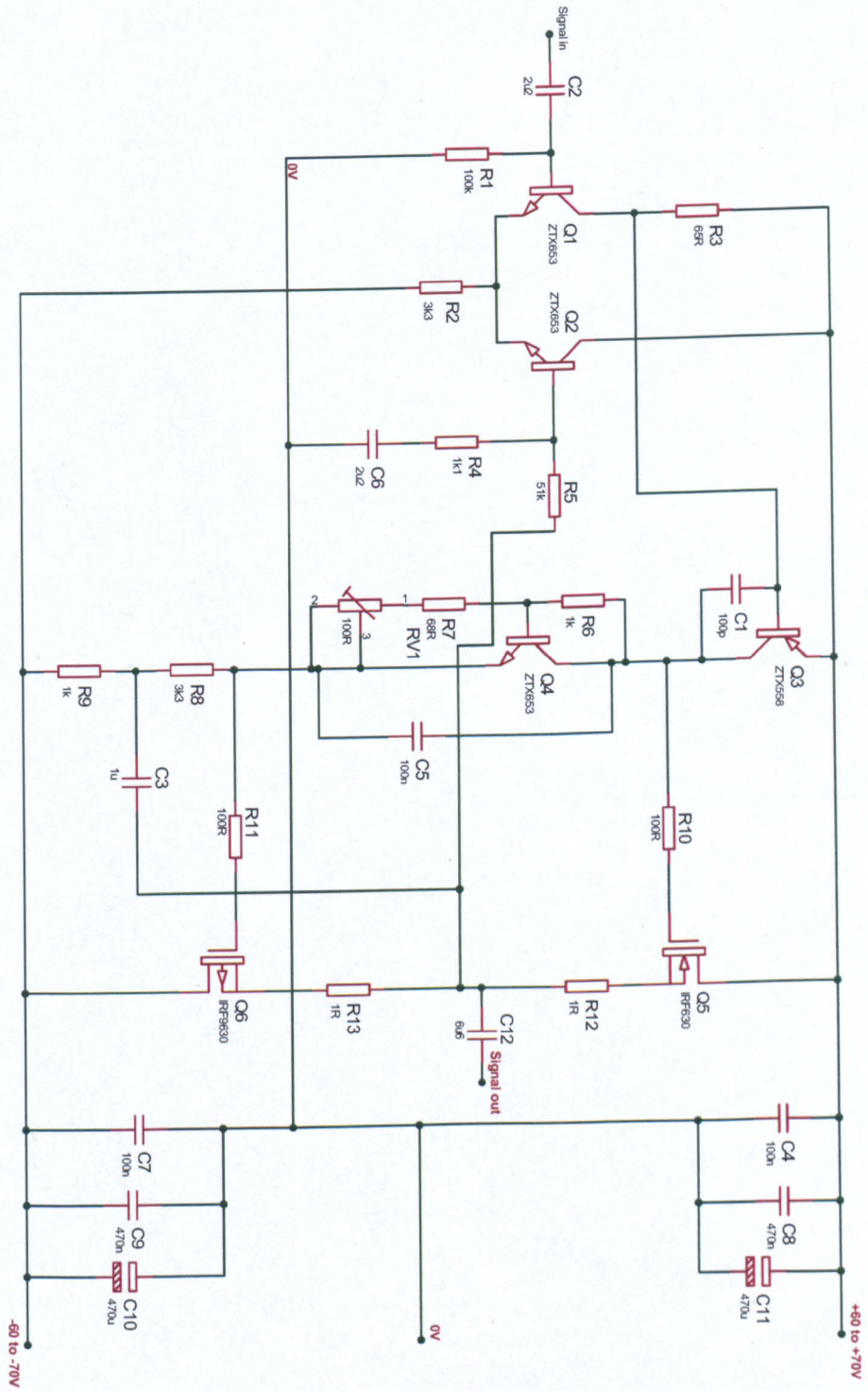

Figure C.1: Amplifier schematic.